

NORTHWESTERN UNIVERSITY

Development of Delivery Vehicles and 3-Dimensional Cancer Models to Investigate
Gli Inhibition in Basal Cell Carcinoma

A DISSERTATION

SUBMITTED TO THE GRADUATE SCHOOL
IN PARTIAL FULFILLMENT OF THE REQUIREMENTS

for the degree

DOCTOR OF PHILOSOPHY

Field of Chemistry

By

Meghan W. Dukes

EVANSTON, ILLINOIS

September 2022

© Copyright by Meghan W. Dukes 2022

All Rights Reserved

Abstract

Development of Delivery Vehicles and 3-Dimensional Cancer Models to Investigate

Gli Inhibition in Basal Cell Carcinoma

Meghan W. Dukes

The worldwide community of patients affected by Basal Cell Carcinoma of the skin (BCC) is larger than that of any other cancer. While BCC is rarely lethal, currently available treatment strategies often leave patients with disfiguring scars on their faces, heads, and necks. Moreover, the high recurrence rates of BCC require patients to be conscious of tumor growth throughout the entirety of their lives. This presents two primary research needs for the BCC field at large: 1) more effective treatment strategies that can circumvent the need for surgical resection and 2) strategies to prevent the re-growth of BCC for existing patients. This thesis describes efforts towards addressing both needs with a focus on fundamental understanding of the driving forces in BCC pathology and intervention.

The first focus is towards rational design of therapeutic strategies to inhibit the Hedgehog (Hh) signaling cascade, the primary oncogenic driver in BCC. Gli transcription factors, the ultimate regulators of Hh signaling, are an attractive target for therapeutic intervention. Cobalt complexes interact with the zinc binding loci of these transcription factors, altering secondary structure and DNA binding affinity. Chapter 2 describes a cobalt complex targeted to Gli and efforts towards delivering it intracellularly for inhibition of Hh pathology in an *in vitro* BCC assay.

The second focus is understanding the process of early Hh activation in cellular systems to elucidate mechanisms connecting pathway activation to oncogenesis. Chapter 3 describes exogenous activation of Hh signaling at two different points in the pathway, mimicking two

different mutations observed in BCC. Hh inhibitors are explored for their potential to prevent Hh activation in a cellular model of organogenesis. Further, the activation of Hh signaling is explored in normal human epidermal keratinocytes (NHEK), the population of cell in which BCC arises.

Chapter 4 describes the development of more complex 2-dimensional and 3-dimensional cellular assays with the ASZ murine BCC cell line to evaluate established disease progression. The first assay explores transwell migration of ASZ cells through a porous membrane and response to Hh inhibition. The second explores the incorporation of ASZ cells into a 3-D organotypic model of the fully stratified human epidermis. The changes in tissue phenotype and pathology are explored in response to increasing cancer incorporation as well as Gli inhibition. Ultimately, the first reported 3D model of BCC is described that mimics pathology of patient BCCs and is responsive to Gli inhibition.

Acknowledgements

There are so many people to thank for helping me get to the point of finishing this degree that a few pages do not seem to do them justice, but each deserves for me to try. I would first like to thank Prof. Tom Meade for giving me a home in his lab. It did not take you long to figure out that I am independent and stubborn. You always pushed me to think about when my stubbornness was productive or foolish but gave me the space to figure that out on my own. You did not second guess me when I wanted to transition my research into the world of biology and supported my goals every step of the way. Thank you for your support and encouragement, and for genuinely caring about my scientific, professional, and personal development.

To Prof. Bethany Perez-White, you are brave for adopting a chemist and giving your time and energy to teaching me how to also be a biologist. I am forever thankful for the techniques I learned and the radically cool experiments I did in your lab. But even more-so, I am thankful for the lasting professional relationship and friendship we have built. Thank you for helping keep me and my husband sane during the summer months by providing us a patch of water and a boat. Your property will always be the place I caught my biggest fish in the Illinois/Indiana area.

To my senior lab mates: there has never been a dull moment or boring season in the Meade lab. Liz, Kaleigh, and Mike; thank you for being voices of wisdom through my earliest years of graduate school and teaching me the tools for survival. Shaunna, I loved our lab chats and every WISER event we did together. You were an inspiration for me to be involved with more than just research in graduate school. Chris, I will never forget the days that you and I supported a 2-man subgroup. You have taught me more than I can ever express. You are an intelligent and downright fun person to have meeping around. Andrew, I always knew we could commiserate over achy-breaky bodies and struggles synthesizing on DNA strands. The three of

you made me feel welcomed into the lab and like a part of the family. To Tyler, Matt, Jian-hong, and Hyun, none of you were there when I joined the lab, but you brought stability and expertise that we greatly benefitted from. Matt, I always enjoyed our rides to the train station and venting about whatever the chosen topic was that day while always reminding ourselves that life is good.

To Hao, Casey, and Megan Kaster: it has been an honor to serve with you as the 2017 Meade lab Fantastic 4. I could not have asked for a better cohort of friends to battle through grad school with. Hao and Casey, I enjoyed listening to you banter in lab and appreciate the way you kept it a positive environment. You were both incredible coworkers. Megan, I never imagined I would be sharing a lab and a desk with someone with my same name. I have cherished your friendship and companionship on this journey: between NRSA season, snack runs, video game nights... I could not have survived or achieved this without you. And if you ever need a career fallback, I will personally recommend you as a bachelorette party planner.

To my mentees: Olivia, Kalea, and Hendryck. Olivia, you were my Guinea pig mentee, and you were such a joy to train. You represent women in STEM on huge stages and I am immensely proud to have been a part of your trajectory. Kalea, you will never know how much your enthusiasm for research got me through the summer of 2021. Every graduate student has (at least) one absolutely insane season where they cannot tell up from down, and you kept me oriented. It was an honor to be your teacher in both orgo and research, and I cannot wait to see where your future takes you. I hope it involves a lot of Excel spreadsheets. Hendryck, you have a passion for both medicine and science that is unmatched. You certainly are not afraid to tackle hard things and dream big. Never forget to celebrate the victories and learn from every loss. I am sad to be leaving before I watch you become a PhD candidate, but I have every faith in you.

To my friends: First to Megan Wasson and Sylvia, the other half of EminemineminEs (Megan, Megan, Meghan, and Sylvia), you have been an endless source of support and fun. We may not have been very good at predicting what events might take place at the start of every new year but at least we had fun guessing. You two are beautiful souls and I am so lucky to know you. To Molly: ever since that first IBiS retreat that I actually knew someone I have been so thankful for our friendship. There are not many people that would run through the snow to buy more cookie dough to bail me out of a shortage preparing for a WISER event. You have been a fiercely loyal friend and I hope to have been the same for you. To Meghan Masotti: I thought my heart was at capacity for Meg(h)ans before you came along. Turns out there was a massive hole only you could fill. Thank you for beach days, long walks, and all of the best conversations. You are a treasure. Tim, Kenton, and Rodrigo, I have had so many fun adventures with you all and am thankful to have been in your cohort. To think that it all started one night at a magic show...

I had the pleasure throughout my experience at Northwestern to be involved in several extracurriculars. To the wonderful women I served with on the WISER board, I am proud of everything we were able to accomplish, especially during an international pandemic when community was hard to find. I would like to particularly thank Becca Harmon and Rebecca Rasmussen for helping me launch an initiative to benefit the broader NU community. I would also like to thank the 2019 HerStory board members, especially my partner-in-crime Jill Rosenberg. It was an honor to co-direct the event with you and devastating that we only got to do it once. Lastly, I would like to thank the Northwestern Athletic Department Tutoring Program for allowing me to hone my teaching skills and meet some truly awesome undergraduate student athletes. I wish you all the best, and hope I was able to make organic chemistry slightly less miserable.

To my family: thank you for always supporting me and believing in me. I do not come from a line of scientists but was taught to believe that I could accomplish anything I set my mind to if I am willing to work hard and sometimes make sacrifices. Mom, you are wise beyond words, but it always makes me laugh when you read something I've written and go "I know some of those words!" But you read it anyway because you are proud. I will never take that for granted. Dad, you raised me to 1) never be late, 2) never be stupid, and 3) never settle. I've tried to stick to those rules as much as possible, and I attribute a lot of where I am today to just that. It seems weird to thank you for having the cancer that inspired this work, but I suppose that is appropriate, too? Michael, we may not always have gotten along very well, but I think I might have to thank you for that. There was a period of my life that I wanted to do the exact opposite of everything you did. Maybe that's why I became a scientist. I love you three dearly.

To save the best for last: thank you to my husband, Cory. This road of ours has not been easy at a single step, but no one could ever support me, make sacrifices for me, and encourage me the way you have and do. You have caught so many tears, shared so many laughs, and witnessed every other emotion that comes with being a graduate student. You have been my rock, my best friend, and my number one fan. I have loved every adventure we have taken in this city as ways of remembering that there is so much more to life than school. And so much more to me than research. Thank you for lifting me up and carrying me when I need you (quite literally when I had to have back surgery in my last four months of graduate school). I love you forever. Thank you for being the reason I can call myself Dr. Dukes.

List of Abbreviations

General

AuNP	gold nanoparticle
BCC	basal cell carcinoma
BSA	bovine serum albumin
CA	contrast agent
CD	circular dichroism
CEST	chemical exchange saturation transfer
CT	computed tomography
DMT	divalent metal transporter
ESC	embryonic stem cell
FBS	fetal bovine serum
FDA	food and drug administration
GS	Gorlin Syndrome
H&E	hematoxylin and eosin
Hh	hedgehog
ICP-MS	inductively coupled plasma-mass spectrometry
iPS	induced pluripotent stem cell
IR	infrared
laBCC	locally advanced basal cell carcinoma
mBCC	metastatic basal cell carcinoma
MMS	Mohs micrographic surgery

MRI	magnetic resonance imaging
MSC	mesenchymal stem cell
NCS	Normal calf serum
NHEK	normal human epidermal keratinocyte
NMSC	non-melanoma skin cancer
NSC	neuronal stem cell
NTC	non-treated control
ParaCEST	paramagnetic chemical exchange saturation transfer
PDT	photodynamic therapy
PDX	patient derived xenograft
PET	positron emission tomography
QD	quantum dots
qPCR	quantitative real time-Polymerase Chain Reaction
ROS	reactive oxygen species
SPECT	single photon emission computed tomography
SPIO	superparamagnetic iron oxide
TGA	thermogravimetric analysis
UV	ultraviolet
UV-Vis	ultraviolet-visible
WLE	wide local excision
ZnFTF	zinc finger transcription factor
ZP	zeta potential

Chemicals/compounds

$^1\text{O}_2$	singlet oxygen
5-FU	5-florouracil
acac	acetylacetone
AMP	acetoxymethoxy carbonyl porphyrin
ATO	arsenic trioxide
CaCl_2	calcium chloride
Co(III)-SB	cobalt (III) Schiff base
CO_2	carbon dioxide
DBN	desferrioxamine-NCS
DOTA	1, 4, 7, 10-tetraazacyclododecane
DTPA	diethylenetriaminepentaacidic acid
EDC	1-ethyl-3-(3-dimethylaminopropyl)carbodiimide
ETP	5, 10, 15, 20-tetrakis(ethoxycarbonyl) porphyrin
GANT	gli antagonist
GlaB	glabrescione B
GO	graphene oxide
GRID	gadolinium rhodamine dextran
H_2O_2	hydrogen peroxide
HCl	hydrochloric acid
MDQ	Bis(2-methyldibenzo[f,h]quinoxaline
MgCl_2	magnesium chloride
NaCl	sodium chloride

NaOH	sodium hydroxide
PEI	polyethyleneimine
PLGA	poly(lactic-co-glycolic acid)
PNH ₂	5-(4-aminophenyl)-10, 15, 20-tris(4-sulfonatophenyl) porphyrin
pNPP	para-nitrophenyl phosphate
PTSM	pyruvaldehyde bis(<i>N</i> 4-methylsemicarbazone
SAG	smoothened agonist
TBDPS	tert-butyl(chloro)diphenylsilane
YAG	yttrium aluminum garnet
ZnCl ₂	zinc chloride

Symbols and Units

°C	degrees Celsius
μg	microgram
μL	microliter
μM	micromolar
μm	micrometer/micron
cm	centimeter
cm ⁻¹	wavenumber
g	gram
hr	hour
IC ₅₀	half maximal inhibitory concentration
kDa	kilodalton

M	molar
M_0	net magnetization vector
mg	milligram
min	minute
mL	milliliter
mm	millimeter
mM	millimolar
mmol	millimole
mV	millivolt
ng	nanogram
nM	nanomolar
nm	nanometer
R_1	longitudinal relaxation rate
R_2	transverse relaxation rate
T_1	longitudinal relaxation time
T_2	transverse relaxation time
W	Watts
λ	Wavelength
<i>Proteins</i>	
ALP	alkaline phosphatase
DSC-1	desmocollin-1
DSG-1	desmoglein 1

ECAD/CDH1	E-cadherin
FLG	filaggrin
Gli	glioma associated oncogene
HECD-1	human E-cadherin
K10	keratin 10
K16	keratin 16
K17	keratin 17
MKL1/2	megakaryoblastic leukemia 1/2
p53	tumor suppressor p53
PTCH1	patched 1
SHH	sonic hedgehog
SMO	smoothened
SUFU	suppressor of fused
ZnFtf	zinc finger transcription factor

List of Figures

Figure 1.1: Chemical structures of imiquimod and 5-fluorouracil. Imiquimod functions through an immunomodulatory response, and 5-fluorouracil inhibits DNA synthesis machinery. These treatments are effective topically against low-risk superficial BCC.....38

Figure 1.2: Key regulators of the Hedgehog signaling cascade. **1.** Hh signaling is activated by the binding of Hh proteins (Sonic hedgehog, Indian hedgehog, and Desert hedgehog) to the transmembrane protein Ptch1. **2.** Ptch1 is a native suppressor of Smo activity. Upon the binding of Hh proteins, inhibition is released. **3.** Upon activation, Smo signals for the Sufu complex to release the Gli family of transcription factors. **4.** Gli transcription factors are activated in the cytosol prior to translocating into the nucleus. **5.** Gli transcription factors transcribe pro-proliferative and migratory genes that lead to tumorigenesis in BCC. Crystal structures images were made from the following Protein Data Bank files: Ptch1/SHH complex, 6N7H. Smo, 6D35. Sufu/Gli complex: 4BLB. Gli1, 2Gli.....40

Figure 1.3: Chemical structures of smoothed inhibitors A) Cyclopamine. B) Vismodegib. C) Sonidegib. While distantly related to Cyclopamine, Vismodegib and Sonidegib contain structural similarities. All three inhibitors bind SMO in the same pocket. D&E) New generation Vismodegib derivatives developed by Li et. al in 2019.....42

Figure 1.4: Chemical structures of withaferin A derivatives, novel SMO inhibitors that structurally deviate from Vismodegib. A) Chemical structure of natural product withaferin A. The highlighted scaffold is believed to be important for SMO binding. B &C) The Waldman group developed derivatives of withaferin A that exhibited stereoselective potent inhibition of SMO. D) The target compound of the Passarella group for SMO inhibition did inhibit the Hh pathway. * represents asymmetric carbon. C&D) Synthetic intermediates 13b and 14b exhibited stereoselective inhibition of SMO, elucidating important polarity considerations for protein interactions.....44

Figure 1.5: Chemical structures for small molecule Gli inhibitors. A) Arsenic trioxide downregulates Gli activity but is unknown to bind directly. B) GANT-61 is the gold standard for direct Gli inhibition. In aqueous solution, it undergoes hydrolysis to unmask the active inhibiting scaffold. C) Glabrescione B binds directly to Gli in disrupt the DNA binding interaction. D) Structural modifications to GlaB elucidate chemical modifications that maintain or prevent Gli inhibition E) A dual-targeted compound that inhibits both SMO and Gli. F) A new bicyclic imidazolium structure found to inhibit Gli proteins.48

Figure 2.1: AlphaFold predicted structure for the Gli1 transcription factor (AlphaFold entry P08151 (GLI1_HUMAN)). The majority of the structure is predicted to adopt random coil secondary structure. The core of the structure, the DNA binding region, is predicted to adopt a series of alpha-helical secondary structure. The software states that blue represents high to moderate confidence (>70 pLDDT), yellow signifies low confidence (between 70 and 50 pLDDT) and orange signifies very low confidence (<50 pLDDT) of the prediction. The overall low prediction confidence is likely due to high degree of protein disorder.....59

Figure 2.2: Crystal structure of the Gli1 DNA binding domain. Within this region, there are 5 Cys₂His₂ zinc(II) coordination sites. The zinc ions are responsible for maintaining alpha-helical structure that interacts with the major and minor grooves of DNA. Blue represents Gli1, orange represents that DNA binding partner, pink represents zinc(II) ions, and green represents the cysteine and histidine residues that coordinate zinc(II).....60

Figure 2.3: Schematic representations of Co(III)-SB complexes binding histidine residues in proteins. A) Co(III)-SB undergoes axial ligand exchange for preferential binding of imidazole motifs in histidine residues. B) In zinc finger proteins, Co(III)-sb punches zinc ions out of tetrahedral pockets and binds histidine residues octahedrally. This elongates alpha-helical structure necessary for DNA binding.....61

Figure 2.4: Co(III)-SB complexes degrade alpha helical content of Gli1 and prevent DNA binding. A) Circular Dichroism results with increasing concentrations of Co(III)-SB in Gli1 buffer. Alpha helical features at 220 and 208 nm are reduced with increasing Co(III)-SB. B) Interferometry results of protein binding to DNA attached to instrument surface. Binding is reduced significantly upon increasing Co(III)-SB concentration. C) EMSA results for Gli1/DNA binding. Fluorescent DNA is used for assaying DNA binding. The Gli-bound DNA band disappears with increased Co(III)-SB which is quantified using image intensity analysis. For all experiments, equivalencies are calculated in respect to the whole protein. For example, 1 eq. of Co(III)-SB means one Co(III)-SB for each protein unit and one Co(III)-SB for 5 zinc binding sites. 5 eq of Co(III)-SB represents a 1:1 Co(III)-SB:zinc finger ratio. *Data by Chris Brue, publication co-authored by Meghan Dukes*.....62

Figure 2.5. Inhibition of Ci and Ebox ZnFTFs in *Drosophila* and *Xenopus* embryos. A) Wild type *Drosophila* show proper formation of denticle belts. B) Treatment with Co(III)-Ci results in fusion of denticle belts, representing improper formation. C) Mutating the DNA sequence tethered to Co(III)-SB by two base pairs causes phenotypic replication of the non-treated wild type. D) Genetic knockdown of Ci causes fusion of denticle belts. E) Experiments of Snail inhibition in *Xenopus*. Treatment with Co(III)-Ebox causes prevention of neural crest migration, whereas mutating the tethered DNA sequence by 2 base pairs phenotypically mimics the untreated control. F) Structure of Co(III)-Ci. G) Structure of Co(III)-Ebox.....64

Figure 2.6. Fluorescence quenching experiments of 5ssCoGli and unmodified GO based on identity and concentration of salt. A) Fluorescent quenching curves in the presence of NaCl. B) Fluorescence quenching curves in the presence of MgCl₂. C) Fluorescence quenching curves in the presence of ZnCl₂. D) Quantification of loading in units of mg 5ssCoGli/g GO. Since the initial conditions contained 23.6 µg of 5ssCoGli and 50 µg GO, the maximum loading potential is calculated at 472, denoted by the dashed horizontal line.....68

Figure 2.7. Fluorescence quenching results of fixed amounts of 5ssCoGli (23.6 µg) and 0.5 and 0.25 mM MgCl₂ and ZnCl₂ as the amount of GO varies. Evaluated ratios were 1:2, 1:2, 2:1, and 4:1 5ssCoGli to GO. A) Results for quantification of mg 5ssCoGli loaded per g of GO. B) Percentages of 5ssCoGli loaded compared to the calculated maxima of 472, 944, 1888, and 3776

mg 5ssCoGli/g GO for 1:2, 1:1, 2:1, 4:1 weight ratios, respectively. Data show that loading is similarly efficient at 0.5 and 0.25 mM salt at a 1:2 weight ratio. Reducing GO past this point results in loss of complete loading, especially for 0.25 mM of either salt.....69

Figure 2.8. Cytotoxicity of ASZ murine BCC cells in the presence of 5ssCoGli@GO at a 1:2 weight ratio loaded by 0.25 mM MgCl₂ and ZnCl₂. No significant differences are observed between the two salt identities at each concentration of 5ssCoGli. However, significant cytotoxicity is observed as the concentration of 5ssCoGli increases, resulting in an unavoidable rise in salt concentration.....71

Figure 2.9. Internalization of 5ssCoGli as determined by ICP-MS as a function of media serum composition and dosing ratio of 5ssCoGli:GO. Internalization is not observed in full serum media. Internalization is slight improved upon reduction of serum, but this is not amplified by the addition of excess GO.....72

Figure 2.10. Tracking media-induced release of 5ssCoGli from GO as a function of serum composition and 5ssCoGli:GO ratio. A) Fluorescence recovery curves. B) Calculated percentage of 5ssCoGli released. In 2% Serum media, 1:2 and 1:4 5ssCoGli experience significant desorption from the GO surface that maximizes in 30 minutes. While the 1:2 weight ratio experiences a similar result in serum free media, the addition of excess GO protects the 5ssCoGli from desorption.....74

Figure 2.11: Synthesis and characterization of GOPEI. A) Schematic representation of GOPEI synthesis from GO-COOH. GO-COOH is prepared via the reaction of chloroacetic acid with reactive oxygen functional groups on GO. Following purification, GO-COOH is combined with PEI and EDC to covalently link PEI to the GO surface. B) IR spectra of GO-COOH and GOPEI variants. Red shifting of carbonyl peak suggests conversion of carboxylic acids to amides. C) TGA of GO-COOH and GOPEI. Increased mass loss of GOPEI represents removal of PEI groups from the surface.....77

Figure 2.12: Fluorescence intensity changes over time. Fluorescence is quenched during capture by PEI and GOPEI. Fluorescence is not quenched by non-PEI bearing GO.....79

Figure 2.13. Loading of dsCoGliF onto PEI and GOPEI species. A) Fluorescence quenching curves of dsCoGli on GO-2kDa-PEI at varying weight ratios of dsCoGli:GOPEI. . B) Fluorescence quenching curves of dsCoGli on GO-25kDa-PEI at varying weight ratios of dsCoGli:GOPEI. C) Quantification of loading of dsCoGli onto GOPEI variants. Loading for GO-2kDa-PEI maximizes around 400 mg/g, whereas loading on GO-25kDa-PEI maximizes around 700 mg/g. D) Quantification of dsCoGli capture by free PEI. Free PEI at 2 and 25 kDa can efficiently capture up to 4x their average weight of dsCoGli.....80

Figure 2.14. 24 hour Cytotoxicity of 2 and 25 kDa free PEI and tethered GOPEI species. A) Toxicity of 2 kDa variants. B) Toxicity 25 kDa species. Lines at 90% viability represent cutoffs for concentrations of delivery vehicles that can be used in further cellular assays. GO-2kDa-PEI

is the least toxic, with GO-25-kDa-PEI and 2 kDa free PEI having similar toxicity, and 25 kDa free PEI is the most cytotoxic.....81

Figure 2.15. Evaluation of GOPEI variant inertness to Hh signaling via qPCR. Both Gli1 and Hhip transcripts are directly produced via activity of Gli transcription factors and the Hh signaling cascade. While GO-2kDa-PEI does not significantly reduce production of these transcripts compared to the non-treated control, GO-25kDa-PEI does to a similar extent as GANT-61, a known Hh inhibitor. This suggests GO-2kDa-PEI is the superior choice for further cellular studies of CoGli delivery.....83

Figure 2.16: Internalization of CoGli. A) Fluorescently labeled (AlexaFluor488) CoGliF is loaded onto PEI or GOPEI and dosed onto ASZ cells in 2% serum media for 24 hours. Internalization is visualized 24 hours later via confocal microscopy. Green channel: CoGliF (excitation @ 488 nm) Blue channel: DAPI nuclear stain (excitation at 405 nm). B) Non fluorescently labeled CoGli is loaded onto PEI or GOPEI and dosed onto ASZ cells. Cells are trypsinized after 24 hours and are counted prior to digestion for ICP-MS analysis of internalized cobalt. Bars represent mean and standard deviation of triplicate samples. PEI and GOPEI loading ratios were 3:1 and 1:4 dsCoGli(F):Nanocarrier, respectively.....84

Figure 2.17: Lysosomal escape of dsCoGli delivered by GO-2kDa-PEI. A) Representative images of lysosomal escape of dsCoGliF. Blue: DAPI nuclear stain (excitation at 405 nm). Green: CoGliF (AlexaFluor488, excitation at 488 nm). Magenta: LysoView633 (excitation at 633 nm). B) Quantification of percent colocalization of CoGliF and LysoView633. Bars represent mean and standard deviation. T-test analysis was performed to show statistically significant reduction in colocalization 24 hours after the removal of CoGliF at a confidence interval of 99% (**)......86

Figure 2.18: ASZ scratch assay results. A) Representative images of (left to right) non-treated control, 300 nM CoGli@GO-2kDa-PEI, 5 μ M GANT-61, and 300 nM GANT-61. White lines are included for clarity and represent the cell-free area of each condition. B) Normalized scratch healing results. Non-treated controls were normalized to 100% scratch healing after 48 hours, and all other conditions were adjusted proportionally. Bars represent the mean and standard deviation of conditions tested in triplicate. The 99.9% confidence interval for statistical significance is represented by ***. No statistical significance was observed for the comparisons between NTC, GOPEI, and 300 nM GANT-61. Similarly, no statistical significance was observed between 300 nM CoGli@GO-2kDa-PEI and 5 μ M GANT-61. A full table of ANOVA results, as well as a T=0 and T=48 hours photos for every replicated are in Experimental Section 2.4 (Table 2.3, Figure 2.20).....87

Figure 2.19. Cytotoxicity of dsCoGli carried by GO-2kDa-PEI and GANT-61 in the ASZ cell line. A) Toxicity of dsCoGli delivered at a 1:4 weight ratio to GO-2kDa-PEI. Significant toxicity is not observed up to 800 nM. B) Toxicity of GANT-61. Some toxicity is observed at 10 μ M, but not at 5 μ M. Dotted lines on each graph represent the concentration texted in the scratch migration assay. Significant toxicity is not observed at these concentrations (300 nM dsCoGli, 5 μ M GANT-61).....89

Figure 2.20: Scratch wound healing images. Triplicate results for scratch wound healing of ASZ cells in response to A) non-treated control, B) GO-2kDa-PEI control, C) 300 nM CoGli@GO-2kDa-PEI, D) 5 μ M GANT-61, and E) 300 nM GANT-61. NTC and GOPEI were tested at n=5 and all other conditions at n=3. The wound area at T=0 and T=48 was measured via ImageJ and statistical analysis was carried out via one-way ANOVA in GraphPad Prism.....98

Figure 3.1: Quantification of ALP concentration in cell lysates in response to Hh activators. Both ALP and total protein concentration were determined and ng of ALP/mg of total protein was calculated for each sample. To normalize across biological replicates, the NTC samples were normalized to 0 by dividing each sample by the group average. The treated samples were normalized similarly by dividing by the same group average of the NTC samples. The multiplicity for 100 nM SAG is 7.6 ± 0.71 and for 30 nM SHH is 9.2 ± 1.3 , which were not statistically different from one another using one-way ANOVA analysis. Analysis was performed in GraphPad Prism and error bar represent the mean \pm the standard error of the mean. A high concentration of SHH, 50 nM, resulted in 22 ± 2.2 fold concentration increase, a concentration that could not be matched by small molecule SAG. Error bars represent the mean \pm one standard error of the mean.....104

Figure 3.2: Cytotoxicity of various Hh inhibitors in the C₃H/10T_{1/2} cell line. A) Cytotoxicity of DMSO at various volume/volume percentages in cell media. The cells display high sensitivity to low percentages of DMSO. B-D) Cytotoxicity of Vismodigeb, Cyclopamine, and GANT-61 respectively. For all three compounds, cytotoxicity is not observed out to 10 μ M. It is concluded that these concentrations can be safely studied for inhibition of Hh initiation without the risk of confounding cell death with prevention of differentiation. The chemical structure for each compound is given in the bottom left corner of each respective graph. Error bars represent the mean \pm one standard deviation.....105

Figure 3.3: Prevention of C₃H/10T_{1/2} differentiation by smoothed inhibitors in response to SHH and SAG activators. A) Inhibition by Vismodigeb. Vismodigeb prevents activation by SHH at an IC₅₀ around 10 nM and activation by SAG at approximately 70 nM. B) Inhibition by Cyclopamine. When activated by SHH, Cyclopamine prevents 50% of differentiation around 100-200 nM. When activated by SAG, inhibitions is not observed. C) Off-competition of Cyclopamine by SAG. When Cyclopamine concentration is held constant at 150 nM, 50 nM SAG is sufficient to produce 73% of differentiation observed by the 100 nM SAG-only positive control. These data suggest that smoothed inhibitor efficacy is dependent on the point of Hh pathological onset, and different inhibitors experience different degrees of this affect. Error bars represent the mean \pm one standard deviation.....107

Figure 3.4: Prevention of C₃H/10T_{1/2} differentiation by GANT-61 with SHH and SAG activators. Regardless of activation point, GANT-61 prevents roughly 50% of differentiation at approximately 3 μ M. Error bars represent the mean \pm one standard deviation.....109

Figure 3.5: Proliferation results of NHEK cells in response to SHH and SAG. A) Acute treatments result in mild increases in proliferation over non-treated cells across 3 biological replicates. B) Chronic treatment 5 days prior to experiment plating results in slight increases in

proliferation in one biological replicate. C&D) Chronic treatment for 5 days does not significantly increase proliferation over acute treatment for both SAG and SHH, respectively. Error bars represent the mean \pm one standard error of the mean.....111

Figure 3.6: Proliferation response to acute SAG and SHH by donor. Donors 1&2 were both sensitive to activators early, but differed in which activator they were more responsive to. Donor 3 was non-responsive until Day 4, and even then only significantly responsive to SHH. Error bars represented the mean \pm one standard error of the mean.....112

Figure 3.7: Influence of SAG and SHH on NHEK migration in a scratch wound healing assay. A) Across four different biological replicates from different cell donors, migration was either unchanged (Donors 2, 3) or reduced (Donor 1,4). This affect is amplified for Donor 4 upon chronic treatment of the inhibitors for 5 days prior to plating the experiment. Bars represent the mean \pm one standard error of the mean. B & C) Representative images for Donor 3 and Donor 4 for acute treatment with SAG and SHH. Donor 3 shows near-complete wound healing for each condition. Donor 4 shows reduced migration for cells treated with Hh activators.....113

Figure 4.1: Transwell migration results of ASZ cells treated with Vismodegib and GANT-61. A) Representative images from non-treated, 250 nM, 500 nM, and 1 μ M Vismodegib treatment. B) Normalized migration results for Vismodegib. C) Representative images from non-treated, 0.5 μ M, 2.5 μ M, and 7.5 μ M GANT-61. D) Normalized migration results for GANT-61. Graphs represent the mean \pm one standard deviation. The number of migrated cells were counted according to a developed ImageJ macro described in Section 4.4.....125

Figure 4.2: Histological (H&E) analysis of 3D co-culture tissues harvested on Day 5. A) 100% NHEK non-diseased tissue. Cells in the stratum spinosum develop structural order and a prolate spheroid (football) shape. B) 90% NHEK/10% ASZ. Organization is lost and shape of cells is elongated. C) 75%NHEK/25% ASZ. All organization and structure of cells is lost, some groups of cells are seen protruding into the dermis layer. D. 50% NHEK/50% ASZ. The basement membrane that separates the dermis from the epidermis is lost completely. The cornified layer that represents the beginnings of terminal differentiation is nearly non-existent.129

Figure 4.3, Part 1: Representative images of co-culture tissues from biological Donors 1 and 2 after 12 days of differentiation. Zoomed-in sections from Donor 2 show loss of keratohyalin granules with as little as 10% cancer incorporation. Thickening of the epidermal layer is also observed with loss of cornified layer thickness with increasing ASZ incorporation.....131

Figure 4.3, Part 2: Representative images of co-culture tissues from biological Donors 3 and 4 after 12 days of differentiation. Consistent trends of overall epidermal thickening, loss of keratohyalin granules, loss of cellular organization and structure, and eventual formation of tumoroid-like pockets can be seen across the range of cancer incorporation for all biological donors.....132

Figure 4.4: Statistical analysis of thickness of epidermal components across four biological donors of 12-day differentiation. A, C, E) Results for total epidermal thickness by donor, % viable layer by donor, and % cornified layer by donor, respectively. B, D, F) Results for combined total epidermal thickness, combined % viable layer, and combined % cornified layer, respectively. Generally, the total epidermal thickness and the % viable layer of the whole are increased across cancer incorporation. Inversely, the % cornified layer of the whole is significantly decreased. Graphs were made in GraphPad Prism, and one-way ANOVA analysis was used to determine statistical significance at $\alpha=0.05$. Bars represent the mean \pm one standard error of the mean. ***= 99.9% confidence interval, ****= 99.99% confidence interval. Ns= not significant.....133

Figure 4.5: qPCR analysis of cytoskeletal components after 5 and 12 days of co-culture differentiation. A) *KRT10* evaluation of Day 5. B) *KRT17* evaluation of Day 5. C) *KRT16* evaluation of Day 5. D) *KRT10* evaluation of Day 12. E) *KRT17* evaluation of Day 12. F) *KRT16* evaluation of Day 12. Each donor has only one data point, so bars represent the mean \pm one standard deviation contributed by 4 biological donors for Day 5 and 4 biological donors for Day 12. Donors 1-3 for Day 5 are the same as donors 1-3 of Day 12. Days 4 and 5 are not the same. Individual donor values are represented as Donor 1: pink triangle, Donor 2: Green square, Donor 3: Blue circle, Donor 4: purple upside-down triangle, Donor 5: orange hexagon. *KRT10* expression is generally decreased while *KRT17* and *KRT16* are increased at Days 5 and 12. Primer sequences used for qPCR were specific to human transcripts.....137

Figure 4.6: Immunostaining of keratin components of cytoskeletal structure in co-culture tissues across the range of cancer incorporation. Left, green KRT10 (donor 1). Middle, green KRT17 (donor 4). Right, pink KRT16 (donor 1). Blue is DAPI nuclear stain. With increasing cancer incorporation, KRT10 is decreased in the human cell populations while KRT17 and Krt16 conversely increase. KRT17 localization changes from the basal layer in 100% NHEK to localizing throughout the suprabasal layer with increasing cancer incorporation. KRT16 localization similarly changes from minimal stratum spinosum localization to being strongly produced throughout the suprabasal layer. Changes for KRT16 and KRT17 are seen immediately in the 90% NHEK/10% ASZ samples.....138

Figure 4.7: qPCR and immunofluorescence analysis of E-cadherin in co-culture models. A) qPCR results for each donor after 5 days of differentiation. B) qPCR results for each donor after 12 days of differentiation. C) Immunofluorescent staining of pan-E-cadherin (green), human specific E-cadherin (pink/white) and DAPI nuclear stain (blue) at day 12. Locations of only green signal represent the murine cell population. There are no trends in ECAD transcription or protein expression.....140

Figure 4.8: qPCR and immunofluorescence analysis of desmocollin-1 and desmoglein-1 in co-culture models. A) Combined DSC-1 qPCR results for each donor after 5 days of differentiation. B) Combined DSC-1 qPCR results for each donor after 12 days of differentiation. C) Immunofluorescent staining of desmocollin-1 (pink), and DAPI nuclear stain (blue). Intensity of DSC-1 staining is lost with increasing ASZ incorporation. The thickness of the stained layer also decreases until it is lost entirely. Inlets showcase the alteration of cellular shape of the stratum

spinosum. D) Combined DSG-1 qPCR results for each donor after 12 days of differentiation. E) Immunofluorescent staining of desmoglein-1 (pink), basement membrane (pan-laminin, green), and DAPI nuclear stain (blue). Intensity of DSG-1 is lost with increasing ASZ incorporation along with the integrity of the basement membrane.....142

Figure 4.9: Evaluation of FLG transcription and immunofluorescent staining after 5 days of differentiation. A) qPCR results. *FLG* transcription is depleted on a logarithmic scale with as little as 10% ASZ incorporation. Bars represent the mean \pm one standard deviation of the three biological donors. B) Immunofluorescence results from Donor 1. Some FLG is observed in the beginnings of the granular layer for the 100% NHEK tissue. This is lost with as little as 10% ASZ incorporation.....145

Figure 4.10: Analysis of FLG transcription and protein expression in biological donors 1-4 after 12 days of differentiation. A) qPCR analysis of *FLG* in donors 1 and 2. Transcription is lost on the logarithmic scale from the 100% NHEK control. B) Immunofluorescence staining of FLG in donor 1. Intensity of signal is decreased for both donors across the range of ASZ incorporation. Zoomed-in image inlets show this reduction of intensity specifically in the granular layer. C) qPCR analysis of *FLG* transcription of donors 3 and 4. Transcription is increased with lower percentages of cancer incorporation but decreased at 50%. D) Immunofluorescent staining of FLG in donor 4. Even though transcription is increased, protein staining is decreased in trend with Donor 1. Inlets show loss of staining specifically in the granular layer.....146

Figure 4.11: Analysis of Gli1 transcription in both mouse and human cell populations in 3D tissues. A) qPCR results for four biological donors across the range of cancer incorporation. All results are normalized to the 100% ASZ tissue. B) qPCR results for the human cell population in four biological donors across the range of cancer incorporation. No trends are observed. C) H&E image of 100% ASZ sample for visual reference of behavior. Cells burrow into the collagen plug instead of expanding on top of the surface.....147

Figure 4.12: Phenotypic analysis of 75%NHEK/25%ASZ tissue response to GANT-61 in donors 4, 6, and 7. A-C) H&E images of 100% NHEK (top)/ non-treated 25% ASZ models (middle), and 25% ASZ models treated with 10 μ M GANT-61 (bottom)for donors 4, 6, and 7. D-F) Image J measurements were used to determine total epidermal thickness reported in microns. Broadly, ASZ incorporation causes increases in thickness that are reduced upon treatment with GANT-61. G-H) Image J measurements were used to determine the percentage of the cornified layer of the total epidermis. The cornified composition is decreased with ASZ incorporation and can be increased with GANT-61 treatment. Bars represent the mean \pm one standard error of the mean. One-way ANOVA analysis with multiple comparisons was used to determine statistical significance at $\alpha=0.05$. NS= not significant, * = 90% confidence interval, ** = 99% confidence interval, *** = 99.9% confidence interval, and **** = 99.99% confidence interval.....149

Figure 4.13: Evaluation of 75% NHEK/25% ASZ cytoskeletal transcripts (*KRT10*, *KRT16*, *KRT17*) in response to treatment with GANT-61 for cell donors 4 (A), 5 (B), 6 (C), and 7 (D). Treatment results in donor-dependent restoration of transcripts towards a non-diseased sample. Donor 4 experienced the greatest degree of restoration, donor 5 was not responsive to treatment,

and donors 6 and 7 show intermediate responses. Bars represent the mean \pm one standard deviation from 2 technical replicates of each condition.....151

Figure 4.14: GANT-61 treatment of 75% NHEK/25% ASZ tissues results in cytoskeletal structure similar to that of the 100% NHEK controls. A-C) Staining for KRT16 (pink) in donors 4, 6, and 7 respectively. D-F) Staining for KRT17 (green) in donors 4, 6, and 7 respectively. Insets show zoomed-in sections for more clear observation of expression patterns.....153

Figure 4.15: Donor-dependent restoration of filaggrin transcription and cellular localization of 75% NHEK/25% ASZ models following treatment with GANT-61. A, C, E) qPCR analysis of transcription for donors 4, 6, and 7. B, D, F) Immunostaining of filaggrin in donors 4, 6, and 7. Graphs represent the mean \pm one standard deviation from 2 technical replicates for each condition. Insets show zoomed in sections of the stratum granulosum for clearer observation of cell staining patterns. For donors 6 and 7, punctate keratohyalin granules become identifiable and occupy a thicker layer of the tissue following treatment with GANT-61.....155

Figure 4.16: Results of ImageJ cell counting macro for ASZ cells. Left: original image. Right: Image overlaid with the cell counting results. In general, this macro effectively determines cell borders to count each individual cell. It can also distinguish discrepancies in cell sizes.....163

List of Schemes

- Scheme 1.1:** Carton representation of epidermal layers and the growth of BCC. Tumor cells originate from the stratum basale where they maintain stemness and hyperproliferative capacity. As the tumors progress, they begin to migrate through the dermis where they eventually detach from the basement membrane.....31
- Scheme 1.2:** Mechanism of PDT for cellular death. A photosensitizer is delivered to tumor tissue and irradiated with laser light that matches its excitation wavelength. Upon relaxation, energetic crossing transfers the energy to oxygen and water, generating cytotoxic singlet oxygen ($^1\text{O}_2$) and hydrogen peroxide (H_2O_2). Cell death is only observed where the laser light is administered, limited damage to nearby healthy tissue.....37
- Scheme 2.1.** Design of 5ssCoGliF@GO delivery construct. A 5-base pair poly-T overhang attracts 5ssCoGliF to the unmodified GO surface through pi-pi stacking. Due to inherent electrostatic repulsion between the negative GO surface and DNA-bearing 5ssCoGliF, ionic partners are required for loading assistance. Loading and release can be tracked through the fluorescence quenching properties of GO. AF488= AlexFluor488, $\lambda_{\text{excitation}}= 488$, $\lambda_{\text{emission}}=520$66
- Scheme 2.2:** Design of dsCoGli delivery construct. The positive charge contribution from PEI attracts the negative backbone of DNA. Fluorescence quenching properties are maintained upon the addition of PEI, permitting tracking of loading and release. AF488= AlexFluor488, $\lambda_{\text{excitation}}= 488$, $\lambda_{\text{emission}}=520$75
- Scheme 4.1:** Representation of the typical pipeline of cancer chemotherapeutic evaluation. Eventual *in vivo* animal work benefits from more complex cellular systems following simple 2D assays. A heterogenous model that mimics aspects of patient BCCs has not yet been reported for BCC.....126
- Scheme 4.2:** Experimental design for 3D co-culture epidermal tissues. Normal human epidermal keratinocytes (NHEK) cells are mixed with ASZ cells in defined ratios and seeded on top of a collagen dermis mimic. After 2 days, plugs are lifted onto a metal support grid and allowed to differentiate for 5 or 12 days before harvesting. Resulting tissues are analyzed by histological staining, qPCR, and immunofluorescence.....128
- Scheme 4.3:** Layers of epidermal differentiation and locations of differentiation checkpoint markers. Proliferative basal cells exit the cell cycle and differentiate into the stratum spinosum. Cytoskeleton structure and cell adhesion are developed in early stages of differentiation. Further differentiation into stratum granulosum accompanies development of protective barrier function which is completed upon differentiation into the stratum corneum.....135
- Scheme 4.4:** Transwell assay experimental setup for ASZ cells. ASZ cells that have been pre-treated with Hh inhibitors are seeded at 200,000 cells onto a porous membrane in 400 μL of serum-free media with the desired treatment. Below the membrane, a well of a 24-well plate

contains 400 μ L of full serum media plus treatment. Cells migrate for 48 hours prior to fixation, staining, and imaging.....161

Scheme 4.5: Sectioning of 3D tissue for post-harvest analysis. Clean cuts are made with a razor blade on the dashed lines. Sections marked with 1 are peeled from the collagen membrane and lysed in TRIzol for mRNA extraction. The section marked 2 is fixed in neutral buffered formalin for paraffin embedding and ultimate hematoxylin and eosin staining. The section marked 3 is embedded in frozen OCT for immunofluorescence staining.....166

List of Tables

Table 1.1: Select list and commentary of treatment options for BCC.....	34
Table 2.1: ZP and TGA results for GO species.....	78
Table 2.2: Cytotoxicity of PEI and GOPEI delivery vehicles.....	81
Table 2.3. Full ANOVA analysis of ASZ scratch migration assay.....	99
Table 4.1: NHEK/ASZ co-culture cell suspension specifics.....	164

Table of Contents

Abstract	3
Acknowledgements	5
List of Abbreviations	9
List of Figures	15
List of Schemes	24
List of Tables	25
 CHAPTER 1: Introduction and Background	
1.1 Overview of Basal Cell Carcinoma: Prevalence, risk factors, recurrence, and survival.....	31
1.2 Predominant Treatment Options for BCC.....	33
1.2.1 Surgical Resection.....	33
1.2.2 Radiation Therapy.....	35
1.2.3 Laser Therapies.....	36
1.2.4 Imiquimod and 5-Fluorouracil Topical Therapies.....	38
1.3 The Hedgehog Signaling Cascade in BCC.....	39
1.4 Chemotherapies that Target Hedgehog Signaling.....	41
1.4.1 Smoothed Inhibitors.....	41
1.4.2 Gli Inhibitors.....	45
1.5 Preclinical models for Hedgehog and BCC Research.....	50
1.5.1 Hedgehog Activation in Cellular Assays.....	50
1.5.2 Murine BCC Models.....	51
1.6 The scope of this thesis.....	55

CHAPTER 2: Delivery of Targeted Cobalt Inhibitors of Gli Family Transcription Factors

2.1 Introduction.....	58
2.1.1 Structure of the Gli-DNA Binding Domain.....	58
2.1.2 Cobalt Inhibition of Zinc Finger Transcription Factors.....	60
2.2 Results and Discussion.....	65
2.2.1 Unmodified Graphene Oxide Delivery Strategies.....	65
2.2.1.1 Optimizing 5ssCoGli loading.....	66
2.2.1.2 Cellular Toxicity.....	70
2.2.1.3 Cellular Internalization.....	71
2.2.2 Polyethyleneimine Functionalized Graphene Oxide Delivery Strategies.....	74
2.2.2.1 Synthesis and Characterization of GOPEI.....	76
2.2.2.2 Calculating dsCoGli loading thresholds.....	78
2.2.2.3 Cellular Toxicity and Inertness of GOPEI variants to Hedgehog Signaling.....	81
2.2.2.4 Evaluating Cellular Internalization and Lysosomal Escape.....	83
2.2.2.5 dsCoGli inhibits Hedgehog Signaling in a 2D Migration Assay of BCC.....	86
2.3 Conclusions and Outlook.....	89
2.4 Experimental Section.....	91

CHAPTER 3: Modeling Hedgehog Pathological Onset in Cellular Systems

3.1 Introduction.....	101
3.2 Results and Discussion.....	102
3.2.1 Activation in the Pluripotent C ₃ H/10T _{1/2} Cell Line (SAG vs. SHH).....	102
3.2.1.1 Optimization of all Activator and Inhibitor Concentrations.....	103
3.2.1.2 Inhibition with Smoothened Antagonists (Vismodigeb, Cyclopamine).....	105

3.2.1.3 Inhibition with Gli Antagonists (GANT-61).....	108
3.2.2 Activation in Normal Human Epidermal Stem Cells.....	109
3.2.2.1 Influence of Exogenous Hh Activation on NHEK Proliferation.....	110
3.2.2.2 Influence of Exogenous Hh Activation on NHEK Migration.....	112
3.3 Conclusions and Outlook.....	114
3.4 Experimental Section.....	116

CHAPTER 4: Modeling Basal Cell Carcinoma disease progression

4.1 Introduction.....	123
4.2 Results and Discussion.....	123
4.2.1 Transwell Migration of ASZ cells.....	123
4.2.2 Incorporation of ASZ cells into a 3D Organotypic Skin Model.....	126
4.2.2.1 Histological Features of Resulting Models.....	128
4.2.2.2 Specific Impact on Keratinocyte Differentiation.....	134
4.2.3 Inhibiting Gli Transcription Factors in a 3D Organotypic Model of BCC.....	147
4.2.3.1 Analysis of Phenotypic Changes.....	148
4.2.3.2 Analysis of Cytoskeletal Structure.....	150
4.2.3.3 Analysis of Barrier Function.....	154
4.3 Conclusions and Outlook.....	156
4.4 Experimental section.....	159

References

Chapter 1.....	169
Chapter 2.....	186
Chapter 3.....	192

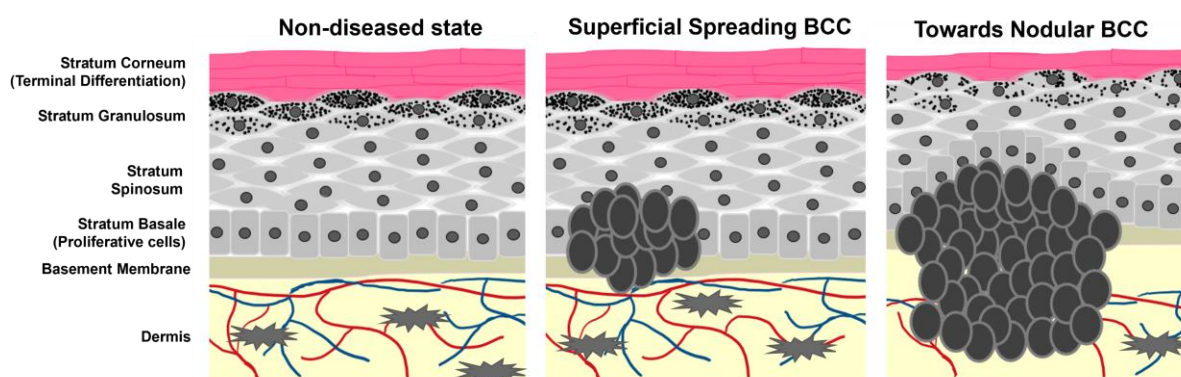
Chapter 4.....	195
Appendix 1: Non-invasive Detection of Stem Cell Therapies Facilitated by Metal Ion- Based Contrast Agents.....	200
Appendix 2: Synthetic Efforts Towards Alkyne and Azide Modified Co(III)-SB complexes...240	240
Appendix 3: Synthesis of Co(III)-DNA complexes.....252	252
Appendix 4: Cell Culture Protocols.....257	257
Appendix 5: Antibody Information and qPCR Primer Sequences.....263	263
Curriculum Vitae.....266	266

Chapter 1

Introduction & Background

1.1 Overview of Basal Cell Carcinoma: Prevalence, risk factors, recurrence, and survival

Keratinocyte cancers, or non-melanoma skin cancers (NMSCs), are the most commonly diagnosed cancers worldwide.^{1, 2} In the United States alone, 1 in every 3-5 Caucasian people are expected to develop an NMSC in their lifetime with estimates as high as 4 million cases diagnosed each year.³⁻⁵ Approximately 80% of all NMSCs are characterized as basal cell carcinomas (BCC) where uncontrolled growth of the basal cell population of the epidermis leads to tumorigenesis (Scheme 1.1).^{6, 7} The overwhelming number of BCC diagnoses requires ample research and medical attention for the development of effective treatment and prevention strategies.



Scheme 1.1: Cartoon representation of epidermal layers and the growth of BCC. Tumor cells originate from the stratum basale where they maintain stemness and hyperproliferative capacity. As the tumors progress, they begin to migrate through the dermis where they eventually detach from the basement membrane.

Gorlin Syndrome (GS) is a rare autosomal dominant disease that comprises a small percentage of the BCC community and approximately 0.05% of the population at-large.⁸ 90% of patients with GS experience the uncontrolled growth of multiple BCCs alongside myriad other developmental abnormalities.⁹ Sporadic BCC accounts for the predominant population of BCC patients. The primary cause of sporadic BCC is prolonged exposure to ultraviolet (UV) radiation from the sun.^{10, 11} The risk of developing BCC increases with light-skin pigmentation, age, and

sunburn frequency during youth.¹¹ Other risk factors include family history of melanoma, blonde/red hair phenotype, and men are more susceptible to BCC than women.^{12, 13}

A significant burden to the BCC patient community is the high rate of recurrence. Depending on the likelihood of recurrence, BCC is clinically designated as low or high risk.¹⁴ However, BCC more commonly recurs on an entirely different location on the body. For primary tumor locations, the recurrence rate depends heavily on the method of treatment (discussed in depth in Section 1.2) with a range from 1-70% after 5 years.^{15, 16} Larger tumors also experience an increased likelihood of relapse.¹⁶ More strikingly, the three-year risk of developing a second BCC lesion is estimated between 41-44%,^{15, 17-19} and the likelihood increases with each additional lesion. Once diagnosed, approximately 50% of patients will battle BCC again.

BCC is classified in three primary identities: superficial (10-30%), nodular (60-80%), and morpheiform/infiltrative BCCs (<10%).^{7, 20} Each differs in both physical and histopathological behavior²¹ and exhibits differential relapse rates. Superficial and nodular BCCs are less likely to recur, whereas infiltrative BCCs are more challenging to permanently treat.²² Additionally, the different subtypes have variable occurrence rates on different skin areas. Nodular BCC is most commonly found on the face while superficial BCC more frequently effects the torso and hands.²³ Infiltrative BCC is the most aggressive form and can often lead to the destruction of nearby healthy tissue.²⁴ Due to these differences in risk classification and behavior, selective care must be taken when deciding which treatment option to pursue for an individual BCC patient.

The overall survivability of BCC is very high with estimates for mortality being less than 0.5%.^{25, 26} However, the extremely high number of BCC diagnoses means that even a small mortality rate produces significant BCC related cancer deaths.⁵ The American Cancer Society

estimates this population effect at around 2,000 NMSC related deaths annually, primarily attributed to complications with advanced, metastatic BCC.

1.2 Predominant treatment options for BCC

Treatment strategies for BCC vary by subtype of disease, size of the lesion, and patient age and preference. While the following list does not represent every option for BCC therapy, several are discussed below. Table 1.1 outlines the advantages and disadvantages of each, including any imperative patient restrictions.

1.2.1 Surgical Resection

Surgical intervention is by far the preferred treatment option for BCC owing to the high rate of complete tumor clearance and low recurrence rates.¹⁵ Two common forms of surgical intervention are wide local excision (WLE) and Mohs micrographic surgery (MMS). WLE relies on over-estimating the boundary of a tumor to completely remove it in one surgical pass. While this can be effective for tumors with well-defined margins, many BCCs are more complex with unpredictable margins.²⁷ WLE can result in recurrence rates as high as 50% over 10 years if a tumor is not completely excised.²⁸

MMS was first described in 1941 by Dr. Frederic Mohs and is used to treat a number of skin malignancies.^{29, 30} The surgery is performed by shaving a lesion in thin sections and evaluating each by microscopy to detect cancerous tissue. Further excision is performed only where the tumor remains detected.³¹ It promotes identification of complete tumor margins while minimizing non-diseased tissue damage.³² For BCC specifically, Mohs surgery is more effective than WLE in preventing tumor recurrence in both primary and recurrent lesions.^{30, 33} As such, MMS is recommended for BCCs that exhibit more aggressive behavior and are situated at

Table 1.1: Select list and commentary of treatment options for BCC

Treatment	Advantages	Disadvantages	Patient Restrictions
Wide local excision (WLE)	<ul style="list-style-type: none"> • Low recurrence rates upon complete excision • Short procedure times 	<ul style="list-style-type: none"> • Excision likely to be incomplete and lead to higher recurrence rates • Highly invasive 	<ul style="list-style-type: none"> • Elderly patients where surgery is considered risky • Patients with tumors on eyelids, lips, ears, nose
Mohs micrographic surgery (MMS)	<ul style="list-style-type: none"> • Promotes excision of poorly defined tumor margins • Suggested for more aggressive/high risk tumors • Minimizes harm to non-diseased tissue 	<ul style="list-style-type: none"> • Long treatment times • Requires highly trained physicians and access may be limited for patients in underdeveloped geographical areas 	<ul style="list-style-type: none"> • Elderly patients where surgery is considered risky • Patients with tumors on eyelids, lips, ears, nose
Radiation therapy	<ul style="list-style-type: none"> • Can reach anatomical locations that surgical excision cannot (eyelids, nose, lips, ears) • Can be used in higher risk BCC • Boosts efficacy of incomplete surgical resection when used in tandem 	<ul style="list-style-type: none"> • Use of ionizing radiation • Increases risk of melanoma • Not as effective in larger tumors • Cannot determine complete clearance of tumor tissue 	<ul style="list-style-type: none"> • NOT ADVISED FOR PATIENTS WITH GORLIN SYNDROME • Not advised for younger patients
Ablative laser therapy	<ul style="list-style-type: none"> • Locally delivered, less destructive to non-diseased tissue • Low recurrence rates • Favorable cosmetic outcomes 	<ul style="list-style-type: none"> • Not applicable to larger, deeper tissues • May induce increased sensitivity to the sun 	<ul style="list-style-type: none"> • Not recommended for patients with high sunlight sensitivity • Patients with nodular or infiltrative BCC
Photodynamic therapy (PDT)	<ul style="list-style-type: none"> • Well characterized mechanisms of cytotoxicity • Local administration of non-harmful laser light • Safe for patients with Gorlin Syndrome 	<ul style="list-style-type: none"> • High variability of treatment efficacy • Multiple treatment sessions • Increased sensitivity to sunlight • Severely limited depth penetration 	<ul style="list-style-type: none"> • Not recommended for patients with high sunlight sensitivity • Patients with nodular or infiltrative BCC

Imiquimod topical therapy	<ul style="list-style-type: none"> • Well characterized induction of immune response • Topical, localized application reduces harm to healthy tissue 	<ul style="list-style-type: none"> • Only approved for small superficial BCCs • Many patients report skin irritation • Recurrence rates understudied 	<ul style="list-style-type: none"> • Patients with nodular or infiltrative BCC
5-Fluorouracil topical therapy	<ul style="list-style-type: none"> • Well characterized inhibition of DNA synthesis • Topical, localized application reduces harm to healthy tissue • High cure rate 	<ul style="list-style-type: none"> • Not specific to tumor tissue and may cause harm to non-diseased skin • Many patients report skin irritation • Recurrence rates understudied 	<ul style="list-style-type: none"> • Patients with nodular or infiltrative BCC

cosmetically sensitive locations to reduce disfiguration of the patient.³⁴ However, Mohs surgery requires surgeons to be highly trained on this complex technique and may be less available to patients in underdeveloped geographical regions.²⁸ Additionally, some patients may refuse surgical intervention in general for personal reasons or are medically excluded as candidates. Of primary concern are the potential cosmetic consequences of such an invasive procedure or elderly patients being able to recover properly.

1.2.2 Radiation Therapy

BCC patients that cannot undergo or refuse surgical treatment for BCC require other therapeutic options. For example, lesions on the eyelids, nose, lips, and ears can be extremely challenging to completely excise surgically. Attempted excision may result in compromised anatomical function or undesired cosmetic outcomes.³⁵ Radiation therapy has emerged as one alternative in these situations, primarily due to its ability to treat both low risk and higher risk tumors.¹⁴ Overall, the recurrence rate following radiation therapy alone is less than 10% over 5

years.³⁶ Radiotherapy is also useful for post-surgical treatment when margins are poorly defined or excision is incomplete.³⁷

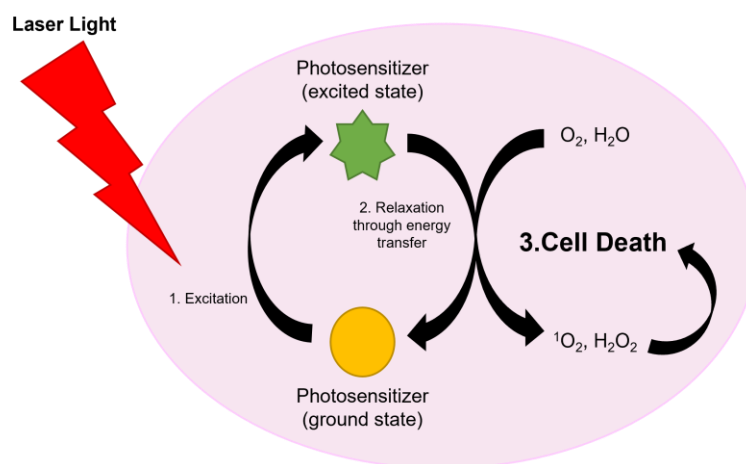
Radiotherapy does, however, have limitations that are important to consider. Firstly, efficacy is dependent on tumor size and should be reserved for smaller tumors.²⁸ While older patients that are not surgical candidates can benefit greatly from radiotherapy, younger patients may experience undesired cosmetic decline over time.³⁶ Additionally, any treatment with ionizing radiation increases the likelihood of the development of other cancers, including melanoma. Most importantly, radiotherapy is rarely recommended for patients with GS.³⁸ Treatment with radiotherapy, even for non-skin cancer GS symptoms, may induce rampant BCC growth.³⁹ Additionally, the complete destruction of tumor tissue cannot be guaranteed or determined without a more invasive follow-up.

1.2.3 Laser therapies

Low-risk nodular and superficial BCCs may also be non-invasively treated through a variety of laser-based surgeries. Ablative therapy can be performed by carbon dioxide (CO₂) or doped yttrium aluminum garnet (YAG) lasers.⁴⁰ Recurrence rates for this type of therapy are remarkably low at less than 3%.⁴¹ Patients generally report favorable cosmetic outcomes compared to surgical resection,⁴² though it is unclear if this is due to inherent differences in tumor type. Mohs surgery is rarely used for smaller, lower risk, nodular/superficial BCCs but laser treatments are. Scarring is logically expected to be less extreme for treatment of a smaller tumor.

Another laser-based technique for BCC treatment is photodynamic therapy (PDT). The mechanism of PDT is well characterized, and truthfully, most useful for the treatment of skin

cancers. A photosensitizer is delivered either topically or systemically to a tumor and irradiated with visible light that matches the excitation frequency of the sensitizer. The excited state transfers energy to water, producing cytotoxic singlet oxygen ($^1\text{O}_2$) and other reactive oxygen species (ROS) (Scheme 1.2).²⁸ Due to the limited depth penetration of visible light, PDT has struggled to gain clinical approval for treatment of most cancers. However, PDT is an approved treatment for BCC in 18 countries, excluding the United States.^{43, 44} In particular, superficial BCC has been extensively studied as a model cancer for evaluating PDT efficacy.⁴⁴



Scheme 1.2: Mechanism of PDT for cellular death. A photosensitizer is delivered to tumor tissue and irradiated with laser light that matches its excitation wavelength. Upon relaxation, energetic crossing transfers the energy to oxygen and water, generating cytotoxic singlet oxygen ($^1\text{O}_2$) and hydrogen peroxide (H_2O_2). Cell death is only observed where the laser light is administered, limited damage to nearby healthy tissue.

The safety profile of PDT is ideal for a tumor that has such a high rate of recurrence.

The laser light is not harmful to tissue that does not contain photosensitizer and is locally

administered with high precision. PDT, however, carries some of the highest variability in treatment efficacy with cure rates between 50-90% for primary tumors and as low as 20% for recurrent tumors.¹⁶ Additionally, PDT can cause severe sensitivity to the sun post-treatment and

may take several rounds to be maximally effective.⁴⁵ In contrast to radiotherapy, PDT is safe for patients with GS and effective in lesions with less than 2 mm depth (deeper tumors are not treatable by PDT due to limited tissue penetration of laser light).^{46, 47} Additional research and optimization is required to improve the general efficacy of PDT against BCC.

1.2.4 Imiquimod and 5-Fluorouracil Topical Treatments

Imiquimod (Aldara; 3M Pharmaceuticals, Figure 1.1 A) and 5-fluorouracil (5-FU, Figure 1.1 B) are topical creams that are applied to BCC lesions for chemotherapeutic treatment. Imiquimod is approved by the Food and Drug Administration (FDA) for the treatment of superficial BCCs less than 2 cm in diameter and is being evaluated for efficacy in nodular BCCs.⁴⁸ Therapeutic effect is achieved through an immune response and induction of apoptosis.⁴⁹ 5-FU is similarly approved by the FDA for treatment of superficial BCCs. The inhibition of nucleic acid synthesis is the primary mechanism of action. One study reported a 90% cure rate with patients experiencing minimal side effects.⁵⁰ In both therapies, intense skin

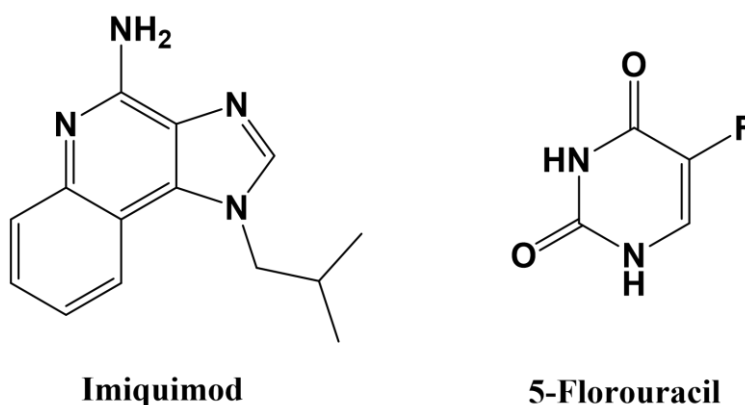


Figure 1.1: Chemical structures of imiquimod and 5-fluorouracil. Imiquimod functions through an immunomodulatory response, and 5-fluorouracil inhibits DNA synthesis machinery. These topical treatments are effective against low-risk superficial BCC.

reactions are observed due to inflammation caused by imiquimod and lack of tumor specificity of 5-FU.^{28, 51, 52} However, both therapies were found to be most effective when used in conjunction with other treatment options, suggesting that their utility might be optimized synergistically.^{51, 53} Topical treatment is ideal for skin cancers- localized delivery minimizes the harm to healthy tissues, specifically parts of the body completely unaffected by the cancer. However, superficial BCC represents only 10-30% of the BCC patient population, severely limiting the number of patients who could access these treatments.

1.3 The Hedgehog signaling cascade in BCC

In the 1990s, genetic evaluation of BCCs of patients with GS revealed the most important discovery in BCC research history: BCC lesions are linked to mutations in the patched1 (*PTCH1*) gene loci.^{54-57 58} Since then, it has become commonly accepted that the Hedgehog (Hh) signaling cascade, of which PTCH1 proteins belong, is the primary oncogenic driver of BCC.⁵⁹⁻⁶¹ The Hh pathway is canonically activated (Figure 1.2) by the binding of Hh proteins to the transmembrane protein PTCH1, which releases inhibition of smoothed (SMO). Suppressor of fused (SUFU) is signaled to release glioma associated oncogene (Gli) transcription factors where they are activated in the cytosol. Translocation into the nucleus activates the expression of target genes for cellular processes such as proliferation and migration.^{62, 63} Dysregulation of this pathway is associated with many cancers but is causative of BCC.^{59-61, 64, 65} As such, it is a promising chemotherapeutic target for BCC.

Approximately 90% of sporadic BCCs arise from mutations of one *PTCH1* allele, and 10% harbor mutations to downstream protein SMO.⁵⁸ Mutations in tumor suppressor p53 (p53) are also commonly observed in BCC.⁶⁶ These mutations are consistent with genetic mutations

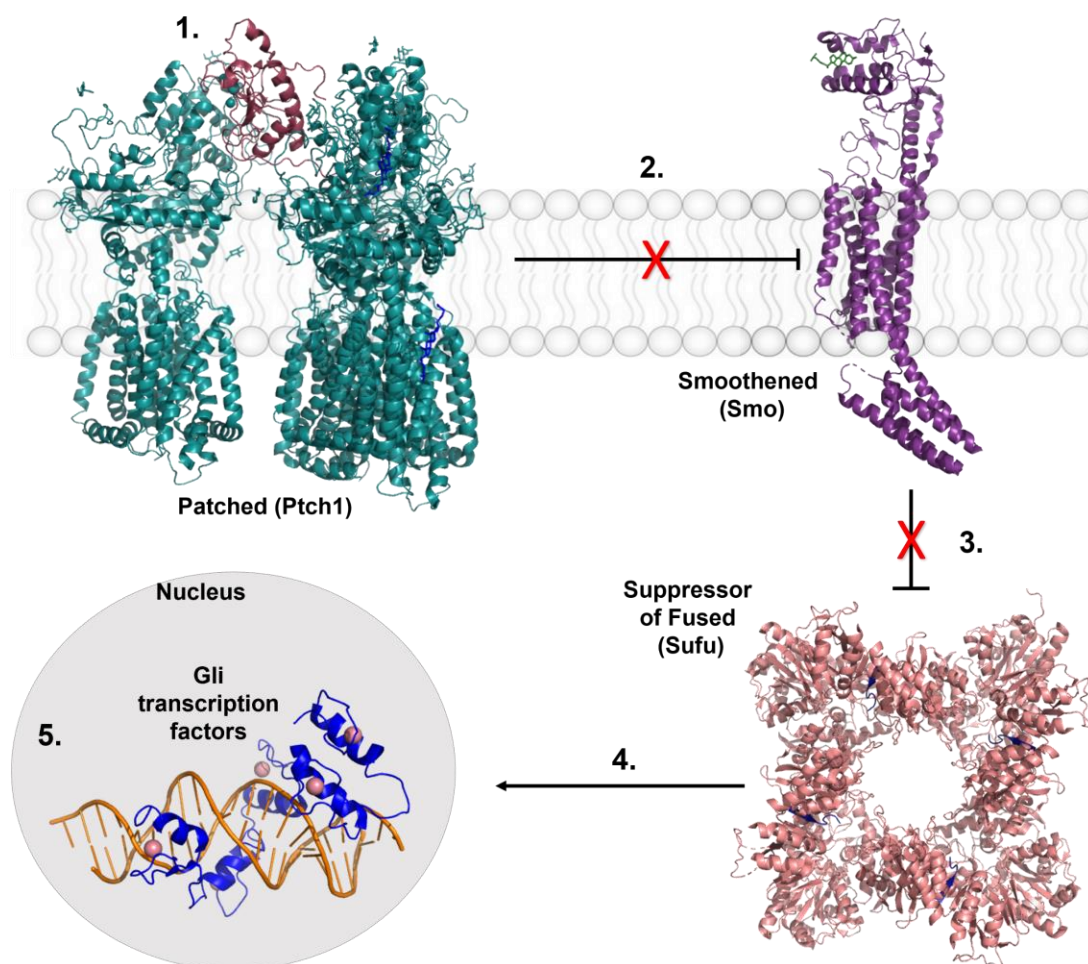


Figure 1.2: Key regulators of the Hedgehog signaling cascade. **1.** Hh signaling is activated by the binding of Hh proteins (Sonic hedgehog, Indian hedgehog, and Desert hedgehog) to the transmembrane protein Ptch1. **2.** Ptch1 is a native suppressor of SMO activity. Upon the binding of Hh proteins, inhibition is released. **3.** Upon activation, SMO signals for the SUFU complex to release the Gli family of transcription factors. **4.** Gli transcription factors are activated in the cytosol prior to translocating into the nucleus. **5.** Gli transcription factors transcribe pro-proliferative and migratory genes that lead to tumorigenesis in BCC. Crystal structures images were made from the following Protein Data Bank files: Ptch1/SHH complex, 6N7H. SMO, 6D35. SUFU/Gli complex: 4BLB. Gli1, 2Gli.

commonly caused by UV exposure that ultimately lead to increased proliferation, maintained stemness, and tumorigenesis.^{23, 58, 67-69}

1.4 Chemotherapies that Target Hedgehog Signaling

While treatment for lower-risk BCCs is largely successful across the myriad treatment options described above, patients who suffer from high risk infiltrative BCCs have fewer treatment options.⁷⁰ Infiltrative BCCs are broken further into locally advanced BCCs (laBCC) and metastatic BCCs (mBCC) and often surgical resection is not an option for these patients. While mBCC only occurs in less than 0.5% of cases,^{70, 71} it presents a unique treatment challenge. The majority of metastasis is observed to the lymph nodes, lungs, liver, and bone.⁷⁰ Prior to the development of chemotherapies targeting Hh signaling, median survivability for mBCC patients was only 8 months.⁷²

1.4.1 Smoothened Inhibitors

The overwhelming majority of Hh specific therapies target the transmembrane protein SMO. The first described SMO antagonist is Cyclopamine (Figure 1.3, A), a natural product found in corn lily.⁷³ Pregnant ewes that grazed on corn lily in Idaho produced offspring with craniospinal defects, including cyclopia, that could not be explained.^{74, 75} During the same time, a connection between mutations in the Hh pathway genome and the occurrence of holoprosencephaly (including cyclopia) in mammals was found.^{76, 77} After extensive research, inhibition of SMO by what is now commonly referred to as Cyclopamine was then determined to be the cause of the birth defects in the ewe litters.^{78, 79} While studied extensively as a chemotherapeutic agent,⁸⁰⁻⁸⁶ Cyclopamine suffers from poor bioavailability due to lack of solubility and stability.⁷³ However, the structural elucidation of Cyclopamine promoted the development of analogs with improved biocompatibility.

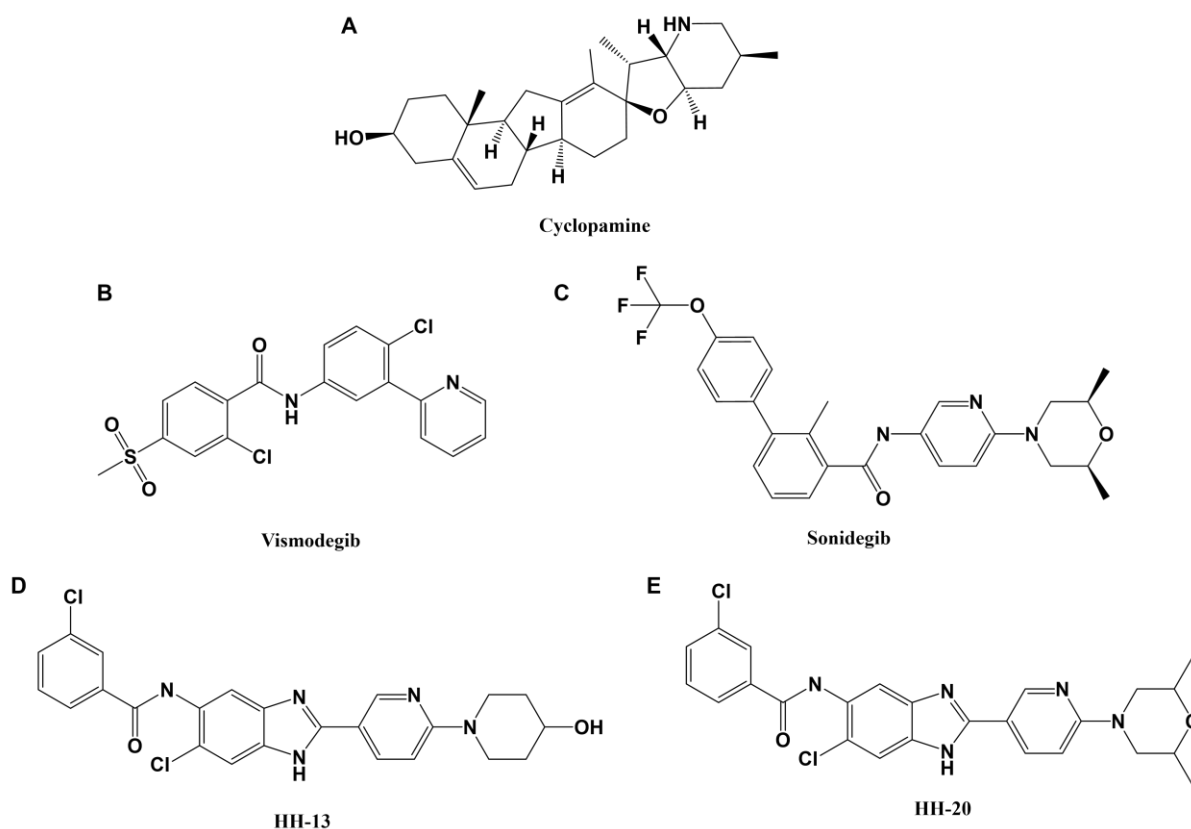


Figure 1.3: Chemical structures of smoothed inhibitors A) Cyclopamine. B) Vismodegib. C) Sonidegib. While distantly related to Cyclopamine, Vismodegib and Sonidegib contain structural similarities. All three inhibitors bind SMO in the same pocket. D&E) New generation Vismodegib derivatives developed by Li et. al in 2019.

Two SMO inhibitors have received FDA approval for the treatment of advanced BCCs. Vismodegib (GDC-0449, Erivedge®) is approved to treat recurrent, locally advanced, and metastatic BCCs in patients who are not candidates for surgery or radiation therapy.⁸⁷ Sonidegib (Odomzo, Novartis) is approved for laBCC in patients who similarly are not candidates for surgery or radiation therapy.⁸⁸ Both inhibitors have shown great efficacy for patients whose outcomes might have otherwise been poor, but they certainly are a far cry from the perfect answer to BCC treatment. Approximately 50% of patients treated with Vismodegib have no initial response, and of those that do, over 20% develop chemo-resistant tumor recurrence.^{89, 90} Many of the mutations that lead to chemoresistance were identified in the drug target, SMO,

suggesting that mutations of SMO structure in primary tumors may explain the lack of response experienced by some patients.^{91, 92} Chemoresistant tumor recurrence is a significant issue considering that BCC already exhibits such high recurrence rates. Vismodegib is administered orally as this is the only way to ensure that metastases are effectively treated but means that all areas of the body are exposed to the drug. BCC lesions that could grow in new locations might also develop resistance to further Vismodegib treatment. Additionally, patients on these treatments often experience untoward side effects such as muscle cramps, nausea, weight loss, and decline of mental health that are not always tolerable.^{93, 94} However, chemoresistant recurrence remains the highest concern.

In one study, researchers attempted to treat Vismodegib resistant tumors with Sonidegib to test the hypothesis that a different SMO inhibitor might still be effective. The results of this study concluded that patients with Vismodegib resistance are likely to progress if treated with Sonidegib.⁹³ A limitation of this study is that Vismodegib and Sonidegib have similar chemical structures (Figure 1.3 B&C, respectively) and bind SMO in the same location.⁹³ It cannot be concluded that all SMO inhibitors would fail to exhibit therapeutic efficacy, but only that Sonidegib was not sufficient to overcome Vismodegib resistance.

Recent studies have expanded upon structural components of Vismodegib that have resulted in more effective therapeutics and attenuation of resistance.^{95, 96} One study identified two new molecules as potent SMO inhibitors that are loosely founded upon the structure of Vismodegib. These compounds, labeled HH-13 and HH-20, displayed 10 and 30 nM IC₅₀ values in cellular assays of Hh activity, respectively.⁹⁵ Most importantly, these compounds remained effective against SMO-D473H, a Vismodegib-resistant SMO mutant. Vismodegib efficacy is diminished by almost 1000-fold between wild type SMO and SMO-D473H whereas efficacy of

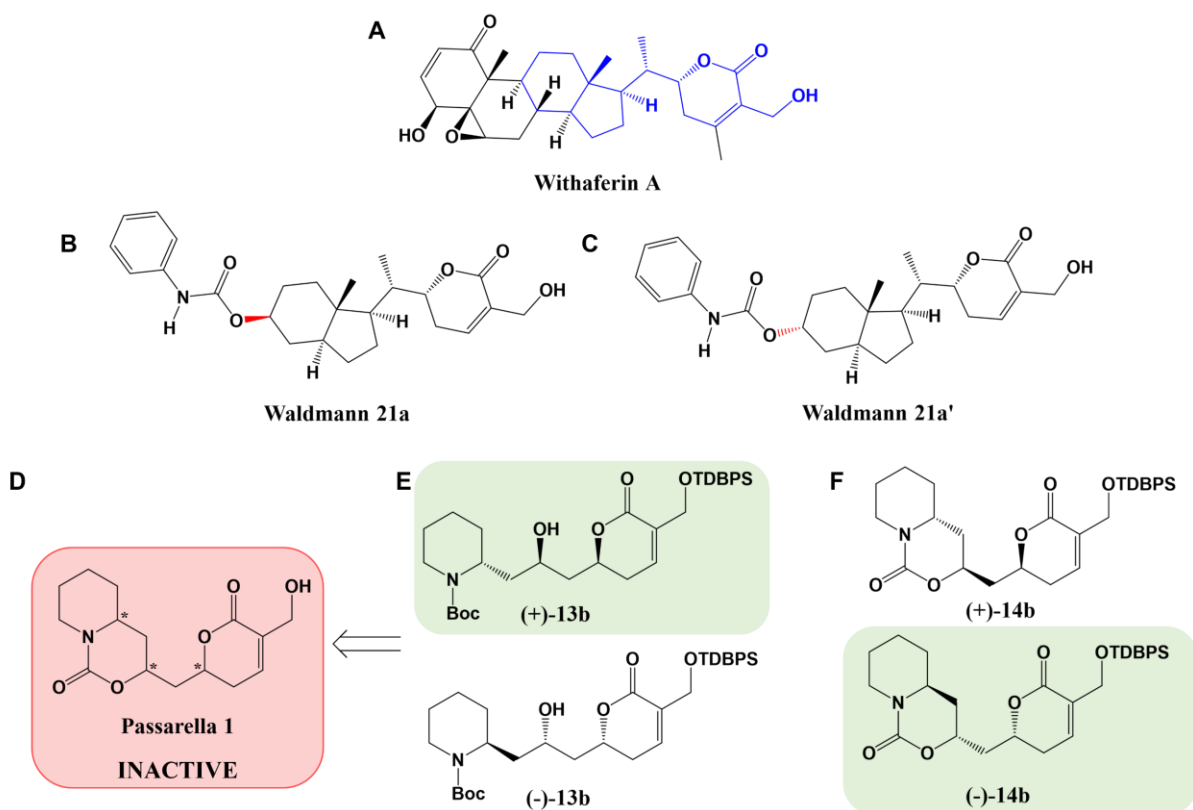


Figure 1.4: Chemical structures of withaferin A derivatives, novel SMO inhibitors that structurally deviate from Vismodegib. A) Chemical structure of natural product withaferin A. The highlighted scaffold is believed to be important for SMO binding. B & C) The Waldman group developed derivatives of withaferin A that exhibited stereoselective potent inhibition of SMO. D) The target compound of the Passarella group for SMO inhibition did not inhibit the Hh pathway. * represents an asymmetric carbon. E&F) Synthetic intermediates 13b and 14b exhibited stereoselective inhibition of SMO, elucidating important polarity considerations for protein interactions.

HH-13 and HH-20 are only diminished by 1.1 and 1.4 fold, respectively. While this is an exciting advancement in the development of SMO inhibitors, only one mutant version of SMO was evaluated. It is likely that HH-13 and HH-20 will not be effective against all SMO mutants.

Another solution to Vismodegib resistance is the exploration of chemical structures that deviate from that of Vismodegib. In 2015, the Waldmann group identified that synthetic modifications to the natural product withaferin A (Figure 1.4, A) produced potent inhibitors of SMO. Specifically, compound 21a exhibited a strong binding affinity for SMO and an IC_{50}

around 2 μM .⁹⁷ However, the synthesis of these complexes is non-trivial and is stereoselective. Diastereomerization of 21a (Figure 1.4, B) to 21a' (Figure 1.4, C) reduced potency by almost 5 fold.⁹⁷

In 2021, the Passarella group proposed simplification of the structure to contain cyclic carbamates with the ultimate goal of synthesizing and evaluating compound 1 (Figure 1.4, D).⁹⁸ However, stereoisomers of this compound were inactive against Hh signaling. Two of the pathway intermediates, 13b (Figure 1.5, E) and 14b (Figure 1.5, F), successfully inhibited SMO with racemic IC_{50} values of 7.4 μM and 13.0 μM , respectively. Enantioselective synthesis revealed that (+)-13b and (-)-14b were the more potent inhibitors with IC_{50} values of 6 μM compared to their enantiomers at 11-16 μM .⁹⁸ While it is surprising that deprotection of 14b to yield compound 1 eliminates activity, the tert-butyl(chloro)diphenylsilane (TBDPS) protecting group is highly lipophilic and might significantly improve protein interaction. While the potency of these complexes does not compare to Vismodegib and Sonidegib, further study is necessary to evaluate inhibition in BCC specifically, as well as the ability to evade resistance.

1.4.2 Gli Inhibitors

While newer generations of SMO inhibitors with structurally diverse scaffolds are promising, it is unclear if they will successfully evade the complications of the already approved inhibitors Vismodegib and Sonidegib. Options that target other regulators of Hh signaling are crucial for patients that either do not initially respond to treatment with SMO inhibitors or develop resistance. In one study addressing Vismodegib resistance, mutations of SMO proteins were the primary focus. Two SMO variants known to be insensitive to Vismodegib were expressed in *Smo* knockout mouse embryonic fibroblasts. Upon treatment with both direct and

indirect Gli transcription factor inhibitors, Hh activity was reduced regardless of the identity of the SMO mutation.⁹² In another study, activation of serum response factor and the transcriptional cofactor megakaryoblastic leukemia 1/2 (MKL1/2) were found to have a novel, non-canonical interaction with Gli1 that amplified Hh transcription independently of SMO. Excellent *in vivo* anticancer activity was achieved through MKL1/2 inhibition in Vismodegib resistant tumors with this characteristic.⁹⁹ Interestingly, both the canonical and non-conical resistance mechanisms ultimately influence the activity of Gli1 transcription factors in a way that is druggable.¹⁰⁰ As such, Gli is a valuable target for chemotherapeutic intervention in BCC.

To date, no therapies targeting the Gli family of zinc finger transcription factors (ZnFtfs) have received clinical approval. This is primarily attributed to the fact that transcription factors, in general, are notoriously challenging to target with traditional small molecules due to a lack of well-defined binding pockets.¹⁰¹⁻¹⁰³ However, a few small molecule inhibitors for Gli proteins have been developed and studied against Hh signaling. Figure 1.5 depicts the inhibitors discussed in this section.

One of the first small molecules found to inhibit Hh signaling through Gli inhibition and downregulation is arsenic trioxide (ATO, Figure 1.5 A).^{104 105} Importantly, ATO is effective in the treatment of tumors that have developed SMO resistance around a dose of 500 nM.¹⁰⁵ However, ATO is not specific to Gli transcription factors and is known to bind numerous intracellular targets.¹⁰⁶ In fact, it is FDA approved (Trisenox, Cell Therapeutics) for the treatment of acute myeloid leukemia due to its ability to potently inhibit promyelogenous leukemia-retinoic acid receptor fusion protein.^{107, 108} Ideally, a Gli inhibitor would be both potent and specific to reduce unwanted off-target complications.

The most prominent small molecule Gli inhibitor is GANT-61, a derivative of the Gli antagonist (GANT) family of compounds. It was discovered in 2007 and has since been used to study Hh inhibition in a variety of cancers.¹⁰⁹⁻¹¹⁶ The general inhibitory concentration at which 50% of Hh signaling is reduced (IC₅₀) is on the order of 5-10 μ M for GANT-61.^{117, 118} GANT-61 is understood to undergo a prodrug mechanism where hydrolysis of the intact molecule produces an inactive side product and the active inhibitor (Figure 1.5 B).¹¹⁹ Computational analysis further suggests a direct binding mechanism of GANT-61 to Gli transcription factors that inhibits DNA binding and therefore transcription, but this has yet to be confirmed experimentally.¹¹⁹⁻¹²¹

Ultimately, GANT-61 is limited by poor solubility and bioavailability.¹²² More recently, the natural product Glabrescione B (GlaB, Figure 1.5 C) was reported as the first confirmed small molecule to directly bind Gli and prevent the Gli/DNA binding interaction. GlaB inhibited BCC growth *in vitro* and *in vivo* at the equivalent of low μ M doses.¹²³ When compared directly to GANT-61 in this work, GlaB was found to have no significant improvement in potency or inhibitory effect. However, GANT-61 efficacy was only directly compared with *in vitro* experiments, not *in vivo*. It is possible that GlaB exhibits higher bioavailability and would be more effective *in vivo*. However, a study of GlaB against Hh activity in medulloblastoma showed that micelle encapsulation improved solubility and potency, revealing that GlaB efficacy similarly suffers from low bioavailability.¹²⁴

The discovery of Gli inhibition by natural product GlaB suggests potential core chemical structures that could be synthetically modified to improve solubility and binding to Gli transcription factors. Specifically, modifications to the isoflavone core (Figure 1.5, C & D) have been made to study the effect of structure on efficacy. Chemical modifications at the meta and para positions of the third ring generate compounds that either lose or maintain inhibitory

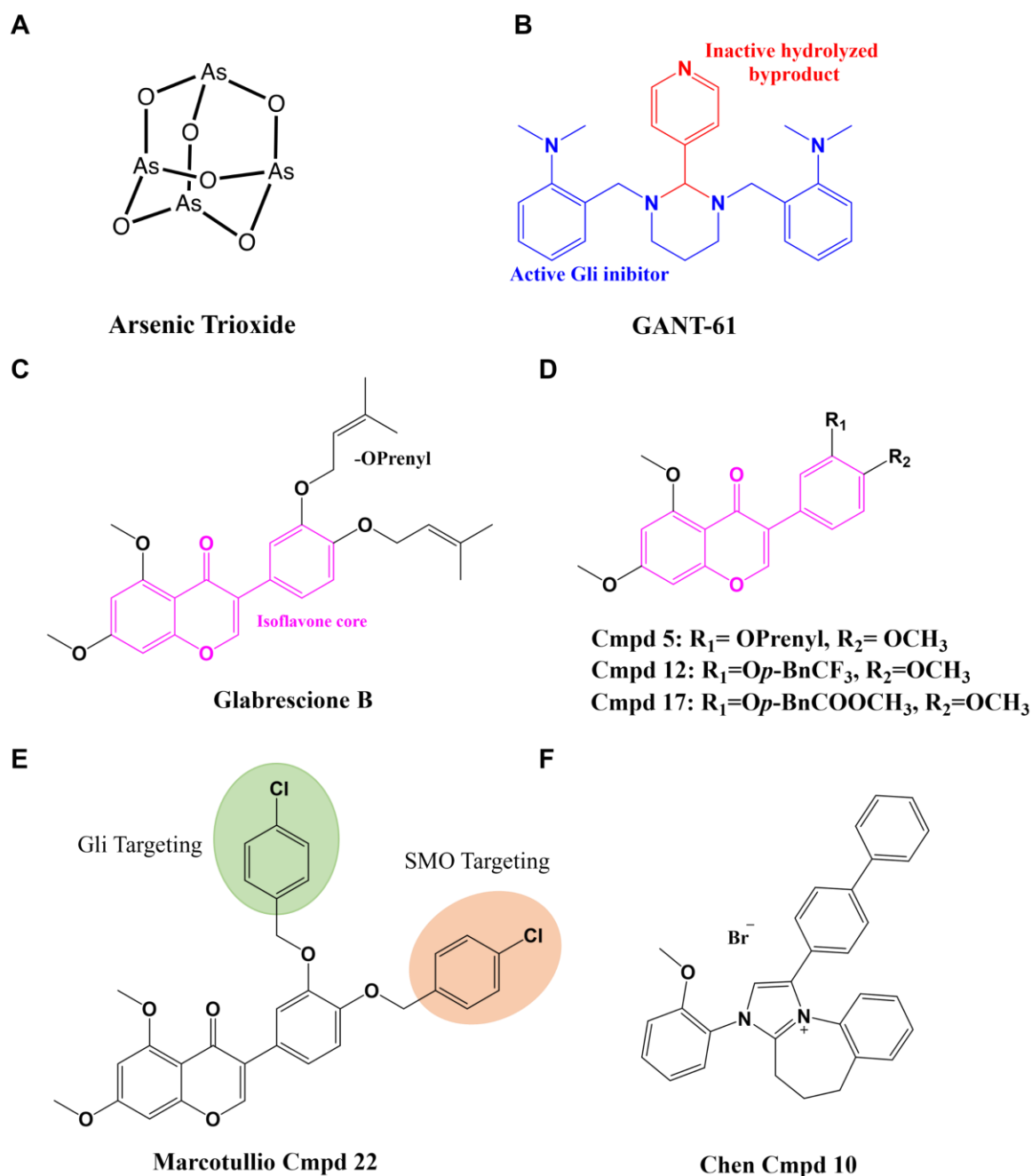


Figure 1.5: Chemical structures for small molecule Gli inhibitors. A) Arsenic trioxide downregulates Gli activity but is unknown to bind directly. B) GANT-61 is the gold standard for direct Gli inhibition. In aqueous solution, it undergoes hydrolysis to unmask the active inhibiting scaffold. C) Glabrescione B binds directly to Gli in disrupt the DNA binding interaction. D) Structural modifications to GlaB elucidate chemical modifications that maintain or prevent Gli inhibition E) A dual-targeted compound that inhibits both SMO and Gli. F) A new bicyclic imidazolium structure found to inhibit Gli proteins.

range, similar to GlaB.¹²⁵ However, compound 17 did not show inhibitory potential under 30 μ M, suggesting that very small structural changes make large differences in protein binding.

Further chemical modification of this scaffold has revealed that bulky substituents at the *meta* position produce isoflavones that target Gli, but bulky substituents at the *para* position generate compounds that target SMO.^{125, 126} Combining these principles yielded compound 22 (Figure 1.5, E) which targets both SMO and Gli transcription factors. This agent successfully inhibited tumor growth in a model of medulloblastoma. However, the ability to target two proteins means that specificity for this compound is questionable. It is unknown what other molecular targets it may bind, producing unwanted off-target effects.

In 2020, a new structural scaffold was reported to inhibit Gli transcription factors. Bicyclic imidazolium compounds were first discovered to inhibit Gli in a high throughput drug screen and were evaluated across a range of structure/activity relationship studies.¹²⁷ Of twelve synthesized molecules, compound 10 (Figure 1.5, F) was found to have the highest anti-Gli activity with an IC₅₀ between 100 nM and 5 μ M depending on the assay. Structural considerations determined that the terminal phenyl group added significant potency to the molecules whereas adding heteroatoms into the bi/tricyclic ring system essentially eliminated anti-Gli activity.¹²⁷ It is worthy to note that these complexes contain a high degree of aromaticity and hydrophobicity, much like GANT-61 and GlaB. It is likely that solubility will continue to be an issue for these compounds, though this was not discussed by the authors. Additionally, these complexes significantly interfered with mitochondrial health and function, something that must be considered within the context of adverse side effects in non-diseased tissue.

While GANT-61 has seemingly exhausted its potential for clinical translation, GlaB and derivatives as well as imidazolium compounds show potential for further development as potent

Gli inhibitors. However, none of these compounds have been thoroughly evaluated for Hh inhibition in BCC. It is challenging to draw conclusions about their applicability to BCC treatment but highlights the need for further study. Specifically, a topical delivery mechanism could be engineered to improve cellular internalization, bypass the necessity of blood solubility and retention time, and minimize contact with non-diseased tissue. However, this would exclude applicability to patients with mBCC who rely on Hh inhibition for treatment.

1.5 Preclinical models for Hedgehog and BCC research

An underdiscussed yet significant challenge for the BCC research community is the overall paucity of preclinical models. This is even more problematic when considering the unavailability of human based models. While animal models are useful, fundamental differences between the skin of different species directly impacts the translation of therapeutics. Here, we outline the current standards and recent developments for therapeutic evaluation in both cell lines of Hh activity and BCC specific model systems.

1.5.1 Hedgehog Activation in Cellular Assays

The first benchmark for evaluating a new Hh inhibitor is often a cellular assay of Hh activity. One example is a luciferase reporter assay performed in a derivative of the NIH-3T3 mouse fibroblast cell line that contains modified Gli binding domains driving expression of firefly luciferase.¹²⁸ When Hh signaling is exogenously activated, luciferase is stably expressed and can be measurably down-regulated by concurrent treatment with Hh inhibitors.¹²⁹⁻¹³¹ The pathway can be activated at PTCH1, SMO, or by transfection of a plasmid encoding for Gli transcription factors to model Gli accumulation.

The C₃H/10T1/2 cell line is a pluripotent mouse embryonic fibroblast routinely used in Hh research.¹³² The cells do not exhibit innate Hh activity, but exogenous activation promotes differentiation into osteoblasts and induces expression of alkaline phosphatase (ALP) proteins.¹³³⁻¹³⁵ Concurrent treatment with Hh inhibitors results in measurable prevention of ALP production. This cellular system has greatly increased the understanding of basic Hh mechanics as well as general efficacy of inhibition strategies.¹³⁶ However, these cellular assays are not representative of Hh dysregulation in a tumor environment and are also not derived from skin cells. While suitable for initial evaluation of Hh inhibitory potential, more specific models are necessary to evaluate applicability to BCC.

1.5.2 Murine BCC Models

Rodents (mice and rats) are choice mammals for most early-stage preclinical investigations of cancer treatments. Development of a rodent model that most closely mimics human disease is essential for successful translation into the clinic. One of the first mouse models that spontaneously developed BCC was generated by causing overexpression of sonic hedgehog (SHH) proteins that initiate Hh signaling in the skin.¹³⁷ However, since SHH is a paracrine signal, activation was not isolated to skin cells and many malformations were observed. The animals had to be examined either in the embryonic or neonatal states due to uncontrollable perinatal lethality. While embryos did develop large BCC like lesions that mimicked patient BCC in phenotype and pathology, they most closely resembled uncontrollable GS BCC growth. Additionally, animals allowed to develop long enough to die in utero had large sections of skin that were completely destroyed from advanced disease.¹³⁷ Ultimately, the untimely death of the animals in this study prevents the development of a breedable line that

could be used to investigate Hh inhibitors. However, it provides evidence for the ability to develop murine BCC models through manipulation of the Hh genome.

Other studies attempted similar generation of spontaneous BCC models through transgenic Hh activation. One report induced expression of a mutant version of SMO under a keratin 5 promoter that allowed for expression only in skin. BCCs developed in embryos that mimicked patient phenotype and pathology.¹³⁸ The authors do not comment on perinatal lethality, but further research determined that animals that do survive cannot reproduce to form a breedable line.¹³⁹ However, localized expression in the skin avoided the craniospinal defects seen in SHH overexpression, reducing potential discomfort and suffering of surviving animals.

PTCH1 alleles are the most common source of mutations leading to sporadic BCCs. As such, knockdown of *Ptch1* has been attempted for the development of spontaneous BCCs in mice. An extensive review of *Ptch1* knockout mice has been previously published.¹⁴⁰ Here, we focus on the broad story of development.

Early efforts towards this aim proved fruitless. Animals developed medulloblastomas¹⁴¹ and rhabdomyosarcomas¹⁴² and even other symptoms of GS, but did not develop BCCs. However, these mice were viable. Further studies revealed that *Ptch1* heterozygous mice at the age of 9 months had small proliferations of BCC like cells that could only be detected microscopically.¹³⁹ To encourage tumorigenesis, mice were subjected to either UV or X-ray irradiation. After UV irradiation, *Ptch1* knockout mice had a 20% incidence of developing lesions that mimicked the phenotype of human BCCs. X-ray irradiation produced primarily trichoblastomas.

The generation of BCCs from *Ptch1* knockout mouse models resulted in an equally important development: the first immortalized cell lines of BCC. Three cell lines were isolated

and immortalized from three different mouse models. The most commonly studied ASZ001, or ASZ, cell line was immortalized from a BCC lesion resulting from UV irradiation three times weekly for 10 months.¹³⁹ These cells retain knockdown of *Ptch1* in culture and are verified to be sensitive to Hh inhibition.

When irradiated, tumors on *Ptch1* knockdown mice develop in a controlled manner where the UV light is applied. This significantly reduces the number of lesions from a truly spontaneous model and allows for a more controlled experimental design. Importantly, some mice developed tumors in as little as four months of UV irradiation.¹³⁹ After histopathological validation of tumor type, these lesions could then be treated with Hh inhibitors on a semi-reasonable time scale. However, from breeding to birth to tumor development, this time scale could certainly be improved upon. For many cancers, the answer to this is patient derived xenograft (PDX) models. Cells from human cancer patients are injected into an immunocompromised animal and develop into a tumor.¹⁴³ The time scale for this is exponentially faster and does not require the use of heavily genetically modified animals, lowering the overall cost. Additionally, the cancer is now fundamentally of human identity.

Unfortunately, developing PDX models of BCC has largely failed. Tumors often do not implant or are met with slow growth rates.^{144, 145} The use of more severely immunocompromised mice improves implantation,^{146, 147} but little is known about the retention of cellular identity and behavior to the original tumor.¹⁴⁸ However, one study successfully allografted murine BCC cells into an immunocompromised mouse model with the assistance of Matrigel. Allografted tumors retained the phenotype and pathology of their parent tumors and were responsive to inhibition. Most importantly, allografts produced visible tumors within only 3 weeks of implantation.¹⁴⁸

This technique is unique and could be applied to the grafting of patient samples for a more human-based model of BCC.

There is an inherent distant relationship between rodents and human species. In the absence of available PDX models, a species more closely related to human identity could prove to be a valuable model. In 2017, a group investigated the ability to generate a BCC model in a non-human primate, the Chinese tree shrew.¹⁴⁹ Chinese tree shrews are small in size and have been used to study many human diseases. Their skin is anatomically similar to human skin, creating a unique opportunity for more accurate BCC model development.¹⁵⁰ Development of the tree shrew model of BCC was accomplished via lentiviral transfection of SmoA1, a constitutively activated form of SMO. Injections were performed in both dorsal and tail skin, and both resulted in the development of BCC lesions that mimic human BCC. While this model has yet to be used for investigation of BCC inhibition, it provides an interesting preclinical link between murine and human species.

Of note, all the preclinical models of BCC are only applicable to evaluating established disease and are not suitable for deeper understanding of how latent potential for BCC development ultimately leads to lesions. This should be a significant research endeavor considering the rate of primary and secondary tumor recurrence of BCC. Understanding these mechanisms in skin cells might elucidate new mechanisms by which BCC can be prevented. Essentially, all BCC patients should be considered at risk for the development of multiple BCCs and effective prevention strategies would significantly improve the lives of BCC patients.

1.6 The Scope of This Thesis

When considering the information above, we identify three holes in the BCC research community that are of paramount importance to address: 1) The development of potent and specific inhibitors of Gli transcription factors that are effective in BCC, 2) Methods for evaluation of BCC prevention, and 3) Preclinical models of BCC that can bridge the gap between basic cellular studies of Hh activity and challenging *in vivo* studies. This thesis describes research advances towards filling these gaps.

Chapter 2 describes the development of targeted cobalt complexes for the selective and potent inhibition of Gli transcription factors in BCC, specifically. Targeting is achieved by conjugating to the active cobalt inhibitor to the DNA sequence that only Gli will recognize. The discussion focuses on the cellular delivery and Hh inhibition of these complexes in cellular assays compared to GANT-61.

Chapter 3 describes the development of cellular assays towards elucidating prevention strategies for BCC. Hh inhibitors are first discussed for their ability to prevent Hh activation in C₃H/10T_{1/2} where signaling is activated at either PTCH1 or SMO, mimicking the most common mutation points in human disease. Secondly, the ability to exogenously activate Hh signaling in primary basal skin cells is discussed. Phenotypic activation is explored through proliferation and migration assays. Successful transformation of basal cells would permit elucidation of the mechanism by which Hh activation in previously healthy cells leads to tumorigenesis and how it can be prevented.

Chapter 4 describes the development of more complex two-dimensional and the first reported *in vitro* 3-dimensional cellular systems for BCC disease progression. It was determined that the Hh pathway drives ASZ cells to migrate through a porous membrane and inhibition can

be achieved through treatment with GANT-61. Moreover, ASZ cells can be combined with human basal cell keratinocytes in a three-dimensional skin organoid models that mimic the phenotype and pathology of BCC. The success of this cellular assay presents a new model of BCC to the research community that bridges the gap between simple *in vitro* work and complex *in vivo* studies. Additionally, the model is generated in only two weeks and can be simultaneously treated with Hh inhibitors with significant impact on tumorigenesis.

Chapter 2

Delivery of Targeted Inhibitors of Gli Family Transcription Factors

Portions of this chapter are adapted from:

Dukes, M.W.; Bajema, L.B.; Whittemore, T.J.; Holmgren, R.A.; Meade, T.J. Delivery of Targeted Co(III)-DNA Inhibitors of Gli Proteins to Disrupt Hedgehog Signaling. *Bioconjugate Chemistry*. **2022**. [doi:10.1021/acs.bioconjchem.2c00063](https://doi.org/10.1021/acs.bioconjchem.2c00063)

Brue, C.B.; **Dukes, M.W.;** Masotti, M.; Holmgren, R.A.; Meade, T.J. Functional Disruption of Gli1-DNA Recognition via a Cobalt(III) Complex. *ChemMedChem*. **2022**. [doi:10.1002/cmdc.202200025](https://doi.org/10.1002/cmdc.202200025)

2.1 Introduction

2.1.1 Structure of the Gli-DNA Binding Domain

The Gli family of transcription factors are the ultimate regulators of Hh signaling that transcribe genes for cellular proliferation and migration in cancer.¹⁻² While traditional chemotherapy prefers to target a protein early in a pathway, efforts towards this aim against Hh signaling have in some ways proven unsuccessful. As discussed in Section 1.4, most chemotherapeutics targeting Hh signaling are specific to the transmembrane protein smoothed (SMO).³⁻⁴ Two such inhibitors (Vismodigeb and Sonidegib) are clinically approved for the treatment of locally advanced and metastatic BCC, respectively. However, patients treated with Vismodigeb and Sonidegib experience to a high recurrence rate of chemoresistant tumor recurrence.^{3, 5-8} Considering BCC experiences such a high general rate of recurrence, this presents a significant problem to the patient population.

Research efforts of many investigators have instead turned to exploring inhibition of the Gli family of transcription factors.⁶ However, transcription factors in general are challenging to target with traditional organic drugs due to a high degree of disorder and lack of targetable hydrophobic binding pockets.⁹ While a full crystal structure of Gli transcription factors has not been obtained, Figure 2.1 shows the AlphaFold prediction for the full structure of Gli1.¹⁰⁻¹¹ The majority of the protein adopts random-coil secondary structure that the prediction software rates at very low confidence, likely due to the extreme disorder of these regions. However, the core of the protein, which corresponds to the DNA binding region, predicts with high confidence a series of alpha-helical structural motifs.

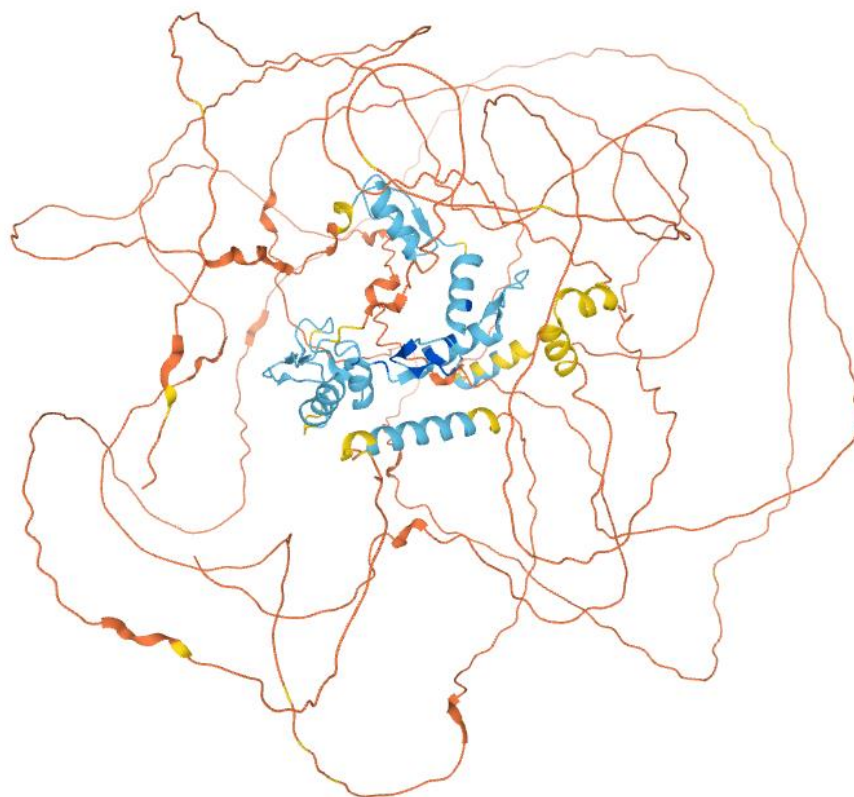


Figure 2.1: AlphaFold predicted structure for the Gli1 transcription factor (AlphaFold entry P08151 (GLI1_HUMAN)). The majority of the structure is predicted to adopt random coil secondary structure. The core of the structure, the DNA binding region, is predicted to adopt a series of alpha-helical secondary structure. The software states that blue represents high to moderate confidence (>70 pLDDT), yellow signifies low confidence (between 70 and 50 pLDDT) and orange signifies very low confidence (<50 pLDDT) of the prediction. The overall low prediction confidence is likely due to high degree of protein disorder.

While the full crystal structure remains aloof, researchers have successfully collected a crystal structure of the Gli1 DNA binding domain co-crystalized with its native DNA binding partner (Figure 2.2, PDB entry 2Gli).¹² Within the DNA binding domain, there are 5 sites where zinc(II) ions are tetrahedrally coordinated to two cysteine residues and two histidine residues (hereto referred to as Cys₂His₂). These are commonly referred to as zinc fingers and classify a subset of the family of zinc finger proteins.¹³ For zinc finger transcription factors (ZnFtfs), the zinc(II) ions are responsible for locking the two histidine residues into alpha helical secondary

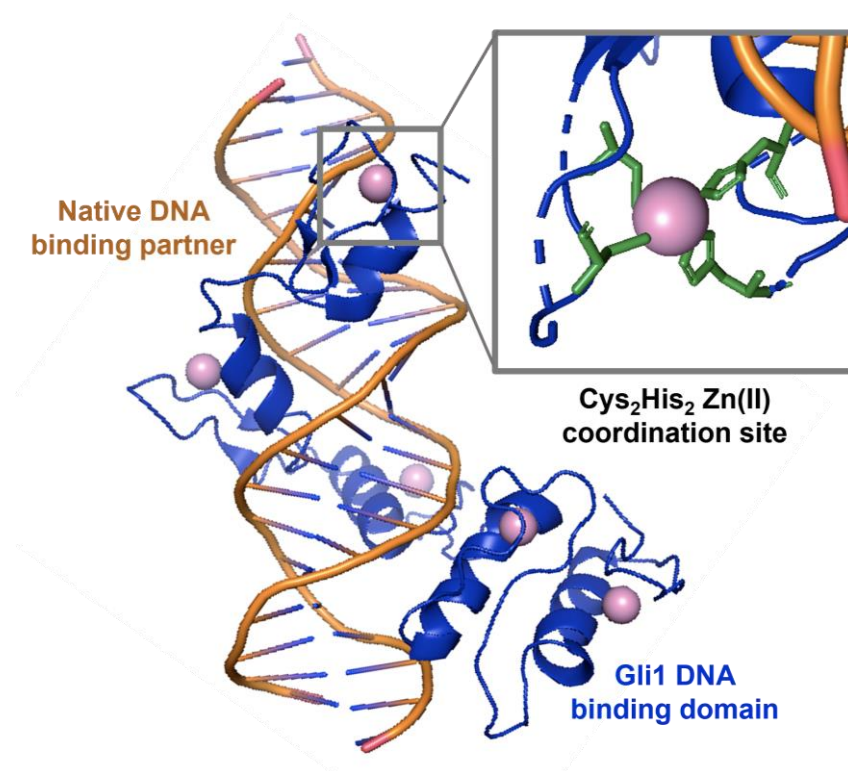


Figure 2.2: Crystal structure of the Gli1 DNA binding domain. Within this region, there are 5 Cys₂His₂ zinc(II) coordination sites. The zinc ions are responsible for maintaining alpha-helical structure that interacts with the major and minor grooves of DNA. Blue represents Gli1, orange represents that DNA binding partner, pink represents zinc(II) ions, and green represents the cysteine and histidine residues that coordinate zinc(II).

structure, allowing interaction with the major and minor grooves of DNA. Just like metal beams provide the framework for buildings to stand upright, the zinc ions provide structure to Gli transcription factors that allow it to ultimately transcribe DNA. The alpha helical structure is lost without these ions and the protein cannot function.

2.1.2 Cobalt Inhibition of Zinc Finger Transcription Factors

Because of the largely structure nature of Gli transcription factors, very few small-molecule organic inhibitors have been developed (those that have are discussed at length in Section 1.4).¹⁴⁻¹⁸ Existing examples largely suffer from both lack of *potency* and *specificity*, two crucial aspects for effective chemotherapeutics.¹⁹⁻²² For many years, the lab of Professor Thomas

Meade has studied cobalt (III) Schiff-base (Co(III)-SB) complexes that have high affinity for histidine residues.²³⁻²⁶ When in proximity to two histidine residues, there is a thermodynamic driving force for His residues to bind in a bidentate, octahedral orientation that is irreversible (Figure 2.3, A).²⁶⁻²⁷ In the context of Cys₂His₂ zinc finger binding domains, Co(III)-SB complexes will displace the zinc(II) ion, bind the two histidine residues octahedrally, degrade alpha-helical structure, and prevent DNA binding and ultimately transcription (Figure 2.3, B).

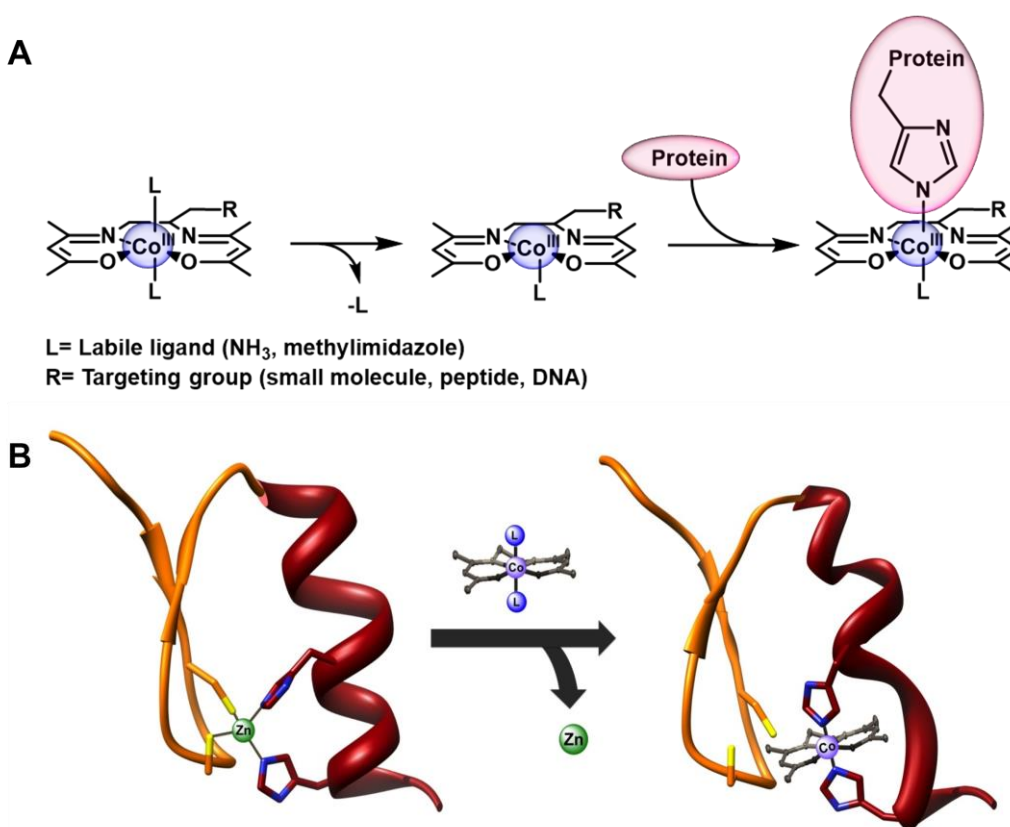


Figure 2.3: Schematic representations of Co(III)-SB complexes binding histidine residues in proteins. A) Co(III)-SB undergoes axial ligand exchange for preferential binding of imidazole motifs in histidine residues. B) In zinc finger proteins, Co(III)-sb punches zinc ions out of tetrahedral pockets and binds histidine residues octahedrally. This elongates alpha-helical structure necessary for DNA binding.

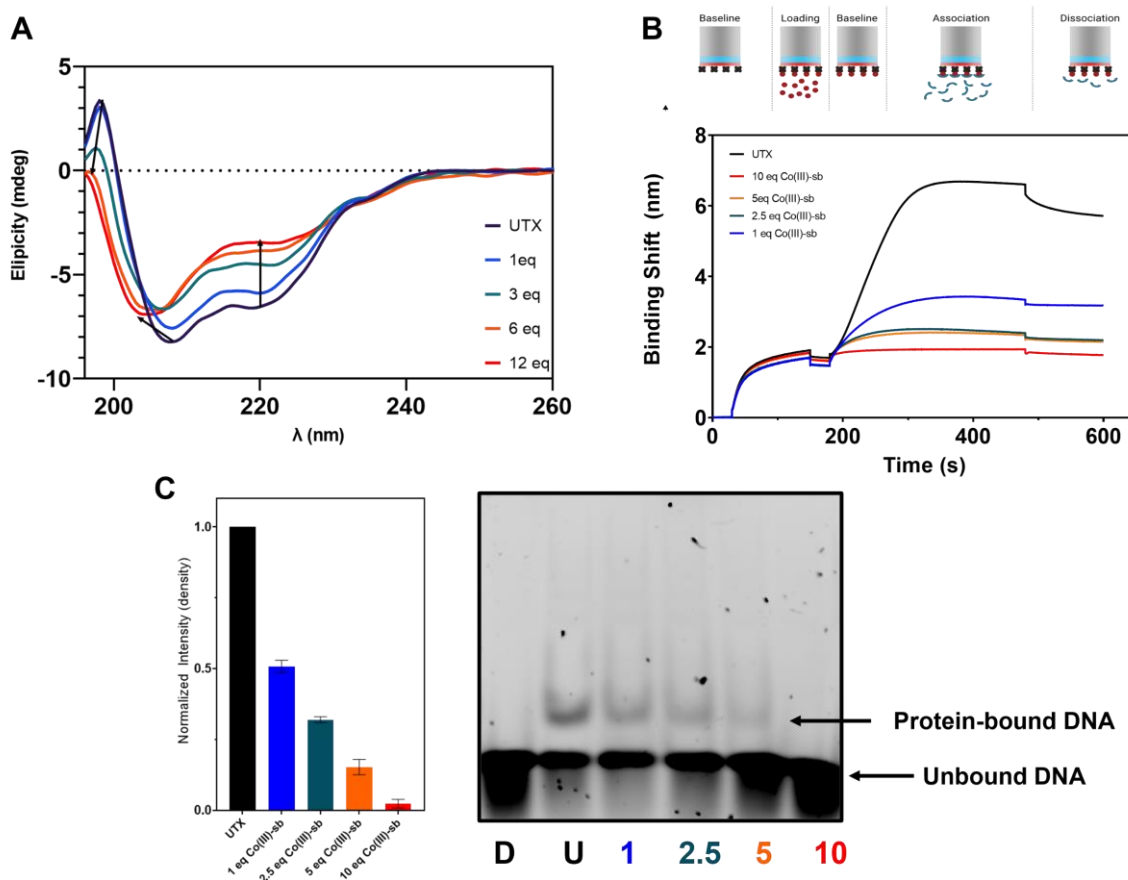


Figure 2.4: Co(III)-SB complexes degrade alpha helical content of Gli1 and prevent DNA binding. A) Circular Dichroism results with increasing concentrations of Co(III)-SB in Gli1 buffer. Alpha helical features at 220 and 208 nm are reduced with increasing Co(III)-SB. B) Interferometry results of protein binding to DNA attached to instrument surface. Binding is reduced significantly upon increasing Co(III)-SB concentration. C) EMSA results for Gli1/DNA binding. Fluorescent DNA is used for assaying DNA binding. The Gli-bound DNA band disappears with increased Co(III)-SB which is quantified using image intensity analysis. For all experiments, equivalencies are calculated in respect to the whole protein. For example, 1 eq. of Co(III)-SB means one Co(III)-SB for each protein unit and one Co(III)-SB for 5 zinc binding sites. 5 eq of Co(III)-SB represents a 1:1 Co(III)-SB:zinc finger ratio. *Data by Chris Brue, publication co-authored by Meghan Dukes.*

In a recent study in the Meade lab, Brue et. al. explored both computationally and experimentally Co(III)-SB inhibition of DNA binding specifically in the Gli1 protein.²⁸ The DNA binding region of Gli1 was recombinantly expressed in E.Coli and incubated with Co(III)-SB complexes at varying Co:Gli1 ratios. Circular Dichroism (CD) analysis showed loss of alpha-

helical structure in a dose-dependent manner (Figure 2.4, A). Alpha helices are characterized by double-peak features around 220 nm and 208 nm that are reduced upon incubation with Co(III)-SB. Additionally, the appearance of a feature at 205 nm indicates an increase of random coil structure. Furthermore, Electromotility Shift Assay (EMSA) and Interferometry analysis reveal dose-dependent loss of DNA binding (Figure 2.4, B&C). Importantly, equivalencies in these experiments were defined as Co:Gli1, not Co:Zn pocket. One eq of Co(III)-SB is 1 cobalt ion for every 5 zinc ions. The data suggests that very few zinc pockets need to be targeted for the DNA binding interaction to be significantly diminished.

While this data highlights the potential of Co(III)-SB complexes as *potent* inhibitors of Gli transcription factors, these complexes lack all *specificity* intracellularly. As a solution to this in previous *in vivo* studies, the Meade lab has deployed a targeted inhibition strategy where the active Co(III)-SB inhibitor is tethered to the DNA consensus sequence that only one ZnFtf will recognize.²³⁻²⁵ This strategy was tested specifically in *Drosophila* and *Xenopus* embryos in the Ci and Snail pathways, respectively.

The Ci pathway is responsible for the proper formation of denticle belts in *Drosophila* embryos which later become the different anatomy of the fly (Figure 2.5, A).²⁹⁻³⁰ If these belts do not form properly, neither will the fly. When treated with Co(III)-Ci (Figure 2.5, F), a targeted Co(III)-SB complex specific to Ci ZnFtfs, denticle belts did not separate properly and were fused (Figure 2.5, B). This is phenotypically mimicked by complete genetic knockdown of the Ci transcription factor (Figure 2.5, D). However, when the DNA sequence tethered to Co(III)-SB is mutated by just two base pairs, denticle belts form properly (Figure 2.5, C). Co(III)-Ci inhibits the Ci transcription factor, preventing denticle belt separation in a way that mimics knocking out

the transcription factor altogether. However, this result requires an exact match to the DNA recognition sequence of Ci, as mutating 2 base pairs eliminates observed inhibition.²⁵

The Snail pathway in *Xenopus* embryos is responsible for migration of neural crests, much like the Hh pathway is responsible for brain hemisphere separation in humans. When embryos were exposed to Co(III)-Ebox inhibitors specific to Snail ZnFtfs (Figure 2.5, G), the neural crests did not migrate (Figure 2.5, E). Mutating the DNA sequence tethered to the Co(III)-SB complex by one base pair resulted in normal neural crest migration.²³⁻²⁴

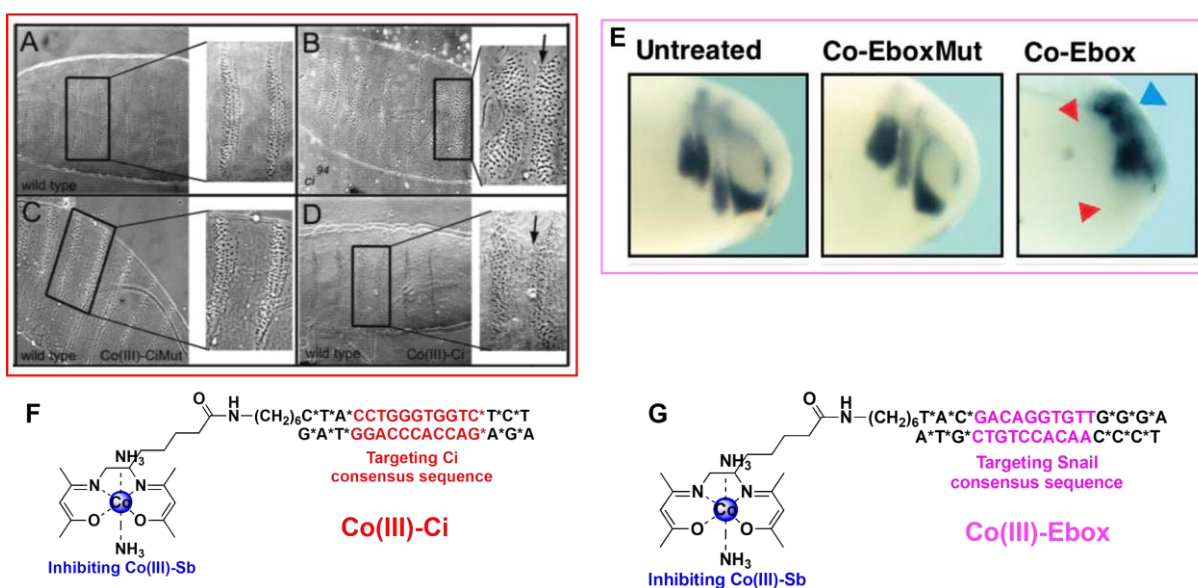


Figure 2.5. Inhibition of Ci and Ebox ZnFTFs in *Drosophila* and *Xenopus* embryos. A) Wild type *Drosophila* show proper formation of denticle belts. B) Treatment with Co(III)-Ci results in fusion of denticle belts, representing improper formation. C) Mutating the DNA sequence tethered to Co(III)-SB by two base pairs causes phenotypic replication of the non-treated wild type. D) Genetic knockdown of Ci causes fusion of denticle belts. E) Experiments of Snail inhibition in *Xenopus*. Treatment with Co(III)-Ebox causes prevention of neural crest migration, whereas mutating the tethered DNA sequence by 2 base pairs phenotypically mimics the untreated control. F) Structure of Co(III)-Ci. G) Structure of Co(III)-Ebox.

It was hypothesized that the same strategy of targeted ZnFtf inhibition could be applied to Co(III)-SB inhibitors of Gli transcription factors (hereto referred to as CoGli). However, Co(III)-DNA complexes were delivered to both *Drosophila* and *Xenopus* embryos via direct injection at

early embryonic stages due to poor membrane permeability. This delivery method would be impossible to translate to fully formed human tissue as you cannot inject each cell individually. A cellular delivery vehicle is required to evaluate CoGli inhibitors.

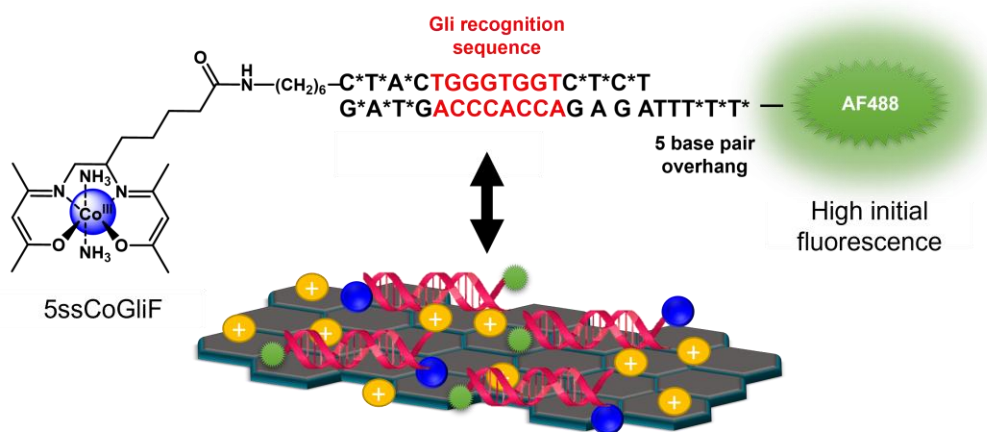
Transfection of DNA-based molecules is often accomplished with liposomal transfection agents and positively charged polymers like branched polyethyleneimine (PEI).³¹⁻³³ However, these agents are often cytotoxic and can introduce complications for studying the influence of cargo on the inhibition of a specific biological pathway.³¹ Nanoparticles are a promising new class of DNA delivery constructs. They are often associated with significantly less cytotoxicity and can be surface-modified with antibodies, peptides, and other tumor-targeting moieties.^{31, 34}

Graphene oxide (GO) has recently emerged as a versatile nanomaterial for cellular delivery due to rich surface chemistry and rapid uptake into cells.³⁵⁻³⁶ Unmodified GO is involved with various biological applications, including bioimaging, drug delivery, and cancer treatment.³⁷⁻³⁹ The surface can be further chemically modified with polymers like PEI, making GOPEI, which can electrostatically attract DNA-based compounds and deliver them intracellularly while reducing cytotoxicity.⁴⁰ In addition, GOPEI promotes endosomal escape and bioavailability and has previously been used in gene and siRNA delivery.⁴⁰⁻⁴² In this chapter, delivery strategies of both unmodified and PEI functionalized GO are explored.

2.2 Results and Discussion

2.2.1 Unmodified Graphene Oxide Delivery Strategies

The aromatic 2-dimensional surface of GO facilitates pi-pi stacking with unpaired nucleic acids, making it a potential candidate for the delivery of CoGli complexes if synthesized with a single-strand overhang.⁴³ Scheme 2.1 represents the design for 5ssCoGli@GO where a 5 ploy-T base pair overhang will facilitate loading onto the GO surface and eventual intracellular release.



Fluorescence quenching upon adsorption

Scheme 2.1. Design of 5ssCoGliF@GO delivery construct. A 5-base pair poly-T overhang attracts 5ssCoGliF to the unmodified GO surface through pi-pi stacking. Due to inherent electrostatic repulsion between the negative GO surface and DNA-bearing 5ssCoGliF, ionic partners are required for loading assistance. Loading and release can be tracked through the fluorescence quenching properties of GO. AF488= AlexFluor488, $\lambda_{\text{excitation}}= 488$, $\lambda_{\text{emission}}=520$.

Since these residues are 4 removed from the Gli DNA recognition sequence (Scheme 2.1, red), this modification is not anticipated to influence protein interaction. In this section, the optimization of loading parameters for 5ssCoGliF are elucidated, as well as cellular toxicity and internalization attempts.

2.2.1.1 Optimizing 5ssCoGli loading

Much work has been done to characterize the interaction of GO and single stranded DNA, all concluding that loading is inadequate at low ionic strengths.⁴³⁻⁴⁵ This is because the GO surface as well as the backbone of DNA are negatively charged, leading to charge-charge repulsion in non-buffered solution. Some studies even suggest that 100 mM of salt is necessary for proper GO/DNA adsorption.⁴³ While many biological researchers study the GO/DNA interaction for *ex vivo* biosensing, the ultimate goal of this research is to produce an effective cellular delivery vehicle for CoGli. Cells are often sensitive to the salts in their environment,

necessitating optimization of the salt identity and minimization of the loading concentration to remain biocompatible.

The identity and concentration of salt required for efficient 5ssCoGli loading was the first optimized parameter. To explore the difference between a 1+ and a 2+ cation, sodium chloride (NaCl) and magnesium chloride (MgCl₂) were evaluated in a fluorescence quenching experiment between 23.6 µg of 5ssCoGliF and 50 µg of GO (approximately a 1:2 5ssCoGli:GO ratio). The final concentrations of salt ranged from 50 mM to 0.1 mM. Since the percentage of fluorescence quenching is proportional to the total percentage of 5ssCoGliF loaded, Eq. 2.1 (found in Experimental Section 2.4) was used to calculate the mass of 5ssCoGliF that is loaded per gram of GO. Theoretical complete loading is calculated at 472 mg 5ssCoGli/g GO at these ratios.

The concentration of NaCl at which loading is no longer near complete is 25 mM (Figure 2.6: A,D). MgCl₂, however, still facilitates complete loading at as low as 0.25 mM (Figure 2.6: B,D). These results suggest that the presence of 2+ cations is superior to 1+ for the minimization of overall salt concentration necessary for proper adherence of DNA. All further experiments were carried out using salts bearing 2+ cations.

Zinc chloride (ZnCl₂) was also explored as a 2+ cation with potentially differential biocompatibility in BCC cells. Since the immortalized ASZ murine BCC cell line is sensitive to Ca²⁺, sensitivity to other metal ions is possible. Zn²⁺ maintained highly efficient loading at 0.25 mM via fluorescence quenching experiments (Figure 6: C,D), showing no significant difference from Mg²⁺. These results suggest that the identity of the 2+ salt is likely irrelevant in terms of facilitating loading, and a choice for further exploration can be made based on cellular compatibility and cytotoxicity. Furthermore, 0.5 mM and 0.25 mM salt arose as the lowest

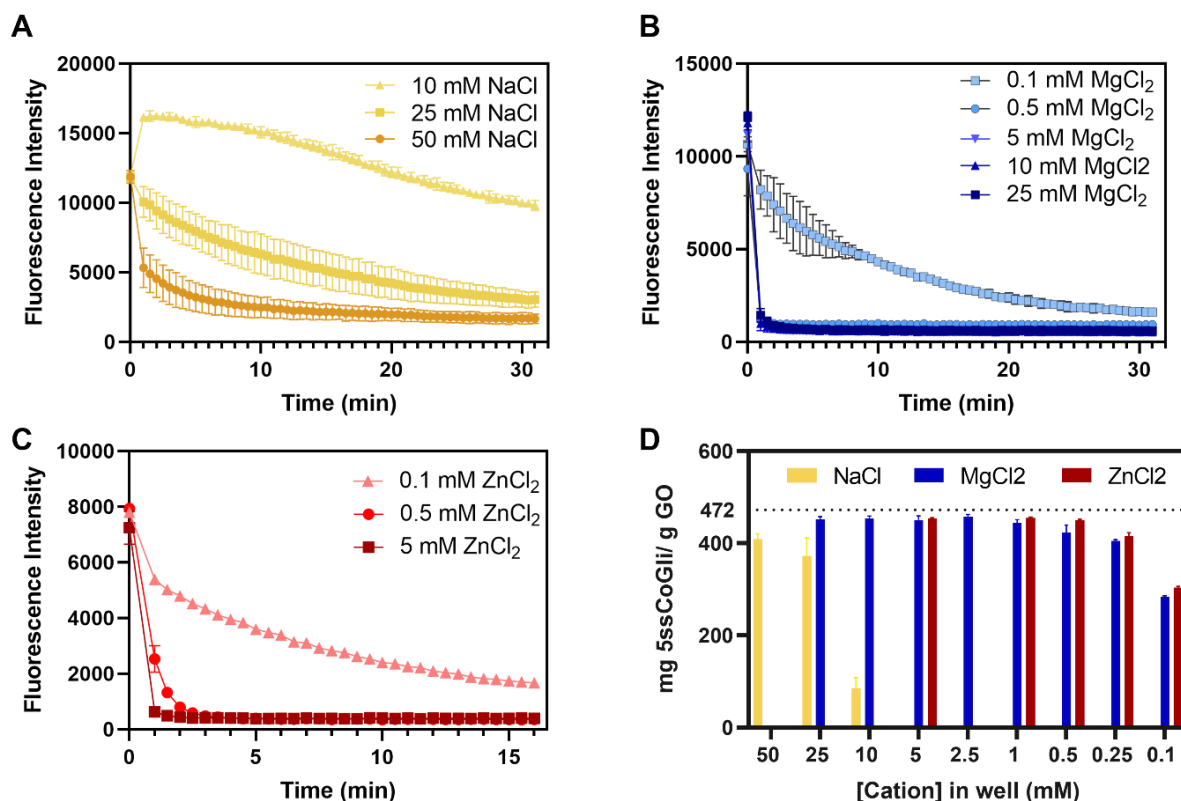


Figure 2.6. Fluorescence quenching experiments of 5ssCoGli and unmodified GO based on identity and concentration of salt. A) Fluorescent quenching curves in the presence of NaCl. B) Fluorescence quenching curves in the presence of MgCl₂. C) Fluorescence quenching curves in the presence of ZnCl₂. D) Quantification of loading in units of mg 5ssCoGli/g GO. Since the initial conditions contained 23.6 μg of 5ssCoGli and 50 μg GO, the maximum loading potential is calculated at 472, denoted by the dashed horizontal line.

concentrations where loading remains nearly complete and were chosen for further loading optimization.

The above loading experiments were carried out under constant amounts of both 5ssCoGli and GO (23.6 μg of 5ssCoGliF and 50 μg of GO). As such, complete loading was mathematically calculated at 472 mg 5ssCoGli/g GO. To optimize loading further, it is necessary to know how loading responds at fixed salt and 5ssCoGli concentrations as the amount of GO is varied. These results elucidate the minimum amount of GO necessary to completely capture a

given weight of 5ssCoGli. Since loading remained near-complete at a 1:2 5ssCoGli/GO ratio at 0.5 and 0.25 mM MgCl₂ and ZnCl₂, these were the concentrations chosen for these experiments. At fixed concentrations of 0.5 mM and 0.25 mM salt and 23.6 μg of 5ssCoGli, loading was calculated at weight ratios of 1:2, 1:1, 2:1, and 4:1 5ssCoGli:GO. At these respective concentrations, the loading maxima are 472, 944, 1888, and 3776 mg of 5ssCoGli/g GO.

Figure 2.7 summarizes the data from these experiments. For both concentrations of MgCl₂ and ZnCl₂, loading capacity is ultimately limited as the amount of GO is reduced

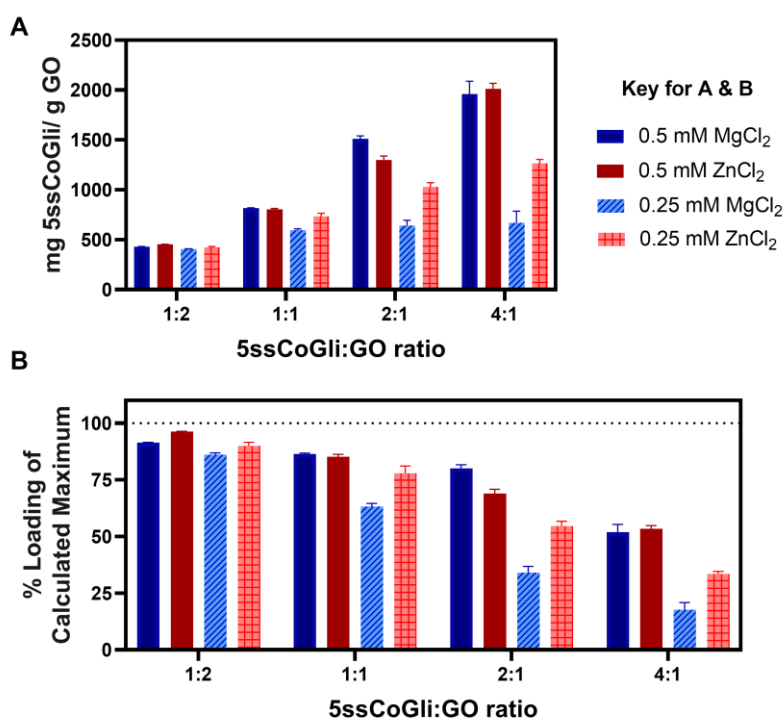


Figure 2.7. Fluorescence quenching results of fixed amounts of 5ssCoGli (23.6 μg) and 0.5 and 0.25 mM MgCl₂ and ZnCl₂ as the amount of GO varies. Evaluated ratios were 1:2, 1:2, 2:1, and 4:1 5ssCoGli to GO. A) Results for quantification of mg 5ssCoGli loaded per g of GO. B) Percentages of 5ssCoGli loaded compared to the calculated maxima of 472, 944, 1888, and 3776 mg 5ssCoGli/g GO for 1:2, 1:1, 2:1, 4:1 weight ratios, respectively. Data show that loading is similarly efficient at 0.5 and 0.25 mM salt at a 1:2 weight ratio. Reducing GO past this point results in loss of complete loading, especially for 0.25 mM of either salt.

compared to the fixed amount of 5ssCoGli. While the raw amounts of mg of 5ssCoGli/g GO do increase (Figure 2.7, A), the more important consideration is the percent loading of what was dosed. A condition is desired where nearly all of the CoGli inhibitor is loaded onto the nanoparticle surface. Computing these percentages reveals that at 0.5 mM and 0.25 mM MgCl₂ and ZnCl₂, the ideal dosing ratio is 1:2 5ssCoGli:GO as it yields the closest to 100% loading (Figure 2.7, B). At the 1:1 ratio, only about 85% of the 5ssCoGli is loaded at 0.5 mM, and approximately 70% at 0.25 mM. Further, there is little difference between the loading at 0.5 mM (95%) and 0.25 mM (90%) at the 1:2 ratio. Thus, to maximize loading and minimize salt necessary for cellular studies, 0.25 mM of salt at 1:2 5ssCoGli/GO were determined to be the optimal conditions for further cellular studies of this system.

2.2.1.2 Cellular Toxicity

Cellular compatibility of MgCl₂ and ZnCl₂ loading conditions were evaluated via MTT analysis of cellular viability. Prior to dosing, 5ssCoGli was incubated for 10 minutes at RT with GO at a weight ratio of 1:2 in 0.25 mM MgCl₂ and ZnCl₂. Cells were incubated for 24 hours with 5ssCoGli@GO before cytotoxicity was evaluated via MTT analysis. Controls included non-treated controls, as well as purely salt conditions that matched the concentrations of MgCl₂ and ZnCl₂ at their highest doses, 12 μM. For reference, the tolerated concentration of CaCl₂ in ASZ media is 50 μM.

Significant differences in cytotoxicity are not observed between the two salt identities at each concentration of 5ssCoGli (Figure 2.8). The *identity* of the salt does not impact cellular viability. However, the concentration of salt appears to play a critical role. The salt-only control that matches the concentration of salt at the highest-dosed condition shows viability reduced to

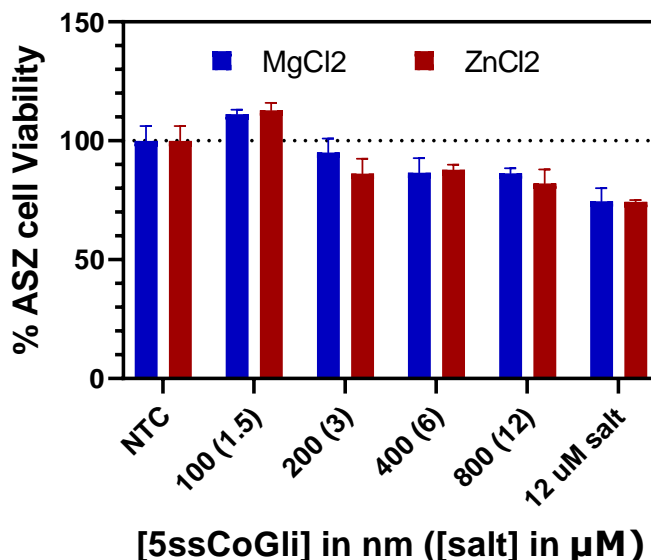


Figure 2.8. Cytotoxicity of ASZ murine BCC cells in the presence of 5ssCoGli@GO at a 1:2 weight ratio loaded by 0.25 mM MgCl₂ and ZnCl₂. No significant differences are observed between the two salt identities at each concentration of 5ssCoGli. However, significant cytotoxicity is observed as the concentration of 5ssCoGli increases, resulting in an unavoidable rise in salt concentration.

approximately 75%, similar to the reduction observed at the highest dosed condition (~80%). Upon initial observation, this suggests that the salts are primarily responsible for cell death. This is not ideal, as surveying changes in the Hh signaling cascade in response to Hh inhibitors requires a delivery vehicle/system that does not influence cellular viability. However, lower concentrations of 5ssCoGli/GO do not show alarming reductions in viability and can be explored further in assays of internalization.

2.2.1.3 Cellular Internalization

GO is a fluorescence quencher; it provides a visual handle for cellular internalization via fluorescence confocal microscopy. Confocal microscopy requires very little agent for detection due to high sensitivity and resolution. ASZ cells were dosed at only 20 nM 5ssCoGliF@GO at a 1:2 loading ratio at 0.25 mM MgCl₂ and ZnCl₂ for uptake evaluation via confocal microscopy.

Ultimately, these experiments were not successful. Cellular internalization was not observed beyond signal that could be attributed to light-scattering and autofluorescence. As an attempt to improve internalization, cells were instead incubated in serum-free media, and this did not improve visualization of cellular internalization. It was then decided to move into more quantitative experimentation for internalization.

Inductively Coupled Plasma-Mass Spectrometry (ICP-MS) is a technique for quantifying metal ions in aqueous solutions. Because 5ssCoGli contains a cobalt ion, this technique can be used for quantifying cobalt inside of cells when combined with cell counting analysis. 5ssCoGli was loaded with 0.25 mM MgCl₂ (only one salt chosen for simplicity) at either 1:2 5ssCoGli:GO or 1:4 5ssCoGli:Go. The 1:4 dosing condition was explored as a potential opportunity for increasing loading and delivery. Uptake was measured in normal ASZ serum media (2%), and reduced serum media (0.1%) in case serum proteins in media were off-competing bound 5ssCoGli compounds.

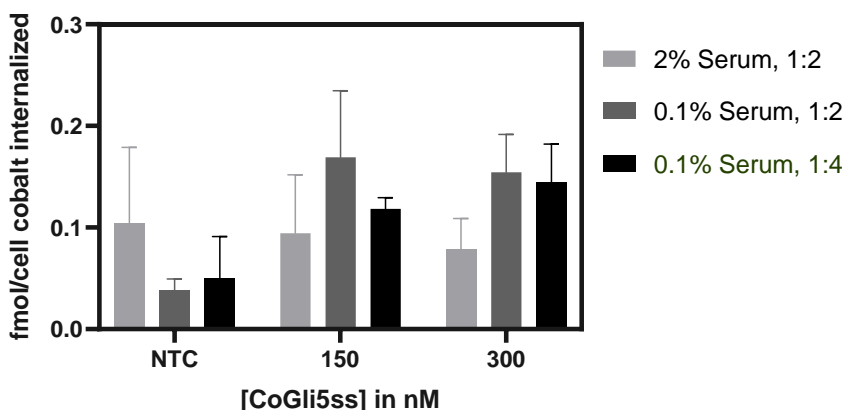


Figure 2.9. Internalization of 5ssCoGli as determined by ICP-MS as a function of media serum composition and dosing ratio of 5ssCoGli:GO. Internalization is not observed in full serum media. Internalization is slight improved upon reduction of serum, but this is not amplified by the addition of excess GO.

Data for these experiments is summarized in Figure 2.9. Not only do the non-treated cells contain higher levels of cobalt inherently, but uptake is not observed when serum is at the normal amount of 2% for ASZ cell culture. Reducing the serum component to 0.1% does decrease baseline levels of cobalt and increase the observed uptake, but this increase is not amplified upon doubling the amount of GO used for delivery. These data result in, at maximum, 6% transfection efficiency of the 5ssCoGli agent (calculated as the total fmol of cobalt total from ICP analysis divided by the total fmol dosed). Combined with the inability to monitor internalization by confocal microscopy, it is concluded that while GO can capture DNA efficiently, it is not sufficient for cellular delivery purposes.

To explain this phenomenon, an off-competition experiment was performed via fluorescence recovery. Once loaded, fluorescence of 5ssCoGli is quenched. Upon desorption, fluorescence recovers. Off-competition was evaluated after loading of 5ssCoGli onto GO in the presence of 0.5 mM MgCl₂. After 15 minutes, a fluorescence was measured to ensure complete loading. At this time, 15 μ L of either 2% serum media or serum free media were added and fluorescence was monitored over the course of 2 hours (Figure 2.10).

Initial fluorescence, complete loading, and fluorescence recovery upon addition of media were tracked with a plate reader (Figure 2.10, A). The final absorbance reading after 2 hours was used to calculate the resulting percentage of fluorescence recovered, which is directly proportional to the percentage of 5ssCoGli released. At a 1:2 5ssCoGli:GO ratio, 5ssCoGli experiences close to 50% release after only 30 minutes in both 2% serum media and serum free media. At a 1:4 weight ratio of 5ssCoGli:GO, even more 5ssCoGli is released upon interaction with 2% serum media, but the excess GO does protect from media-induced release in serum free media (Figure 2.10, B). Ultimately, these results support the hypothesis that interaction with

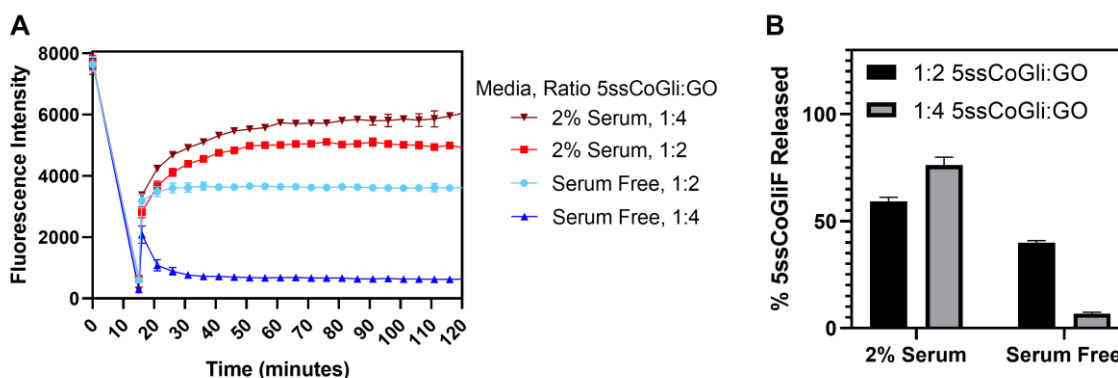


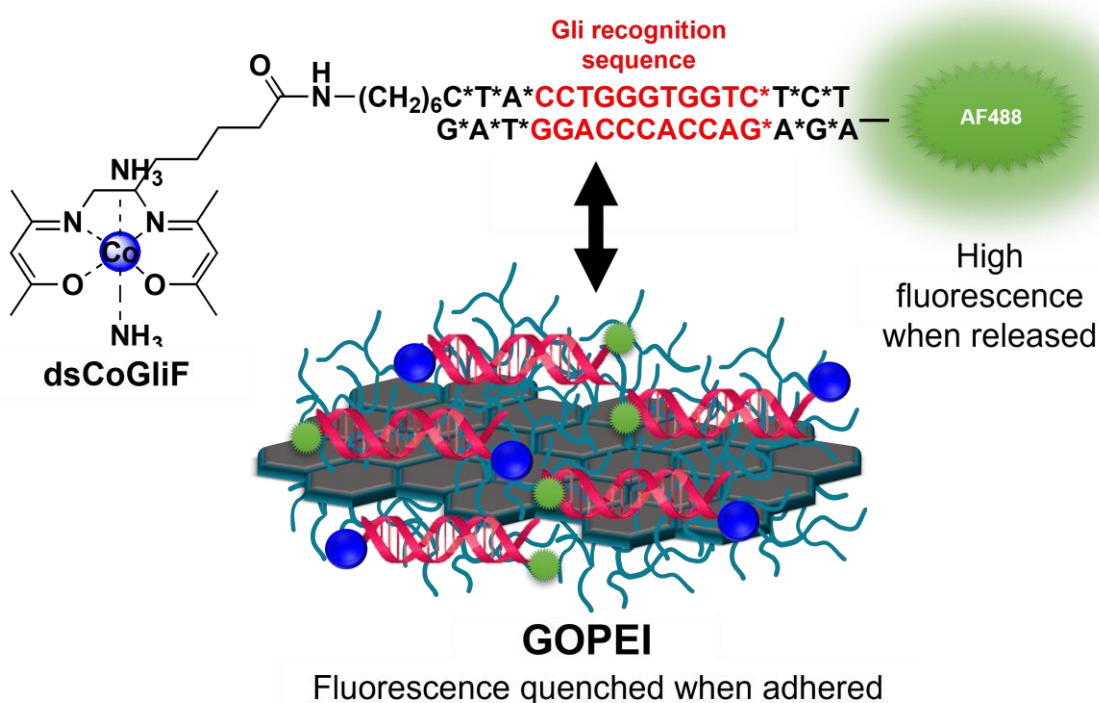
Figure 2.10. Tracking media-induced release of 5ssCoGli from GO as a function of serum composition and 5ssCoGli:GO ratio. A) Fluorescence recovery curves. B) Calculated percentage of 5ssCoGli released. In 2% Serum media, 1:2 and 1:4 5ssCoGli experience significant desorption from the GO surface that maximizes in 30 minutes. While the 1:2 weight ratio experiences a similar result in serum free media, the addition of excess GO protects the 5ssCoGli from desorption.

proteins and other biological compounds in media/serum results in 5ssCoGli off-competition from the GO surface. This happens on such a fast timescale that a majority of 5ssCoGli would be desorbed before cellular internalization could take place. In combination, these results suggest that GO is an effective method for loading 5ssCoGli but is not a successful cellular delivery vehicle.

2.2.2 Polyethyleneimine Functionalized Graphene Oxide Delivery Strategies

Even though unmodified GO ultimately failed as a cellular internalization strategy, GO is still desirable as the base of a delivery vehicle due to its typical cellular uptake profiles, fluorescence quenching capabilities, and biocompatibility.³⁵⁻³⁶ The concluded problem for unmodified GO was the weakness of the GO/DNA interaction in the presence of other biomolecules in cell media and serum. From previous research, we hypothesized that functionalizing the GO surface with a positively charged polymer would improve the binding affinity of negatively charged DNA when contested with other biomolecules in media.⁴⁰⁻⁴² As

such, this section discusses the synthesis and characterization of GOPEI, or GO that is chemically modified with polyethyleneimine (PEI). Specifically, GO-2kDa-PEI and GO-25-kDa-PEI will be discussed where each was synthesized with either 2kDa average molecular weight branched PEI or 25 kDa average molecular weight branched PEI, respectively. Since the mechanism of loading is now independent of pi-pi stacking, a fully double stranded version of CoGli, or dsCoGli, is utilized for these experiments. Scheme 2.2 represents the resulting dsCoGli@GOPEI nanosystem.



Scheme 2.2: Design of dsCoGli delivery construct. The positive charge contribution from PEI attracts the negative backbone of DNA. Fluorescence quenching properties are maintained upon the addition of PEI, permitting tracking of loading and release. AF488= AlexFluor488, $\lambda_{\text{excitation}}=488$, $\lambda_{\text{emission}}=520$.

2.2.2.1 Synthesis and Characterization of GOPEI

GOPEI was synthesized via a covalent linkage of 2 or 25 kDa average molecular weight PEI to GO functionalized with carboxylic acids (GO-COOH, Figure 2.11, A). GO was prepared from graphite flakes with sulfuric acid and KMnO₄ in a modified Hummer's method.³⁹ GO-COOH was then synthesized by combining sodium hydroxide with a GO suspension to activate the functional epoxides and hydroxides on the GO surface for substitution with chloroacetic acid. Following purification, PEI free amines were coupled to the carboxylic acids via peptide coupling by 1-ethyl-3-(3-dimethylaminopropyl)carbodiimide (EDC). The resulting GOPEI was purified by centrifugation. Both GO-COOH and GOPEI were characterized by Infrared (IR) spectroscopy, Zeta Potential (ZP), and Thermogravimetric Analysis (TGA).

Conversion of GO-COOH to GOPEI was initially observed via IR spectroscopy. (Figure 2.11, B) A C=O carboxylic acid stretch at 1705 cm⁻¹ is observed for GO-COOH but disappears in the spectra of both GOPEI variants. Instead, there is a shift of the C=O stretch to lower wavenumbers, 1620 cm⁻¹, consistent with formation of amide binds and covalent linkage of PEI to the GO surface.

Quantification of PEI on GOPEI variants was determined via TGA. (Figure 2.11 C) Mass loss resulting from steadily increasing temperature is due to the weakening and breaking of functionalized bonds. At 200 °C, the mass loss seen for GO-COOH corresponds to the breaking of unstable oxo bonds, specifically carboxylic acid functionalization. Further mass loss to 450 °C is associated with the prolonged breaking of more stable oxo bonds.⁴⁶ For GOPEI, initial mass loss up to 200 °C also corresponds to the destabilization of remaining unfunctionalized carboxylic acid bonds. Mass loss up to 450 °C is attributed to the loss of PEI.⁴⁶ Results are given

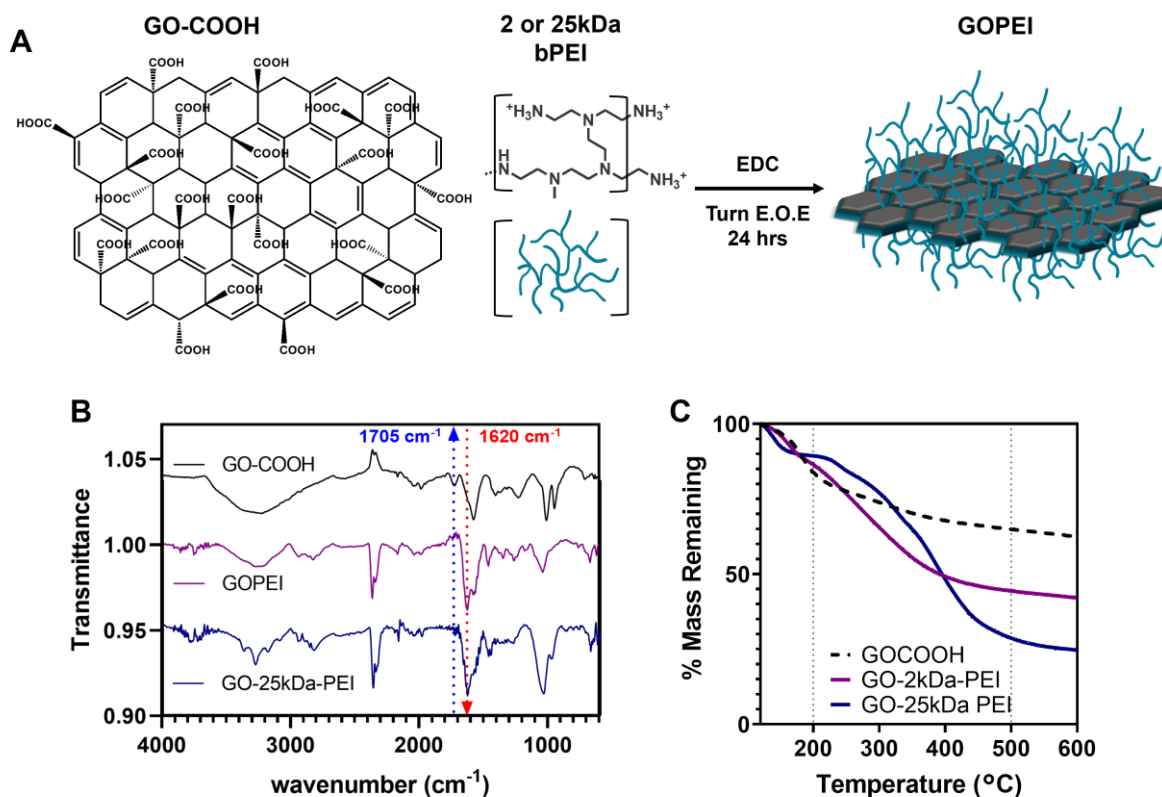


Figure 2.11: Synthesis and characterization of GOPEI. A) Schematic representation of GOPEI synthesis from GO-COOH. GO-COOH is prepared via the reaction of chloroacetic acid with reactive oxygen functional groups on GO. Following purification, GO-COOH is combined with PEI and EDC to covalently link PEI to the GO surface. B) IR spectra of GO-COOH and GOPEI variants. Red shifting of carbonyl peak suggests conversion of carboxylic acids to amides. C) TGA of GO-COOH and GOPEI. Increased mass loss of GOPEI represents removal of PEI groups from the surface.

in Table 2.1. The percent mass lost leading to each temperature is equivalent to the percent of the original sample that contained that functionalization. GO-COOH has 33.75% by mass unstable oxo groups, where GO-2kDa-PEI contains only 13.54% by mass unstable oxo groups and 40.38% by mass PEI functionalization. GO-25-kDaPEI contains even less unfunctionalized unstable oxo groups at 10.67%, and more PEI by weight at 54.98%.

Table 2.1: ZP and TGA results for GO species

GO Species	Zeta Potential in UltraPure water	% Functionalization
GO-COOH	-20.7 ± 5.0 mV	33.75 (unstable oxo)
GO-2kDa-PEI	$+28.3 \pm 3.1$ mV	13.54 (unstable oxo) 40.38 (PEI)
GO-25kDa-PEI	$+40.4 \pm 1.6$ mV	10.67 (unstable oxo) 54.98 (PEI)

ZP measurements were recorded in UltraPure water to ensure that the hypothesized positive charges would indeed be observed in aqueous solution for GOPEI variants. At neutral and physiological pH, the carboxylic acid groups of GO-COOH are deprotonated, resulting in a negatively charged species that repels the negative backbone of DNA. After functionalization, the terminal amines of PEI are protonated at equivalent pH, resulting in a positively charged species that will attract DNA electrostatically. Results for ZP are given in Table 2.1. GO-COOH is negatively charged (-20.7 ± 5.0 mV), whereas GOPEI variants are positively charged (2kDa: 28.3 ± 3.1 mV, 25 kDa: $+40.4 \pm 1.6$ mV) under identical conditions. These results further support functionalization and the synthesis of nanocarriers that will interact strongly with DNA-bearing CoGli.

2.2.2.2 Calculating dsCoGli Loading Thresholds

Due to the fluorescence quenching properties of PEI and GO,^{44, 47} a fluorescently labeled version of dsCoGli (dsCoGliF) was used to determine the interactions between dsCoGli and PEI or GOPEI (Figure 12). Fluorescence is quenched when dsCoGliF is in proximity to any of these materials. Therefore, dsCoGliF was incubated with GO, PEI, and GO-2kDa-PEI at 5 $\mu\text{g}/\text{mL}$ final concentrations, and fluorescence intensity was tracked for 30 minutes, with maximum quenching

achieved within five minutes of mixing (Figure 2.12). Preliminary fluorescence quenching experiments demonstrate that dsCoGliF is only quenched by PEI and GOPEI, not unmodified GO. These results are consistent with the electrostatic attraction between positively charged PEI and the negative backbone of DNA.

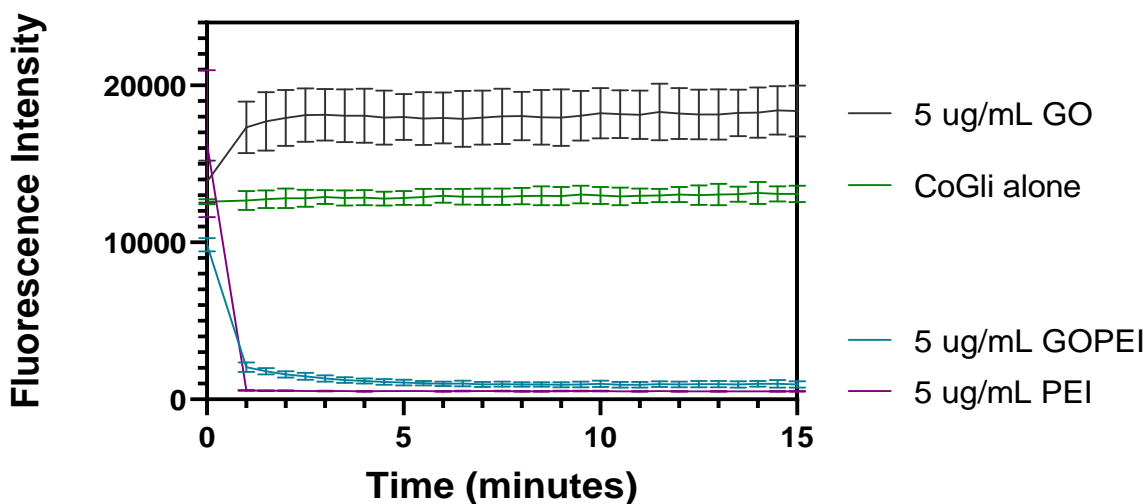


Figure 2.12: Fluorescence intensity changes over time. Fluorescence is quenched during capture by PEI and GOPEI. Fluorescence is not quenched by non-PEI bearing GO.

Quantification of the maximum dsCoGliF loading capacity of PEI and GOPEI variants was determined by fixing the amount of dsCoGliF at 23.6 μg and varying the final concentration of the nanocarrier at 1:4, 1:2, 1:1, and 2:1 weight ratios of dsCoGli:GOPEI. Fluorescence quenching curves (Figure 2.13, GO-2kDa-PEI: A and GO-25kDa-PEI: B) show that the identity of the GOPEI species does have an influence over the amount of fluorescence that is quenched. Since the percentage of fluorescence quenching is proportional to the total percentage of dsCoGliF loaded, Eq. 2.1 was used to calculate the mass of CoGliF that is loaded per gram of PEI or GOPEI. For GO-2kDa-PEI, loading maximizes around 400 mg dsCoGliF/g GOPEI. For GO-25kDa-PEI, this is increased to approximately 700 mg dsCoGliF/g GOPEI (Figure 2.13, C).

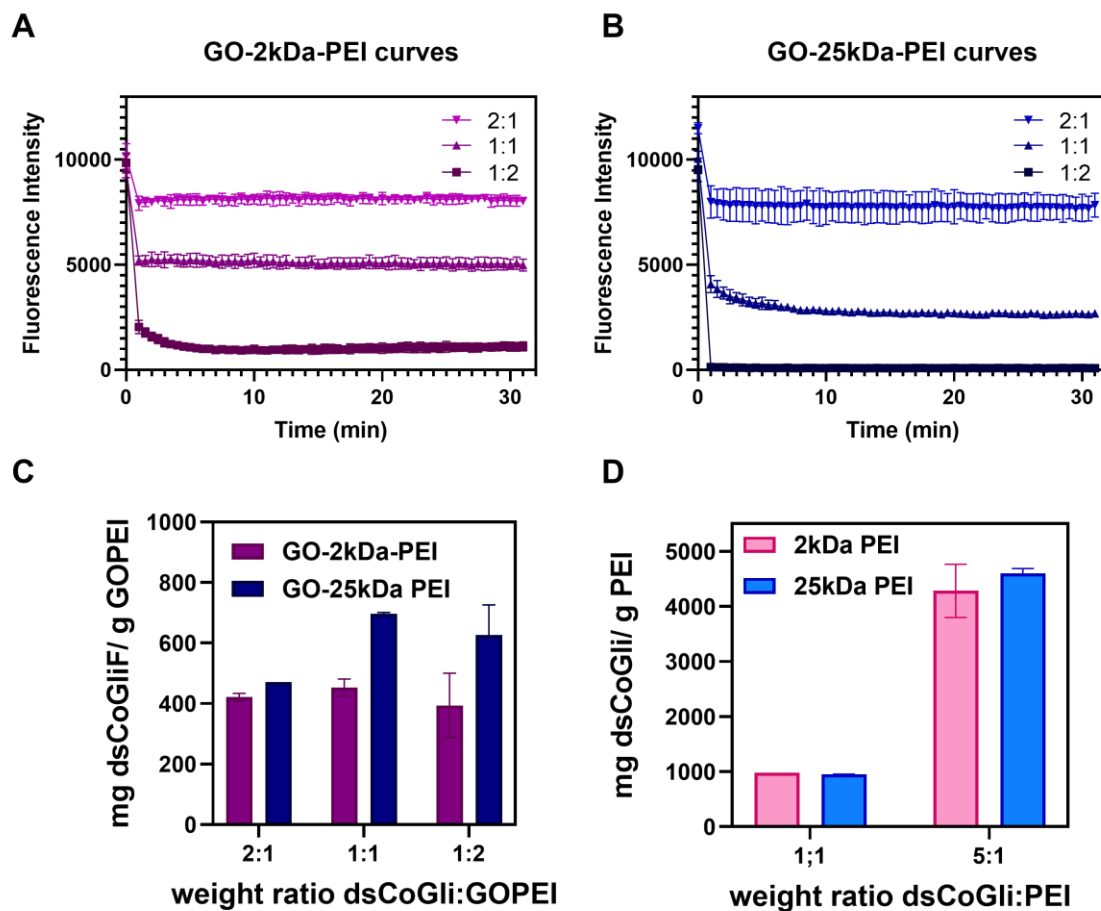


Figure 2.13. Loading of dsCoGliF onto PEI and GOPEI species. A) Fluorescence quenching curves of dsCoGli on GO-2kDa-PEI at varying weight ratios of dsCoGli:GOPEI. . B) Fluorescence quenching curves of dsCoGli on GO-25kDa-PEI at varying weight ratios of dsCoGli:GOPEI. C) Quantification of loading of dsCoGli onto GOPEI variants. Loading for GO-2kDa-PEI maximizes around 400 mg/g, whereas loading on GO-25kDa-PEI maximizes around 700 mg/g. D) Quantification of dsCoGli capture by free PEI. Free PEI at 2 and 25 kDa can efficiently capture up to 4x their average weight of dsCoGli.

Fluorescence quenching properties of free PEI were also used to calculate the amount of dsCoGli that free PEI can capture. For both 2 and 25 kDa PEI, PEI captures up to 4-fold its weight in dsCoGli (Figure 2.13, D). To ensure complete loading in following cellular studies, dsCoGli was delivered by a 1:4 weight ratio of GO-2kDa-PEI, 1:2 weight ratio of GO-25kDa-PEI, or 3:1 weight ratio of free PEI.

2.2.2.3 Cellular Toxicity and Inertness of GOPEI variants to Hedgehog Signaling

Cellular Toxicity: It is imperative that a delivery system be non-cytotoxic and inert to the Hh signaling cascade to study the isolated efficacy of dsCoGli as an inhibitor. For the first consideration, it is also of interest to ascertain whether tethering PEI to the GO surface reduces the toxicity of PEI as hypothesized. If so, it will contribute to determining if GOPEI is superior to free PEI as a delivery vehicle. Toxicity was determined in the ASZ cell line after 24 hours of incubation with both 2 and 25 kDa PEI and GOPEI (Figure 2.14, 2kDa species: A, 25kDa species: B). Since it is ideal for the delivery vehicle to not influence cellular viability, the IC₁₀

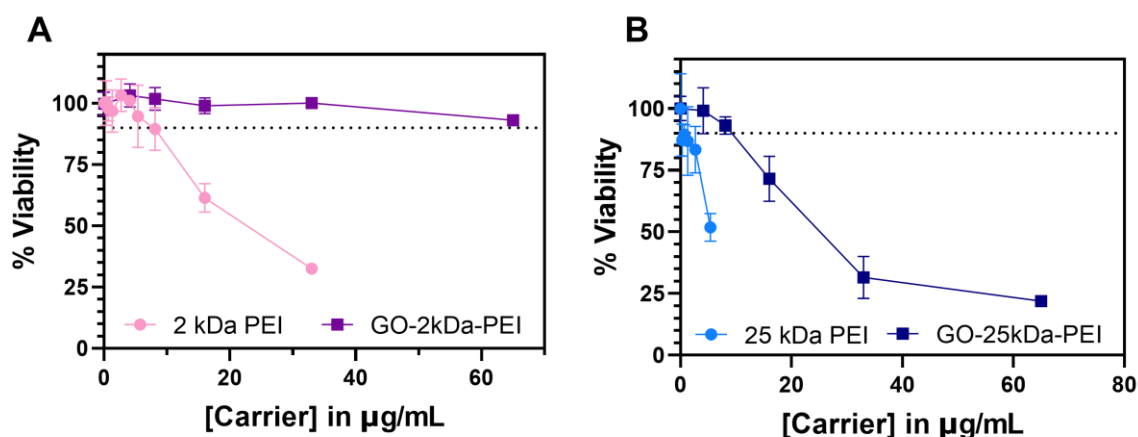


Figure 2.14. 24 hour Cytotoxicity of 2 and 25 kDa free PEI and tethered GOPEI species. A) Toxicity of 2 kDa variants. B) Toxicity 25 kDa species. Lines at 90% viability represent cutoffs for concentrations of delivery vehicles that can be used in further cellular assays. GO-2kDa-PEI is the least toxic, with GO-25-kDa-PEI and 2 kDa free PEI having similar toxicity, and 25 kDa free PEI is the most cytotoxic.

Table 2.2: Cytotoxicity of delivery vehicles

Species	2kDa PEI	GO-2kDa-PEI	25kDa PEI	GO-25kDa-PEI
Approx. IC ₉₀	8 µg/mL	>65 µg/mL	<1 µg/mL	8 µg/mL

was determined to be an absolute cutoff for maximum concentration of the vehicle that can be used. Dosing will not be higher than when 90% of the cells remain viable. Table 2.2 summarizes these results.

GO-2kDa-PEI is the least cytotoxic with an IC_{10} greater than 65 $\mu\text{g/mL}$. Free PEI at 2kDa and GO-25kDa-PEI share similar cutoffs around 8 $\mu\text{g/mL}$, and 25 kDa free PEI is the most cytotoxic with an IC_{10} of less than 1 $\mu\text{g/mL}$. For both molecular weights, toxicity associated with free PEI is significantly reduced upon coupling to GO. This is initial data suggesting that GOPEI is a superior delivery vehicle choice for further cellular studies but will be explored further in section 2.2.2.4 evaluating cellular internalization.

Inertness to Hh signaling: With cellular toxicity in mind, it is also imperative that a delivery vehicle bear no impact on the Hh signaling cascade. As an initial test, ASZ cells were dosed with GO-2kDa-PEI and GO-25kDa-PEI. After 24 hours, cells were harvested in TRIzol lysis reagent for analysis via quantitative real time- Polymerase Chain Reaction (qPCR) for Hh mRNA transcripts. This technique elucidates quantitatively the amount of a transcript actively produced by Gli transcription factors as a measure of Hh activity. Specifically, both *Gli1* and *Hhip* transcripts were monitored as they are directly transcribed through the Hh cascade.

For a negative control, 3 wells were incubated in the absence of any delivery vehicles. As a positive control, 3 wells were incubated with 5 μM GANT-61, the IC_{50} of a known Gli inhibitor. The experimental conditions contained 3 wells each of either 5 $\mu\text{g/mL}$ GO-2kDa-PEI or 2.5 $\mu\text{g/mL}$ GO-25kDa PEI (Figure 2.15). Half the concentration of GO-25kDa-PEI was chosen due to the differences in loading capabilities determined in Section 2.2.2.2. Notably, both experimental conditions represent concentrations that are lower than the established cutoffs of 65 and 8 $\mu\text{g/mL}$, respectively. At 5 $\mu\text{g/mL}$, GO-2kDa-PEI did not exhibit changes to *Gli1* and *Hhip*

transcripts compared to the non-treated control. However, 2.5 $\mu\text{g}/\text{mL}$ GO-25kDa-PEI did result in reduction of these transcripts to a similar extent as 5 μM GANT-61. This suggests that while non-toxic concentrations of GO-2kDa-PEI are inert to Hh signaling, the same conclusion cannot be made for GO-25kDa PEI. As such, GO-2kDa-PEI was determined to be the superior choice for further evaluation of delivery of dsCoGli for the inhibition of Gli transcription factors.

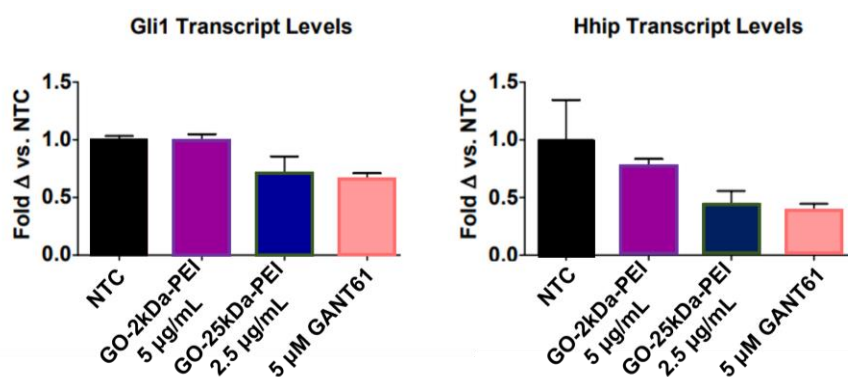


Figure 2.15. Evaluation of GOPEI variant inertness to Hh signaling via qPCR. Both Gli1 and Hhip transcripts are directly produced via activity of Gli transcription factors and the Hh signaling cascade. While GO-2kDa-PEI does not significantly reduce production of these transcripts compared to the non-treated control, GO-25kDa-PEI does to a similar extent as GANT-61, a known Hh inhibitor. This suggests GO-2kDa-PEI is the superior choice for further cellular studies of CoGli delivery.

2.2.2.4 Evaluating Cellular Internalization and Lysosomal Escape

Cellular Internalization: Comparative intracellular delivery of dsCoGli by 2 kDa PEI and GO-2kDa-PEI was evaluated by confocal fluorescence microscopy (Figure 2.16, A) and ICP-MS (Figure 2.16, B). For confocal microscopy, ASZ murine BCC cells were dosed with 20 nM dsCoGliF@PEI and dsCoGliF@GO-2kDa-PEI for 24 hours before imaging. ASZ cells were dosed with non-fluorescently labeled dsCoGli@PEI and dsCoGli@GO-2kDa-PEI for 24 hours before ICP-MS analysis for ^{59}Co quantification.

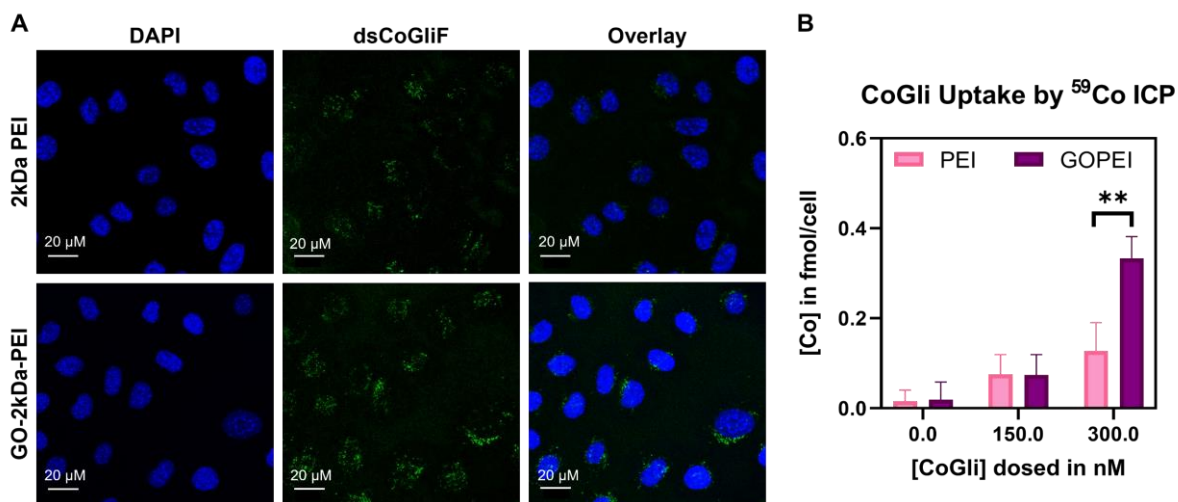


Figure 2.16: Internalization of CoGli. A) Fluorescently labeled (AlexaFluor488) CoGliF is loaded onto PEI or GOPEI and dosed onto ASZ cells in 2% serum media for 24 hours. Internalization is visualized 24 hours later via confocal microscopy. Green channel: CoGliF (excitation @ 488 nm) Blue channel: DAPI nuclear stain (excitation at 405 nm). B) Non fluorescently labeled CoGli is loaded onto PEI or GOPEI and dosed onto ASZ cells. Cells are trypsinized after 24 hours and are counted prior to digestion for ICP-MS analysis of internalized cobalt. Bars represent mean and standard deviation of triplicate samples. PEI and GOPEI loading ratios were 3:1 and 1:4 dsCoGli(F):Nanocarrier, respectively. **=99% confidence interval determined by Multiple Unpaired t-tests in GraphPad Prism.

A fluorescent signal for dsCoGliF is detected when delivered by both PEI and GOPEI (Figure 2.16, A). This suggests both internalization and release from the nanocarriers, as fluorescence would be quenched in proximity to PEI and GOPEI. The signal for GO-2kDa-PEI appears more substantial than that of PEI, suggesting the possibility of either improved internalization or retention. However, more quantitative analysis cannot be performed via confocal microscopy. This is further explored via ICP-MS analysis of cell samples for ⁵⁹Co after incubation with dsCoGli. A dose-dependent uptake pattern is observed for both PEI and GOPEI CoGli nanocarriers (Figure 2.16, B). However, a 3.5-fold improvement in accumulation is observed for 300 nM dsCoGli@GO-2kDa-PEI over dsCoGli@PEI (p=0.0106). This could be attributed to either improved internalization, improved intracellular release and retention, or a

combination of both. Considering both the improved cytotoxicity profile and internalization capability of GO-2kDa-PEI, it was the only delivery vehicle chosen for further cellular studies.

Lysosomal Escape: A common concern with nanoparticles as intracellular delivery vehicles is the difficulty of endosomal/lysosomal escape.⁴⁸ Gli proteins are activated in the cytosol before entering the nucleus; thus, it is imperative that CoGli inhibitors can escape the cytosolic endosomal/lysosomal pathway to target Gli proteins before they cross into the nuclear envelope. To determine compartmental localization of dsCoGli upon delivery with GO-2kDa-PEI, ASZ cells were incubated with CoGli@GO-2kDa-PEI for 24 hours before washing and replacing the media. Cells were simultaneously stained with a lysosome-responsive fluorophore and imaged via confocal microscopy (Figure 2.17, A). After an additional 24 hours, the washed cells were re-stained for lysosomes and imaged. The percentage of lysosomal colocalization at each time point was determined by calculating the percentage of green pixels (dsCoGliF) overlapping with magenta pixels (LysoView633) in the same image field.

As seen previously in Figure 2.16, internalization of dsCoGliF is observed after 24 hours of incubation. The percent colocalization with lysosomes was determined to be $82.3 \pm 6.8 \%$, suggesting that CoGliF@GO-2kDa-PEI is internalized by endocytosis. After 24 hours of removing any un-internalized dsCoGliF, the lysosomal colocalization fell almost 50% to 42.2 ± 12.4 (Figure 2.17, B), a difference that is significant to the 99% confidence interval ($p=0.0045$). This demonstrates that dsCoGli is retained in the cells 48 hours since initial dosing and provides evidence that dsCoGli escapes the lysosomal pathway. These results suggest that dsCoGli delivered by GO-2kDa-PEI will exhibit sufficient bioavailability for Gli inhibition.

It is notable that after 48 hours of access to dsCoGli, colocalization in the nucleus is not observed to a significant degree. Nuclear colocalization is ideal for transcription factor inhibitors

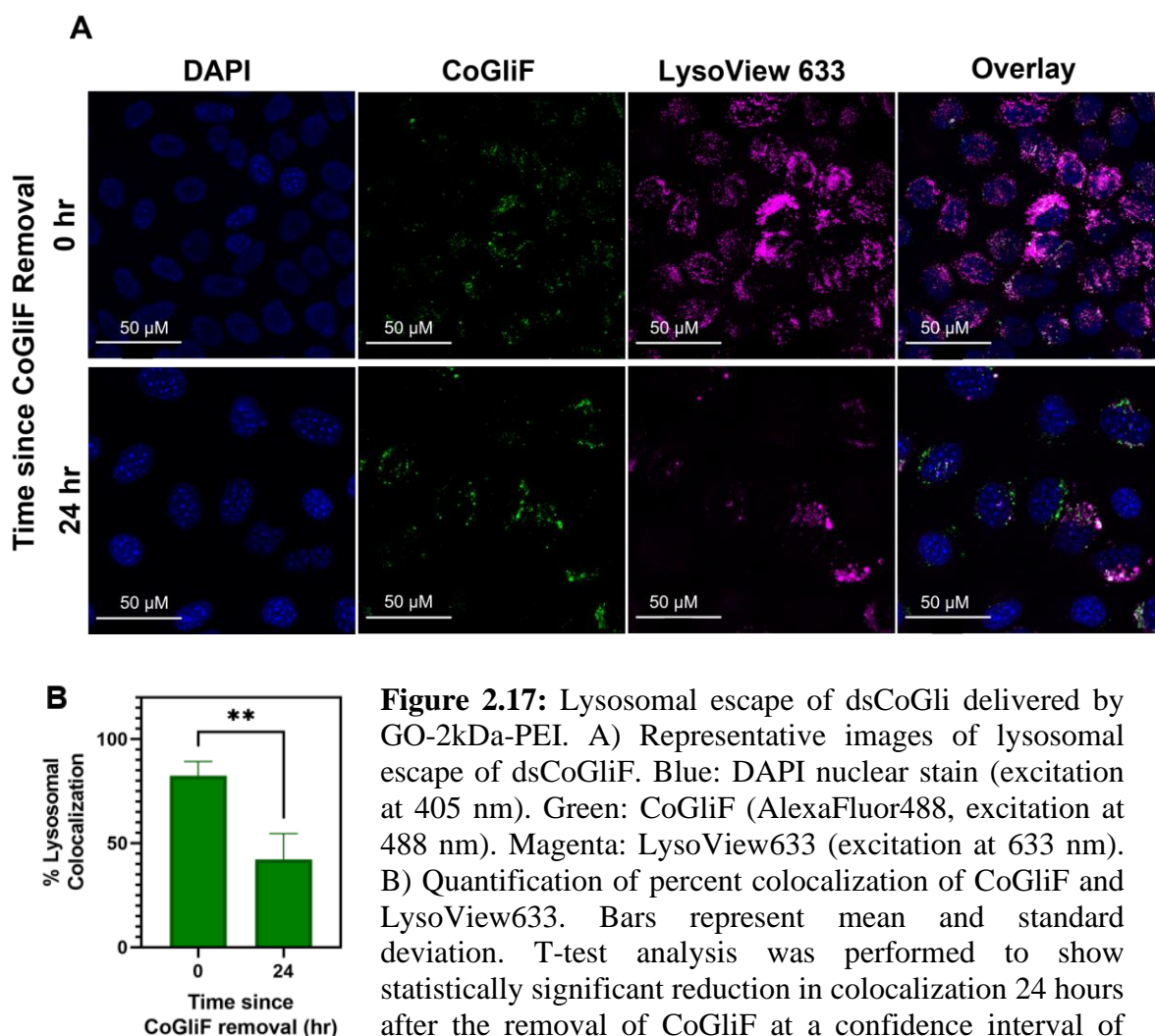


Figure 2.17: Lysosomal escape of dsCoGli delivered by GO-2kDa-PEI. A) Representative images of lysosomal escape of dsCoGliF. Blue: DAPI nuclear stain (excitation at 405 nm). Green: CoGliF (AlexaFluor488, excitation at 488 nm). Magenta: LysoView633 (excitation at 633 nm). B) Quantification of percent colocalization of CoGliF and LysoView633. Bars represent mean and standard deviation. T-test analysis was performed to show statistically significant reduction in colocalization 24 hours after the removal of CoGliF at a confidence interval of 99% (***) by one-way ANOVA analysis.

at large as that is where they actively transcribe DNA. However, Gli proteins are activated in the cytosol following release from the SUFU complex.⁴⁹⁻⁵⁰ This presents a unique advantage for Gli protein inhibition, as intercepting the transcription factor in the cytosol before translocation is sufficient for inhibition.

2.2.2.5 dsCoGli inhibits Hedgehog Signaling in a 2D Migration Assay of BCC

A scratch migration assay was performed to evaluate how the collective of delivery and endosomal escape combine to inhibit Hh pathology. Since Hh signaling is responsible for the

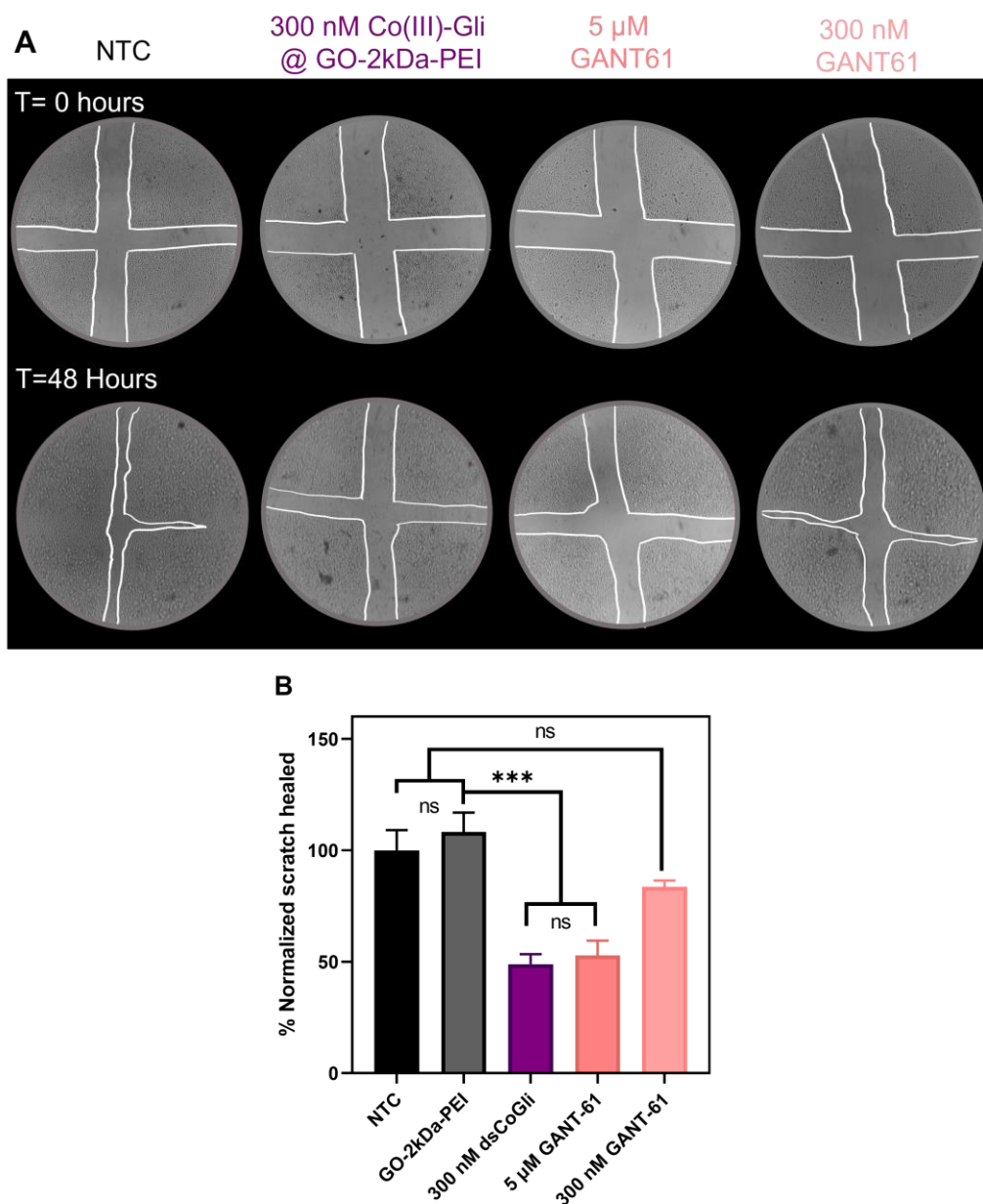


Figure 2.18: ASZ scratch assay results. A) Representative images of (left to right) non-treated control, 300 nM CoGli@GO-2kDa-PEI, 5 μ M GANT-61, and 300 nM GANT-61. White lines are included for clarity and represent the cell-free area of each condition. B) Normalized scratch healing results. Non-treated controls were normalized to 100% scratch healing after 48 hours, and all other conditions were adjusted proportionally. Bars represent the mean and standard deviation of conditions tested in triplicate. The 99.9% confidence interval for statistical significance is represented by ***. No statistical significance was observed for the comparisons between NTC, GOPEI, and 300 nM GANT-61. Similarly, no statistical significance was observed between 300 nM CoGli@GO-2kDa-PEI and 5 μ M GANT-61. A full table of ANOVA results, as well as a T=0 and T=48 hours photos for every replicated are in Experimental Section 2.4 (Table 2.3, Figure 2.20).

migration of ASZ cells, the ability of dsCoGli@GO-2kDa-PEI to halt the migration of a monolayer of ASZ cells into a scratched cross-section was tested (Figure 2.18, A).⁵¹

After 48 hours, nontreated ASZ cells healed most of the scratched area; this healing was normalized to 100%. GO-2kDa-PEI alone was evaluated and showed statistically non-significant differences in migration from the non-treated control (Figure 2.18, B). However, dsCoGli carried by an identical amount of GO-2kDa-PEI resulted in approximately a 50% reduction in the ability to close the scratch that was statistically significant to the 99.9% confidence interval (Figure 2.18, B). These results suggest that the inhibition of migration is solely due to dsCoGli with no interference from GO-2kDa-PEI.

GANT-61 served as a positive control to confirm that direct inhibition of Gli will produce the observed changes in phenotype and that reduction in cell migration is indeed due to inhibition of the Hh pathway. At an identical concentration of 300 nM, GANT-61 did not prevent migration to the extent that it was statistically different from the nontreated cells (Figure 2.18, B). However, cell migration is significantly reduced at the IC₅₀ of GANT-61 (5 μM). These results confirm that direct inhibition of Gli does inhibit Hh-driven migration. Furthermore, inhibition of migration by 5 μM GANT-61 and 300 nM dsCoGli were not statistically different from one another, demonstrating that dsCoGli is a more potent inhibitor than the current standard for Gli inhibition by approximately 17-fold.

Importantly, the reduction in migration observed by 300 nM dsCoGli@GO-2kDa-PEI and 5 μM GANT-61 represent non-cytotoxic concentrations of both inhibitors. Cytotoxicity data in the ASZ cell line for both species is represented in Figure 2.19. While the IC₅₀ of each species was not identified due to limitations of increasing concentrations of both species, the concentrations responsible for reducing ASZ cell migration by about 50% do not show

significant changes in cell proliferation/viability from the non-treated controls. This suggests that while cell proliferation processes are not perturbed, the movement and migration of the cells is halted in the presence of Gli inhibitors.

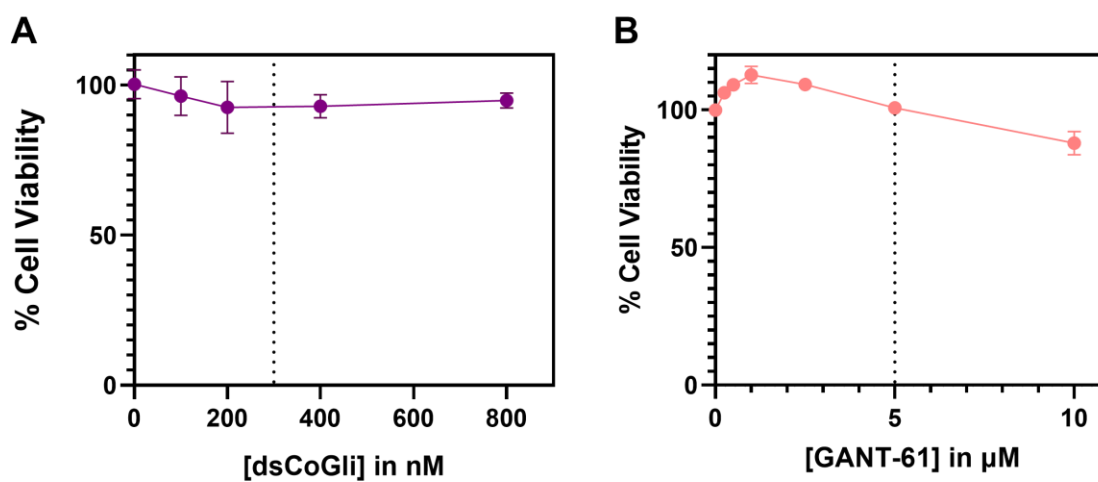


Figure 2.19. Cytotoxicity of dsCoGli carried by GO-2kDa-PEI and GANT-61 in the ASZ cell line. A) Toxicity of dsCoGli delivered at a 1:4 weight ratio to GO-2kDa-PEI. Significant toxicity is not observed up to 800 nM. B) Toxicity of GANT-61. Some toxicity is observed at 10 μ M, but not at 5 μ M. Dotted lines on each graph represent the concentration texted in the scratch migration assay. Significant toxicity is not observed at these concentrations (300 nM dsCoGli, 5 μ M GANT-61).

2.3 Conclusions and Outlook

In summary, this chapter explores the potential efficacy of graphene-oxide based delivery vehicles for CoGli inhibitors of Hh signaling. Two strategies were proposed: 1) utilizing the pi-pi stacking interaction of unmodified GO with single stranded DNA and 2) functionalizing GO with positively charged PEI to generate an electrostatic attraction with the negatively charged DNA backbone.

The first strategy required the addition of salts to overcome electrostatic repulsions between GO and DNA. The identity and concentration of salt were optimized to maximize loading of CoGli synthesized with a 5 single strand overhang and minimize cellular toxicity. Results suggested that 2+ cations promoted a lower concentration necessary for loading, and this was determined to be no less than 0.25 mM. Additionally, the optimal loading ratio of 5ssCoGli:GO was determined to be 1:2 at this concentration. However, these delivery vehicles ultimately failed to internalize CoGli due to off-competition with serum-containing media. One possible solution for future investigation would be extending the single-stranded overhand to 10 or 20 base pairs to strengthen the pi-pi stacking interaction and the media stability of the construct.

The second strategy of functionalization with PEI was explored with both 2 kDa average molecular weight PEI and 25 kDa average molecular weight PEI. The GOPEI variants were synthesized via direct chemical coupling of PEI to the GO surface and characterized by IR, TGA, and ZP. Loading thresholds and cytotoxicity were evaluated for each construct, with GO-25kDa-PEI requiring less delivery vehicle to fully load dsCoGli but being significantly more cytotoxic. This, in addition to the fact to GO-25kDa-PEI is not inert to Hh signaling, eliminated GO-25kDa-PEI as an effective vehicle. GO-2kDa-PEI, however, exhibited less toxicity and is inert to Hh signaling. As such, it was further explored for internalization, lysosomal escape, and ultimately its ability to deliver CoGli inhibitors of Hh signaling in an assay of BCC migration.

Ultimately, dsCoGli escapes the lysosomal pathway when delivered by GO-2kDa-PEI and is biologically available for Gli inhibition. When assayed against GANT-61 in a wound healing assay of ASZ cells, 300 nM CoGli and 5 μ M GANT-61 reduce Hh-driven wound healing by about 50% at a 99.9% confidence level of significance from non-treated controls and GO-

2ka-PEI vehicle controls. However, they were not statistically different for one another. It can be concluded that CoGli, when delivered by GO-2kDa-PEI, exhibits approximately a 17-fold improvement in reduction of Hh-driven wound migration over GANT-61, the current gold standard.

For the community of BCC and cancer research as a whole, developing more effective Hh inhibitors remains an important goal. For CoGli complexes specifically, work towards improving the synthesis of the complex will be paramount for future preclinical work and potential clinical translation. While GOPEI constructs proved efficacious *in vitro* for this first investigation of CoGli inhibitors, it is possible they would be less effective *in vivo* due to lack of targetability and likely poor tissue penetration. Future work will need to be dedicated for optimizing delivery of CoGli agents for therapeutic success.

2.4 Experimental Section

General. All chemicals were purchased from Sigma-Aldrich. The ASZ and BSZ cell lines were obtained from Professor Robert Holmgren at Northwestern University. FBS, M154 media, DPBS, and NucBlue stain were obtained from ThermoFisher (MT35010CV, M154CF500, 14190250, and R37605, respectively). Trypsin was obtained from Gibco (TrypLE, 12563011). Pen/Strep was obtained from Sigma-Aldrich (P0781). All DNA sequences were obtained from IDT with standard desalting.

Synthesis of dsCo(III)-DNA and 5ssCo(III)-DNA Conjugates. The synthesis of CoDNA conjugates (CoGli and CoGliF) was performed according to literature protocols and is described in Appendix 3. DNA sequences contain phosphorothioate linkages (denoted by *) at both the 3' and 5' end to prevent degradation by endonucleases. Due to the challenges of HPLC purification,

single-stranded DNA with Co–Sb attached was purified through size-exclusion Nap25 columns (Cytiva Life Sciences Illustra, 17085201). The samples were run through two columns to remove excess uncoupled Co(III)-Sb. Fractions were collected from the final column and analyzed by UV–vis and ICP-MS for DNA:Co ratio. Samples used experimentally exhibited a 1:1 ratio.

Synthesis of GO-COOH: Graphene oxide (1.375 mg/mL) was prepared via a modified Hummer's method from the reaction of graphite flakes with sulfuric acid and KMnO₄. A slurry in water and H₂O₂ was prepared, vacuum filtered, and washed with 1:10 HCl solution. The GO was then resuspended and purified with multiple rounds of centrifugation, resuspending the GO pellet in water each time. The purified GO was probe-sonicated with a Fisher Scientific model 500 Sonic Dismembrator with a 1/2 inch tip for 1 h at 50% amplitude (~55 W). A total of 12 mL (16.5 mg) was combined with 2 g of NaOH (50 mmol) and 1.42 g of chloroacetic acid (15 mmol). The resulting suspension was probe-sonicated for 2 hours at 25% amplitude. The pH was lowered to 4.5 via dropwise additions of 1M HCl. GO-COOH was purified via centrifugation by washing x4 in UltraPure water. After the final wash, the pellet was resuspended in UltraPure water, freeze-dried, and weighed. Approximately 10 mg were stored as solid for characterization. A 2 mg/mL stock of GO-COOH was made with the remaining particle in UltraPure water by probe sonicating at 25% amplitude for 30 minutes.

Synthesis of GO-2kDa-PEI: In a 15 ml centrifuge tube, 6 mL of 2 mg/mL GO-COOH stock (12 mg) and 6 mL of a 3 mg/mL solution of 2kDa PEI (18 mg) were combined in a centrifuge tube. The mixture was bath sonicated for 10 minutes before adding 0.1 mL 1-ethyl-3-(3-dimethylaminopropyl)carbodiimide. The centrifuge tube was turned end-over-end for 24 hours. GO-2kDa-PEI was purified via centrifugation by washing 1x in PBS and 3x in UltraPure water.

After the final wash, GO-2kDa-PEI was freeze-dried and weighed. Approximately 10 mg of solid were stored for characterization. Next, a 0.8 mg/mL GO-2kDa-PEI stock was made from the remaining solid by probe sonicating in UltraPure water at 25% amplitude for 30 minutes.

Synthesis of GO-25kDa-PEI: In a 15 ml centrifuge tube, 8 mL of 2 mg/mL GO-COOH stock (16 mg) and 40 mg of 25kDa PEI were combined in a centrifuge tube. The mixture was bath sonicated for 10 minutes before adding 0.4 mL 1-ethyl-3-(3-dimethylaminopropyl)carbodiimide. The centrifuge tube was turned end-over-end for 24 hours. GO-25kDa-PEI was purified via centrifugation by washing 1x in PBS and 3x in UltraPure water. After the final wash, GO-25kDa-PEI was freeze-dried and weighed. Approximately 10 mg of solid were stored for characterization. Next, a 0.8 mg/mL GO-25kDa-PEI stock was made from the remaining solid by probe sonicating in UltraPure water at 25% amplitude for 30 minutes.

Thermogravimetric analysis of GO species: Thermogravimetric analysis (TGA) experiments were carried out on a Q500 thermogravimetric analyzer (TA Instruments Inc., New Castle, DE). Before analysis, GO-COOH and GOPEI samples were lyophilized to remove as much adsorbed water as possible. Approximately 3 mg of nanocarrier were weighed precisely before samples were heated from room temperature to 800 °C with a nitrogen gas flow (90 mL min⁻¹) at a heating rate of 5 °C min⁻¹. Mass loss represents the removal of covalent oxo/PEI groups.

Zeta Potential Measurements of GO species: The zeta potentials of GO-COOH and GOPEI species were determined by dynamic light scattering using a Zetasizer (Malvern, UK). Nanocarriers were diluted to a 0.07 mg/mL suspension concentration in UltraPure water. One mL of sample was injected into a Zetasizer cuvette for analysis. Triplicate measurements were taken to ensure reproducibility.

CoGliF loading by GO and GOPEI: In a 364 black-walled plate, 10 μL of 2.36 $\mu\text{g}/\mu\text{L}$ dsCoGliF or 5ssCoGliF was added. Initial fluorescence measurements were taken with excitation at 490 nM and emission at 520 nM on a Synergy H1M plate reader. Next, the plate was removed, and 10 μL of GO, GO-2kDa-PEI, or GO-25kDa-PEI nanocarriers at 2x concentrations were added quickly. For GO measurements containing NaCl, MgCl_2 and ZnCl_2 , the 2x GO stocks also contained 2x the desired final concentration of respective salt. Fluorescent readings were then taken every 30 seconds for 30 minutes to monitor fluorescence quenching. Finally, mass loading ratios were calculated from the percent of fluorescence quenching and the masses of CoGliF and PEI/GOPEI nanocarriers present in the well, corresponding to Equation 2.1

$$\frac{\text{mg CoGli}}{\text{g GO}} = \frac{\% \text{CoGli}_{\text{loaded}} \times \text{mg CoGliF}_{\text{dosed}}}{\text{gGOPEI or GO}_{\text{dosed}}}$$

Equation 2.1: Where $\% \text{CoGli}_{\text{loaded}} = \% \Delta_{\text{Fluorescence}}$, $\text{mg dsCoGliF}_{\text{dosed}} = 2.11 \text{E-}5 \text{ mg}$, $5\text{ssCoGliF} = 2.37 \text{E-}5 \text{ mg}$, and g of GO or GOPEI varies by condition.

Cell Culture: ASZ and BSZ murine BCC cells are cultured in 154 Calcium Free media supplemented with 2% “chelexed” FBS, 1x pen/strep, and 0.05 mM CaCl_2 . Since ASZ and BSZ cells are sensitive to calcium, calcium is stripped from FBS by Chelex-100 (Bio-Rad 142-1253) to achieve a known final concentration of 0.05 mM. Cells were passaged in 75 cm^2 flasks. To split, cells were incubated in DPBS for 10 minutes before lifting in 2 mL of Trypsin for 10 minutes. The Trypsin reaction was quenched in M154 2% serum media, and Trypsin was removed by centrifugation at 200 rcf for 10 minutes. The resulting cell pellet was resuspended in 2% serum M154 and passaged or counted for cell plating.

Visualizing CoGliF Internalization and Lysosomal escape via Confocal microscopy:

Fluorescence images were taken on a Lecia SP5 II Scanning Confocal Microscope. For internalization experiments, cells were plated at a density of 50,000 cells/dish on a FluoroDish (Fisher, 35100) in 500 μ L of 2% serum media. Once 60-70% confluent, cells were treated with 20nM CoGliF carried by weight ratios of 3:1 for 2kDa PEI, 1:4 for GO-2kDa-PEI, 3:1 for 25kDa PEI, and 1:2 of GO-25kDa-PEI of PEI. For GO attempted internalization, the weight ratio was 1:1 5ssCoGliF/GO. For lysosomal staining, 1 μ L of 1000x LysoView 633 (Biotium, 70058) was added to the media for 1 hr. Media was swapped after 4x washing with DPBS, and DAPI stain was added 10 minutes before imaging. Percent colocalization with lysosomes was determined using ImageJ software analysis. Background signals were excluded from the threshold in both images. A selection was created using the signal in the CoGliF channel and was superimposed onto the LysoView channel. The percent colocalization was calculated by the percentage of CoGliF pixels that overlap with LysoView 633 pixels. Data were plotted in GraphPad Prism and represent mean \pm one standard deviation. T-test comparisons were used to determine the statistical significance of the resulting changes in colocalization from 0 hours post-CoGliF removal to 24 hours post removal.

Cellular Toxicity: ASZ cells were seeded at a density of 5,000 cells/well in a 96 well plate (Fisher, 012931) and grown to approximately 70% confluence. Cells were then treated with PEI, GOPEI, CoGli@PEI, or CoGli@GOPEI for 24 hours in triplicate. To analyze, 20 μ L of MTS reagent (Promega, G3580) were added to each well, and the plate was incubated at 37 $^{\circ}$ C for 1-2 hours before 70 μ L of media was removed from each well and transferred to a new 96 well plate to eliminate interference from cells in absorbance readings. The absorbance at 490 nm was measured on a Synergy H1M plate reader. The absorbance of the nontreated controls was

normalized to 100%, and all other conditions were adjusted proportionally. The graphs represent the mean \pm one standard deviation of the triplicate conditions.

Quantitative real time-Polymerase Chain Reaction of GOPEI species: ASZ cells were plated at 175,000 cells/well in 12-well plates. Once confluent, cells were either A) non-treated (3), B) treated at 5 $\mu\text{g}/\text{mL}$ GO-2kDa-PEI, treated at 2.5 $\mu\text{g}/\text{mL}$ GO-25-kDa-PEI, or 5 μM GANT61. After 24 hours, cells were washed 2x in DPBS before harvesting in TRIzol total mRNA isolation buffer (Invitrogen Life Technologies, Catalog # 15596-026) and storing at $-80\text{ }^{\circ}\text{C}$ in RNAase free microcentrifuge tubes. The Qiagen miRNeasy minikit (Qiagen Technologies, Part Number 217004) was used to extract mRNA from all samples. The total quantity of mRNA extracted was verified through nano-drop Ultraviolet-Visible absorption with NanoDrop adaptation. Complimentary DNA sequences were transcribed from 1 μg of mRNA from each sample using Superscript III First-Strand Synthesis SuperMix for qRT-PCR (Invitrogen, Part Number 11752050). Quantitative rt-PCR was performed on a Roche Light Cycler $\text{\textcircled{R}}$ 96 with Faststart essential DNA green master (Roche catalog number 6402712001). The transcript 18s was used as a control. All forward and reverse sequences can be found in Appendix 5.

Determining CoGli internalization via ICP-MS: ASZ cells were plated in 24 well plates (Corning 3526) at a density of 30,000 cells/well. Once confluent, cells were treated with 0, 150, or 300 nM dsCoGli in triplicate carried in at CoGli/carrier weight ratios of 3:1 for 2kDa PEI and 1:4 for GO-2kDa-PEI. For GO attempted internalization, the weight ratio was 1:1 5ssCoGli/GO. After 24 hours, cells were trypsinized and counted via Flow Cytometry using a Guava PCA system using the Guava ViaCount protocol provided by the manufacturer. Immediately, 350 μL of cell suspension were dissolved in trace metals grade HNO_3 for 16 hours at $60\text{ }^{\circ}\text{C}$. Samples

were diluted to an exact final volume of 10 mL and analyzed on a computer-controlled (Plasmalab software) Thermo X series II ICP-MS (Thermo Fischer Scientific, Waltham, MA) equipped with an ESI SC-2 autosampler (Omaha, NE). Each sample was acquired using one survey run (10 sweeps) followed by three main (peak jumping) runs (100 sweeps). ^{59}Co was the primary isotope analyzed, and ^{89}Y and ^{115}In were analyzed as internal standards for data interpolation and instrument control. ICP-MS data was back-calculated in combination with cell counting to calculate [Co] in fmol/cell, subtracting the amount of cobalt determined to be in equivalent amounts of M154 media. Graphs represent the mean \pm one standard deviation of triplicate conditions.

Scratch assay: ASZ cells were plated at a density of 30,000 cells/well in 12 well plates (Corning 3512) and grown to 100 % confluence in 2% serum media. On Day 0, wells were pre-treated in triplicate with controls or respective Hh inhibitors for 24 hours. On Day 1, the monolayer of cells was scratched using a sterile 200 μL pipette tip in a cross. The wells were washed 3x with DPBS to remove detached cells, and the media was reduced to 0.4% serum to encourage migration and not proliferation into the scratched area. Cells were then re-treated with controls or respective Hh inhibitors, and T=0 images were taken on a wide-field microscope at 4x magnification. Plates were incubated at 37 $^{\circ}\text{C}$, and wells were re-imaged at 24 and 48 hours. The percentage of wound healed was measured by comparing cell-free areas calculated in ImageJ at T=0 and T=48 hours. Data were plotted in GraphPad Prism and report the mean \pm one standard deviation of triplicate conditions. One-way ANOVA statistical analysis showed the significance of percent wound healing amongst the various conditions. Complete ANOVA Analysis is shown in Table 2.3.

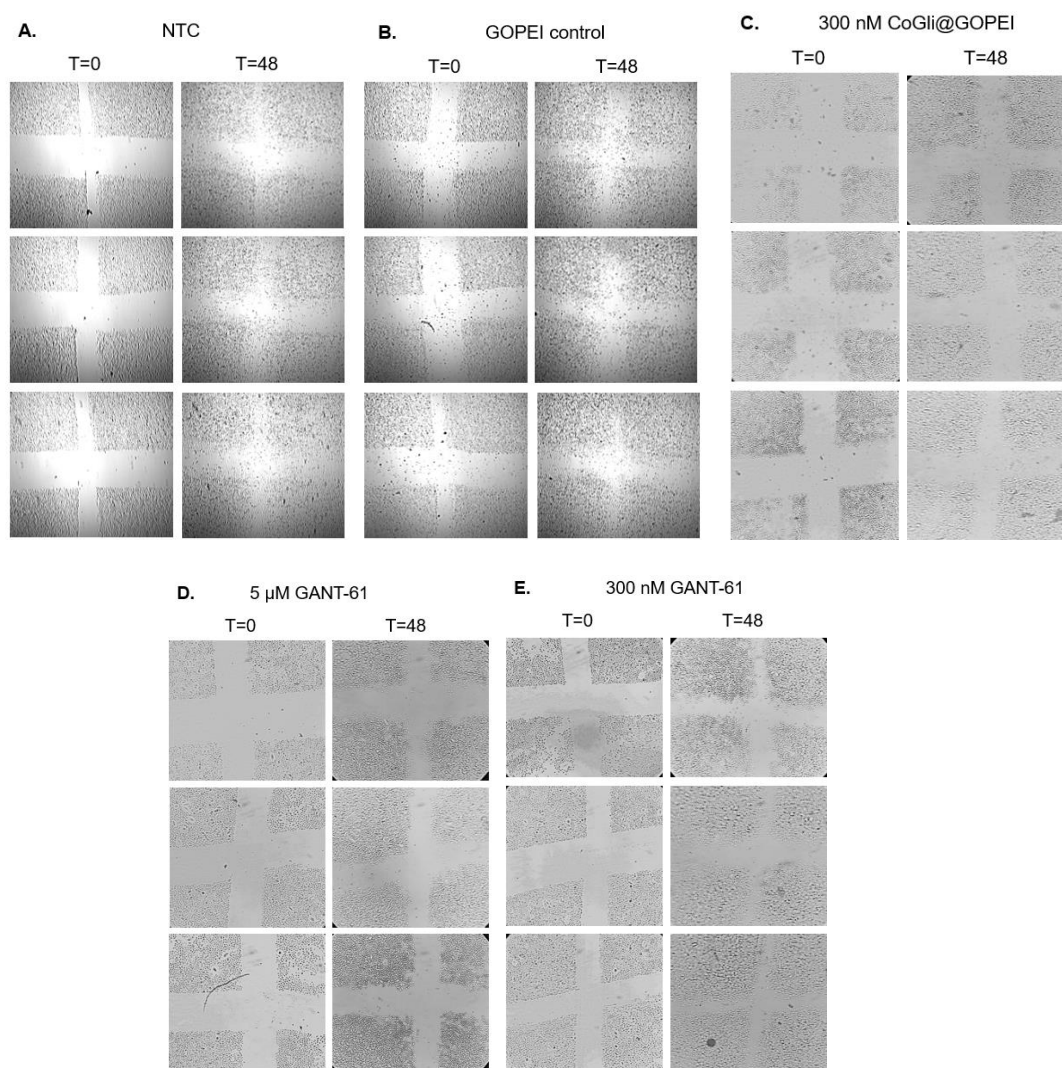


Figure 2.20: Scratch wound healing images. Triplicate results for scratch wound healing of ASZ cells in response to A) non-treated control, B) GO-2kDa-PEI control, C) 300 nM CoGli@GO-2kDa-PEI, D) 5 μ M GANT-61, and E) 300 nM GANT-61. NTC and GOPEI were tested at $n=5$ and all other conditions at $n=3$. The wound area at T=0 and T=48 was measured via ImageJ and statistical analysis was carried out via one-way ANOVA in GraphPad Prism.

Table 2.3. Full ANOVA analysis of ASZ scratch migration assay

Tukey's Multiple Comparisons Test	Mean Diff.	95% CI of diff	Below Threshold?	Summary	Adjusted p-value
NTC vs. GOPEI	0.6612	-24.4 to 25.72	No	Ns	>0.9999
NTC v. 300nM CoGli@GOPEI	58.18	33.11 to 83.24	Yes	***	0.0001
NTC vs. 300nM GANT-61	19.83	-5.23 to 44.9	No	Ns	0.1427
NTC vs. 5 μ M GANT-61	50.93	25.87 to 75.99	Yes	***	0.0004
GOPEI vs. 300nM CoGli@GOPEI	57.51	32.45 to 82.58	Yes	***	0.0001
GOPEI vs. 300nM GANT-61	19.17	-5.89 to 44.23	No	Ns	0.1622
GOPEI vs. 5 μ M GANT-61	50.27	25.2 to 75.33	Yes	***	0.0005
300 nM CoGli@GOPEI vs. 300 nM GANT-61	-38.34	-63.4 to 13.28	Yes	**	0.0036
300 nM CoGli@GOPEI vs. 5 μ M GANT-61	-7.249	-32.31 to 17.81	No	Ns	0.8701
300 nM GANT-61 vs. 5 μ M GANT-61	31.09	6.03 to 56.15	Yes	*	0.0147

Chapter 3

Investigating Hedgehog Pathological Onset in Cellular Systems

3.1 Introduction

The focus of research efforts for BCC therapeutics has centered on treating existing lesions. This is common for cancer treatment as a whole, but BCC is unique from other cancers in that its recurrence rate is remarkably high.¹ This includes lesions that have been treated that come back in the same location but also includes entirely new lesions appearing at another location on the body. It is estimated that approximately 30-45% of patients diagnosed with BCC will develop at minimum one more lesion during their lifetime.^{2, 3} However, this number has varied widely across numerous countries including Japan,⁴ Australia,^{5, 6} Brazil,⁷ Germany,⁸ and the Netherlands.⁹ From these studies, some risk factors for recurrence can be predicted such as younger age, lighter skin tone, superficial BCC subtype at time of diagnosis, red hair phenotype, and male gender.^{2, 10} For patients with these risk factors worldwide, preventative strategies for BCC become equally as important as treatment. Preventative measures focus on reducing sun exposure, which is crucial, but is not enough for many patients to prevent disease recurrence.

The connection between Hh signaling and BCC is well understood- aberrant or unregulated Hh activity is causative of BCC.^{11, 12} This occurs through a hyperproliferative mechanism where basal cells also resist their natural differentiation or cell death cycles.^{13, 14} Over time, tumors develop within the skin and ultimately lead to sores and lesions. However, the molecular driving forces throughout the process of cancer progression remain largely unknown, specifically in relation to how initial Hh pathological dysregulation leads to the vast subtypes, phenotypes, and outcomes associated with BCC. While several new driving forces have been discovered in developed disease,¹⁵ the initial onset of disease has remained largely unstudied.

In this section the first fundamental question discussed is: Can currently available Hh inhibitors prevent the onset of Hh signaling in a cellular system? While parallel driving forces of

BCC onset may be unknown, it is clear that Hh signaling plays a crucial role. If currently available Hh inhibitors effectively prevent dysregulation, they could be the first choice for studying BCC prevention in existing patients. The second portion of this chapter focuses on studying exogenous Hh activation in basal cells isolated from human skin tissue. It was hypothesized that exogenous manipulation of Hh signaling would result in amplified proliferative and migratory phenotypes in these cells which could be probed molecularly to identify biological cascades working in tandem with Hh signaling during BCC phenotypic onset.

3.2 Results and Discussion

3.2.1 Activation in the pluripotent C₃H/10T1/2 cell line

While section 3.2.2 of this chapter will discuss efforts towards studying the onset of Hh signaling in skin cells specifically, a literature standard for evaluating the onset of general Hh activity is performed in the C₃H/10T1/2 cell line.¹⁶⁻¹⁹ This line is a pluripotent murine fibroblast identity that undergoes osteogenic differentiation in response to Hh signaling activation.²⁰ This transition is further characterized by the onset in expression of alkaline phosphatase (ALP),²¹ a membrane bound glycoprotein that catalyzes the cleavage of phosphate esters.

It was hypothesized that this system could be used to study the effectiveness of currently available Hh inhibitors in prevention of Hh pathological onset if C₃H/10T1/2 cells were concurrently treated with an Hh activator and an Hh inhibitor. While this is not uncommon to the literature, studies primarily focus on sonic hedgehog (SHH) proteins as the activator at PTCH1 as it is the natural initiator of the pathway.¹⁶ The goal of this research was to take this system one step further and also evaluate inhibition response when smoothened (SMO) is the point of pathway overactivation. In BCC, loss of PTCH1 function and gain of SMO function mutations

are the most common,^{11, 15} and it was hypothesized that inhibitors may exhibit differential response dependent on the point of activation. In this section, both SHH and smoothed agonist (SAG) are explored as Hh activators while Vismodigeb and Cyclopamine, smoothed inhibitors, and GANT-61, a Gli inhibitor, are evaluated for their ability to prevent Hh initiation.

3.2.1.1 Optimizing all activator and inhibitor concentrations

It is important that the different activators enact similar differentiation onto the cells so that inhibition can be directly compared. To optimize this, the C₃H/10T1/2 cell line was allowed to differentiate either in response to SHH recombinant protein (30 nM or 50 nM) or Smoothened Agonist (SAG, 100 nM).

The resulting data is summarized in Figure 3.1. Both 100 nM SAG and 30 nM SHH produced similar increases in ALP concentration in differentiated C₃H/10T1/2 cells over the non-treated control. Specifically, 100 nM SAG produced ALP relative fold concentration of 7.6 ± 0.71 and SHH at 9.2 ± 1.3 which were not statistically different when analyzed by one-way ANOVA analysis ($p=0.4106$). However, 50 nM SHH resulted in a significantly higher relative fold concentration of 22 ± 2.2 . As such, 30 nM SHH and 100 nM SAG were chosen for all further activation experiments.

Before performing concurrent inhibition experiments with Vismodigeb, Cyclopamine, and GANNT-61, cytotoxicity was determined for each compound. DMSO was also evaluated as it is the solvent for each of the three compounds. The C₃H/10T1/2 cell line was found to be quite sensitive to DMSO at low percentages in cell media (Figure 3.2, A). Due to the constraints of

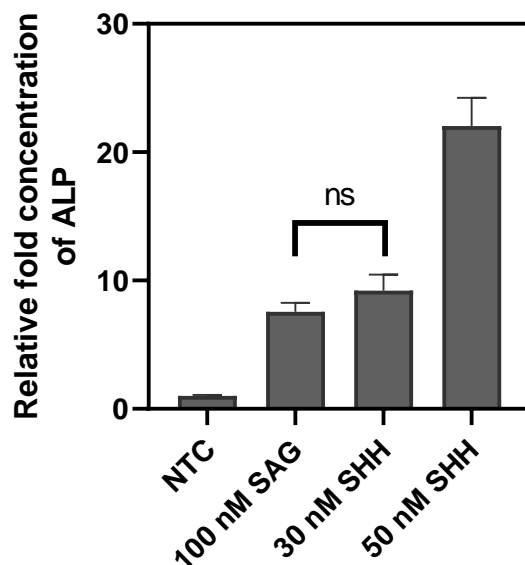


Figure 3.1: Quantification of ALP concentration in cell lysates in response to Hh activators. Both ALP and total protein concentration were determined and ng of ALP/mg of total protein was calculated for each sample. To normalize across biological replicates, the NTC samples were normalized to 0 by dividing each sample by the group average. The treated samples were normalized similarly by dividing by the same group average of the NTC samples. The multiplicity for 100 nM SAG is 7.6 ± 0.71 and for 30 nM SHH is 9.2 ± 1.3 , which were not statistically different from one another using one-way ANOVA analysis ($p=0.4106$). Analysis was performed in GraphPad Prism and error bar represent the mean \pm the standard error of the mean. A high concentration of SHH, 50 nM, resulted in 22 ± 2.2 fold concentration increase, a concentration that could not be matched by small molecule SAG. Error bars represent the mean \pm one standard error of the mean.

pipetting small volumes for toxicity assays in 96 well plates, 0.33% DMSO was determined to be the maximal percentage for evaluating the Hh inhibitors for cytotoxicity.

For all compounds, cell death was not observed out to 10 μ M (Figure 3.2, B-D). Interestingly, each compound at low concentrations slightly increased cell viability compared to the non-treated controls. While there is not currently a hypothesis to explain this, the more important factor is that higher concentrations of the inhibitors do not result in cellular death and this full range is acceptable for studying in differentiation assays.

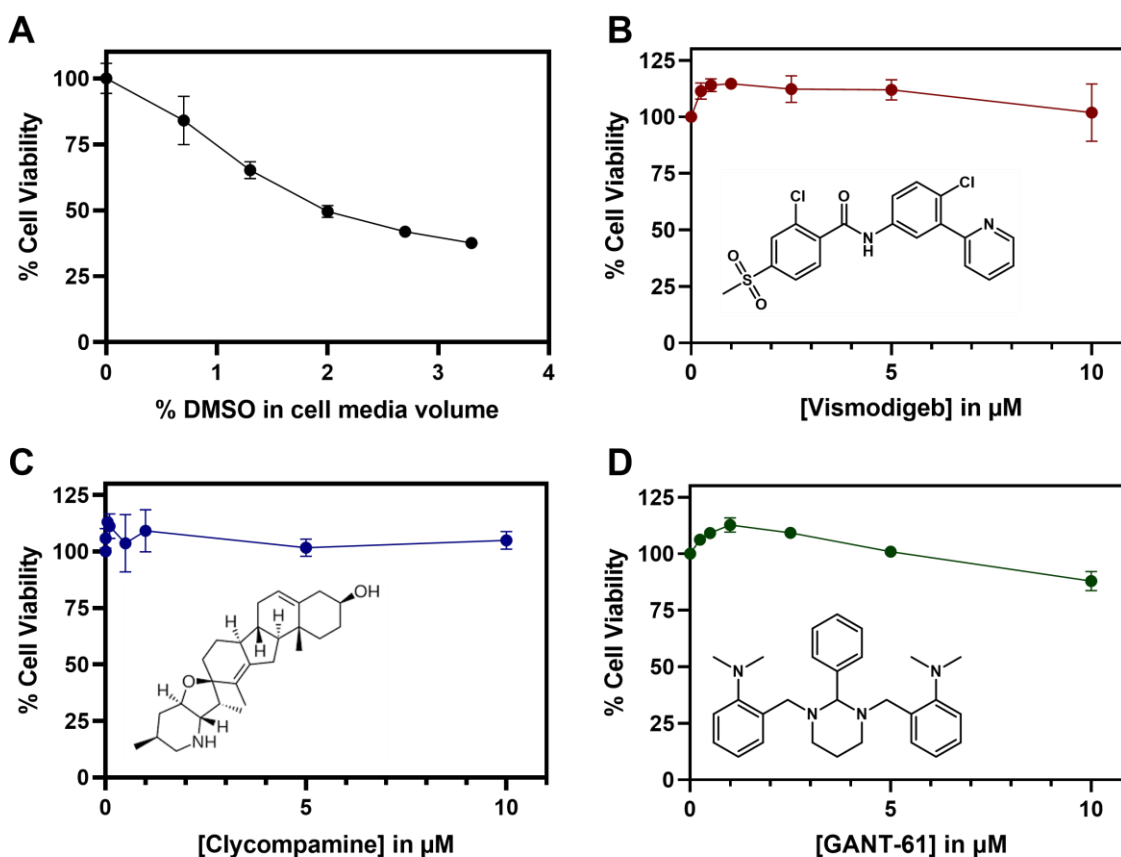


Figure 3.2: Cytotoxicity of various Hh inhibitors in the C₃H/10T₁/2 cell line. A) Cytotoxicity of DMSO at various volume/volume percentages in cell media. The cells display high sensitivity to low percentages of DMSO. B-D) Cytotoxicity of Vismodigeb, Cyclopamine, and GANT-61 respectively. For all three compounds, cytotoxicity is not observed out to 10 μM . It is concluded that these concentrations can be safely studied for inhibition of Hh initiation without the risk of confounding cell death with prevention of differentiation. The chemical structure for each compound is given in the bottom left corner of each respective graph. Error bars represent the mean \pm one standard deviation.

3.2.1.2 Inhibition with smoothened antagonists (Vismodigeb, Cyclopamine)

The ability of currently available SMO inhibitors to prevent Hh pathological onset in the C₃H/10T₁/2 cell line was tested against pathway activation at both PTCH1 by SHH incubation and at SMO by SAG incubation. To note, SAG was chosen because it shares a binding pocket with many of the common smoothened inhibitors including Vismodigeb and Cyclopamine. The idea was to build a model cellular system that mimicked a potential “mutation” of the binding

site for these inhibitors which might reduce binding affinity and therefore efficacy. The inhibitors chosen were Vismodigeb and Cyclopamine (both discussed in detail in Chapter 1). Vismodegib and Cyclopamine have different structural components, and it was anticipated that they would produce differences in their ability to prevent point-dependent pathway activation. Each biological experiment contained non-treated controls that received no activator or inhibitor, positive controls that contained only the activator, and 3-4 varying concentrations of inhibitors with concurrent activation held constant at 100 nM SAG or 30 nM SHH.

When activated with SHH, Vismodigeb inhibited Hh activation with an estimated IC_{50} of approximately 10 nM. When activated by SAG, this inhibitor effect falls approximately 7.5-fold to an IC_{50} around 75 nM (Figure 3.3, A). While this is still an excellent inhibitory concentration, it provides initial evidence in support of the hypothesis. The point of pathway activation has a significant effect on prevention of pathway activation, but inhibition is still observed with both SHH and SAG activators. However, Cyclopamine did not experience the same result. When activated with SHH, Cyclopamine exhibits approximately a 100 nM IC_{50} for prevention of Hh activation. When activated with SAG, an IC_{50} could not be determined out to 1 μ M (Figure 3.3, B), suggesting at least a 10-fold reduction in inhibitory effect.

To summarize, Vismodigeb inhibition with SHH or SAG activation produces model systems where the inhibitory efficacy of a smoothed inhibitor is impacted by the point of pathway activation, but inhibition is ultimately achieved at low nM concentrations. Cyclopamine, however, produces a model system where the efficacy is obliterated at low nM concentrations. This can be explained by the binding affinity of each compound for the desired location. This data suggests that Vismodigeb can successfully out-compete SAG from the

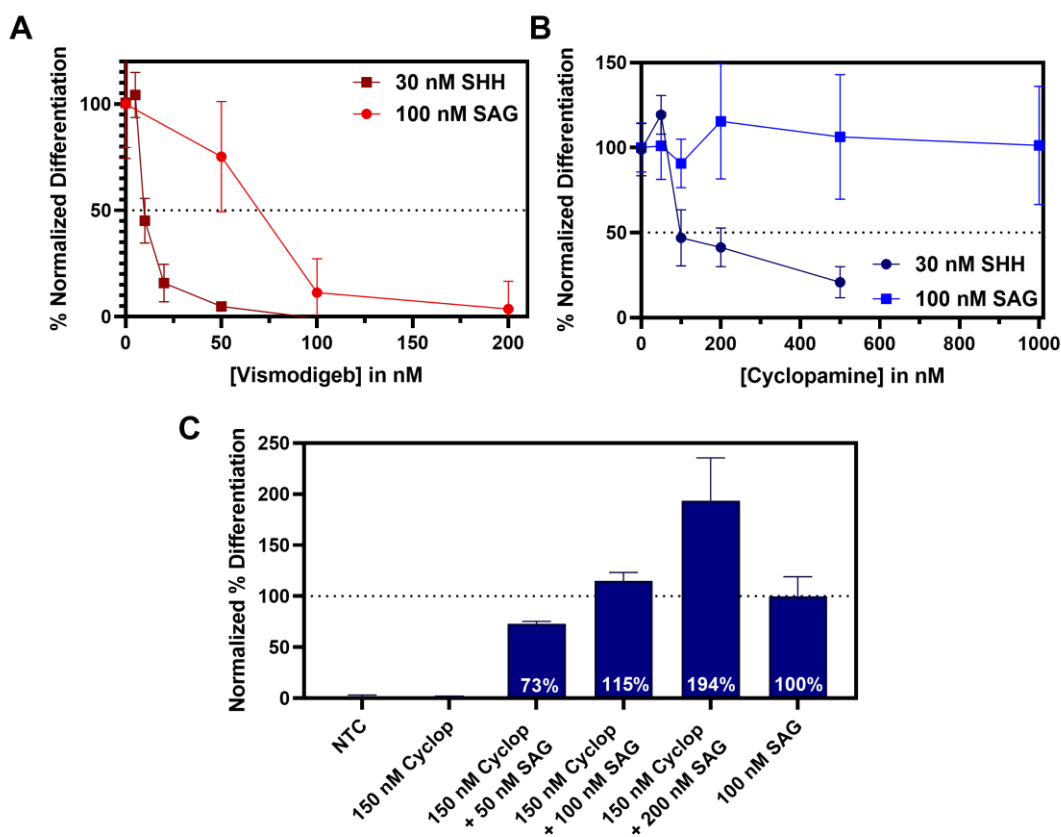


Figure 3.3: Prevention of C₃H/10T₁/2 differentiation by smoothed inhibitors in response to SHH and SAG activators. A) Inhibition by Vismodigeb. Vismodigeb prevents activation by SHH at an IC₅₀ around 10 nM and activation by SAG at approximately 70 nM. B) Inhibition by Cyclopamine. When activated by SHH, Cyclopamine prevents 50% of differentiation around 100-200 nM. When activated by SAG, inhibitions is not observed. C) Off-competition of Cyclopamine by SAG. When Cyclopamine concentration is held constant at 150 nM, 50 nM SAG is sufficient to produce 73% of differentiation observed by the 100 nM SAG-only positive control. These data suggest that smoothed inhibitor efficacy is dependent on the point of Hh pathological onset, and different inhibitors experience different degrees of this affect. Error bars represent the mean \pm one standard deviation.

pocket, but Cyclopamine cannot. In other words, the mimicked “mutation” can be overcome by Vismodigeb but not Cyclopamine.

To confirm this, an off-competition experiment between Cyclopamine and SAG was performed where the concentration of Cyclopamine was held constant at 150 nM and the concentration of SAG was varied from 0 to 200 nM. The percentage of differentiation for each condition was normalized to 100 nM SAG only positive controls (Figure 3.3, C). At 150 nM

Cyclopamine, 50 nM SAG restores differentiation to 73% of what is observed from the positive control. Treating concurrently with 100 nM SAG restores differentiation to 115% (within error of the positive control) and 200 nM SAG boosts differentiation to almost 200% when normalized to 100 nM SAG only. This data supports the hypothesis that treating the C₃H/10T_{1/2} cell line with SAG as the Hh activator mimics a system where Cyclopamine cannot bind its target pocket and cannot exhibit any inhibitory effect. Vismodigeb, however, overcomes that challenge in this system, but that is often not the case for real mutations seen in human cancer.

3.2.1.3 Inhibition with Gli antagonists (GANT-61)

As discussed in Chapter 1, smoothened has been the primary target for chemotherapeutic intervention of the Hh pathway, but mutations often lead to chemoresistant tumor recurrence that even Vismodegib cannot overcome. Studies have shown the Gli transcription factors are a valuable alternative target.^{22, 23} As shown in section 3.2.1.3, the efficacy of smoothened inhibitors is dependent upon the point of pathway activation. Both Vismodigeb and Cyclopamine are most effective at preventing Hh activation when PTCH1 is the activated protein. This is logical, as smoothened directly follows PTCH1 in the pathway and inhibiting an “un-mutated” SMO would easily block the activation signal from cascading. However, SAG activation mimics a “mutation” or competition for SMO binding sites that the inhibitors must be able to overcome.

One of the reasons Gli transcription factors have gained attention is their potential ability to bypass sensitivity to the point of pathway activation. To test that in this system, GANT-61 was employed as a Hh inhibitor in identical C₃H/10T_{1/2} differentiation experiments. Unlike both Vismodigeb and Cyclopamine, GANT-61 efficacy is not dependent on the point of pathway activation (Figure 3.4). Regardless of activation point, the observed IC₅₀ for preventing

differentiation was approximately 3 μM . Combined, the data collected from Vismodigeb, Cyclopamine, and GANT-61 inhibition support the ability of currently available Hh inhibitors to prevent activation without influencing cellular viability. Vismodigeb and Cyclopamine efficacy are dependent on the point of activation. GANT-61, however, bypasses this complication in this cellular system and would be worth studying in more skin specific systems.

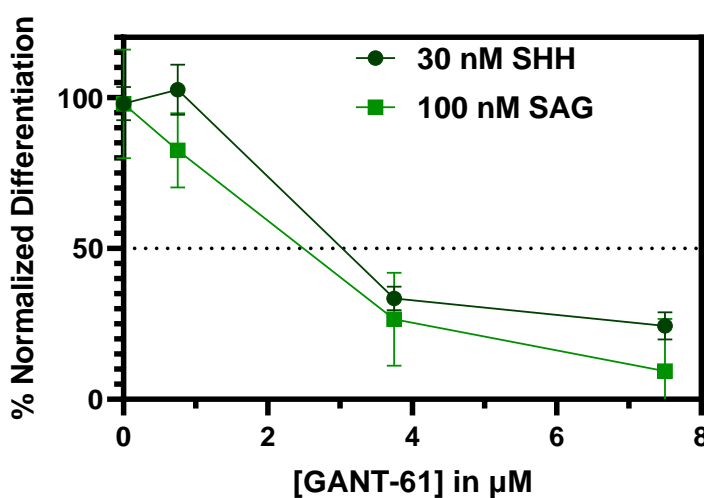


Figure 3.4: Prevention of C₃H/10T1/2 differentiation by GANT-61 with SHH and SAG activators. Regardless of activation point, GANT-61 prevents roughly 50% of differentiation at approximately 3 μM . Error bars represent the mean \pm one standard deviation.

3.2.2 Activation in Normal Human Epidermal Stem Cells

While results from section 3.2 are encouraging for the ability of currently available Hh inhibitors to prevent Hh activation, it cannot necessarily be directly translated to what might be observed in BCC. Additionally, it does not provide insight into what other cellular mechanisms translate initial Hh overactivation to a phenotype of cancer. To explore this further, normal human epidermal keratinocytes (NHEK) were isolated from human tissue. The basal cell population of the epidermis (from which BCC originates)^{24,25} is the predominant cell population

obtained during isolation. As such, it is a perfect cell system for evaluating the influence of exogenous Hh activation on phenotypes associated with BCC. In this section, both proliferation and migration changes associated with activation by SHH and SAG are discussed.

3.2.2.1 Influence of Exogenous Hh Activation on NHEK Proliferation

A reliable characteristic of BCC phenotype is hyperproliferation, especially early-stage BCC.^{13, 14} Therefore it was hypothesized that incubating NHEK cells with Hh activators would cause an increase in NHEK proliferation. To assay this, NHEK cells were plated sparsely for multi-day proliferation analysis as detailed in Section 3.4. Both SHH and SAG were evaluated as Hh activators acutely (cells only begin treatment on Day 1 of the assay) or chronically (cells began receiving treatment in culture 5 days prior to plating the experiment).

Data for experiments containing acute treatments represent the average of results from 3 biological replicates with cells originating from different human donors (Figure 3.5, A). Both SAG and SHH produce a slight increase in proliferation over non-treated cells on average. However, this result is mild and for SAG diminishes after 4 days of proliferation. Chronic activation results were performed only once, and data represents the average of 4 technical replicates (Figure 3.5, B). A similar trend is observed where the increased proliferation is mild and is lost altogether at Day 4 of proliferation. Additionally, when compared to the averages of acute SAG and SHH treatments, 5 days of chronic treatment did not produce a more profound increase in proliferation (Figure 3.5, C&D).

Of note, while the averages of acute treatment show mild increases in proliferation, individual biological replicates showed differential responses (Figure 3.6). Donor 1 was most responsive to SAG, Donor 2 was most responsive to SHH, and Donor 3 was non-responsive to

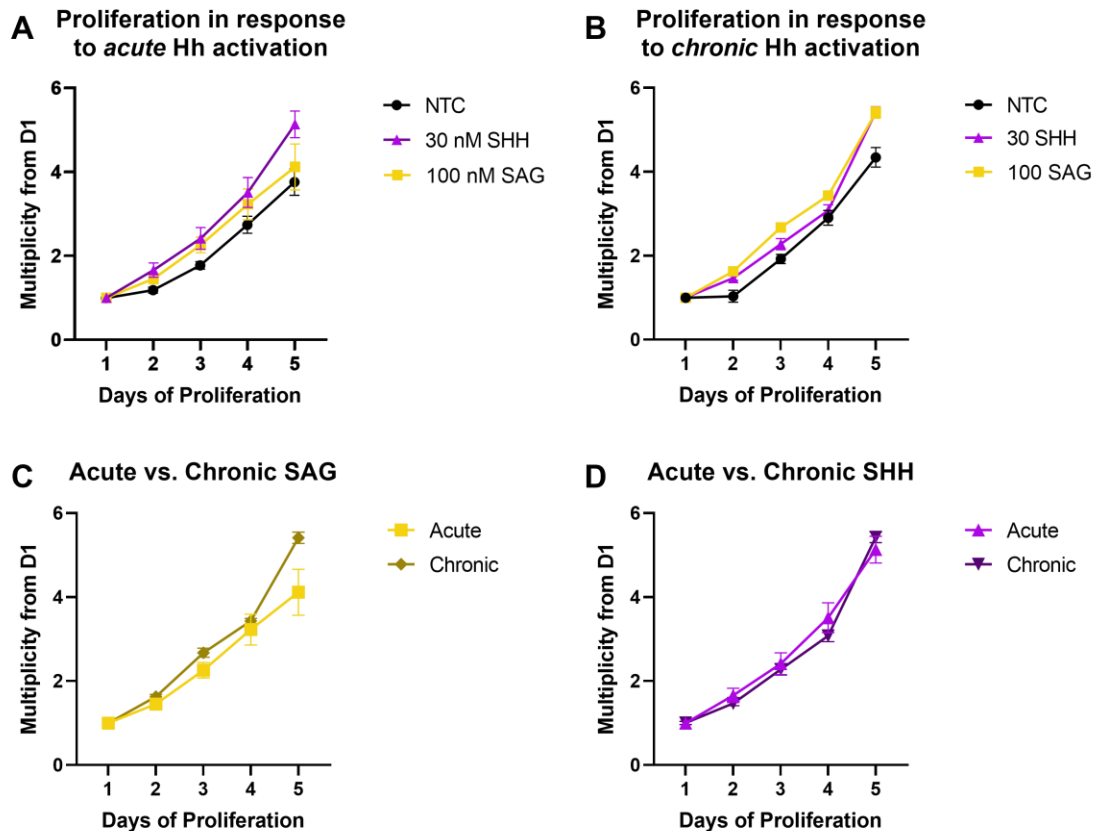


Figure 3.5: Proliferation results of NHEK cells in response to SHH and SAG. A) Acute treatments result in mild increases in proliferation over non-treated cells across 3 biological replicates. B) Chronic treatment 5 days prior to experiment plating results in slight increases in proliferation in one biological replicate. C&D) Chronic treatment for 5 days does not significantly increase proliferation over acute treatment for both SAG and SHH, respectively. Error bars represent the mean \pm one standard error of the mean.

both activators until Day 4. This data highlights a fundamental benefit of this methodology of research- donor differences are built into the experiment inherently. But combined, it can be inferred that resistance mechanisms to Hh activation that are present in healthy cells (Hhip, PTCH1, p53) are likely working to prevent the overactivation of a pathway that will lead to a diseased phenotype. Both Western blot and qPCR analysis were attempted, but insufficient cellular material specifically at early experimental days prevented this analysis from providing

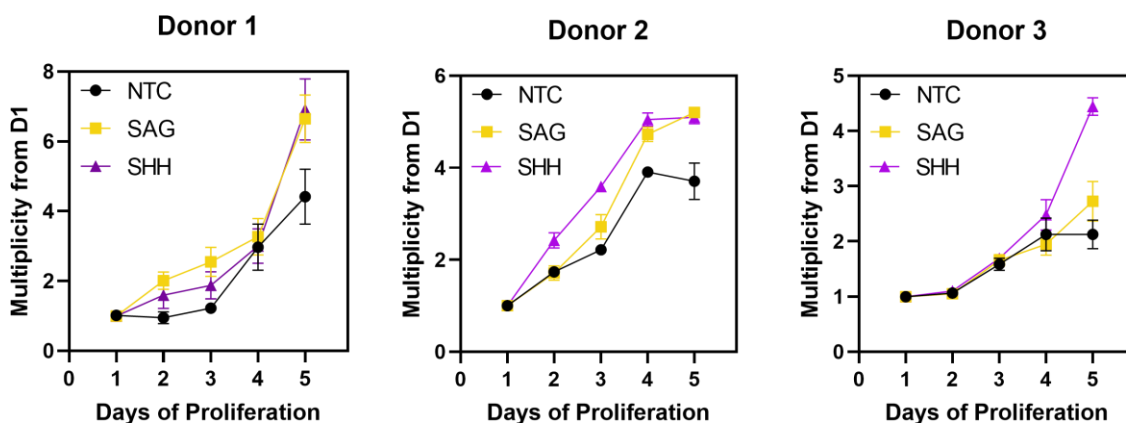


Figure 3.6: Proliferation response to acute SAG and SHH by donor. Donors 1&2 were both sensitive to activators early, but differed in which activator they were more responsive to. Donor 3 was non-responsive until Day 4, and even then only significantly responsive to SHH. Error bars represented the mean \pm one standard error of the mean.

further insight. To address this in the future, it is recommended for more wells of each condition to be plated and ultimately lysed.

3.2.2.2 Influence of exogenous Hh activation on NHEK migration

The second seminal phenotype of BCC is migration, which is predominantly observed in later stages of BCC but has some influence in the beginning stages.^{26, 27} It was similarly hypothesized that exogenous Hh activation would produce an increase in the migratory potential of NHEK cells. To test this, NHEK cells were plated to confluence for scratch wound healing assays detailed in Section 3.4. Images were taken every 6 hours from T=0 until any of the replicates of any condition were nearly closed (usually between 16-24 hours depending on the donor). ImageJ software was used to measure the area of the wound remaining at each time point and the healed percentage was computed by dividing the final area by the initial.

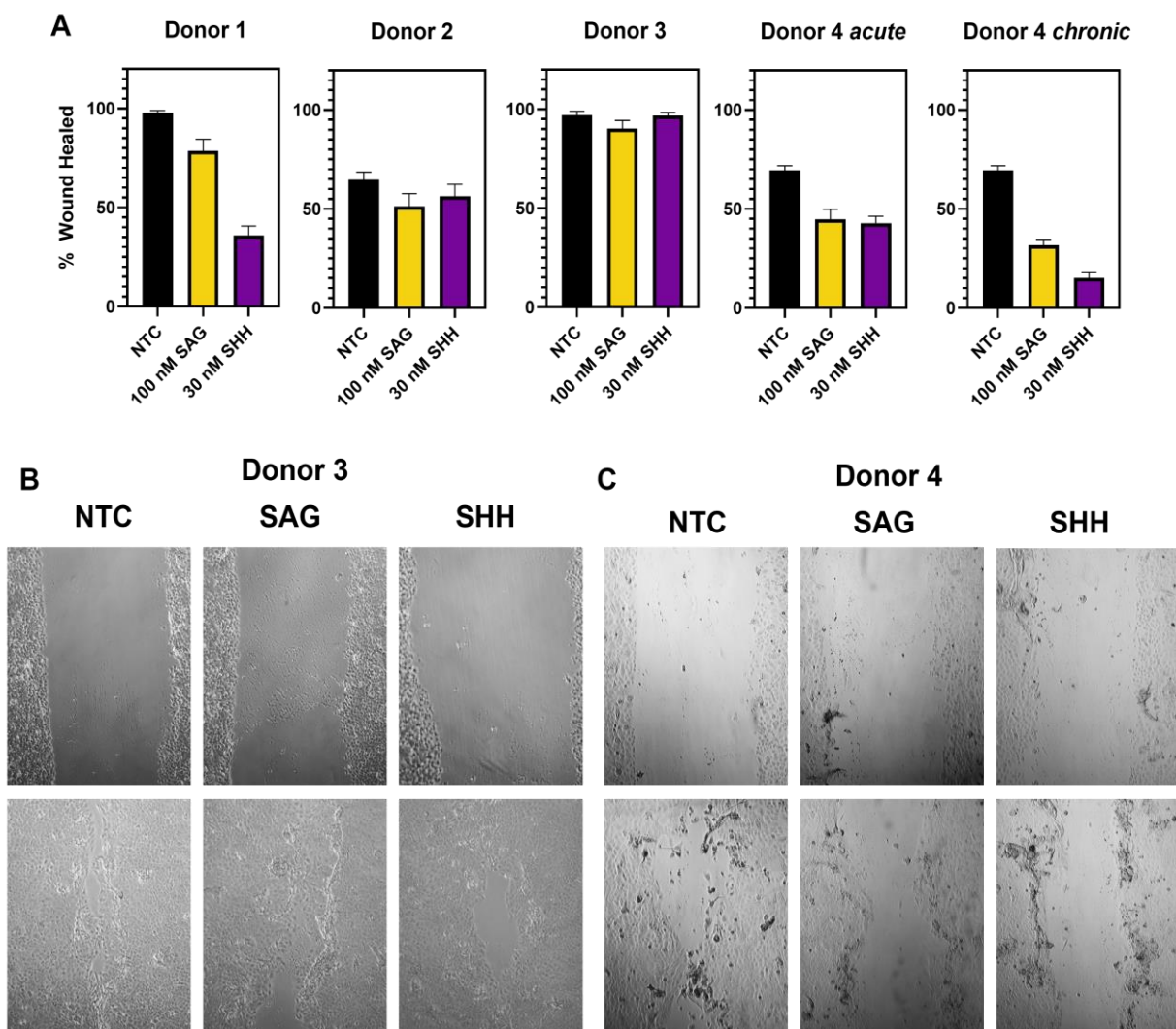


Figure 3.7: Influence of SAG and SHH on NHEK migration in a scratch wound healing assay. A) Across four different biological replicates from different cell donors, migration was either unchanged (Donors 2, 3) or reduced (Donor 1,4). This affect is amplified for Donor 4 upon chronic treatment of the inhibitors for 5 days prior to plating the experiment. Bars represent the mean \pm one standard error of the mean. B & C) Representative images for Donor 3 and Donor 4 for acute treatment with SAG and SHH. Donor 3 shows near-complete wound healing for each condition. Donor 4 shows reduced migration for cells treated with Hh activators.

The results reveal, in some ways, a consistency to proliferation results. Each donor experiences a different response to SAG and SHH. However, the result was the opposite of what was hypothesized. Instead of increasing migration, acute SAG and SHH incubation either

produced no changes in migration or migration was decreased (Figure 3.7). This affect was amplified for Donor 4 when cells were dosed chronically for 5 days with SAG and SHH. The inhibition of migration was more extreme in the chronically dosed cells.

Interestingly, the degree of non-treated control (NTC) migration over the time frame did not have an influence over response to exogenous Hh activators. Both Donor 1 and Donor 3 NTC cells averaged almost 100% migration after 16-18 hours. Hh activators reduced migration in Donor 1 but not in Donor 3. Similarly, both Donor 2 and Donor 4 NTCs only achieved an average of ~70% migration at the end of the experiment. Hh activators reduced migration in Donor 4 but not in Donor 2. This suggests that the overall migration rate of the non-treated cell line does not predict the response to SAG and SHH. While these results do not yet have a data supported explanation, it is possible again that innate Hh control mechanisms are preventing an activation of migration. It is likely that in samples where migration is unchanged, this control mechanism is not sufficient to stunt normal cell function but is in donors where migration was halted.

3.3 Conclusions and Outlook

In summary, this chapter explores 1) the ability of Hh inhibitors to prevent Hh pathological onset in the C₃H/10_T1/2 cell line and 2) exogenous Hh activation of NHEK cells in 2D assays of proliferation and migration. In the C₃H/10_T1/2 system, no innate Hh resistance mechanisms exist to prevent activation. As such, there are no barriers towards studying concurrent inhibition. Ultimately, smoothed inhibitors were found to have differential inhibition efficacy dependent on the point of pathway activation (SAG vs SHH). Cyclopamine could not overcome competition for its binding site by SAG, but Vismodigeb could, imitating

pathway mutations that could influence smoothed inhibitor efficacy. GANT-61, however, exhibited the same potency regardless of pathway activation. This data supports other literature claims that perhaps Gli is the more valuable target for Hh inhibition.

While this data is promising, it is not directly translatable to understanding how Hh initiation leads to BCC phenotype and if that process can be prevented with currently available Hh inhibitors. To assay this, NHEK cells isolated from a variety of tissue donors were exposed to SAG and SHH both acutely and chronically in proliferation and migration assays. Hh activators produced a mild increase in cell proliferation but experienced a degree of donor dependency across the three donors studied. Furthermore, 5-day chronic treatment with SAG and SHH did not result in amplified proliferation. For these experiments to yield more conclusive results, it is necessary to assay even more donors. Additionally, these results suggest that short-term activation is insufficient to largely overcome innate Hh regulation mechanisms. The duration of chronic treatment could be increased to see if long periods of inundation with activators would eventually trigger a spike in proliferative phenotype.

Migration experiments produced a rather different result. Incubation with SAG and SHH either did not change migration rate or resulted in reduced migration instead of the hypothesized increase. These results are not yet understood, and alternative methods of pathological analysis would be necessary to unpack it further. Because the only cell population actively involved in migration are the ones at the edge of the scratch, bulk analysis by qPCR and Western blot are not ideal analysis methods. Future work towards elucidating reasonings for these trends should focus on immunostaining for relevant proteins at the scratch edge. However, it is important to remember that migration is a phenotype of later stages of BCC and increased migration may not be achievable by short-term Hh activation. However, understanding the source of migratory

reduction could elucidate connected pathways that are imperative for controlling Hh overactivity that may start to fail during the development of BCC.

3.4 Experimental Section

General: Cell culture supplies FBS, DPBS, and calcium-free M154 media were obtained from ThermoFisher (MT35010CV, 14190250, and M154CF500, respectively). L-glutamine solution was obtained from Sigma-Aldrich (200 mM, G7513). Basal Medium Eagle media was purchased from Life Technologies (21010046). Trypsin for C₃H/10T_{1/2} cells was obtained from Gibco (TrypLE, 12563011). Smoothened Agonist (1 mg, 501490076), Vismodigeb (10 mg, GDC-0449, ApexBio Technology LLC, 50-101-3792), GANT-61 (2 mg in DMSO solution, 37-340-32MG) and Cyclopamine (1 mg, 50464348) were purchased through Fisher Scientific. Recombinantly expressed sonic hedgehog protein was purchased through Abclonal (100 µg, RP0056). The C₃H/10T_{1/2} cell line was purchased through American Type Culture Collection (CCL-226, Clone 8). Trypsin for NHEK cells is made in-house by diluting 9 mL of 0.25% trypsin-EDTA solution (Sigma T-4049) in 36 mL of Versene (500 mL DPBS supplemented with 1 mL of 0.5M EDTA).

C₃H/10T_{1/2} cell culture: The media for culturing C₃H/10T_{1/2} cell lines is a BME media base (500 mL) supplemented with 50 mL of FBS (10%) and 5 mL of 200 mM L-glutamine solution (final concentration 2 mM). For a serum free media formulation, the BME base was supplemented only with 5 mL of L-glutamine solution. Cells were passaged in 75 cm² flasks and not allowed to pass 70% confluence before splitting to maintain stem-like nature. To split, cells were lifted in 1 mL of Trypsin for 5 minutes while incubating at 37° C. The trypsin reaction was quenched with 10% serum containing BME. Cells were not centrifuged prior to passaging or

counting. Once past passage 15, cells were discarded and new cells were thawed for continued experiments. Cells were frozen at early passages in 10% DMSO and 90% media and stored long-term at -196°C .

NHEK cell culture: The media for NHEK cell culture is calcium-free media M154 supplemented with 1 human keratinocyte growth supplement (ThermoFisher, S0015) 175 μL of 0.2 M CaCl_2 (final concentration 70 μM), Amphotericin B (Sigma A2942, 250 $\mu\text{g}/\text{mL}$), and gentamycin (Sigma G1307, 50 mg/mL), hereby referred to as M154 complete. Cells were passaged in 10cm^2 tissue culture dishes. To split, cells were lifted in 2 mL of Trypsin solution for 7 minutes while incubating at 37°C . The trypsin reaction was quenched in 10% serum containing media and trypsin/serum-containing media were removed via centrifugation at 500 rcf for 5 minutes. Cells were resuspended in M154 complete prior to passaging or counting. NHEK cells isolated from patient tissue (performed by various members of the Perez-White laboratory) were only used for experiments if they had been passaged 5 or less time and had been in culture for 21 days. Past passage 5 or day 21, cells were discarded.

C₃H/10T1/2 differentiation assay: Cells were plated at 15,000 cells/well in 12 well plates in full 10% serum media (D0). The next day (D1), the media was swapped to 0.1% serum containing media (a 100-fold dilution) and both Hh pathway activators and inhibitors were added. Activators included 100 nM SAG and 30 nM SHH. Inhibitors included Vismodigeb and Cyclopamine SMO inhibitors, and GANT-61 Gli inhibitor. On Day 4, the wells were harvested for alkaline phosphatase activity and total protein assay. In each biological replicate, conditions were evaluated in triplicate or quadruplicate technical replicates.

Alkaline Phosphatase Assay: The SensoLyte® pNPP Alkaline Phosphatase Assay Kit (AnaSpec AS-72146) was used to quantify alkaline phosphatase. The assay was performed following guidelines from the manufacturer's protocol. Briefly, cells were washed twice with 1X assay buffer prior to lysing each well with 100 μ L of a solution of Triton-100 in 1X assay buffer (20 μ L of Triton-100 per 10 mL of assay buffer). Lysis occurred at 4°C with agitation. Cell lysates were collected following gentle scraping of each well to ensure complete collection into individual microcentrifuge tubes kept on ice. The tubes were centrifuged at 2,500 x g for 10 minutes at 4°C to pellet any insoluble proteins. The supernatants were used for ALP quantification and concurrent total protein analysis. For ALP quantification, 35 μ L of supernatant from each sample was transferred to a clear 96-well plate. Assay volumes for ALP standards were also prepared at 35 μ L, as well as para-nitrophenyl phosphate (pNPP) substrate so the total volume of each well is 70 μ L. Once all samples were plated, 35 μ L of pNPP solution was added to each well and incubated at 37°C for 30 minutes. Absorbance was measured at 490 nm using a BioTek Synergy 4 multi-mode microplate reader.

Total protein assay: Total protein concentration in cell lysate supernatants was determined via Pierce™ BCA Protein Assay Kit (ThermoFisher 23225) to normalize ALP quantification. Serial dilutions of Bovine Serum Albumin (BSA) solutions from 2 mg/mL to 0.063 mg/mL (diluting by ½ with each step) were prepared in 1X assay buffer at a final volume of 25 μ L in a 96 well plate. Sample supernatants were similarly plated at 25 μ L volume. The working reagent was prepared by combining Part A to Part B in a 1:50 ratio. Each well (standard and sample) received 200 μ L of the resulting working reagent. The plate was incubated at 37°C for 30 minutes before the absorbance was read at 562 nm using a BioTek Synergy 4 multi-mode microplate reader.

Calculating and normalizing ALP/total protein: The standard curves for each assay were used to determine total ng of ALP and total mg of protein. Dividing ALP by total protein produces ng ALP/mg of protein. The negative control (no activator) and the positive control (activator only, no inhibitor) are then used to normalize the samples. To normalize to the negative control, the average of those replicates was subtracted from every sample to set the negative control to 0. From here, each sample (positive control replicates included) was divided by the average of the positive control to normalize it to 100% and everything else accordingly. All bar graphs represent the mean \pm one standard deviation.

Cellular Toxicity: C₃H/10T_{1/2} cells were seeded at a density of 10,000 cells/well in a 96 well plate (Fisher, 012931) and grown to approximately 70% confluence. Cells were then treated with Vismodigeb, Cyclopamine, or GANT-61. Importantly, the C₃H/10T_{1/2} cell line is very sensitive to DMSO (Figure 3.2, A), which is the solvent for each compound tested for toxicity. When treating, each well is held consistently at 0.33% by making compound stocks at 300x the desired final concentration. Then 1 μ L of the stock is combine with 31 μ L of media and 10 μ L is added to each of triplicate wells for each condition. To analyze after 24 hours, 20 μ L of MTS reagent (Promega, G3580) were added to each well, and the plate was incubated at 37 °C for 1-2 hours before 70 μ L of media was removed from each well and transferred to a new 96 well plate to eliminate interference from cells in absorbance readings. The absorbance at 490 nm was measured on a Synergy H1M plate reader. The absorbance of the nontreated controls was normalized to 100%, and all other conditions were adjusted proportionally. The graphs represent the mean \pm one standard deviation of the triplicate conditions.

NHEK proliferation assay: NHEK proliferation studies were performed by tracking cellular growth over multiple days. On D0, cells are plated sparsely at 15,000 cells/well in 24 well plates with one plate for every day of the experiment (6 days = 6 24 well plates). When plating, 500 μ L of M154 complete is added to each well. NHEK cells are counted and diluted to 30,000 cells/mL with a total volume corresponding to adding 0.5 mL of the suspension to each desired well (example, 100 wells=50 mL). Cells are added to the wells slowly in a snake-like motion with the pipette tip submerged below the media level to ensure dispersion. After each well contains cells, the plates are left to sit undisturbed for 20 minutes so the cells can naturally settle to the bottom and maintain dispersity. On Day 1, one plate is taken for an initial DNA assay while all other plates are treated with Hedgehog activators SAG and SHH in M154 complete. To do this, the media was removed prior to adding fresh media supplemented with the desired final concentration of activator. The media of non-treated cells was also swapped. For the DNA assay, the media was removed from each well and 600 μ L of M154 (phenol red free) was added to the wells. A solution of Hoechst 33342 DNA intercalating dye (ThermoFisher, H3570 10 mg/mL solution in water) was diluted x10 to a final volume that allows adding 200 μ L to each well analyzed. The plate was incubated at 37°C for exactly one hour prior to measuring fluorescence with $\lambda_{\text{excitation}}=355$ and $\lambda_{\text{emission}}=460$ on a PerkinElmer VICTOR™ X5 plate reader. A plate was read every day for 4-5 days, and remaining plates were retreated every 2 days. Data was analyzed by normalizing the average fluorescence intensities of Day 1 to 1 and dividing the readings for each day after by the average fluorescence intensity form Day 1 to achieve a multiplicity from Day 1. This normalizes each biological replicate and can account for some donor differences.

Scratch migration assay: Before plating, a horizontal line was drawn on the bottom of each plate with an ethanol resistant marker. NHEK cells were then plated at confluence (500,000 cells/well) in 12 well plates in 1 mL total of full M154 complete. After 1 day, the monolayer of cells was scratched using a sterile 200 μ L pipette tip and the cells were washed x5 in DPBS to remove detached cells. The media was then replaced with non-proliferative media by achieving a final concentration of 200 μ M CaCl_2 in the M154 complete (as opposed to 70 μ M in normal growth media). Wells receiving Hh activator SHH were simultaneously treated, and images were immediately taken for T=0. For imaging, pictures were taken on a Zeiss Axioplane 2 microscope with Zeiss AxioCam HRC color camera directly above and directly below the lab marker line of each well to ensure imaging in identical locations at each time point. Images were then taken every 6 hours until a given condition was nearly closed. ImageJ analysis software was used to carefully measure the area of each wound at each time point.

Chapter 4

Modeling Basal Cell Carcinoma Disease Progression

4.1 Introduction

It was discovered almost 30 years ago that BCC onset and progression are caused by aberrant expression in Hh signaling.¹⁻⁵ In the last 30 years, only two chemotherapeutics that specifically target the Hh signaling cascade, Vismodegib and Sonidegib, have been clinically approved for the treatment of BCC.^{6, 7} Even so, they are only approved for disease that is classified as untreatable by surgical removal. It is assumed that they are not approved for earlier stages of BCC because surgical removal is the most effective treatment option. However, this often leaves patients with multiple, visible, and disfiguring scars that negatively impact their quality of life. Non-scarring chemotherapeutics may be more attractive treatment options for many patients.

A unique challenge for BCC research is the overall lack of cellular model systems in which therapeutics can be evaluated in early stages. As discussed in Chapter 1, there are basic cellular assays for evaluating Hh inhibition and some *in vivo* models for BCC, but there is very little in between. Cancer is complex, necessitating model systems that grow in complexity as a drug candidate progresses through evaluations. Moreover, the models that do exist have failed to successfully incorporate human skin identity. This chapter first discusses efforts towards developing 2D *in vitro* cellular systems that are more complex than the most basic cellular studies. It further reports a 3D model of a fully differentiated human epidermis that was grown in the presence of established BCC cells as the first heterogenous 3D model of BCC.

4.2 Results and Discussion

4.2.1 Transwell Migration of ASZ cells

The Hedgehog-driven migration and movement of BCC cells is an ideal phenotype for the evaluation of Hedgehog therapeutics in 2D cell culture systems. Many researchers turn to

scratch migration assays (as described in Chapter 2) for these experiments, but the complexity of this movement is not robustly representative of cells in 3D environments. For many other cancer types, researchers instead perform transwell migration experiments that require cells seeded on the top of a porous membrane to actively detach from one another, pass through a small pore, and reattach on the other side.^{8, 9} Cells are serum starved on the top of the membrane to encourage movement towards serum on the other side.

Transwell migration assays, however, have been rarely performed with BCC cells. The few reported instances of this were recently published in 2019.¹⁰⁻¹² However, none of these reports or subsequent reports have evaluated chemotherapeutics against Hh signaling as a method for inhibiting migration.¹³ It was hypothesized that this assay would be particularly useful for determining the ability of Hh inhibitors to prevent BCC cell migration observed in early stages of BCC development as well as eventual metastasis. This data also provides information for the development and subsequent inhibition of 3D models discussed in this chapter, as it is imperative to study a chemotherapeutic that effectively inhibits the cancer cell population.

The murine ASZ BCC cell line was pre-treated with either Vismodegib (a smoothed inhibitor) or GANT-61 (a Gli inhibitor) for 24 hours prior to seeding onto porous membranes for transwell migration experiments. Access to the inhibitors was maintained throughout the experiment. Migrated cells were fixed and stained for microscopic evaluation after 48 hrs. Images were captured and a cell counting protocol was developed in ImageJ. When treated with Vismodegib, the cells showed little sensitivity towards reducing migration. While migration is mildly decreased, the effect stabilizes at approximately a 30% reduction out to 1 μ M (Figure 4.1,

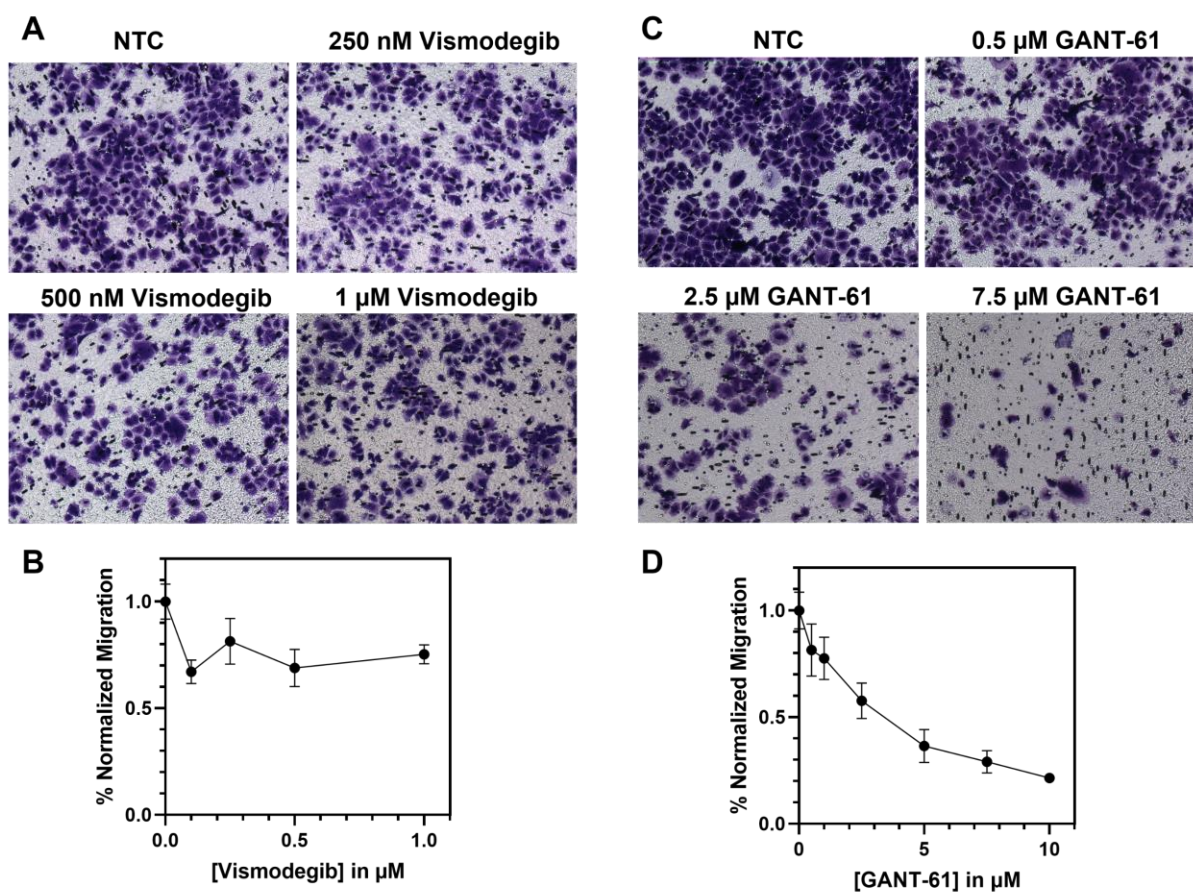


Figure 4.1: Transwell migration results of ASZ cells treated with Vismodegib and GANT-61. A) Representative images from non-treated, 250 nM, 500 nM, and 1 μM Vismodegib treatment. B) Normalized migration results for Vismodegib. C) Representative images from non-treated, 0.5 μM, 2.5 μM, and 7.5 μM GANT-61. D) Normalized migration results for GANT-61. Graphs represent the mean \pm one standard deviation. The number of migrated cells were counted according to a developed ImageJ macro described in Section 4.4.

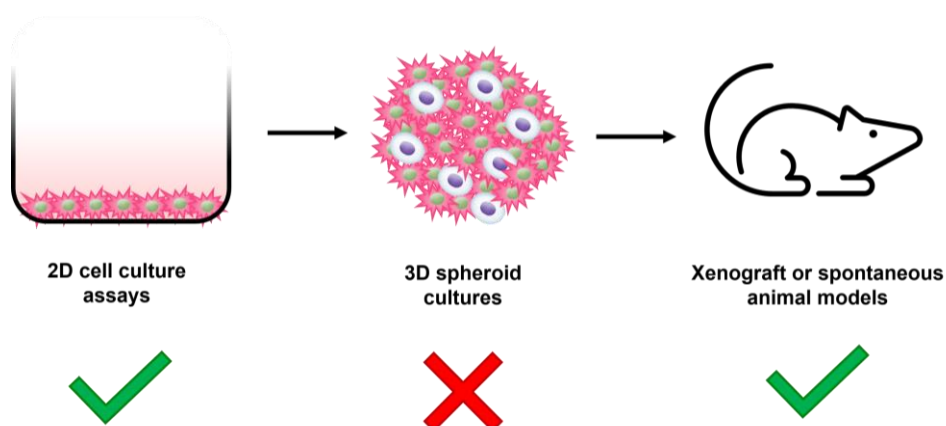
A&B). With the normal IC_{50} of Vismodegib being in the low nM range, it was concluded that the ASZ cell line is resistant to this inhibitor.

ASZ cells, however, experience a reproducible dose-dependent reduction in migration when treated with GANT-61 (Figure 4.1, C&D). Each concentration was tested in at least 2 biological replicates with 5 random image fields being taken of each membrane for technical replicates. The IC_{50} is approximately 3 μM (Figure 4.1, D) which corresponds to literature

reported values as well as Meade lab previously published results.¹⁴ This data is promising as it shows that the phenotype of Hh-driven ASZ cells can be regulated by direct inhibition of Gli transcription factors even when SMO inhibition is not effective. The optimization of this assay provides a very useful tool for the BCC research community at large and is easily performed with non-specialized laboratory equipment and little expertise.

4.2.2 Incorporation of ASZ cells into a 3D Organotypic Skin Model

Basic 2-dimensional cellular assays are excellent tools for very early evaluations of chemotherapeutics. However, they are not accurately representative of how cells behave in heterogeneous 3D environments. Many cancer research groups have addressed this concern through the development of 3D spheroid models of cancer cells in culture (Scheme 4.1).¹⁵ These models allow for the incorporation of heterogeneity and complexity in small tumor-like masses. However, this is not completely applicable to BBC, especially early stages where tumor masses

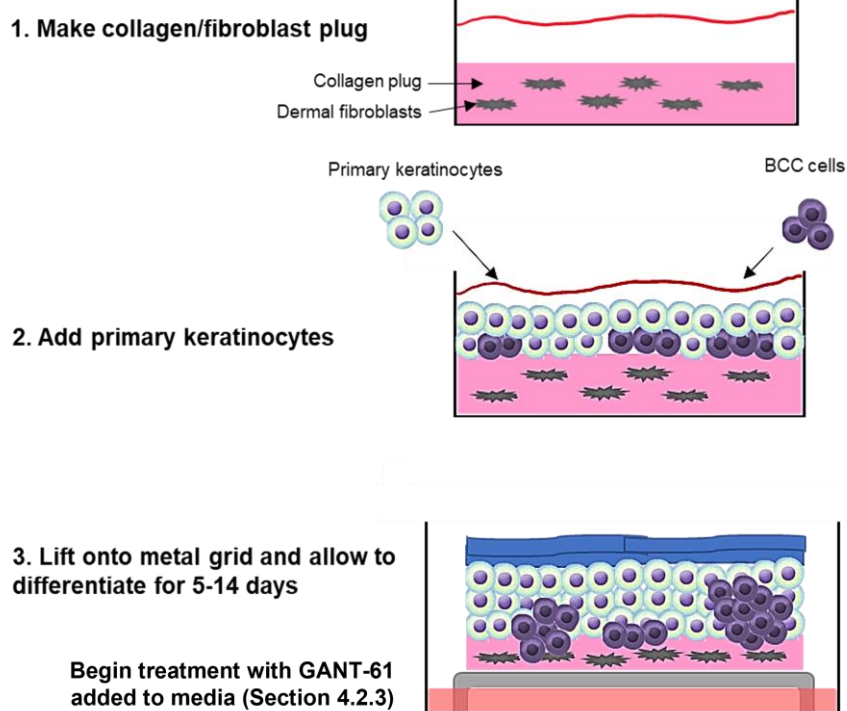


Scheme 4.1: Representation of the typical pipeline of cancer chemotherapeutic evaluation. Eventual *in vivo* animal work benefits from more complex cellular systems following simple 2D assays. A heterogeneous model that mimics aspects of patient BCCs has not yet been reported for BCC.

have yet to fully form. These models are also isolated and exclude the role that surrounding non-diseased tissues play in the phenotypes and pathology of the cancer.

In 1975, the isolation and culture of human epidermal keratinocytes (NHEK cells) was first published.¹⁶ In 1981, the first report was published developing NHEK cells into a 3D tissue that comprised the totality of a differentiated epidermis.^{17, 18} Briefly, NHEK cells are seeded onto a collagen plug that mimics the dermal layer of skin. Plugs are then lifted to an air-media interface where differentiation occurs spontaneously. These models have been utilized to study a variety of skin properties, disorders, and diseases.¹⁹ In one instance, keratinocytes were co-cultured with squamous cell carcinoma cells to create what was termed “disease-in-a-dish”.²⁰ More recently, a model of Merkle Cell Carcinoma was similarly generated.²¹ We hypothesized similar models could be developed with established BCC cells.

Specifically, it was hypothesized that co-culturing NHEK cells with the murine ASZ BCC cell line in a 3D differentiation assay would generate tissues that mimic characteristics of patient BCCs (Scheme 4.2). This model was desired for two primary purposes. The first is mechanistic- since the cancer cell and healthy cell populations originate from different species, they can be analyzed independently by qPCR and immunofluorescence. Particularly of interest was the transformation the healthy cells undergo in response to the cancer cells. This will be discussed in this section. The second purpose was for the development of a preclinical tool that could be used for 3-dimensional analysis of BCC chemotherapeutics. This will be discussed in section 4.2.3. As a final benefit of this technique, NHEK cells isolated from multiple donors can be used to study these affects across a range of biological replicates. For these studies, NHEK cells were selected for Caucasian race/light pigmentation because this population suffers the most from BCC.



Scheme 4.2: Experimental design for 3D co-culture epidermal tissues. Normal human epidermal keratinocytes (NHEK) cells are mixed with ASZ cells in defined ratios and seeded on top of a collagen dermis mimic. After 2 days, plugs are lifted onto a metal support grid and allowed to differentiate for 5 or 12 days before harvesting. Resulting tissues are analyzed by histological staining, qPCR, and immunofluorescence.

4.2.2.1 Histological Features of Resulting Models

NHEK and ASZ cells were seeded onto dermal mimics in the following ratios for the development of control or diseased 3D-models: 100% NHEK (control), 90%NHEK/10% ASZ, 75% NHEK/25% ASZ, 50% NHEK/50% ASZ, and 100% ASZ (control). Tissues were allowed to differentiate for 5 or 12 days prior to harvesting. Thus far, 4 biological donors of NHEK cells have been investigated at 5 days of differentiation and 4 biological donors have been investigated at Day 12.

The first method of analysis for the resulting tissues was routine staining with hematoxylin and eosin (H&E). H&E staining reveals phenotypic changes with increasing cancer incorporation. Figure 4.2 shows representative images of Day 5 tissue samples. With 10% ASZ incorporation, cellular shape in the developing stratum spinosum is altered. When healthy, these cells develop a prolate spheroid, or football, shape. In the 90% NHEK/10% ASZ sample, this shape is stretched along the horizontal axis. With the incorporation of 25% ASZ cells, organization of the cellular layers is lost entirely with no distinguishable difference between basal and spinosa layers. Additionally, some groupings of cells have begun to protrude into the collagen plug. By 50% cancer incorporation, the basement membrane separating the dermis and epidermis is lost all-together. Cellular structures are not easily distinguished, and the uppermost

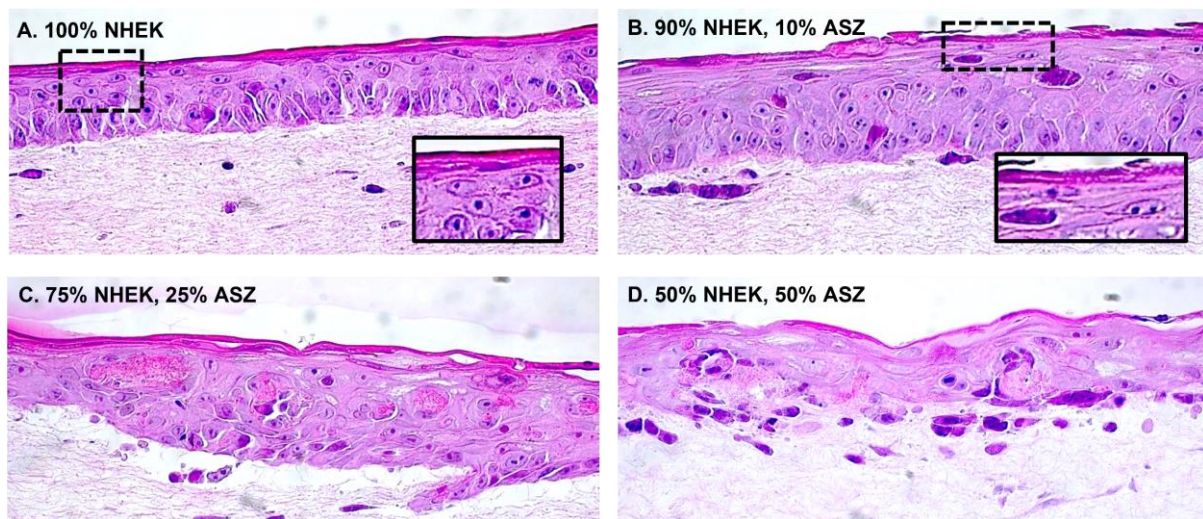


Figure 4.2: Histological (H&E) analysis of 3D co-culture tissues harvested on Day 5. A) 100% NHEK non-diseased tissue. Cells in the stratum spinosum develop structural order and a prolate spheroid (football) shape. B) 90% NHEK/10% ASZ. Organization is lost and shape of cells is elongated. C) 75%NHEK/25% ASZ. All organization and structure of cells is lost, some groups of cells are seen protruding into the dermis layer. D. 50% NHEK/50% ASZ. The basement membrane that separates the dermis from the epidermis is lost completely. The cornified layer that represents the beginnings of terminal differentiation is nearly non-

pink staining of the cornified layer is greatly diminished.

At Day 12, these differences are even more striking (Figure 4.3, Parts 1 & 2). 100% NHEK tissues show the full, uninfluenced differentiation of the epidermis. Specifically, organization of cells is seen in the stratum spinosum, dense staining of keratohyalin granules is observed in the stratum granulosum, and a thick cornified layer is stained brightly pink. For all donors, alterations to phenotype are observed with as little as 10% cancer incorporation. The basal layer of cells becomes disorganized and the clean line separating the epidermis from the collagen plug deteriorates. Additionally, keratohyalin granules are less densely observed in the stratum granulosum. Development of these granules is a crucial component to the barrier function of skin. Loss of granulation suggests that the barrier function is not forming properly, and keratinocytes are not differentiating normally.

When increased to 75% cancer incorporation, further loss of cellular organization is observed alongside an apparent shrinking of the cornified layer. This specific result is even more drastic with 50% cancer incorporation. The 50% ASZ model loosely resembles a later-stage of disease where densely stained tumor pockets have begun to form. However, patient BCCs would experience these pockets migrating into the dermis, not incorporating into the epidermis. It is likely that the presence of vasculature in mammalian skin encourages the growth into the dermis. Without blood vessels, the tumor pockets do not have sufficient driving force to proliferate and migrate into the plug and instead grow within the epidermis.

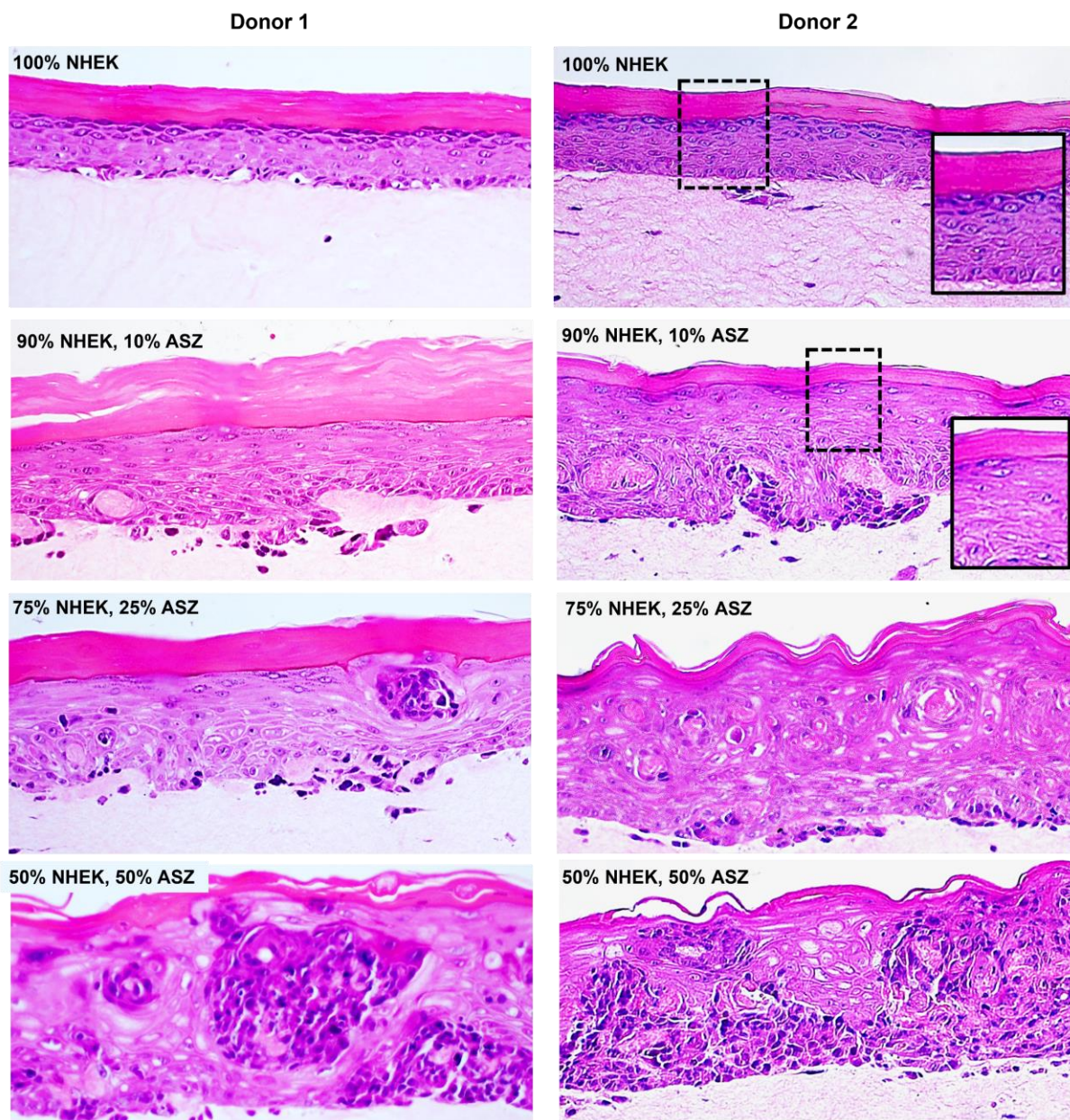


Figure 4.3, Part 1: Representative images of co-culture tissues from biological Donors 1 and 2 after 12 days of differentiation. Zoomed-in sections from Donor 2 show loss of keratohyalin granules with as little as 10% cancer incorporation. Thickening of the epidermal layer is also observed with loss of cornified layer thickness with increasing ASZ incorporation.

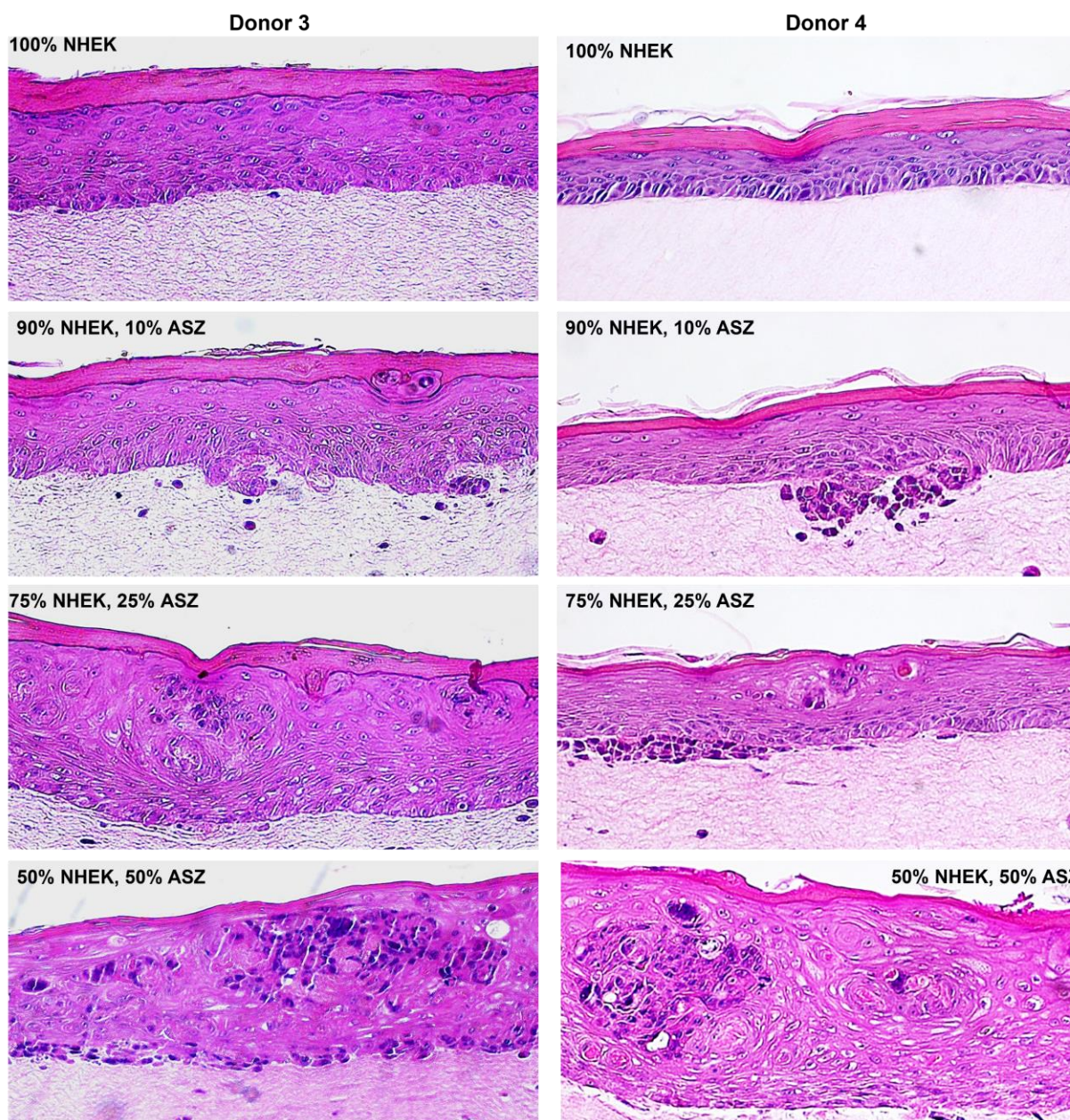


Figure 4.3, Part 2: Representative images of co-culture tissues from biological Donors 3 and 4 after 12 days of differentiation. Consistent trends of overall epidermal thickening, loss of keratohyalin granules, loss of cellular organization and structure, and eventual formation of tumoroid-like pockets can be seen across the range of cancer incorporation for all biological donors.

To quantify observed changes, ImageJ analysis software was used to measure the thickness of the total epidermal layer, the viable layer (defined as the distance from the bottom of the basal layer to the top of the granular layer), and the cornified layer at randomly selected sections of tissue images. Viable layer and cornified layer analyses were calculated as percentages of the total epidermal thickness to account for donor differences in overall tissue thickness.

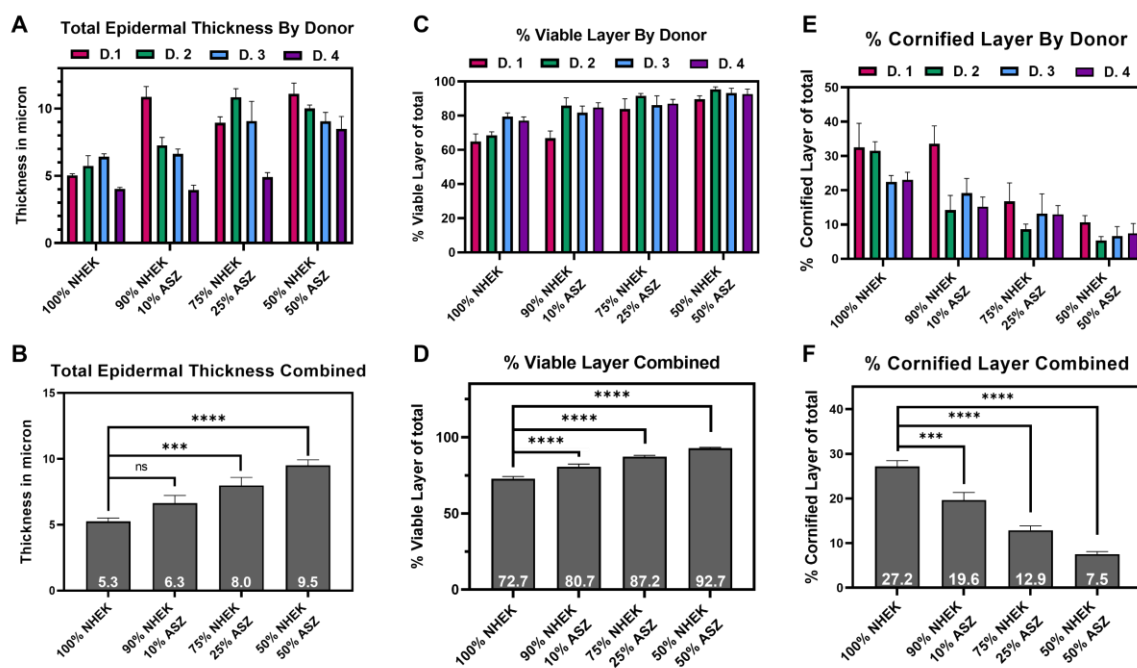


Figure 4.4: Statistical analysis of thickness of epidermal components across four biological donors of 12-day differentiation. A, C, E) Results for total epidermal thickness by donor, % viable layer by donor, and % cornified layer by donor, respectively. B, D, F) Results for combined total epidermal thickness, combined % viable layer, and combined % cornified layer, respectively. Generally, the total epidermal thickness and the % viable layer of the whole are increased across cancer incorporation. Inversely, the % cornified layer of the whole is significantly decreased. Graphs were made in GraphPad Prism, and one-way ANOVA analysis was used to determine statistical significance at $\alpha=0.05$. Bars represent the mean \pm one standard error of the mean. ***= 99.9% confidence interval, ****= 99.99% confidence interval. Ns= not significant.

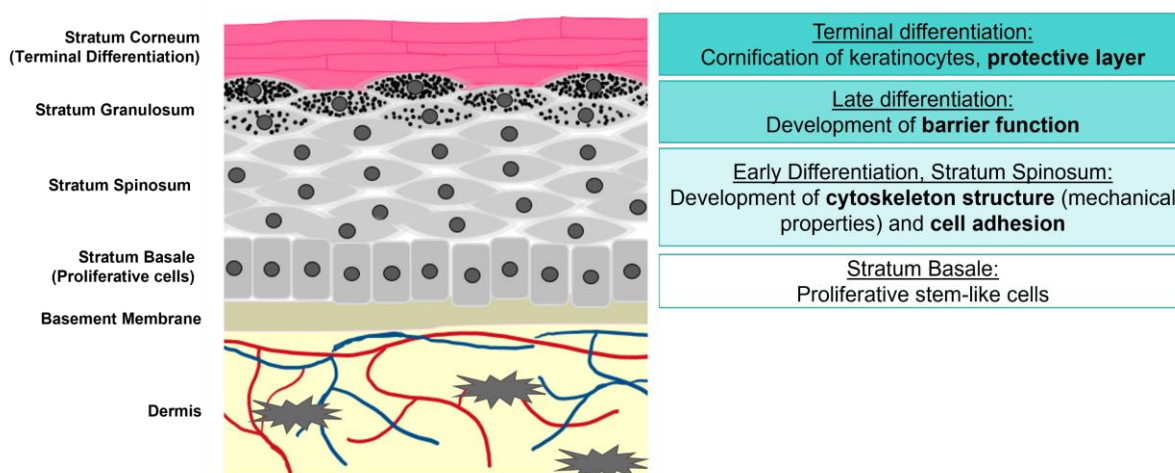
The overall epidermal thickness was significantly increased from 100% NHEK controls at the 25% and 50% cancer incorporation models at 99.9% ($p = 0.0008$) and 99.99% ($p < 0.0001$) confidence intervals, respectively (Figure 4.4, B). Due to donor discrepancies in thickness of even the 100% NHEK model (Figure 4.4, A), the 10% cancer incorporation was not statistically different. The percentage of the viable layer of the total is significantly increased at the 99.99% confidence interval ($p < 0.0001$) even beginning at 10% ASZ incorporation (Figure 4.4, C & D).

Most importantly, the changes observed for the percent cornified layer of the whole are significantly reduced beginning at the 10% cancer incorporation (Figure 4.4, D & E, $p = 0.0001$). While this is not surprising since the two percentages are interrelated, this difference signifies an impactful alteration to NHEK differentiation patterns. Cornification represents terminal differentiation of keratinocytes. Lack of cornification suggests that the NHEK population is not properly differentiating in the presence of the cancer cells. Patient BCC shares this characteristic²² - the observation of loss of cornification provides initial support that co-culture models mimic patient BCC.

4.2.2.2 Specific Impact on Keratinocyte Differentiation

Further pathological investigations are necessary to determine the biochemical impacts that BCC incorporation has on keratinocyte differentiation. Normal keratinocyte differentiation is shown in Scheme 4.3. Briefly, cells exit their proliferative cell cycle in the stratum basale, or basal layer, and enter early-stage differentiation in the stratum spinosum. Here they develop cytoskeletal structure and cell adhesion that imparts the tough but flexible mechanical properties of skin. As they differentiate further into the stratum granulosum, or granular layer, they develop the characteristics of the skin's protective barrier function. This is followed by terminal

differentiation into the stratum corneum, or cornified layer. Development of cytoskeleton structure, cell adhesion, and barrier function can be treated as differentiation “checkpoints” throughout this process.



Scheme 4.3: Layers of epidermal differentiation and locations of differentiation checkpoint markers. Proliferative basal cells exit the cell cycle and differentiate into the stratum spinosum. Cytoskeleton structure and cell adhesion are developed in early stages of differentiation. Further differentiation into stratum granulosum accompanies development of protective barrier function which is completed upon differentiation into the stratum corneum.

BCC is characterized as a cancer that results in poor/abnormal keratinocyte differentiation.²² Analysis of differentiation checkpoints in patient BCCs reveals altered or compromised development. For co-culture models to have potential preclinical utility, it is imperative to ensure they mimic these pathological components of patient BCC. Analysis of differentiation checkpoints is accomplished through qPCR analysis of transcripts at the time of harvesting as well as immunofluorescent staining of OCT frozen tissues.

Cytoskeleton structure. The cytoskeleton is comprised of keratin filaments that provide the tough but flexible mechanical properties of skin. In normal epidermal tissue, Keratin 10 (KRT10) is the primary component of this architecture. *KRT10* transcription is often

downregulated in diseases like BCC that express poor keratinocyte differentiation.^{23, 24} Other keratins are often overexpressed to compensate for this loss.

Analysis of mRNA transcripts after 5 days of differentiation shows logarithmic loss of *KRT10* starting with 10% cancer incorporation and is maintained for all ASZ-containing models (Figure 4.5, A). At day 12, three donors showed similar logarithmic loss of *KRT10*, but Donor 4 experienced an increase in *KRT10* expression at 10% and 25% cancer incorporation (Figure 4.5, D). This data exemplifies the reality that no two donors or patients will experience cancer in precisely the same way. However, a majority trend of loss of *KRT10* in model systems is observed and would likely be reproducible with increased biological replicates.

Keratin 17 (*KRT17*) is overexpressed in the majority of patient BCCs^{25, 26} and was evaluated to validate co-culture models. Indeed, *KRT17* was generally increased at 5 days of differentiation (Figure 4.5, B) and consistently increased with cancer incorporation at 12 days of differentiation (Figure 4.5, E). Because qPCR analysis is performed for human transcripts specifically, this elucidates that while *KRT17* may be overexpressed in BCC cancer cells, nearby healthy keratinocytes are also transformed to express *KRT17*.

Interestingly, Keratin 16 (*KRT16*) was also overexpressed at the mRNA level in co-cultures across the range of ASZ incorporation (Figure 4.5, C, F). *KRT16* is often defined as a proliferation marker and is overexpressed in hyperproliferative skin diseases such as psoriasis and pachyonychia congenita.²⁷⁻²⁹ *KRT16* is, however, very poorly studied in BCC literature. One report did find overexpression of *KRT16* in approximately 1/3 of patient BCC tissues examined but noted that this was localized in the overlying epidermis and not in the cancer cells themselves.^{26, 30} This is consistent with our data, as it is the human cell population that would constitute the overlying epidermis to which the qPCR primer sequences are specific. However,

an orthogonal technique such as immunofluorescence is necessary to confirm localization in the tissue.

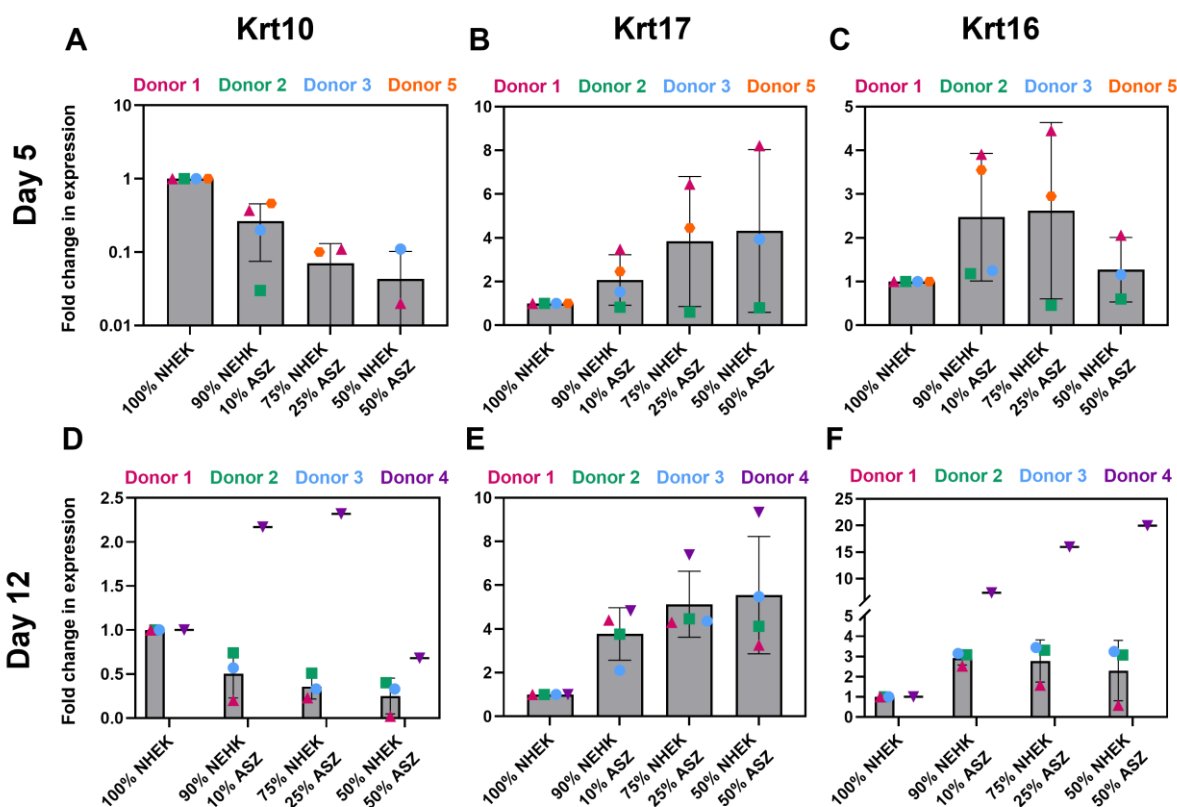


Figure 4.5: qPCR analysis of cytoskeletal components after 5 and 12 days of co-culture differentiation. A) *KRT10* evaluation of Day 5. B) *KRT17* evaluation of Day 5. C) *KRT16* evaluation of Day 5. D) *KRT10* evaluation of Day 12. E) *KRT17* evaluation of Day 12. F) *KRT16* evaluation of Day 12. Each donor has only one data point, so bars represent the mean \pm one standard deviation contributed by 4 biological donors for Day 5 and 4 biological donors for Day 12. Donors 1-3 for Day 5 are the same as donors 1-3 of Day 12. Days 4 and 5 are not the same. Individual donor values are represented as Donor 1: pink triangle, Donor 2: Green square, Donor 3: Blue circle, Donor 4: purple upside-down triangle, Donor 5: orange hexagon. *KRT10* expression is generally decreased while *KRT17* and *KRT16* are increased at Days 5 and 12. Primer sequences used for qPCR were specific to human transcripts.

Immunofluorescent staining for KRT10, KRT16, and KRT17 was performed on OCT frozen sections of tissues that differentiated for 12 days. This is to ensure that changes observed in qPCR are also reflected in the ultimate production and location of protein. For KRT10, a

visual difference was not observed at 10% cancer incorporation, but an obvious reduction of KRT10 signal intensity is seen for 25% and 50% ASZ incorporation (Figure 4.6, left).

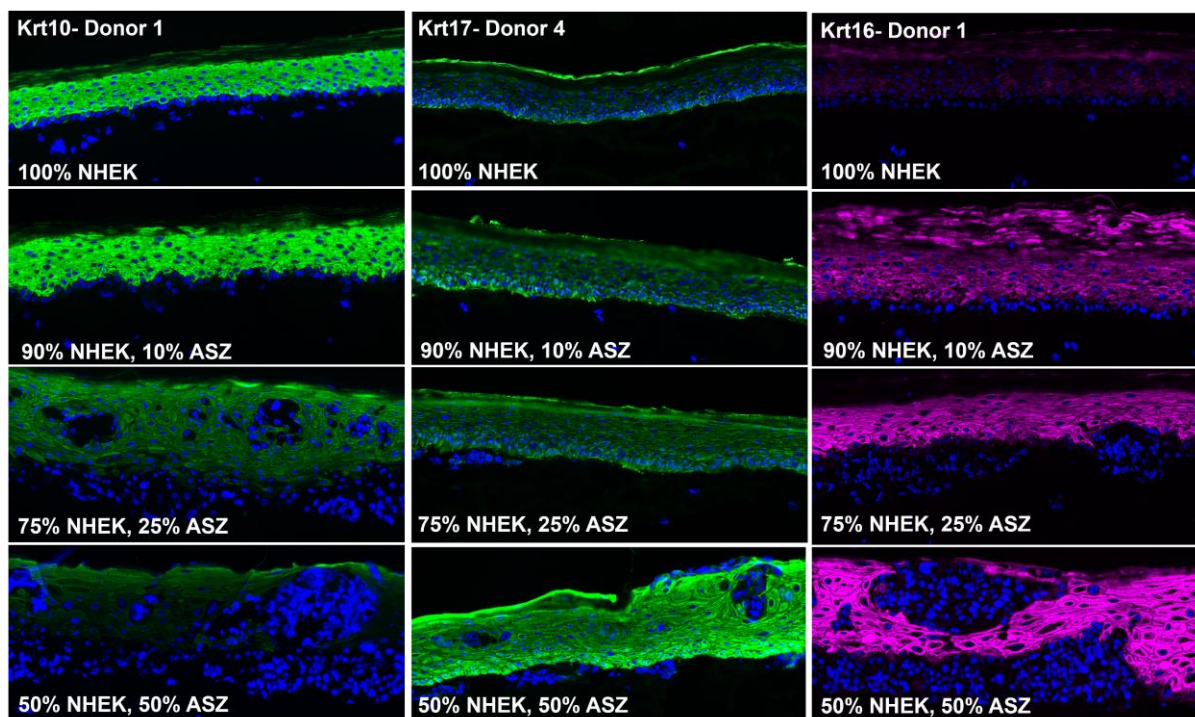


Figure 4.6: Immunostaining of keratin components of cytoskeletal structure in co-culture tissues across the range of cancer incorporation. Left, green KRT10 (donor 1). Middle, green KRT17 (donor 4). Right, pink KRT16 (donor 1). Blue is DAPI nuclear stain. With increasing cancer incorporation, KRT10 is decreased in the human cell populations while KRT17 and Krt16 conversely increase. KRT17 localization changes from the basal layer in 100% NHEK to localizing throughout the suprabasal layer with increasing cancer incorporation. KRT16 localization similarly changes from minimal stratum spinosum localization to being strongly produced throughout the suprabasal layer. Changes for KRT16 and KRT17 are seen immediately in the 90% NHEK/10% ASZ samples.

In 100% NHEK tissue, KRT17 primarily localizes in the basal layer near the basement membrane. Very little expression is observed in the stratum spinosum and stratum granulosum. With increasing cancer incorporation, expression is more widely observed throughout the layers of the epidermis (Figure 4.6, middle), supporting improper development of cytoskeletal structure. Recently, it has been reported that KRT17 is a direct target of increased Hh activity. In

oral squamous cell carcinoma, the increase in KRT17 induced by Gli protected cells against apoptosis and encouraged tumor growth.^{31, 32} It is likely that the increase of KRT17 causes similar outcomes in BCC and hinders the proper differentiation of surrounding healthy tissue.

Very little KRT16 signal intensity is observed in the stratum spinosum of the 100% NHEK sample. However, stark increases in signal intensity are observed across the range of ASZ incorporation. Even the 50/50 co-culture that did not experience a significant increase in *KRT16* transcription showed a very striking increase via immunofluorescence. This suggests that increases in *KRT16* mRNA levels and subsequent translation into protein are maintained throughout the course of differentiation to ultimately increase KRT16 composition of cytoskeleton structure. KRT16 transcription and protein expression are not thoroughly characterized in BCC, but this data suggests that perhaps studying KRT16 further in patient BCCs might reveal new mechanistic insights. Superficial BCC phenotypically shares similarities to eczema and psoriasis, both of which exhibit overexpression of KRT16.³³⁻³⁵ Perhaps KRT16 overexpression is more likely to be seen in superficial BCCs and the model reflects this BCC subtype.

Cell adhesion. Alongside skeletal structure, cell adhesion is developed in the stratum spinosum during early stages of differentiation. Two primary components of cell adhesion in skin are adherens junctions and desmosomes. Adherens junctions are responsible for cell-cell contact. They are comprised of cadherin proteins that cross-link with one another on neighboring cells.³⁶ Desmosomes are unique to organs that commonly experience mechanical stress and are an important component to healthy skin integrity.³⁷⁻⁴⁰ Desmoglein and desmocollin proteins are the primary cadherins involved in desmosome adhesion.⁴¹ Both adherens and desmosome components are required for the healthy development of cell adhesion and are often

compromised in skin diseases.³⁸ Unlike in many cancers, E-cadherin (ECAD/CDH1) proteins in adherens junctions are often preserved at normal levels in early stages of superficial and nodular BCC.^{42, 43} More advanced stages and recurring BCC will experience a loss of E-cadherin.⁴⁴ Moreover, decreases noticed within tumor cell populations are not translated to the surrounding or overlying epidermis. For desmosomes, desmoglein proteins are more frequently lost in nodular and infiltrative BCCs,^{43, 45-47} though little is known about the changes to desmocollins.⁴⁷

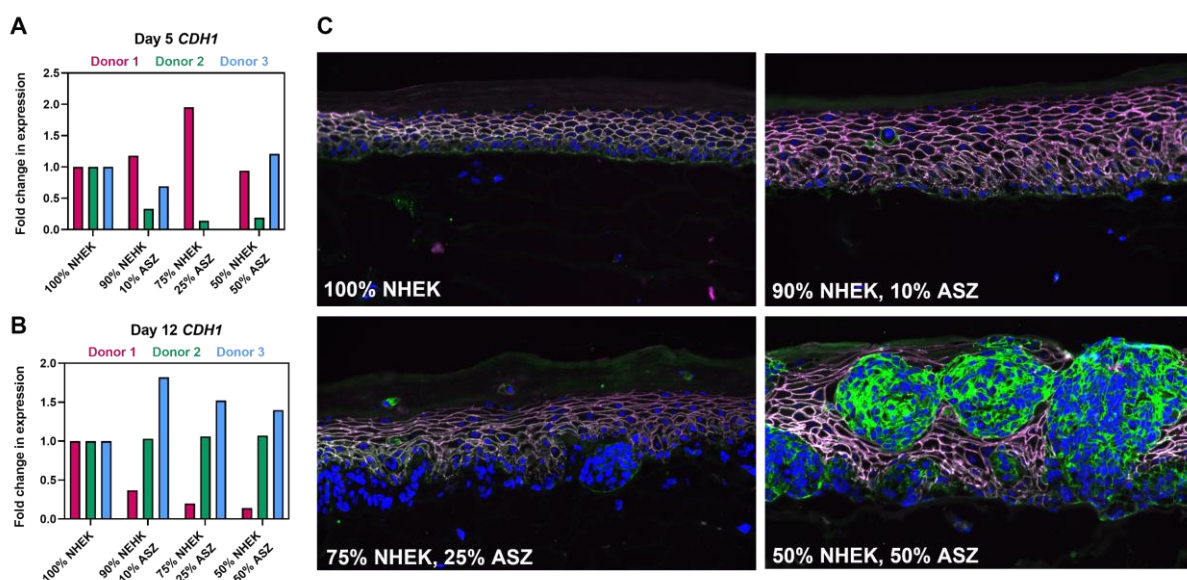


Figure 4.7: qPCR and immunofluorescence analysis of E-cadherin in co-culture models. A) qPCR results for each donor after 5 days of differentiation. B) qPCR results for each donor after 12 days of differentiation. C) Immunofluorescent staining of pan-E-cadherin (green), human specific E-cadherin (pink/white) and DAPI nuclear stain (blue) at day 12. Locations of only green signal represent the murine cell population. There are no trends in ECAD transcription or protein expression.

To explore cell adhesion, qPCR and immunofluorescence were performed across the range of ASZ incorporation. In general, *CDH1* expression after both 5 and 12 days of differentiation showed no trend in the human cell population (Figure 4.7, A, B). Donor 1 experienced an increase in *CDH1* at day 5 and a drop in expression at day 12. Donor 2 experienced a drop at day 5 with no change at day 12, and Donor 3 experienced no change at day

5 and a mild increase at day 12. As an orthogonal method, day 12 tissues from donor 1 were analyzed by immunofluorescence. Pan-ECAD (green) shows both human and murine ECAD expression, and human specific HECD-1 staining (pink/white) overlays where the human cells are incorporated (Figure 4.7, C). No obvious changes were observed in intensity or localization of ECAD staining in the human cell population. Taken together, this data suggests that the model more closely mimics earlier stages of patient BCC development where changes in ECAD are not significantly observed. The staining experiment, however, is useful for observing where the ASZ cells are incorporating into the model at the different cellular ratios.

Evaluation of desmoglein (DSG) and desmocollin (DSC) revealed more conclusive trends. *DSCI* experienced the most dynamic changes by qPCR. After 5 days of differentiation, *DSCI* is consistently reduced on a logarithmic scale (Figure 4.8, A). Cell adhesion components are developed in the earlier stages of development. The extreme reduction of transcription at day 5 corroborates significant and early differentiation abnormality. While less extreme, *DSCI* expression is still generally reduced at day 12 (Figure 4.8, B). When day 12 tissues were analyzed by immunofluorescence, decreased intensity is observed with as little as 10% ASZ incorporation (Figure 4.8, C), signifying that even less striking differences in transcription still result in decreased protein accumulation.

By qPCR, *DSGI* transcript analysis did not reveal any significant trends with increasing ASZ incorporation (Figure 4.8, D). However, immunofluorescent staining of donor 1 day 12 tissues did show a decrease in staining intensity of DSG-1 (Figure 4.8, E). This staining experiment also analyzed pan-laminin, the primary component of the basement membrane that separates the dermis from the epidermis. A strong signal is observed for 100% NHEK samples that is gradually lost with increasing ASZ incorporation. A compromised basement membrane

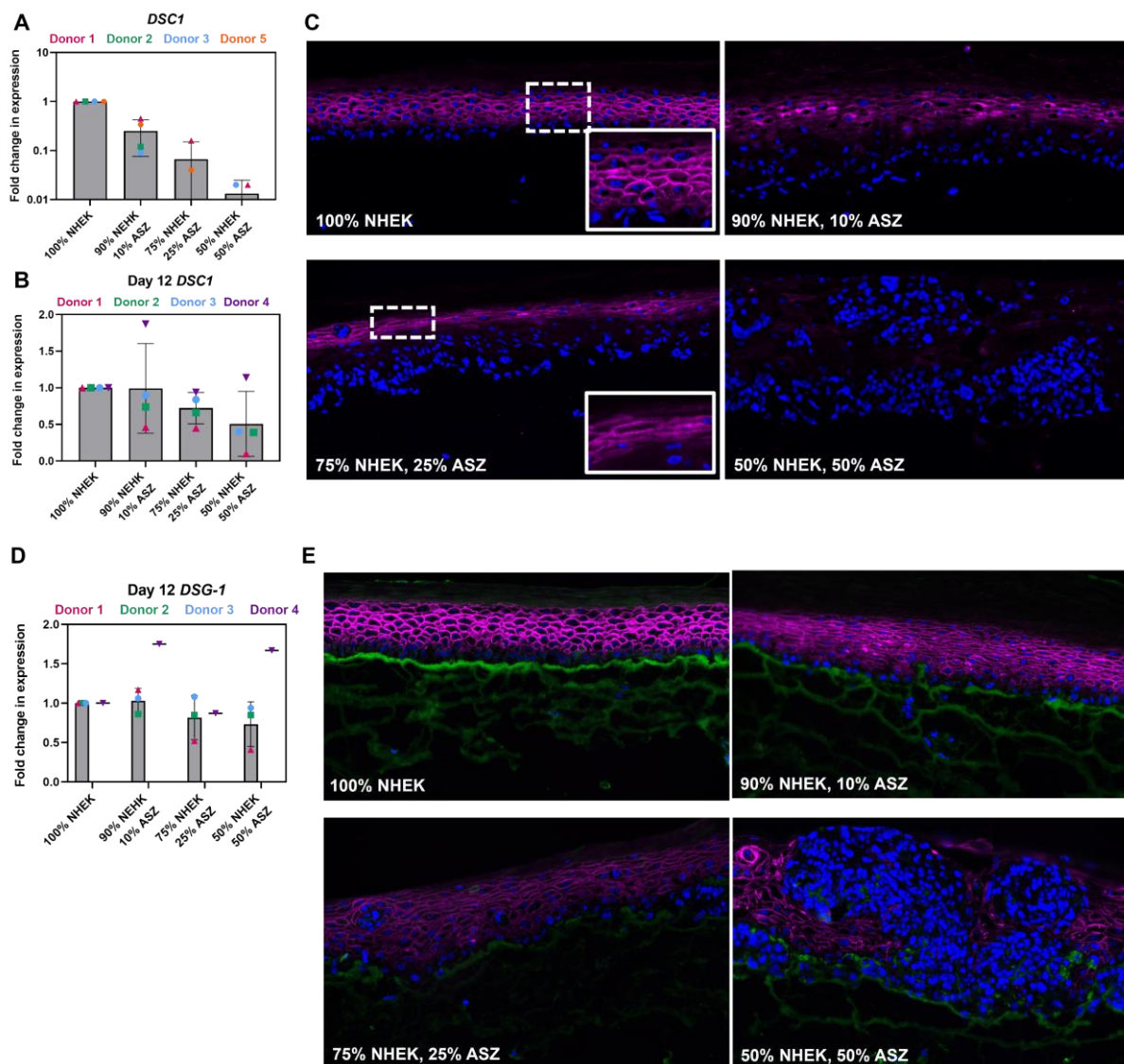


Figure 4.8: qPCR and immunofluorescence analysis of desmocollin-1 and desmoglein-1 in co-culture models. A) Combined DSC-1 qPCR results for each donor after 5 days of differentiation. B) Combined DSC-1 qPCR results for each donor after 12 days of differentiation. C) Immunofluorescent staining of desmocollin-1 (pink), and DAPI nuclear stain (blue). Intensity of DSC-1 staining is lost with increasing ASZ incorporation. The thickness of the stained layer also decreases until it is lost entirely. Inlets showcase the alteration of cellular shape of the stratum spinosum. D) Combined DSG-1 qPCR results for each donor after 12 days of differentiation. E) Immunofluorescent staining of desmoglein-1 (pink), basement membrane (pan-laminin, green), and DAPI nuclear stain (blue). Intensity of DSG-1 is lost with increasing ASZ incorporation along with the integrity of the basement membrane.

opens a gateway for migratory cells to invade into the dermal layer. Loss of basement membrane is a characteristic of early stages of BCC when superficial islands begin palisading into the dermis.⁴⁸ Combined, these data suggest both the loss of integrity for cell adhesion as well as the basement membrane, ultimately creating a scenario where cell migration is permitted. Loss of basement membrane provides further evidence that the model more closely mimics early, superficial BCC.

Staining of membrane bound proteins (ECAD, DSC1, and DSC1) also reveals the alteration of cellular shape that accompanies cancer incorporation. Cells are generally elongated in the horizontal direction and grow in overall size (Figure 4.8, C, insets). This has been observed previously in keratinocyte differentiation assays when DSG1 was genetically mutated.⁴⁹ Cells lacking wild type DSG1 could not proceed through terminal differentiation and developed shapes identical to those observed in these studies. Mechanistically, the loss of adhesion components contributes to the overall loss of differentiation observed in transformed keratinocytes.

Barrier function. There are many contributing components to the barrier function of skin, including cell adhesion described above. More imperative components of barrier function are the existence and composition of the stratum granulosum and stratum corneum.⁵⁰ Their primary functions are to keep unwanted environmental influences from entering the body and to prevent evaporative water loss from the body.⁵⁰⁻⁵² The structure of the stratum corneum has been referred to as “bricks in mortar” where the terminally differentiated keratinocytes, or corneocytes, are the bricks; and dense lipid networks are the mortar holding them together.^{52, 53} The corneocytes themselves consist of densely crosslinked layers of the proteins filaggrin (FLG), loricrin, and involucrin.⁵² FLG specifically provides natural moisturization to the skin and aggregates keratin

filaments during terminal differentiation to ultimately assist the collapse of cells into corneocytes.⁵⁴

Loss of FLG is seen in a number of skin diseases such as ichthyosis and atopic dermatitis that experience poor keratinocyte differentiation.^{54, 55} Recently, in an immunohistochemical study of 144 BCC patient tissues, most tissues did not express FLG.⁵⁶ In a small sample study, mutations in the *FLG* gene were commonly observed in BCC tumors compared to normal tissue samples from the same patient.⁵⁷ Together these reports highlight filaggrin as an important marker of BCC pathology. It was hypothesized that the incorporation of ASZ cells into the tissues would negatively impact the production of FLG components of barrier function.

By qPCR, *FLG* experiences a rapid and extreme decrease in transcription after 5 days of differentiation (Figure 4.9, A). While *FLG* production is more relevant for later differentiation stages, this extreme loss of early transcription provides evidence for early onset abnormal keratinocyte differentiation. Some cells are reaching the granular stage of differentiation and *FLG* should be actively transcribed at day 5. This is further confirmed through immunofluorescent staining (Figure 4.9, B). The beginnings of granular layer formation are observed in the 100% NHEK tissue. This is, however, immediately lost with 10% ASZ incorporation and is maintained with 25% and 50% incorporation. Overall, it can be concluded that terminal differentiation after 5 days has at least been slowed down if the pathway has not been altered altogether.

After 12 days of differentiation, *FLG* transcription across four biological donors can be divided into two distinct groups. Two donors (1 & 2) experienced logarithmic reduction of *FLG* transcription as determined by qPCR (Figure 4.10, A). By immunofluorescent staining of FLG proteins in donor 1, loss of transcription correlates to a decrease in staining intensity (Figure

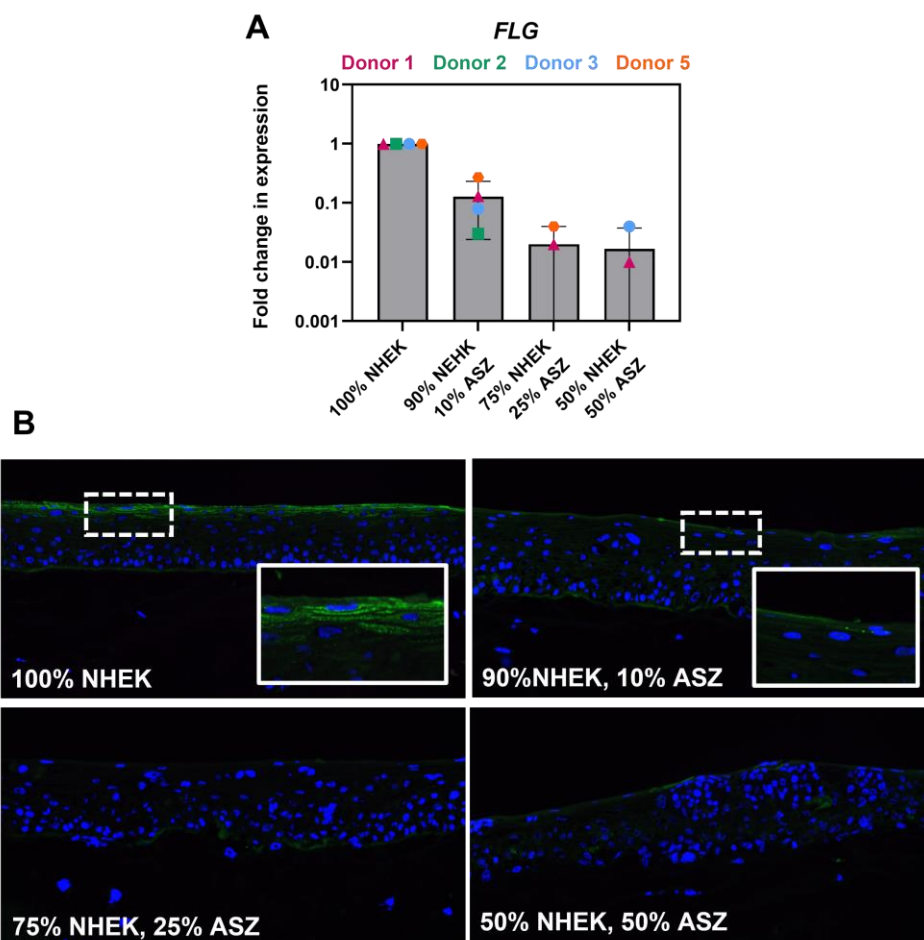


Figure 4.9: Evaluation of *FLG* transcription and immunofluorescent staining after 5 days of differentiation. A) qPCR results. *FLG* transcription is depleted on a logarithmic scale with as little as 10% ASZ incorporation. Bars represent the mean \pm one standard deviation of the three biological donors. B) Immunofluorescence results from Donor 1. Some *FLG* is observed in the beginnings of the granular layer for the 100% NHEK tissue. This is lost with as little as 10% ASZ incorporation.

4.10, B). Specifically, there is a loss of the density and cell thickness of staining of keratohyalin granules with increasing cancer incorporation. This corroborates the loss of staining of granules by H&E and provides further validation of co-culture models mimicking patients BCCs.

The other two donors (3 & 4) experienced an increase in *FLG* transcription with 10% cancer incorporation, no difference in transcription from 100% NHEK at 25% incorporation, and only a decrease at 50% (Figure 4.10, C). However, immunofluorescent staining reveals that an increase in transcription for these donors does not correlate to increased staining intensity

(Figure 4.10, D). Staining is not observed in keratohyalin granules where it is expected to localize during proper differentiation, most noticeably beginning at 25% ASZ incorporation. This signifies the possibility that for patients with BCC, continued transcription of *FLG* may not correlate to proper protein production and must be evaluated by more than one method. Ultimately, loss of barrier FLG in co-cultures mirrors loss of integrity of barrier function that is experienced by BCC patients.

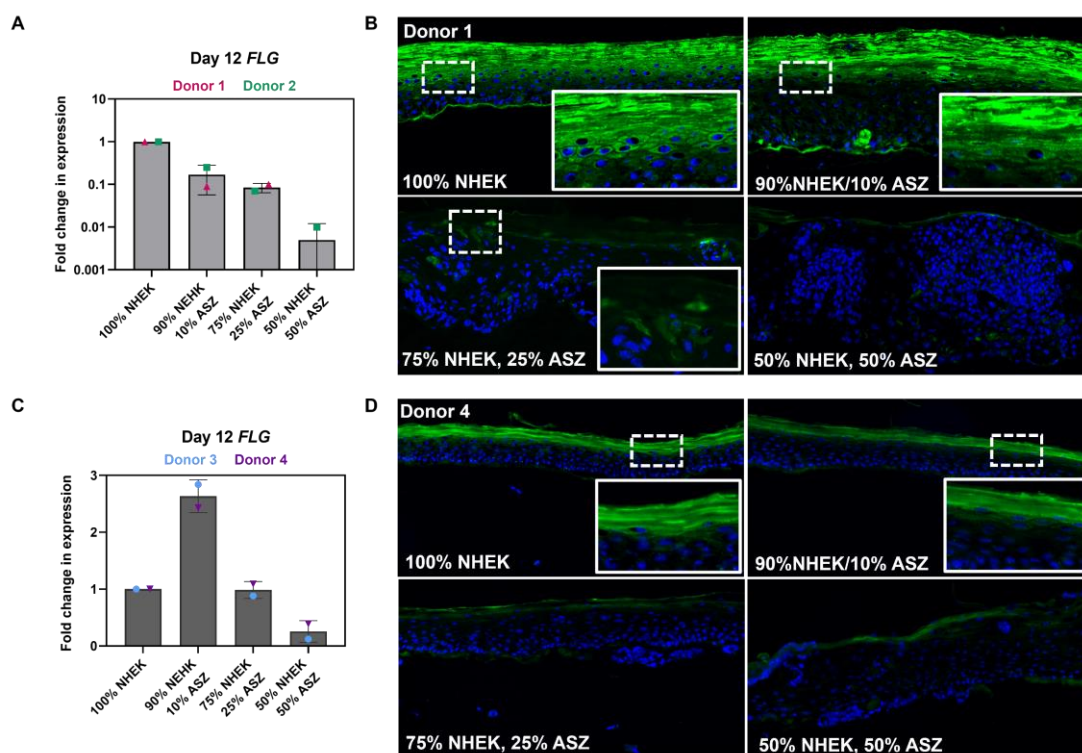


Figure 4.10: Analysis of *FLG* transcription and protein expression in biological donors 1-4 after 12 days of differentiation. A) qPCR analysis of *FLG* in donors 1 and 2. Transcription is lost on the logarithmic scale from the 100% NHEK control. B) Immunofluorescence staining of *FLG* in donor 1. Intensity of signal is decreased for both donors across the range of ASZ incorporation. Zoomed-in image inlets show this reduction of intensity specifically in the granular layer. C) qPCR analysis of *FLG* transcription of donors 3 and 4. Transcription is increased with lower percentages of cancer incorporation but decreased at 50%. D) Immunofluorescent staining of *FLG* in donor 4. Even though transcription is increased, protein staining is decreased in trend with Donor 1. Inlets show loss of staining specifically in the granular layer.

4.2.3 Inhibiting Gli Transcription Factors in a 3D Organotypic Model of BCC

A major benefit of this mixed species 3D model is the ability to study the human non-diseased and murine cancerous cell populations independently. The analysis discussed above all pertains to the human cell population and the changes observed in the presence of cancerous murine cells. Of further interest is Hh activity in the cancer cell population. By qPCR, *Gli1* transcription was found to be approximately 3x overexpressed in co-culture models when compared even to the 100% ASZ control (Figure 4.11, A, C). This effect was the highest for the 25% ASZ model, as donor 2 experienced an 11-fold increase in *Gli1* transcription. However,

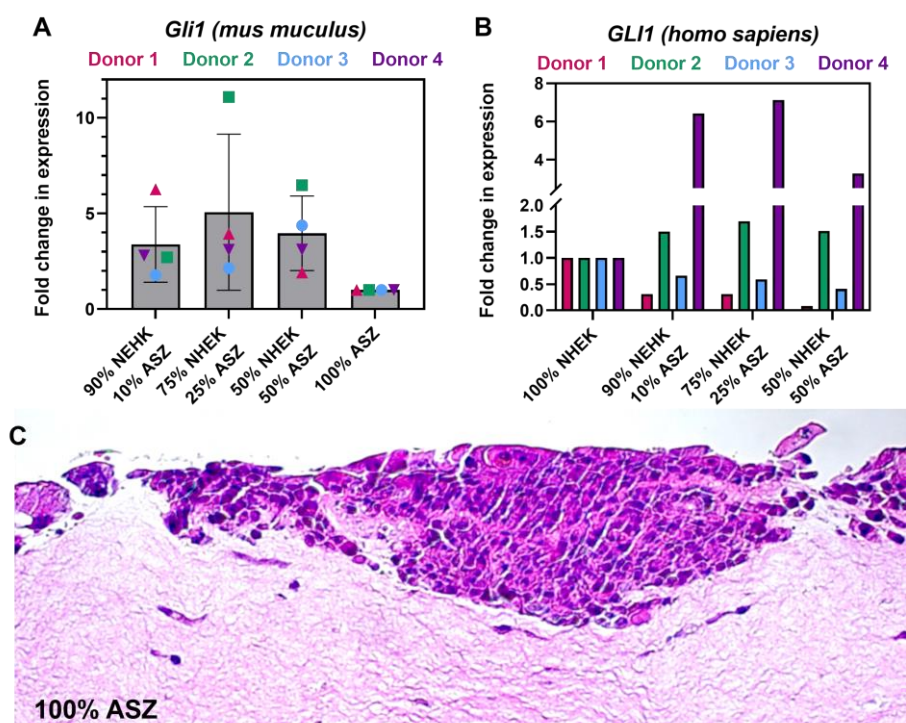


Figure 4.11: Analysis of *Gli1* transcription in both mouse and human cell populations in 3D tissues. A) qPCR results for four biological donors across the range of cancer incorporation. All results are normalized to the 100% ASZ tissue. B) qPCR results for the human cell population in four biological donors across the range of cancer incorporation. No trends are observed. C) H&E image of 100% ASZ sample for visual reference of behavior. Cells burrow into the collagen plug instead of expanding on top of the surface.

Gli1 transcription in the human cell population was largely inconsistent across the range of cancer incorporation at day 12, suggesting that Hh activity is not playing a consistently critical role in the pathology of differentiating keratinocytes. Donors 1 & 3 experienced transcription decreased whereas donors 2 & 4 experienced increases (Figure 4.11, B) It was hypothesized that the ASZ cell population could be specifically modulated with Hh inhibitors while restoring the human cell population towards a non-diseased phenotype and pathology.

As elaborated in section 4.2.1, ASZ cells are sensitive to GANT-61 but insensitive to Vismodegib. As such, GANT-61 was chosen as a small-molecule inhibitor for testing this hypothesis. On day 0 when plugs are lifted to the air-media interface, the media for experimental 75%NHEK/25%ASZ co-culture models was supplemented with 10 μ M GANT-61. Experiments for these cell donors (4-7) also contained 100% NHEK and non-treated 75% NHEK/ 25% ASZ controls. All samples were analyzed via H&E, qPCR, and immunofluorescence.

4.2.3.1 Analysis of phenotypic changes

H&E staining was performed on 100% NHEK, non-treated 25% ASZ, and 25% ASZ samples treated with 10 μ M GANT-61 to elucidate phenotypic changes induced by GANT-61. Figure 4.12 shows the resulting images for keratinocyte donors 4, 6 and 7 (4.12 A, B, and C respectively). Consistent with donors 1-3, the thickness of the samples increases with 25% cancer incorporation for each donor. Upon treatment with GANT-61, the epidermis is thinner. Quantification was performed to determine statistical significance of these changes. For donors 4 and 6, the increase was significant at the 99.99% confidence interval (Figure 4.12, D&E, $p < 0.0001$). For donor 7, the increase was significant at the 99 % confidence interval (Figure 4.12, F,

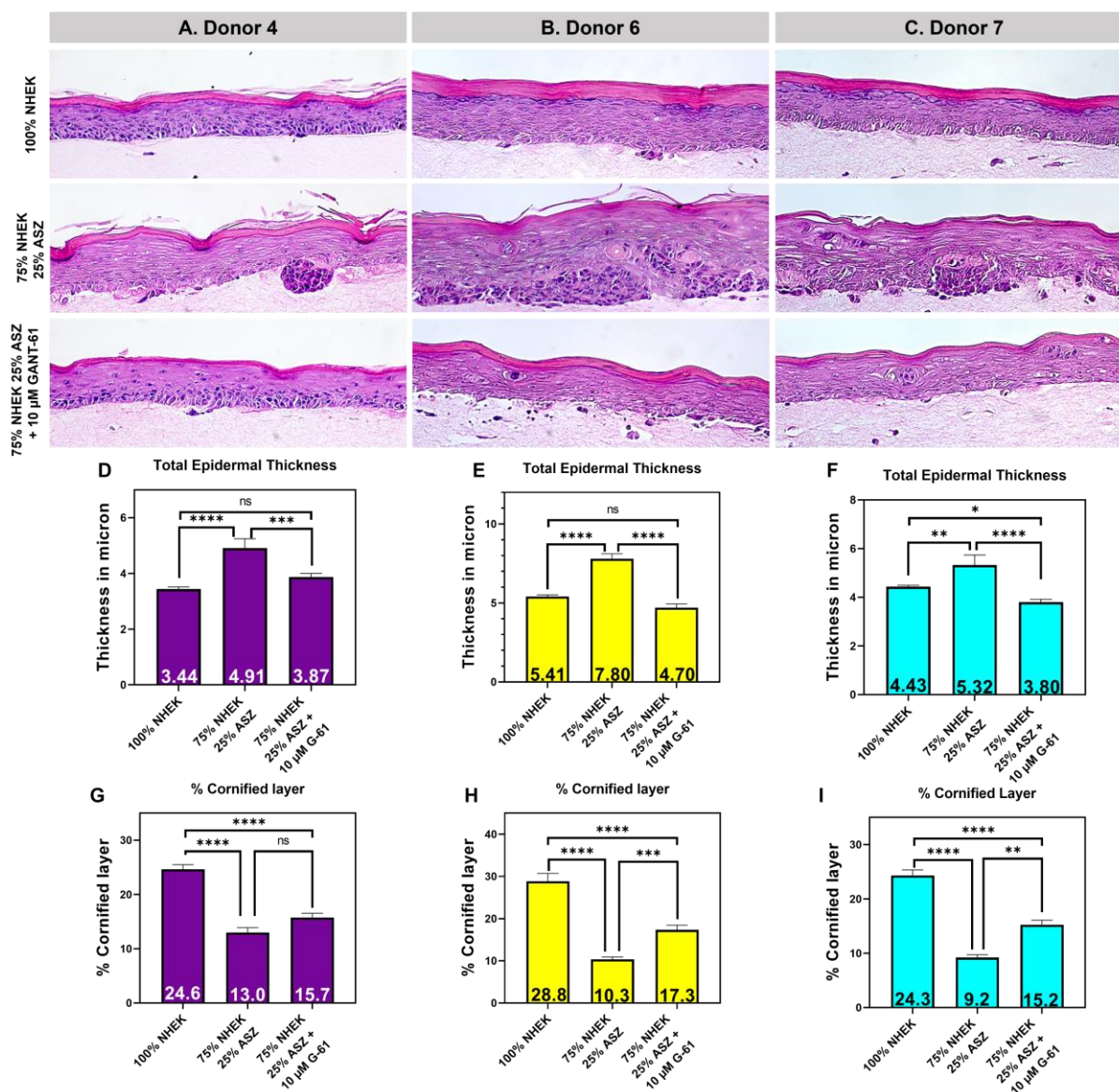


Figure 4.12: Phenotypic analysis of 75%NHEK/25%ASZ tissue response to GANT-61 in donors 4, 6, and 7. A-C) H&E images of 100% NHEK (top)/ non-treated 25% ASZ models (middle), and 25% ASZ models treated with 10 μ M GANT-61 (bottom) for donors 4, 6, and 7. D-F) Image J measurements were used to determine total epidermal thickness reported in microns. Broadly, ASZ incorporation causes increases in thickness that are reduced upon treatment with GANT-61. G-H) Image J measurements were used to determine the percentage of the cornified layer of the total epidermis. The cornified composition is decreased with ASZ incorporation and can be increased with GANT-61 treatment. Bars represent the mean \pm one standard error of the mean. One-way ANOVA analysis with multiple comparisons was used to determine statistical significance at $\alpha=0.05$. NS= not significant, * = 90% confidence interval, ** = 99% confidence interval, *** = 99.9% confidence interval, and **** = 99.99% confidence interval.

$p = 0.0065$). For all three donors, thickness was significantly decreased following treatment with GANT-61 ($p = 0.0003$ for donor 4, $p < 0.0001$ for donors 6 and 7). Most importantly, treatment with GANT-61 produced non-statistically different thickness from the 100% NHEK control in donors 4 and 6 ($p = 0.0555$ and 0.1248 , respectively). The decrease was mildly significant from 100% NHEK controls for donor 7 ($p = 0.0198$) in the opposite direction- the 100% NHEK tissue was thicker than GANT treated. Generally, GANT-61 restores the overall thickness of co-culture models towards a non-diseased phenotype.

Treatment with GANT-61 partially restores the appearance and the integrity of the cornified layer of tissues. The percent cornification of the whole tissue is significantly increased with 25% ASZ incorporation for donors 4, 6, and 7 (Figure 4.12, G-I, $p < 0.0001$ for all three). Upon treatment with GANT-61, donors 6 and 7 experienced significant increases in percentage of cornification ($p = 0.0003$ and 0.0013). Donor 4, however, did not ($p = 0.1655$). Each donor saw significant differences between non-treated 100% NHEK samples and GANT-treated 25% ASZ samples, but the slight restoration observed is promising for further pathological evaluation.

4.2.3.2 Analysis of cytoskeletal structure

A consistent alteration to keratinocyte differentiation in response to ASZ incorporation is a loss of KRT10 and gain of KRT16 and KRT17 components of cytoskeletal structure. It was therefore hypothesized that successful inhibition of the ASZ population would result in restoration of proper cytoskeletal structure. Evaluation of cytoskeletal markers reveals that treatment with GANT-61 results in donor-dependent restoration of the 75% NHEK/ 25% ASZ model towards a non-diseased pathology. Analysis of *KRT10*, *KRT16*, and *KRT17* transcription for donor 4 revealed all were overexpressed compared to 100% NHEK at 25% ASZ

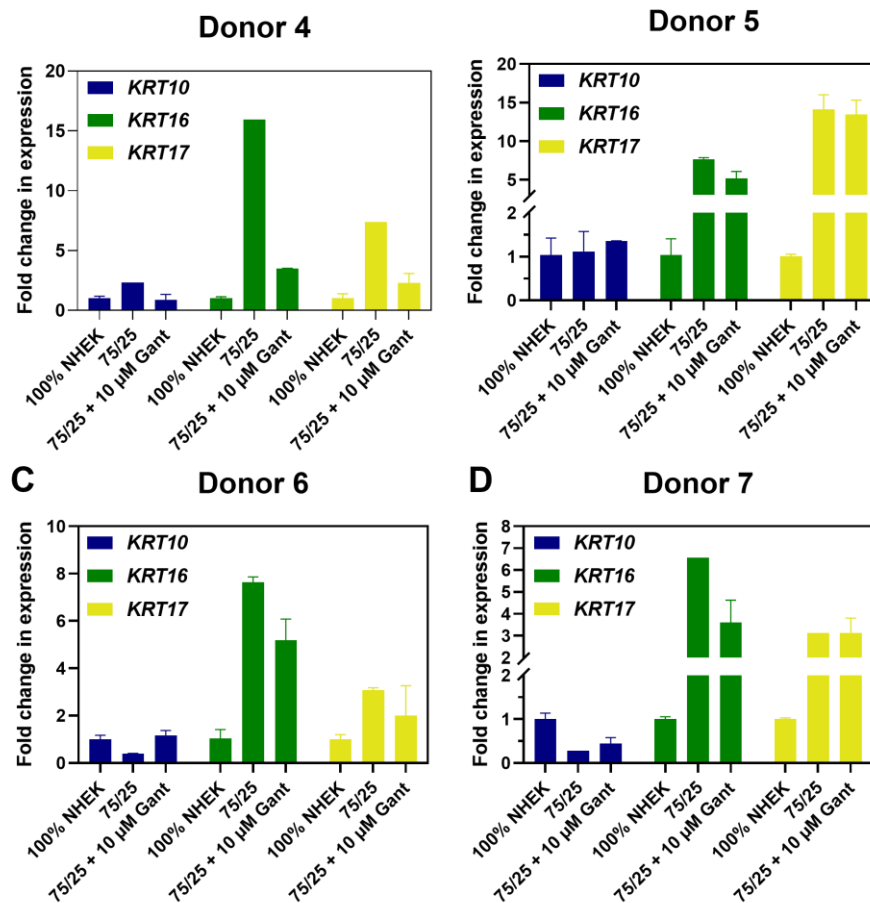


Figure 4.13: Evaluation of 75% NHEK/25% ASZ cytoskeletal transcripts (*KRT10*, *KRT16*, *KRT17*) in response to treatment with GANT-61 for cell donors 4 (A), 5 (B), 6 (C), and 7 (D). Treatment results in donor-dependent restoration of transcripts towards a non-diseased sample. Donor 4 experienced the greatest degree of restoration, donor 5 was not responsive to treatment, and donors 6 and 7 show intermediate responses. Bars represent the mean \pm one standard deviation from 2 technical replicates of each condition.

incorporation (Figure 4.13, A). Treatment with 10 μ M GANT-61 reduced transcript levels by approximately 50%, 75%, and 70% respectively. For *KRT10*, 50% reduction brings transcription within error of 100% NHEK samples. Incorporation of 25% ASZ cells into donor 5 tissues did not change expression of *KRT10*, but *KRT16* and *KRT17* were both overexpressed. Unlike donor 4, treatment with GANT-61 did not decrease the transcription of *KRT16* and *KRT17* (Figure 4.13, B).

Donors 6 and 7 experienced intermediate levels of altered transcription in response to GANT-61 (Figure 4.13, C&D). *KRT10* was lost upon ASZ incorporation for both donors but was recovered upon treatment (100% recovered for donor 6, approximately 39% recovered for donor 7). *KRT16* and *KRT17* were overexpressed in both donors with 25% ASZ incorporation. Donor 6 experienced mild reduction of both transcripts upon treatment with GANT-61 (approximately 32% and 35%, respectively). *KRT16* was similarly reduced for donor 7, (approximately 55% reduction) but *KRT17* transcription was not.

Further evaluation of changes in cytoskeletal structure was performed via immunofluorescence for KRT16 and KRT17 in donors 4, 6, and 7. KRT16 is sporadically localized in the lower layers of the stratum spinosum in 100% NHEK samples and is rarely observed in the upper layers and the stratum granulosum (Figure 4.14, A-C top). With 25% ASZ incorporation, expression is more ubiquitously observed throughout the epidermis (Figure 4.14, A-C middle). Treatment with GANT-61 reduces expression in the upper layers of the epidermis and localizes it again to the lower layers of the stratum spinosum for donors 4 and 7 (Figure 4.14, A& C bottom). While intensity of staining in donor 6 seemingly decreases upon treatment, expression is still observed throughout the epidermis (Figure 4.14, B bottom). This correlates well to the qPCR data in which donor 6 had the least reduction in KRT16 transcription following treatment.

Restoration of KRT17 localization was observed via immunofluorescence for donor 4 but was observed less for donors 6 and 7 (Figure 4.14, D-F). KRT17 is primarily expressed in the basal, proliferative layer of the epidermis. Tissues grown with 75% NHEK and 25% ASZ cells result in more ubiquitous expression of KRT17 (Figure 4.14, D-F middle). Treatment with GANT-61 restored this localization pattern for donor 4 (Figure 4.14, D bottom) which correlates

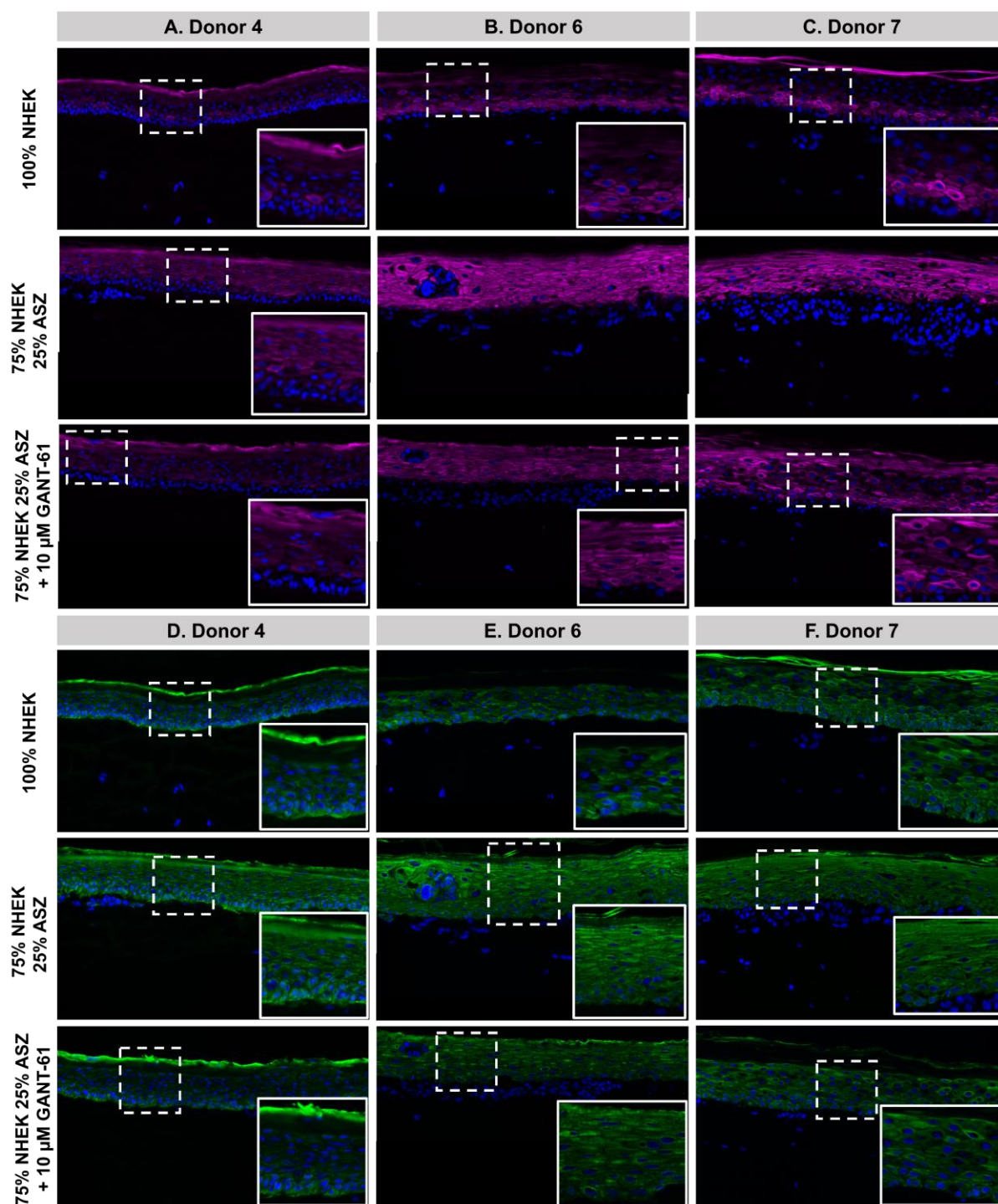


Figure 4.14: GANT-61 treatment of 75% NHEK/25% ASZ tissues results in cytoskeletal structure similar to that of the 100% NHEK controls. A-C) Staining for KRT16 (pink) in donors 4, 6, and 7 respectively. D-F) Staining for KRT17 (green) in donors 4, 6, and 7 respectively. Inlets show zoomed-in sections for more clear observation of expression patterns.

with the restoration of transcription discussed above. Donors 6 and 7, however, do not show obvious alterations of expression patterns upon treatment (Figure 4.14, E&F bottom). This too corroborates the qPCR data where *KRT17* was not reduced with treatment.

4.2.3.3 Analysis of barrier function

Analysis of keratinocyte differentiation checkpoints revealed consistent loss of FLG protein expression across cellular donors. Loss of barrier function contributes to the growth and appearance of BCC lesions and is imperative to restore for treatment/prevention of BCC. Similar to cytoskeletal structure, *FLG* transcription was not consistently restored across the donors analyzed. Incorporating 25% ASZ cells into donor 4 models did not change *FLG* transcription from 100% NHEK (Figure 4.15, A) Treatment with GANT-61 also did not result in significant changes to transcription. These results are corroborated by immunofluorescent staining of FLG where differences were not observed in protein localization or staining intensity (Figure 4.15, B).

Donors 6 and 7 did experience mild restoration of *FLG* transcription upon treatment following significant reductions with 25% ASZ incorporation (Figure 4.15, C&E). Transcription is increased to 47% of the 100% NHEK average for donor 6 and 24% for donor 7. Immunofluorescent staining further reveals slight restoration towards non-diseased localization and intensity of FLG. Both donors express FLG in the top 3-4 cell layers of the stratum granulosum in 100% NHEK samples (Figure 4.15, D&F top). With 25% ASZ incorporation, this falls to one cell layer or less with a loss of distinguishable keratohyalin granules (Figure 4.15, D&F middle). Treatment with GANT-61 restores approximately 2 cell layers of FLG staining with more intensely identifiable granules (Figure 4.15, D&F bottom).

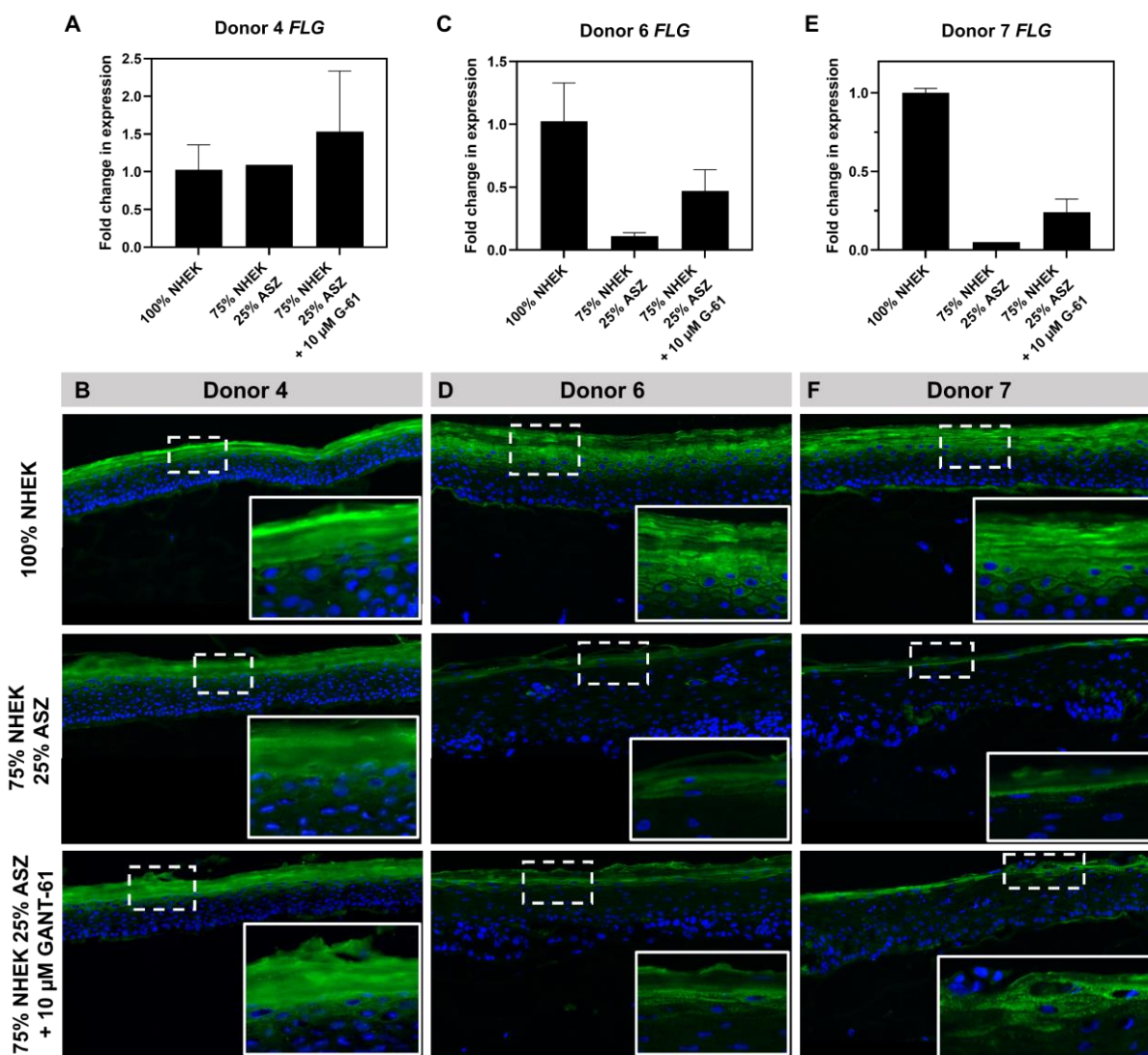


Figure 4.15: Donor-dependent restoration of filaggrin transcription and cellular localization of 75% NHEK/25% ASZ models following treatment with GANT-61. A, C, E) qPCR analysis of transcription for donors 4, 6, and 7. B, D, F) Immunostaining of filaggrin in donors 4, 6, and 7. Graphs represent the mean \pm one standard deviation from 2 technical replicates for each condition. Inlets show zoomed in sections of the stratum granulosum for clearer observation of cell staining patterns. For donors 6 and 7, punctate keratohyalin granules become identifiable and occupy a thicker layer of the tissue following treatment with GANT-61.

4.3 Conclusions and Outlook

In this chapter, 3-dimensional migration assays and 3-dimensional co-culture models of BCC are described. They are further evaluated for their ability to assay Hh inhibitors for BCC chemotherapeutic intervention. In a simple transwell model of ASZ cell migration, GANT-61 effectively inhibited migration with an IC_{50} around 3 μ M, well within literature reported IC_{50} values for this molecule. Vismodegib did not successfully prevent ASZ migration. While this was surprising, it demonstrates both the lack of initial response for many patients undergoing Vismodegib treatment and the inevitable Vismodegib resistance that many patients develop. It does, however, also inform inhibition experiments in 3D co-culture models.

A successful co-culture model of differentiated epidermal keratinocytes with murine ASZ cells is described. Cells were combined and seeded on top of a collagen dermis mimic and allowed to differentiate at the air-media interface for 5 and 12 days. Four biological donors were investigated at 5 days and four have been investigated at 12 days. Incorporation of cancer cells causes overall epidermal thickening, thickening of the viable layer of cells, and depletion of the cornified layer. This is combined with loss of density of keratohyalin granule staining, suggesting pathological alterations to keratinocyte differentiation. The changes in differentiation are further elucidated by qPCR and immunofluorescence analysis of cytoskeleton structure, cell adhesion, and barrier function.

Loss of *KRT10* transcription was measured on a logarithmic scale after 5 days of differentiation. *KRT10* loss was also generally observed after 12 days. *KRT17* often compensates for loss of *KRT10* in BCC. This was consistently observed in co-culture models across the range of ASZ incorporation. Interestingly, *KRT16* was also found to be overexpressed at both the transcript and protein levels. *KRT16* is associated with hyperproliferative skin diseases and is

largely understudied in BCC. These results confirm that changes in cytoskeletal structure do mimic what is seen in patients BCCs and highlight this heterogeneous model system as a valuable tool for identifying new molecular markers in BCC pathology.

Evaluation of cell adhesion components also served to validate these models as mimics of patient BCCs. Specifically, E-cadherin proteins are rarely altered in patient BCCs. The data presented herein aligns with this finding. Little is known about the contribution of desmoglein and desmocollin proteins in BCC development. Results from qPCR and immunostaining analysis reveal that in co-culture models, these aspects of cell adhesion are compromised in response to ASZ incorporation. DSC-1 and DSG-1 both show reduced immunofluorescent staining, and *DSC-1* transcription is greatly reduced. This data further highlights the utility of this model to reveal markers that may be significant for BCC pathogenesis that have been understudied in patients.

The final differentiation checkpoint evaluated was filaggrin. FLG is responsible for aggregating keratin filaments and ultimately collapsing cellular structure during terminal differentiation. FLG is commonly lost in BCC, and co-culture models reflect this characteristic. After 5 days of differentiation, *FLG* transcription and protein expression are greatly reduced in the presence of ASZ cells compared to 100% NHEK controls. At day 12, two out of four donors experienced a similar depletion of *FLG* transcription, but the other two experienced an initial spike. However, immunofluorescent staining revealed that increases in transcription did not correlate to increases in protein expression. FLG was still lost in the granular layers.

It was hypothesized that the ASZ cell population could be specifically inhibited with Hh antagonists to restore the phenotype and pathology of the model towards non-diseased identity. GANT-61 was chosen to study as ASZ cells are not sensitive to Vismodegib. Inhibitor efficacy

varied by donor but ultimately produced mild restoration towards a non-diseased phenotype for each. Overall epidermal thickness is increased with 25% ASZ incorporation but significantly reduced upon treatment with GANT-61. Similarly, the percentage of cornification in the tissues was increased with treatment.

Treatment with GANT-61 had the most profound impact on the cytoskeletal structure of co-culture models, but this effect was still donor dependent. Donor 4 responded the most to treatment in restoration of cytoskeletal structure, donors 6 and 7 experienced intermediate restoration, and donor 5 was insensitive to treatment. Similar effects were observed for restoration of FLG barrier proteins. Donors 6 and 7 did show mild restoration of FLG in the granular layer of tissues while donor 4 showed no significant changes.

It is important to note that GANT-61 has not been thoroughly studied by any research groups for BCC inhibition. It is not an ideal candidate for testing the hypothesis that Hh inhibition will produce tissues with closer to non-diseases phenotypes and pathologies. As such, this makes the observed influences of GANT-61 treatment promising and provides a baseline control for the exploration of other Gli inhibitors. Of particular interest is the evaluation of Co(III)-DNA complexes described in Chapter 2 of this thesis. While delivery and treatment logistics must be considered, Co(III)-DNA is almost 20-fold more potent than GANT-61 in inhibiting Hh pathology in ASZ cells. It is hypothesized that it would also be more effective in restoring co-culture models to a non-diseased state.

Other future work within these 3D systems is almost limitless. Keratinocytes were selected for white/light pigmentation as this is the population that suffers the most from BCC. Quite simply, researchers understand BCC best in white skin and literature knowledge validates the pathology of this model. However, keratinocytes can be isolated from any human skin tissue.

Cells can be selected for race, age, BCC risk factors, previous BCC diagnosis, family history of skin cancer, and more. Additionally, the successful co-culturing of human and mouse cells is promising for the incorporation of human BCC cells. Patient cells of different BCC subtypes and classifications could be built into the model to study how cancer cell identity impacts the raft tissue and to study treatment and prevention options. Everyone experiences cancer differently and having a broader understanding of BCC mechanisms will allow for precision medicine to treat individual patients more effectively.

4.4 Experimental section

General: Widefield microscopic images of migrated ASZ cells were taken using instrumentation at Northwestern University's Biological Imaging Facility. Keratinocytes and dermal fibroblasts were provided by the Skin Biology and Diseases Resource-Based Center (SBDRC) Skin Tissues Engineering and Morphology (STEM) core at Northwestern University. Sectioning of frozen OCT blocks and routine paraffin embedding were also performed by the STEM core, and H&E staining was performed by the Northwestern University Dermatopathology core. Special acknowledgements are given to Dr. Ljuba Lyass and Shuangni Yang.

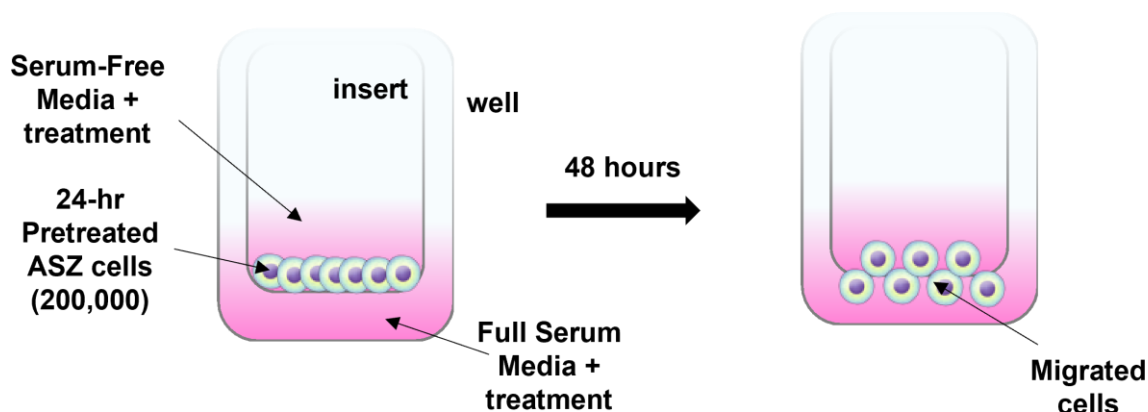
ASZ Cell Culture: ASZ and murine BCC cells are cultured in 154 Calcium Free media supplemented with 2% "chelexed" FBS, 1x pen/strep, and 0.05 mM CaCl₂. Since ASZ cells are sensitive to calcium, calcium is stripped from FBS by Chelex-100 (Bio-Rad 142-1253) to achieve a known final concentration of 0.05 mM. Cells were passaged in 75 cm² flasks. To split, cells were incubated in DPBS for 10 minutes before lifting in 2 mL of Trypsin for 10 minutes. The Trypsin reaction was quenched in M154 2% serum media, and Trypsin was removed by

centrifugation at 200 rcf for 10 minutes. The resulting cell pellet was resuspended in 2% serum M154 and passaged or counted for cell plating.

J2 Fibroblast cell culture: 3T3-J2 murine fibroblast cells are cultured in blah media supplemented with 10% calf serum, Amphotericin B (Sigma A2942, 250 $\mu\text{g}/\text{mL}$), and gentamycin (Sigma G1397, 50 mg/mL). Cells are passaged in 10 cm^2 tissue culture dishes, never passing 70% confluency. To split, cells are lifted in 1 mL of Trypsin solution for 4-5 minutes at room temperature and are quenched with 10% serum containing media. Cells are always centrifuged to remove trypsin before resuspension and counting or passaging.

NHEK cell culture: The media for NHEK cell culture is calcium-free media M154 supplemented with 1 human keratinocyte growth supplement (ThermoFisher, S0015) 175 μL of 0.2 M CaCl_2 (final concentration 70 μM), Amphotericin B (Sigma A2942, 250 $\mu\text{g}/\text{mL}$), and gentamycin (Sigma G1397, 50 mg/mL), hereby referred to as M154 complete. Cells were passaged in 10 cm^2 tissue culture dishes. To split, cells were lifted in 2 mL of Trypsin solution for 7 minutes while incubating at 37°C. The trypsin reaction was quenched in 10% serum containing media and trypsin/serum-containing media were removed via centrifugation at 500 rcf for 5 minutes. Cells were resuspended in M154 complete prior to passaging or counting. NHEK cells isolated from patient tissue (performed by various members of the Perez-White laboratory) were only used for experiments if they had been passaged 5 or less time and had been in culture for 21 days. Past P5D21, cells were discarded.

Transwell migration assays: ASZ cells were seeded in 6-well plates at 300,000 cells/well with one well for every desired control and experimental condition. Once confluent, cells were either media swapped for non-treated controls or treated with desired concentration of Hh inhibitor



Scheme 4.4: Transwell assay experimental setup for ASZ cells. ASZ cells that have been pre-treated with Hh inhibitors are seeded at 200,000 cells onto a porous membrane in 400 μL of serum-free media with the desired treatment. Below the membrane, a well of a 24-well plate contains 400 μL of full serum media plus treatment. Cells migrate for 48 hours prior to fixation, staining, and imaging.

(Vismodegib or GANT-61) for 24 hours. Prior to lifting cells, transwell inserts (ThermoFisher, PI8P01250 Millicell Cell Culture Insert, 12 mm, polycarbonate, 8.0 μm) were half prepared in 24-well plates. First, 400 μL of full serum ASZ media was added to the bottom of the well of a desired condition to serve as the chemoattractant for cell migration. To ensure that both the top and bottom of the inserts contain treatment, 0.4 μL of 1000x GANT-61 or Vismodegib were added and mixed by pipetting. Inserts themselves were prepared in empty wells and then placed inside the matching media-containing wells once fully ready. At this point, the cells were lifted with Trypsin, quenched with serum-containing media, and transferred into individual centrifuge tubes for Trypsin removal via centrifugation. The cells were then resuspended in 1 mL serum-free M154 media each for cell counting. Generally, a 6-well dish of confluent ASZs yields 1 million cells in 1mL. Optimal cell count for migration assays was determined to be 200,000 cells per insert. For the top of the inserts, the volume was 400 μL total. The volume necessary for 200,000 cells was combined with a volume of serum-free media to reach 400 μL in the insert.

Generally, this came to around 200 μL of each. Lastly, 0.4 μL of 1000x treatment was added and pipetted gently to mix. Inserts were then transferred to their matching media-containing wells using sterile forceps and allowed to migrate for 48 hours. Scheme 4.4 summarizes the transwell setup.

After 48 hours, intact membranes are fixed (10 minutes in 4% paraformaldehyde), permeabilized (10 minutes in methanol), and stained (30 minutes in 1% aqueous Crystal Violet, Sigma Aldrich V5265-250ML). At the completion of staining, a cotton swap was used to gently remove non-migrated cells from the upper portion of the membrane. The inserts were then washed $\times 4$ in DPBS to remove background staining and were immediately imaged (Northwestern Biological Imaging Facility Olympus IX53 Inverted Color Microscope).

ImageJ macro for cell counting: To streamline cell counting, an ImageJ macro was developed to consistently and reproducibly count cells in every image taken. First, the image is duplicated and converted into an 8-bit (black and white) image. A Gaussian Blur at Sigma=2 is performed (Process \rightarrow Filters \rightarrow Gaussian Blur). Thresholding is performed to select the area of cell stain, and the “Li” thresholding algorithm was found to be best suited for this type and shape of cell (Image \rightarrow Adjust \rightarrow Threshold). At this point, the background is set to black and the thresholded area of interest becomes white. The “Convert to mask” command is then run (Process \rightarrow Binary \rightarrow Convert to Mask), followed by an opening protocol under Process \rightarrow Binary \rightarrow Options \rightarrow do = open, count = 1, iterations = 5. To identify where cell boundaries are between each other, the watershed function is performed (Process \rightarrow Binary \rightarrow Watershed) and then the particles are analyzed from size 1250-infinity (Analyze \rightarrow Analyze Particles). To check the success of the macro, the outlines of the results are overlaid with the original image. Figure 4.16 shows an example of this after the cell counting protocol.

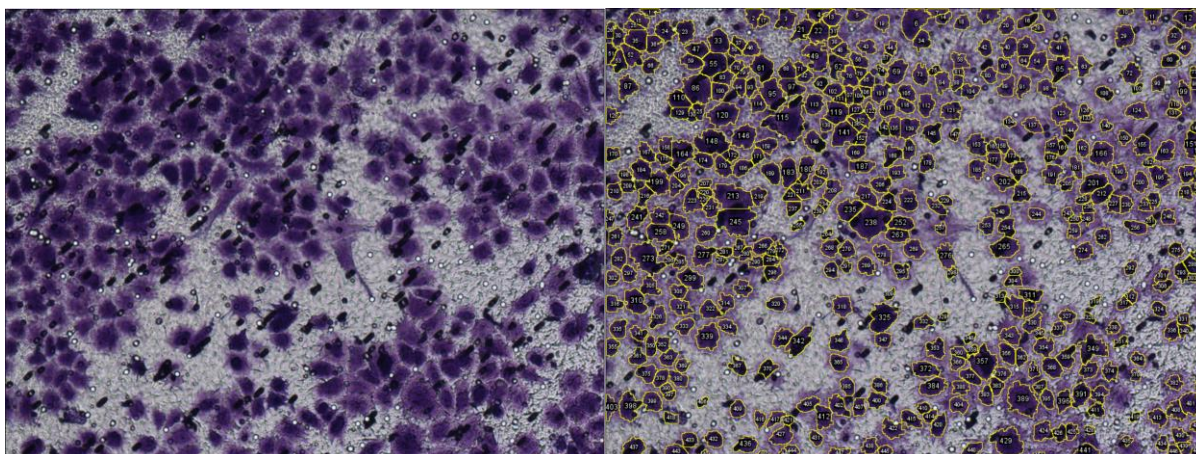


Figure 4.16: Results of ImageJ cell counting macro for ASZ cells. Left: original image. Right: Image overlaid with the cell counting results. In general, this macro effectively determines cell borders to count each individual cell. It can also distinguish discrepancies in cell sizes.

Preparation of collagen plugs: Sterile reconstitution buffer (1.1 g NaHCO_3 , 2.3 g HEPES in 50 mL of 0.05 N NaOH), DMEM (low glucose, Sigma D2429), water, collagen (Corning 354249), and 0.5N NaOH are first placed on ice to ensure they are cold when ready to use. Mouse 3T3-J2 fibroblast cells are lifted and counted. Between 300,000 and 400,000 J2 cells are needed for each collagen plug- typically aim to have 20 plates of J2 cells to lift for every 12 plugs. Additionally, each plug is 1.5 mL total (for 12 plugs, 18 mL). After counting, cells are centrifuged to move cell counting media and resuspended in “10x” reconstitution buffer (for 12 plugs, 1.8 mL) in a 50 mL centrifuge tube with clearly marked volumes. “10x” DMEM and “10x” water are then added to the cell suspension (for 12 plugs, 1.8 mL of each). Collagen is then carefully poured into the center of the tube, avoiding contact with the walls, to the final volume (for 12 plugs, 18 mL total). To achieve the desired color of “watermelon jolly rancher” pink, 50-150 μL of 0.5N NaOH are added at a time. Between additions, the tube is gently rocked and spun to mix the contents without creating bubbles. Once the desired color is achieved, pipettes stored at -20°C are used to carefully pipette 1.5 mL of the collagen mixture into each well of a 12 well plate. After 5

plugs, a new pipette is gotten from the freezer to ensure the collagen does not begin to harden inside a warmed pipette. After all plugs are poured, incubate at 37°C for 20 minutes until the collagen has set. Add 2 mL of J2 media and return to the incubator. Plugs can be used anywhere from 1-4 days after pouring to begin a 3D experiment.

E-media recipe for 1L: Media D5671 (463.5 mL) + media D6421 (463.5 mL), gentamycin (10 µg/mL final), amphotericin B (0.25 µg/mL), L-glutamine (4 mM final), hydrocortisone (0.4 µg/mL final), cholera toxin (10 ng/mL final), FBS (5% final), and 10 mL E-cocktail (180 µM adenine, 5 µg/mL bovine pancreatic insulin, 5 µg/mL human apo-transferrin, 5 µg/mL tiiodothyronine, final volume 200 mL in PBS)

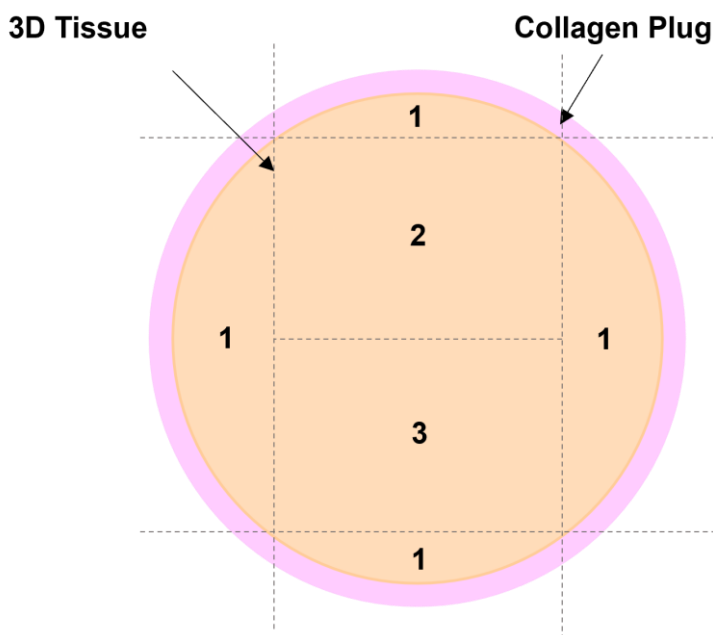
Seeding NHEK/ASZ co-culture experiments (Day -2): Before cells are lifted, the media for each collagen plug is aspirated and replaced with 1 mL of E-media + EGF (epidermal growth factor, final concentration 5 ng/mL) For a 3D differentiation assay, each plug is seeded with a total of 600,000 cells with 1 mL of total cell suspension being added to each plug (that already contains 1 mL of E-media + EGF). Table 4X breaks down the number of each cell type needed for co-culture experiments, as well as the volume of cell suspension (specified below).

Table 4.1: NHEK/ASZ co-culture cell suspension specifics

Co-culture ratio	# of NHEK cells/plug	# of ASZ cells/plug	µL of NHEK cell suspension	µL of ASZ cell suspension
100% NHEK	600,000	-	1000	-
90% NHEK/ 10% ASZ	540,000	60,000	900	1000
75% NHEK/ 25% ASZ	450,000	150,000	750	250
50% NHEK/ 50% ASZ	300,000	300,000	500	500
100% ASZ	-	600,000	-	1000

NHEK and ASZ cells are lifted and counted separately. Stock suspensions of each cell are made at 600,000 cells /mL in E-media + EGF. To make co-culture mixtures, appropriate volumes of each stock are combined in centrifuge tubes to 1 mL, mixed thoroughly, and then added to a labeled collagen plug. For example, for 1 plug of 75% NHEK/ 10% ASZ, 750 μ L of NHEK cell suspension is combined with 250 μ L of ASZ cell suspension and mixed thoroughly prior to evenly dispersing the mixture across the surface of the plug. This is achieved by slowly pipetting the suspension in a snake-like motion across the entire area of the plug. Once all plugs are seeded, the plates are incubated at 37°C. Seeding day is defined as Day -2. On Day -1, the E-media + EGF is swapped for fresh E-media + EGF. This is done again on Day 0 1 hour prior to lifting the plugs.

Lifting collagen plugs to air-media interface (Day 0): E-media + EGF should be swapped for fresh E-media + EGF 1 hour prior to lifting. During this hour, culture dishes are prepped with E-media (no EGF) and a sterile metal support grid. First, one metal grid is added to a 60 mm culture dish for each plug (each plug gets a separate dish and metal grid). Each dish receives 6 mL of E-media (no EGF) that may also contain GANT-61 treatment for treated cultures. Plugs are lifted with a sterile spatula by gently releasing the plug from the sides of the well before scooping and placing in the center of the metal grid. The spatula is used to unfold any tucked edges of the plug to ensure it lays totally flat. After all plugs are lifted, the dishes are carefully returned to the incubator taking precaution against media splashing onto the tops of the tissues for the remaining duration of experimentation. The media is replaced (with or without GANT-61 treatment) every other day until harvest.



Scheme 4.5: Sectioning of 3D tissue for post-harvest analysis. Clean cuts are made with a razor blade on the dashed lines. Sections marked with 1 are peeled from the collagen membrane and lysed in TRIzol for mRNA extraction. The section marked 2 is fixed in neutral buffered formalin for paraffin embedding and ultimate hematoxylin and eosin staining. The section marked 3 is embedded in frozen OCT for immunofluorescence

Harvesting 3D tissues: Tissues were either harvested 5 days after lifting or 12 days after lifting. The procedure is the same regardless, and each tissue is harvested one at a time. First, the media is aspirated from the dish and the plug/metal grid are submerged in DPBS. While submerged, small curved scissors were used to gently cut away any tissue that is connected to the metal support grid. Once released, the DPBS is decanted and the plug (with tissue still on top) is moved to the center of the dish. Razor blades were used to precisely cut the tissue into a long rectangle. This rectangle is then cut in half so that one half is fixed in neutral buffered formalin for paraffin embedding and the other half is frozen in OCT solution. The tissue on the edge pieces originally cut off were lysed in TRIzol total mRNA isolation buffer (Invitrogen Life Technologies, Catalog # 15596-026) for qPCR analysis. Scheme 4.5 pictorially represents the

tissue cutting process. Formalin samples are fixed for 24 hours before transferring to 70% ethanol in cassettes and delivery to Northwestern's Skin Tissue Engineering & Morphology (STEM) Core for routine sectioning and H&E analysis. OCT blocks were also sectioned by the STEM core.

Analysis of H&E stained images tissues: Images of H&E stained slides were taken on a Zeiss microscope fitted with a color camera at 20x magnification. At this magnification on this instrument, the pixel/micron ratio is 5.9005. This ratio was used to set the scale for images in ImageJ so that the thickness of the total epidermis, the viable layer, and the cornified layer could all be determined across biological replicates and multiple images. To calculate the % of viable and cornified layers of the whole, the raw micron measurements for viable or cornified layers were divided by that of the total and multiplied by 100. One-way ANOVA analysis for multiple statistical comparisons was performed in GraphPad Prism.

Quantitative real time-Polymerase Chain Reaction analysis: Tissues lysed in TRIzol total mRNA isolation buffer (Invitrogen Life Technologies, Catalog # 15596-026) were storing at -80 °C in RNAase free microcentrifuge tubes until ready for mRNA extraction. The Qiagen miRNeasy minikit (Qiagen Technologies, Part Number 217004) was used to extract mRNA from all samples. The total quantity of mRNA extracted was verified through nano-drop Ultraviolet-Visible absorption with Nanodrop adaptation. Complimentary DNA sequences were transcribed from 1 µg of mRNA from each sample using Superscript III First-Strand Synthesis SuperMix for qRT-PCR (Invitrogen, Part Number 11752050). Quantitative rt-PCR was performed on a Roche Light Cycler ® 96 with Faststart essential DNA green master (Roche catalog number 6402712001). Acidic ribosomal protein p0 (Rplp0) was used as a control for human mRNA

analysis, and murine ribosomal protein L19 (Rpl19) was used as a control for mouse mRNA analysis. All forward and reverse sequences can be found in Appendix 5.

Immunofluorescent staining of OCT frozen tissues: OCT blocks were sectioned onto slides by Shuangni Yang in Northwestern's Skin Tissue Engineering and Morphology (STEM) core. Slides were stored at -80°C until ready for use. Tissues were fixed in 50% methanol at -20°C for 20 minutes before allowed to completely dry in air. Slides were then was in PBS for 5 minutes. Blocking was performed in 5% normal serum that will not be represented in one of the antibodies (typically this is goat, but if a goat antibody is used, block in donkey serum) for 1 hour. Slides are briefly dipped in PBS to remove excess before adding 100 μ L of primary antibody concoction to each slide and covering with a thin strip of parafilm. Clones and dilution factors for all antibodies tested can be found in Appendix 5. Primary antibodies reacted overnight at 4°C in a humidity chamber. The following day, the slides were washed 3x5 minutes in DPBS. After washing, slides were placed back into the humidity chamber and 100 μ L of secondary antibody concoction was added to each slide before covering with a thin strip of parafilm. For each experiment, the secondary antibodies were Goat α Mouse 647 and Goat α Rabbit 488 at 1:300 dilution. Secondary antibodies incubated for 1 hour. Slides were washed 3x10 minutes in DPBS. Between the second and third washed, slides were incubated with 1x DAPI for 5 minutes as a nuclear stain. Slides were mounted with coverslips and gelvatol and were stored in the dark and allowed to dry for 3 days prior to imaging via fluorescence microscopy.

Chapter 1 References

- (1) Lai, V.; Cranwell, W.; Sinclair, R. Epidemiology of skin cancer in the mature patient. *Clinics in Dermatology* **2018**, *36* (2), 167-176. DOI: <https://doi.org/10.1016/j.clindermatol.2017.10.008>.
- (2) Albert, M. R.; Weinstock, M. A. Keratinocyte Carcinoma. *CA: A Cancer Journal for Clinicians* **2003**, *53* (5), 292-302, <https://doi.org/10.3322/canjclin.53.5.292>. DOI: <https://doi.org/10.3322/canjclin.53.5.292>.
- (3) Stern, R. S. Prevalence of a history of skin cancer in 2007: results of an incidence-based model. *Arch Dermatol* **2010**, *146* (3), 279-282. DOI: 10.1001/archdermatol.2010.4 From NLM.
- (4) Rogers, H. W.; Weinstock, M. A.; Feldman, S. R.; Coldiron, B. M. Incidence Estimate of Nonmelanoma Skin Cancer (Keratinocyte Carcinomas) in the U.S. Population, 2012. *JAMA Dermatol* **2015**, *151* (10), 1081-1086. DOI: 10.1001/jamadermatol.2015.1187 From NLM.
- (5) Wong, C. S. M.; Strange, R. C.; Lear, J. T. Basal cell carcinoma. *BMJ* **2003**, *327* (7418), 794-798. DOI: 10.1136/bmj.327.7418.794.
- (6) Delishaj, D.; Rembielak, A.; Manfredi, B.; Ursino, S.; Pasqualetti, F.; Laliscia, C.; Orlandi, F.; Morganti, R.; Fabrini, M. G.; Paiar, F. Non-melanoma skin cancer treated with high-dose-rate brachytherapy: a review of literature. *J Contemp Brachytherapy* **2016**, *8* (6), 533-540. DOI: 10.5114/jcb.2016.64112.
- (7) Cojocaru, A.; Marinescu, E.-A.; Nica, O.; Ilinoiu, E.; Negri, A.; Ciurea, M.-E. Basal Cell Carcinoma and its Impact on Different Anatomical Regions. *Curr Health Sci J* **2021**, *47* (1), 75-83. DOI: 10.12865/CHSJ.47.01.12.
- (8) Jones, E. A.; Sajid, M. I.; Shenton, A.; Evans, D. G. Basal Cell Carcinomas in Gorlin Syndrome: A Review of 202 Patients. *Journal of Skin Cancer* **2011**, *2011*, 217378. DOI: 10.1155/2011/217378.
- (9) Kiwilsza, M.; Sporniak-Tutak, K. Gorlin-Goltz syndrome--a medical condition requiring a multidisciplinary approach. *Med Sci Monit* **2012**, *18* (9), RA145-RA153. DOI: 10.12659/msm.883341.

(10) Hoban, P. R.; Ramachandran, S.; Strange, R. C. Environment, phenotype and genetics: risk factors associated with BCC of the skin. *Expert Review of Anticancer Therapy* **2002**, *2* (5), 570-579. DOI: 10.1586/14737140.2.5.570.

(11) Situm, M.; Buljan, M.; Bulat, V.; Lugović Mihić, L.; Bolanca, Z.; Simić, D. The role of UV radiation in the development of basal cell carcinoma. *Coll Antropol* **2008**, *32 Suppl 2*, 167-170.

(12) Wu, S.; Han, J.; Li, W.-Q.; Li, T.; Qureshi, A. A. Basal-cell carcinoma incidence and associated risk factors in U.S. women and men. *Am J Epidemiol* **2013**, *178* (6), 890-897. DOI: 10.1093/aje/kwt073.

(13) Berlin, N. L.; Cartmel, B.; Leffell, D. J.; Bale, A. E.; Mayne, S. T.; Ferrucci, L. M. Family history of skin cancer is associated with early-onset basal cell carcinoma independent of MC1R genotype. *Cancer Epidemiol* **2015**, *39* (6), 1078-1083. DOI: 10.1016/j.canep.2015.09.005.

(14) Puig, S.; Berrocal, A. Management of high-risk and advanced basal cell carcinoma. *Clin Transl Oncol* **2015**, *17* (7), 497-503. DOI: 10.1007/s12094-014-1272-9.

(15) Chung, S. Basal cell carcinoma. *Arch Plast Surg* **2012**, *39* (2), 166-170. DOI: 10.5999/aps.2012.39.2.166.

(16) Bøgelund, F. S.; Philipsen, P. A.; Gniadecki, R. Factors affecting the recurrence rate of basal cell carcinoma. *Acta Derm Venereol* **2007**, *87* (4), 330-334. DOI: 10.2340/00015555-0236.

(17) Marcil, I.; Stern, R. S. Risk of developing a subsequent nonmelanoma skin cancer in patients with a history of nonmelanoma skin cancer: a critical review of the literature and meta-analysis. *Arch Dermatol* **2000**, *136* (12), 1524-1530. DOI: 10.1001/archderm.136.12.1524.

(18) Levi, F.; Randimbison, L.; Maspoli, M.; Te, V. C.; La Vecchia, C. High incidence of second basal cell skin cancers. *Int J Cancer* **2006**, *119* (6), 1505-1507. DOI: 10.1002/ijc.22000.

(19) Bartos, V. Development of Multiple-Lesion Basal Cell Carcinoma of the Skin: A Comprehensive Review. *Sisli Etfal Hastan Tip Bul* **2019**, *53* (4), 323-328. DOI: 10.14744/SEMB.2019.08058.

(20) Villani, R.; Murigneux, V.; Alexis, J.; Sim, S.-L.; Wagels, M.; Saunders, N.; Soyer, H. P.; Parmentier, L.; Nikolaev, S.; Fink, J. L.; et al. Subtype-Specific Analyses Reveal Infiltrative

Basal Cell Carcinomas Are Highly Interactive with their Environment. *Journal of Investigative Dermatology* **2021**, *141* (10), 2380-2390. DOI: <https://doi.org/10.1016/j.jid.2021.02.760>.

(21) Cameron, M. C.; Lee, E.; Hibler, B. P.; Barker, C. A.; Mori, S.; Cordova, M.; Nehal, K. S.; Rossi, A. M. Basal cell carcinoma: Epidemiology; pathophysiology; clinical and histological subtypes; and disease associations. *J Am Acad Dermatol* **2019**, *80* (2), 303-317. DOI: <https://doi.org/10.1016/j.jaad.2018.03.060>.

(22) Armstrong, L. T. D.; Magnusson, M. R.; Guppy, M. P. B. Risk factors for recurrence of facial basal cell carcinoma after surgical excision: A follow-up analysis. *Journal of Plastic, Reconstructive & Aesthetic Surgery* **2017**, *70* (12), 1738-1745. DOI: <https://doi.org/10.1016/j.bjps.2017.04.006>.

(23) Fania, L.; Didona, D.; Morese, R.; Campana, I.; Coco, V.; Di Pietro, F. R.; Ricci, F.; Pallotta, S.; Candi, E.; Abeni, D.; et al. Basal Cell Carcinoma: From Pathophysiology to Novel Therapeutic Approaches. *Biomedicines* **2020**, *8* (11), 449. DOI: 10.3390/biomedicines8110449.

(24) Hendrix, J. D., Jr.; Parlette, H. L. Duplicitous growth of infiltrative basal cell carcinoma: Analysis of clinically undetected tumor extent in a paired case-control study. *Dermatol Surg* **1996**, *22* (6), 535-539..

(25) Wehner, M. R.; Cidre Serrano, W.; Nosrati, A.; Schoen, P. M.; Chren, M.-M.; Boscardin, J.; Linos, E. All-cause mortality in patients with basal and squamous cell carcinoma: A systematic review and meta-analysis. *J Am Acad Dermatol* **2018**, *78* (4), 663-672.e663. DOI: 10.1016/j.jaad.2017.11.026.

(26) Kim, D. P.; Kus, K. J. B.; Ruiz, E. Basal Cell Carcinoma Review. *Hematol Oncol Clin North Am* **2019**, *33* (1), 13-24. DOI: 10.1016/j.hoc.2018.09.004.

(27) Quazi, S. J.; Aslam, N.; Saleem, H.; Rahman, J.; Khan, S. Surgical Margin of Excision in Basal Cell Carcinoma: A Systematic Review of Literature. *Cureus* **2020**, *12* (7), e9211-e9211. DOI: 10.7759/cureus.9211.

(28) Ceilley, R. I.; Del Rosso, J. Q. Current modalities and new advances in the treatment of basal cell carcinoma. *International Journal of Dermatology* **2006**, *45* (5), 489-498. DOI: <https://doi.org/10.1111/j.1365-4632.2006.02673.x>.

(29) Mohs, F. E. CHEMOSURGERY: A MICROSCOPICALLY CONTROLLED METHOD OF CANCER EXCISION. *Archives of Surgery* **1941**, 42 (2), 279-295. DOI: 10.1001/archsurg.1941.01210080079004.

(30) Tolkachjov, S. N.; Brodland, D. G.; Coldiron, B. M.; Fazio, M. J.; Hruza, G. J.; Roenigk, R. K.; Rogers, H. W.; Zitelli, J. A.; Winchester, D. S.; Harmon, C. B. Understanding Mohs Micrographic Surgery: A Review and Practical Guide for the Nondermatologist. *Mayo Clin Proc* **2017**, 92 (8), 1261-1271. DOI: <https://doi.org/10.1016/j.mayocp.2017.04.009>.

(31) Smeets, N. W. J.; Kuijpers, D. I. M.; Nelemans, P.; Ostertag, J. U.; Verhaegh, M. E. J. M.; Krekels, G. A. M.; Neumann, H. A. M. Mohs' micrographic surgery for treatment of basal cell carcinoma of the face—results of a retrospective study and review of the literature. *British Journal of Dermatology* **2004**, 151 (1), 141-147. DOI: <https://doi.org/10.1111/j.1365-2133.2004.06047.x>.

(32) Bittner, G. C.; Cerci, F. B.; Kubo, E. M.; Tolkachjov, S. N. Mohs micrographic surgery: a review of indications, technique, outcomes, and considerations. *An Bras Dermatol* **2021**, 96 (3), 263-277. DOI: 10.1016/j.abd.2020.10.004.

(33) ROWE, D. E.; CARROLL, R. J.; DAY Jr., C. L. Mohs Surgery Is the Treatment of Choice for Recurrent (Previously Treated) Basal Cell Carcinoma. *The Journal of Dermatologic Surgery and Oncology* **1989**, 15 (4), 424-431. DOI: <https://doi.org/10.1111/j.1524-4725.1989.tb03249.x>.

(34) Lawrence, C. M. Mohs surgery of basal cell carcinoma--a critical review. *Br J Plast Surg* **1993**, 46 (7), 599-606. DOI: 10.1016/0007-1226(93)90114-q.

(35) Likhacheva, A.; Awan, M.; Barker, C. A.; Bhatnagar, A.; Bradfield, L.; Brady, M. S.; Buzurovic, I.; Geiger, J. L.; Parvathaneni, U.; Zaky, S.; et al. Definitive and Postoperative Radiation Therapy for Basal and Squamous Cell Cancers of the Skin: Executive Summary of an American Society for Radiation Oncology Clinical Practice Guideline. *Practical Radiation Oncology* **2020**, 10 (1), 8-20. DOI: <https://doi.org/10.1016/j.prro.2019.10.014>.

(36) Silverman, M. K.; Kopf, A. W.; Gladstein, A. H.; Bart, R. S.; Grin, C. M.; Levenstein, M. J. Recurrence rates of treated basal cell carcinomas. Part 4: X-ray therapy. *J Dermatol Surg Oncol* **1992**, 18 (7), 549-554. DOI: 10.1111/j.1524-4725.1992.tb03508.x.

(37) Baheti, A. D.; Tirumani, S. H.; Giardino, A.; Rosenthal, M. H.; Tirumani, H.; Krajewski, K.; Ramaiya, N. H. Basal Cell Carcinoma: A Comprehensive Review for the Radiologist. *American Journal of Roentgenology* **2015**, 204 (2), W132-W140. DOI: 10.2214/AJR.14.13160.

(38) Baker, S.; Joseph, K.; Tai, P. Radiotherapy in Gorlin Syndrome: Can It Be Safe and Effective in Adult Patients? *J Cutan Med Surg* **2016**, *20* (2), 159-162. DOI: 10.1177/1203475415612481 From NLM.

(39) Lo Muzio, L. Nevroid basal cell carcinoma syndrome (Gorlin syndrome). *Orphanet J Rare Dis* **2008**, *3*, 32-32. DOI: 10.1186/1750-1172-3-32.

(40) Salavastru, C.; Tiplica, G. S.; Fritz, K. Lasertherapie des Basalzellkarzinoms. *Der Hautarzt* **2018**, *69* (1), 10-16. DOI: 10.1007/s00105-017-4092-3.

(41) Moskalik, K.; Kozlov, A.; Demin, E.; Boiko, E. The efficacy of facial skin cancer treatment with high-energy pulsed neodymium and Nd:YAG lasers. *Photomed Laser Surg* **2009**, *27* (2), 345-349. DOI: 10.1089/pho.2008.2327.

(42) Ahluwalia, J.; Avram, M. M.; Ortiz, A. E. The Evolving Story of Laser Therapeutics for Basal Cell Carcinoma. *Dermatologic Surgery* **2020**, *46* (8).

(43) Wong, T. H.; Morton, C. A.; Collier, N.; Haylett, A.; Ibbotson, S.; McKenna, K. E.; Mallipeddi, R.; Moseley, H.; Seukeran, D. C.; Rhodes, L. E.; et al. British Association of Dermatologists and British Photodermatology Group guidelines for topical photodynamic therapy 2018. *British Journal of Dermatology* **2019**, *180* (4), 730-739. DOI: <https://doi.org/10.1111/bjd.17309>.

(44) Collier, N. J.; Rhodes, L. E. Photodynamic Therapy for Basal Cell Carcinoma: The Clinical Context for Future Research Priorities. *Molecules* **2020**, *25* (22), 5398. DOI: 10.3390/molecules25225398.

(45) Szeimies, R. M.; Ibbotson, S.; Murrell, D. F.; Rubel, D.; Frambach, Y.; De Berker, D.; Dummer, R.; Kerrouche, N.; Villemagne, H.; on behalf of the Excilight Study, G. A clinical study comparing methyl aminolevulinate photodynamic therapy and surgery in small superficial basal cell carcinoma (8–20 mm), with a 12-month follow-up. *Journal of the European Academy of Dermatology and Venereology* **2008**, *22* (11), 1302-1311. DOI: <https://doi.org/10.1111/j.1468-3083.2008.02803.x>.

(46) Basset-Seguin, N.; Bissonnette, R.; Girard, C.; Haedersdal, M.; Lear, J. T.; Paul, C.; Piaserico, S. Consensus recommendations for the treatment of basal cell carcinomas in Gorlin syndrome with topical methylaminolaevulinate-photodynamic therapy. *Journal of the European Academy of Dermatology and Venereology* **2014**, *28* (5), 626-632. DOI: <https://doi.org/10.1111/jdv.12150>.

(47) Marous, M.; Mueller, K.; Tausk, F. Multiple basal cell carcinomas in Gorlin Syndrome treated with pulsed dye laser. *J Cosmet Laser Ther* **2020**, *22* (6-8), 230-231. DOI: 10.1080/14764172.2021.1914852.

(48) Shumack, S.; Robinson, J.; Kossard, S.; Golitz, L.; Greenway, H.; Schroeter, A.; Andres, K.; Amies, M.; Owens, M. Efficacy of Topical 5% Imiquimod Cream for the Treatment of Nodular Basal Cell Carcinoma: Comparison of Dosing Regimens. *Archives of Dermatology* **2002**, *138* (9), 1165-1171. DOI: 10.1001/archderm.138.9.1165.

(49) Dummer, R.; Urosevic, M.; Kempf, W.; Hoek, K.; Hafner, J.; Burg, G. Imiquimod in basal cell carcinoma: how does it work? *Br J Dermatol* **2003**, *149 Suppl 66*, 57-58. DOI: 10.1046/j.0366-077x.2003.05630.x.

(50) Gross, K.; Kircik, L.; Kricorian, G. 5% 5-Fluorouracil Cream for the Treatment of Small Superficial Basal Cell Carcinoma: Efficacy, Tolerability, Cosmetic Outcome, and Patient Satisfaction. *Dermatologic Surgery* **2007**, *33* (4), 433-440. DOI: <https://doi.org/10.1111/j.1524-4725.2007.33090.x>

(51) Epstein, E. Fluorouracil paste treatment of thin basal cell carcinomas. *Arch Dermatol* **1985**, *121* (2), 207-213.

(52) Marks, R.; Gebauer, K.; Shumack, S.; Amies, M.; Bryden, J.; Fox, T. L.; Owens, M. L. Imiquimod 5% cream in the treatment of superficial basal cell carcinoma: results of a multicenter 6-week dose-response trial. *J Am Acad Dermatol* **2001**, *44* (5), 807-813. DOI: 10.1067/mjd.2001.113689.

(53) Torres, A.; Niemeyer, A.; Berkes, B. Treatment of basal cell carcinoma using imiquimod 5% cream as an adjuvant therapy to Mohs micrographic surgery. *J Eur Acad Dermatol Venereol* **2004**, *30* (12), 1462-1469.

(54) Gailani, M. R.; Bale, S. J.; Leffell, D. J.; DiGiovanna, J. J.; Peck, G. L.; Poliak, S.; Drum, M. A.; Pastakia, B.; McBride, O. W.; Kase, R.; et al. Developmental defects in Gorlin syndrome related to a putative tumor suppressor gene on chromosome 9. *Cell* **1992**, *69* (1), 111-117. DOI: 10.1016/0092-8674(92)90122-s.

(55) Hahn, H.; Wicking, C.; Zaphiropoulos, P. G.; Gailani, M. R.; Shanley, S.; Chidambaram, A.; Vorechovsky, I.; Holmberg, E.; Uden, A. B.; Gillies, S.; et al. Mutations of the human homolog of *Drosophila* patched in the nevoid basal cell carcinoma syndrome. *Cell* **1996**, *85* (6), 841-851. DOI: 10.1016/s0092-8674(00)81268-4.

(56) Johnson, R. L.; Rothman, A. L.; Xie, J.; Goodrich, L. V.; Bare, J. W.; Bonifas, J. M.; Quinn, A. G.; Myers, R. M.; Cox, D. R.; Epstein, E. H., Jr.; et al. Human homolog of patched, a candidate gene for the basal cell nevus syndrome. *Science* **1996**, 272 (5268), 1668-1671. DOI: 10.1126/science.272.5268.1668.

(57) Klein, R. D.; Dykas, D. J.; Bale, A. E. Clinical testing for the nevoid basal cell carcinoma syndrome in a DNA diagnostic laboratory. *Genet Med* **2005**, 7 (9), 611-619. DOI: 10.1097/01.gim.0000182879.57182.b4.

(58) Epstein, E. H. Basal cell carcinomas: attack of the hedgehog. *Nat Rev Cancer* **2008**, 8 (10), 743-754. DOI: 10.1038/nrc2503.

(59) Gupta, S.; Takebe, N.; Lorusso, P. Targeting the Hedgehog pathway in cancer. *Therapeutic advances in medical oncology* **2010**, 2 (4), 237-250. DOI: 10.1177/1758834010366430.

(60) Ming, J. E.; Nanni, L.; Muenke, M.; Meinecke, P.; Pierpont, M. E. M.; Robin, N. H.; Young, I. D.; Roessler, E.; Steinhaus, K.; Bocian, M.; et al. The Mutational Spectrum of the Sonic Hedgehog Gene in Holoprosencephaly: SHH Mutations Cause a Significant Proportion of Autosomal Dominant Holoprosencephaly. *Human Molecular Genetics* **1999**, 8 (13), 2479-2488. DOI: 10.1093/hmg/8.13.2479.

(61) di Magliano, M. P.; Hebrok, M. Hedgehog signalling in cancer formation and maintenance. *Nature Reviews Cancer* **2003**, 3, 903, Review Article. DOI: 10.1038/nrc1229.

(62) Fujii, K.; Miyashita, T. Gorlin syndrome (nevoid basal cell carcinoma syndrome): Update and literature review. *Pediatrics International* **2014**, 56 (5), 667-674. DOI: 10.1111/ped.12461.

(63) Sahebjam, S.; Siu, L. L.; Razak, A. A. The Utility of Hedgehog Signaling Pathway Inhibition for Cancer. *The Oncologist* **2012**, 17 (8), 1090-1099. DOI: 10.1634/theoncologist.2011-0450.

(64) Chahal, K. K.; Parle, M.; Abagyan, R. Hedgehog pathway and smoothed inhibitors in cancer therapies. *Anti-Cancer Drugs* **2018**, 29 (5).

(65) Skoda, A. M.; Simovic, D.; Karin, V.; Kardum, V.; Vranic, S.; Serman, L. The role of the Hedgehog signaling pathway in cancer: A comprehensive review. *Bosn J Basic Med Sci* **2018**, 18 (1), 8-20. DOI: 10.17305/bjbm.2018.2756.

(66) Ouhtit, A.; Nakazawa, H.; Armstrong, B. K.; Krickler, A.; Tan, E.; Yamasaki, H.; English, D. R. UV-radiation-specific p53 mutation frequency in normal skin as a predictor of risk of basal cell carcinoma. *J Natl Cancer Inst* **1998**, *90* (7), 523-531. DOI: 10.1093/jnci/90.7.523.

(67) Furth, N.; Aylon, Y.; Oren, M. p53 shades of Hippo. *Cell Death Differ* **2018**, *25* (1), 81-92. DOI: 10.1038/cdd.2017.163.

(68) Mancuso, M.; Pazzaglia, S.; Tanori, M.; Hahn, H.; Merola, P.; Rebessi, S.; Atkinson, M. J.; Di Majo, V.; Covelli, V.; Saran, A. Basal Cell Carcinoma and Its Development: Insights from Radiation-Induced Tumors in Ptch1-Deficient Mice. *Cancer Research* **2004**, *64* (3), 934-941. DOI: 10.1158/0008-5472.CAN-03-2460.

(69) Mercurio, L.; Albanesi, C.; Madonna, S. Recent Updates on the Involvement of PI3K/AKT/mTOR Molecular Cascade in the Pathogenesis of Hyperproliferative Skin Disorders. *Front Med (Lausanne)* **2021**, *8*, 665647-665647. DOI: 10.3389/fmed.2021.665647.

(70) Weiss, G. J.; Korn, R. L. Metastatic basal cell carcinoma in the era of hedgehog signaling pathway inhibitors. *Cancer* **2012**, *118* (21), 5310-5319. DOI: <https://doi.org/10.1002/cncr.27532>.

(71) Ozgediz, D.; Smith, E. B.; Zheng, J.; Otero, J.; Tabatabai, Z. L.; Corvera, C. U. Basal cell carcinoma does metastasize. *Dermatol Online J* **2008**, *14* (8), 5.

(72) von Domarus, H.; Stevens, P. J. Metastatic basal cell carcinoma. Report of five cases and review of 170 cases in the literature. *J Am Acad Dermatol* **1984**, *10* (6), 1043-1060. DOI: 10.1016/s0190-9622(84)80334-5.

(73) Lee, S. T.; Welch, K. D.; Panter, K. E.; Gardner, D. R.; Garrossian, M.; Chang, C.-W. T. Cyclopamine: From Cyclops Lambs to Cancer Treatment. *Journal of Agricultural and Food Chemistry* **2014**, *62* (30), 7355-7362. DOI: 10.1021/jf5005622.

(74) Binns, W.; Shupe, J. L.; Keeler, R. F.; James, L. F. Chronologic evaluation of teratogenicity in sheep fed *Veratrum californicum*. *J Am Vet Med Assoc* **1965**, *147* (8), 839-842.

(75) James, L. F. Teratological research at the USDA-ARS poisonous plant research laboratory. *J Nat Toxins* **1999**, *8* (1), 63-80.

(76) Chiang, C.; Litingtung, Y.; Lee, E.; Young, K. E.; Corden, J. L.; Westphal, H.; Beachy, P. A. Cyclopia and defective axial patterning in mice lacking Sonic hedgehog gene function. *Nature* **1996**, *383* (6599), 407-413. DOI: 10.1038/383407a0.

(77) Litingtung, Y.; Lei, L.; Westphal, H.; Chiang, C. Sonic hedgehog is essential to foregut development. *Nat Genet* **1998**, *20* (1), 58-61. DOI: 10.1038/1717.

(78) Cooper, M. K.; Porter, J. A.; Young, K. E.; Beachy, P. A. Teratogen-mediated inhibition of target tissue response to Shh signaling. *Science* **1998**, *280* (5369), 1603-1607.

(79) Incardona, J. P.; Gaffield, W.; Kapur, R. P.; Roelink, H. The teratogenic Veratrum alkaloid cycloamine inhibits sonic hedgehog signal transduction. *Development* **1998**, *125* (18), 3553-3562. DOI: 10.1242/dev.125.18.3553.

(80) Sanchez, P.; i Altaba, A. R. In vivo inhibition of endogenous brain tumors through systemic interference of Hedgehog signaling in mice. *Mechanisms of development* **2005**, *122* (2), 223-230.

(81) Berman, D. M.; Karhadkar, S. S.; Hallahan, A. R.; Pritchard, J. I.; Eberhart, C. G.; Watkins, D. N.; Chen, J. K.; Cooper, M. K.; Taipale, J.; Olson, J. M. Medulloblastoma growth inhibition by hedgehog pathway blockade. *Science* **2002**, *297* (5586), 1559-1561.

(82) Clement, V.; Sanchez, P.; de Tribolet, N.; Radovanovic, I.; Ruiz i Altaba, A. HEDGEHOG-GLI1 signaling regulates human glioma growth, cancer stem cell self-renewal, and tumorigenicity. *Curr Biol* **2007**, *17* (2), 165-172. DOI: 10.1016/j.cub.2006.11.033.

(83) Stecca, B.; Mas, C.; Clement, V.; Zbinden, M.; Correa, R.; Piguet, V.; Beermann, F.; Ruiz i Altaba, A. Melanomas require HEDGEHOG-GLI signaling regulated by interactions between GLI1 and the RAS-MEK/AKT pathways. *Proc Natl Acad Sci U S A* **2007**, *104* (14), 5895-5900. DOI: 10.1073/pnas.0700776104.

(84) Varnat, F.; Duquet, A.; Malerba, M.; Zbinden, M.; Mas, C.; Gervaz, P.; Ruiz i Altaba, A. Human colon cancer epithelial cells harbour active HEDGEHOG-GLI signalling that is essential for tumour growth, recurrence, metastasis and stem cell survival and expansion. *EMBO molecular medicine* **2009**, *1* (6-7), 338-351.

(85) Feldmann, G.; Dhara, S.; Fendrich, V.; Bedja, D.; Beaty, R.; Mullendore, M.; Karikari, C.; Alvarez, H.; Iacobuzio-Donahue, C.; Jimeno, A. Blockade of hedgehog signaling inhibits

pancreatic cancer invasion and metastases: a new paradigm for combination therapy in solid cancers. *Cancer research* **2007**, *67* (5), 2187-2196.

(86) Karhadkar, S. S.; Steven Bova, G.; Abdallah, N.; Dhara, S.; Gardner, D.; Maitra, A.; Isaacs, J. T.; Berman, D. M.; Beachy, P. A. Hedgehog signalling in prostate regeneration, neoplasia and metastasis. *Nature* **2004**, *431* (7009), 707-712.

(87) Frampton, J. E.; Basset-Séguin, N. Vismodegib: A Review in Advanced Basal Cell Carcinoma. *Drugs* **2018**, *78* (11), 1145-1156. DOI: 10.1007/s40265-018-0948-9.

(88) Jain, S.; Song, R.; Xie, J. Sonidegib: mechanism of action, pharmacology, and clinical utility for advanced basal cell carcinomas. *Onco Targets Ther* **2017**, *10*, 1645-1653. DOI: 10.2147/ott.S130910.

(89) Chang, A. L. S.; Solomon, J. A.; Hainsworth, J. D.; Goldberg, L.; McKenna, E.; Day, B.-m.; Chen, D. M.; Weiss, G. J. Expanded access study of patients with advanced basal cell carcinoma treated with the Hedgehog pathway inhibitor, vismodegib. *J Am Acad Dermatol* **2014**, *70* (1), 60-69.

(90) Chang, A. L. S.; Oro, A. E. Initial assessment of tumor regrowth after vismodegib in advanced basal cell carcinoma. *Archives of dermatology* **2012**, *148* (11), 1324-1325.

(91) Sharpe, H. J.; Pau, G.; Dijkgraaf, G. J.; Basset-Séguin, N.; Modrusan, Z.; Januario, T.; Tsui, V.; Durham, A. B.; Dlugosz, A. A.; Haverty, P. M. Genomic analysis of smoothed inhibitor resistance in basal cell carcinoma. *Cancer cell* **2015**, *27* (3), 327-341.

(92) Atwood, S. X.; Sarin, K. Y.; Whitson, R. J.; Li, J. R.; Kim, G.; Rezaee, M.; Ally, M. S.; Kim, J.; Yao, C.; Chang, A. L. S. Smoothed variants explain the majority of drug resistance in basal cell carcinoma. *Cancer cell* **2015**, *27* (3), 342-353.

(93) Danial, C.; Sarin, K. Y.; Oro, A. E.; Chang, A. L. S. An Investigator-Initiated Open-Label Trial of Sonidegib in Advanced Basal Cell Carcinoma Patients Resistant to Vismodegib. *Clinical Cancer Research* **2016**, *22* (6), 1325-1329. DOI: 10.1158/1078-0432.CCR-15-1588.

(94) Gutzmer, R.; Solomon, J. A. Hedgehog Pathway Inhibition for the Treatment of Basal Cell Carcinoma. *Targeted Oncology* **2019**, *14* (3), 253-267. DOI: 10.1007/s11523-019-00648-2.

(95) Li, Q.-r.; Zhao, H.; Zhang, X.-s.; Lang, H.; Yu, K. Novel-smoothened inhibitors for therapeutic targeting of naïve and drug-resistant hedgehog pathway-driven cancers. *Acta Pharmacologica Sinica* **2019**, *40* (2), 257-267. DOI: 10.1038/s41401-018-0019-5.

(96) Zárata, A. M.; Espinosa-Bustos, C.; Guerrero, S.; Fierro, A.; Oyarzún-Ampuero, F.; Quest, A. F. G.; Di Marcotullio, L.; Loricchio, E.; Caimano, M.; Calcaterra, A.; et al. A New Smoothened Antagonist Bearing the Purine Scaffold Shows Antitumour Activity In Vitro and In Vivo. *Int J Mol Sci* **2021**, *22* (16), 8372.

(97) Švenda, J.; Sheremet, M.; Kremer, L.; Maier, L.; Bauer, J. O.; Strohmam, C.; Ziegler, S.; Kumar, K.; Waldmann, H. Biology-Oriented Synthesis of a Withanolide-Inspired Compound Collection Reveals Novel Modulators of Hedgehog Signaling. *Angewandte Chemie International Edition* **2015**, *54* (19), 5596-5602. DOI: <https://doi.org/10.1002/anie.201500112>.

(98) Bonandi, E.; Mori, M.; Infante, P.; Basili, I.; Di Marcotullio, L.; Calcaterra, A.; Catti, F.; Botta, B.; Passarella, D. Design and Synthesis of New Withaferin A Inspired Hedgehog Pathway Inhibitors. *Chemistry – A European Journal* **2021**, *27* (32), 8350-8357. DOI: <https://doi.org/10.1002/chem.202100315>.

(99) Whitson, R. J.; Lee, A.; Urman, N. M.; Mirza, A.; Yao, C. Y.; Brown, A. S.; Li, J. R.; Shankar, G.; Fry, M. A.; Atwood, S. X.; et al. Noncanonical hedgehog pathway activation through SRF-MKL1 promotes drug resistance in basal cell carcinomas. *Nat Med* **2018**, *24* (3), 271-281. DOI: 10.1038/nm.4476.

(100) Infante, P.; Alfonsi, R.; Botta, B.; Mori, M.; Di Marcotullio, L. Targeting GLI factors to inhibit the Hedgehog pathway. *Trends in Pharmacological Sciences* **2015**, *36* (8), 547-558. DOI: <https://doi.org/10.1016/j.tips.2015.05.006>.

(101) Hopkins, A. L.; Groom, C. R. The druggable genome. *Nature reviews Drug discovery* **2002**, *1* (9), 727-730.

(102) Overington, J. P.; Al-Lazikani, B.; Hopkins, A. L. How many drug targets are there? *Nature reviews Drug discovery* **2006**, *5* (12), 993-996.

(103) Imming, P.; Sinning, C.; Meyer, A. Drugs, their targets and the nature and number of drug targets. *Nature reviews Drug discovery* **2006**, *5* (10), 821-834.

(104) Kim, J.; Lee, J. J.; Kim, J.; Gardner, D.; Beachy, P. A. Arsenic antagonizes the Hedgehog pathway by preventing ciliary accumulation and reducing stability of the Gli2 transcriptional effector. *Proceedings of the National Academy of Sciences* **2010**, *107* (30), 13432, 10.1073/pnas.1006822107.

(105) Kim, J.; Aftab, Blake T.; Tang, Jean Y.; Kim, D.; Lee, Alex H.; Rezaee, M.; Kim, J.; Chen, B.; King, Emily M.; Borodovsky, A.; et al. Itraconazole and Arsenic Trioxide Inhibit Hedgehog Pathway Activation and Tumor Growth Associated with Acquired Resistance to Smoothed Antagonists. *Cancer Cell* **2013**, *23* (1), 23-34. DOI: <https://doi.org/10.1016/j.ccr.2012.11.017>.

(106) Miller, W. H., Jr. Molecular Targets of Arsenic Trioxide in Malignant Cells. *The Oncologist* **2002**, *7* (S1), 14-19. DOI: 10.1634/theoncologist.7-suppl_1-14.

(107) Soignet, S. L.; Maslak, P.; Wang, Z.-G.; Jhanwar, S.; Calleja, E.; Dardashti, L. J.; Corso, D.; DeBlasio, A.; Gabrilove, J.; Scheinberg, D. A.; et al. Complete Remission after Treatment of Acute Promyelocytic Leukemia with Arsenic Trioxide. *New England Journal of Medicine* **1998**, *339* (19), 1341-1348. DOI: 10.1056/NEJM199811053391901.

(108) Cohen, M. H.; Hirschfeld, S.; Honig, S. F.; Ibrahim, A.; Johnson, J. R.; O'Leary, J. J.; White, R. M.; Williams, G. A.; Pazdur, R. Drug Approval Summaries: Arsenic Trioxide, Tamoxifen Citrate, Anastrozole, Paclitaxel, Bexarotene. *The Oncologist* **2001**, *6* (1), 4-11. DOI: 10.1634/theoncologist.6-1-4.

(109) Wang, Y.; Han, C.; Lu, L.; Magliato, S.; Wu, T. Hedgehog signaling pathway regulates autophagy in human hepatocellular carcinoma cells. *Hepatology* **2013**, *58* (3), 995-1010.

(110) Chen, Q.; Xu, R.; Zeng, C.; Lu, Q.; Huang, D.; Shi, C.; Zhang, W.; Deng, L.; Yan, R.; Rao, H. Down-regulation of Gli transcription factor leads to the inhibition of migration and invasion of ovarian cancer cells via integrin β 4-mediated FAK signaling. *PloS one* **2014**, *9* (2), e88386.

(111) Kebenko, M.; Drenckhan, A.; Gros, S. J.; Jücker, M.; Grabinski, N.; Ewald, F.; Grottko, A.; Schultze, A.; Izbicki, J. R.; Bokemeyer, C. ErbB2 signaling activates the Hedgehog pathway via PI3K–Akt in human esophageal adenocarcinoma: Identification of novel targets for concerted therapy concepts. *Cellular signalling* **2015**, *27* (2), 373-381.

(112) Santini, R.; Vinci, M. C.; Pandolfi, S.; Penachioni, J. Y.; Montagnani, V.; Olivito, B.; Gattai, R.; Pimpinelli, N.; Gerlini, G.; Borgognoni, L. Hedgehog-GLI signaling drives

self-renewal and tumorigenicity of human melanoma-initiating cells. *Stem cells* **2012**, *30* (9), 1808-1818.

(113) Fu, J.; Rodova, M.; Roy, S. K.; Sharma, J.; Singh, K. P.; Srivastava, R. K.; Shankar, S. GANT-61 inhibits pancreatic cancer stem cell growth in vitro and in NOD/SCID/IL2R gamma null mice xenograft. *Cancer letters* **2013**, *330* (1), 22-32.

(114) Lauth, M.; Bergstrm, s.; Shimokawa, T.; Toftgrd, R. Inhibition of GLI-mediated transcription and tumor cell growth by small-molecule antagonists. *Proceedings of the National Academy of Sciences* **2007**, *104* (20), 8455--8460. DOI: 10.1073/PNAS.0609699104.

(115) Huang, L.; Walter, V.; Hayes, D. N.; Onaitis, M. Hedgehog–GLI signaling inhibition suppresses tumor growth in squamous lung cancer. *Clinical Cancer Research* **2014**, *20* (6), 1566-1575.

(116) Mazumdar, T.; DeVecchio, J.; Agyeman, A.; Shi, T.; Houghton, J. A. Blocking Hedgehog survival signaling at the level of the GLI genes induces DNA damage and extensive cell death in human colon carcinoma cells. *Cancer research* **2011**, *71* (17), 5904-5914.

(117) Kiran Riaz, S.; Ke, Y.; Wang, F.; Kayani, M.; Malik, F. Influence of SHH/GLI1 axis on EMT mediated migration and invasion of breast cancer cells. *Scientific Reports* **2019**, *9*. DOI: 10.1038/s41598-019-43093-x.

(118) Geng, L.; Zhou, X.; Li, X.; Lu, K.; Li, P.; Wang, X. Gli1 Inhibitor GANT61 Exhibits Antitumor Efficacy in T-Cell Lymphoma Cells through Down-Regulation of p-STAT3 and SOCS3 Pathways. *Blood* **2015**, *126* (23), 1287. DOI: <https://doi.org/10.1182/blood.V126.23.1287.1287>.

(119) Calcaterra, A.; Iovine, V.; Botta, B.; Quaglio, D.; D'Acquarica, I.; Ciogli, A.; Iazzetti, A.; Alfonsi, R.; Lospinoso Severini, L.; Infante, P.; et al. Chemical, computational and functional insights into the chemical stability of the Hedgehog pathway inhibitor GANT61. *J Enzyme Inhib Med Chem* **2018**, *33* (1), 349-358. DOI: 10.1080/14756366.2017.1419221.

(120) Agyeman, A.; Jha, B. K.; Mazumdar, T.; Houghton, J. A. Mode and specificity of binding of the small molecule GANT61 to GLI determines inhibition of GLI-DNA binding. *Oncotarget* **2014**, *5* (12), 4492-4503. DOI: 10.18632/oncotarget.2046.

(121) Zhang, R.; Wu, J.; Ferrandon, S.; Glowacki, K. J.; Houghton, J. A. Targeting GLI by GANT61 involves mechanisms dependent on inhibition of both transcription and DNA licensing. *Oncotarget* **2016**, *7* (49), 80190-80207. DOI: 10.18632/oncotarget.13376.

(122) Ankita Borah, V. P., Aswathy Ravindran Girija, Sivakumar Balasubramanian, Ankit K. Rochani, Toru Maekawa and D. Sakthi Kumar. Poly-lactic-co-glycolic acid Nanof ormulation of Small Molecule Antagonist GANT61 for Cancer Annihilation by Modulating Hedgehog Pathway. *Nano World Journal* **2017**, *3* (1), 10. DOI: 10.17756/nwj.2017-038.

(123) Infante, P.; Mori, M.; Alfonsi, R.; Ghirga, F.; Aiello, F.; Toscano, S.; Ingallina, C.; Siler, M.; Cucchi, D.; Po, A.; et al. Gli1/DNA interaction is a druggable target for Hedgehog-dependent tumors. *The EMBO Journal* **2015**, *34* (2), 200-217. DOI: <https://doi.org/10.15252/embj.201489213>.

(124) Infante, P.; Malfanti, A.; Quaglio, D.; Balducci, S.; De Martin, S.; Bufalieri, F.; Mastrotto, F.; Basili, I.; Garofalo, M.; Lospinoso Severini, L.; et al. Glabrescione B delivery by self-assembling micelles efficiently inhibits tumor growth in preclinical models of Hedgehog-dependent medulloblastoma. *Cancer Letters* **2021**, *499*, 220-231. DOI: <https://doi.org/10.1016/j.canlet.2020.11.028>.

(125) Berardozzi, S.; Bernardi, F.; Infante, P.; Ingallina, C.; Toscano, S.; De Paolis, E.; Alfonsi, R.; Caimano, M.; Botta, B.; Mori, M.; et al. Synergistic inhibition of the Hedgehog pathway by newly designed Smo and Gli antagonists bearing the isoflavone scaffold. *European Journal of Medicinal Chemistry* **2018**, *156*, 554-562. DOI: <https://doi.org/10.1016/j.ejmech.2018.07.017>.

(126) Lospinoso Severini, L.; Quaglio, D.; Basili, I.; Ghirga, F.; Bufalieri, F.; Caimano, M.; Balducci, S.; Moretti, M.; Romeo, I.; Loricchio, E.; et al. A Smo/Gli Multitarget Hedgehog Pathway Inhibitor Impairs Tumor Growth. *Cancers* **2019**, *11* (10), 1518.

(127) Hom, M. E.; Ondrus, A. E.; Sakata-Kato, T.; Rack, P. G.; Chen, J. K. Bicyclic Imidazolium Inhibitors of Gli Transcription Factor Activity. *ChemMedChem* **2020**, *15* (12), 1044-1049. DOI: <https://doi.org/10.1002/cmdc.202000169>.

(128) Sasaki, H.; Nishizaki, Y.; Hui, C.-c.; Nakafuku, M.; Kondoh, H. Regulation of Gli2 and Gli3 activities by an amino-terminal repression domain: implication of Gli2 and Gli3 as primary mediators of Shh signaling. *Development* **1999**, *126* (17), 3915-3924.

(129) Yun, T.; Wang, J.; Yang, J.; Huang, W.; Lai, L.; Tan, W.; Liu, Y. Discovery of Small Molecule Inhibitors Targeting the Sonic Hedgehog. *Frontiers in Chemistry* **2020**, *8*, Original Research. DOI: 10.3389/fchem.2020.00498.

(130) Riobó, N. A.; Lu, K.; Ai, X.; Haines, G. M.; Emerson, C. P., Jr. Phosphoinositide 3-kinase and Akt are essential for Sonic Hedgehog signaling. *Proceedings of the National Academy of Sciences of the United States of America* **2006**, *103* (12), 4505-4510. DOI: 10.1073/pnas.0504337103.

(131) Gordon, R. E.; Zhang, L.; Peri, S.; Kuo, Y.-M.; Du, F.; Egleston, B. L.; Ng, J. M. Y.; Andrews, A. J.; Astsaturov, I.; Curran, T.; et al. Statins Synergize with Hedgehog Pathway Inhibitors for Treatment of Medulloblastoma. *Clin Cancer Res* **2018**, *24* (6), 1375-1388. DOI: 10.1158/1078-0432.CCR-17-2923.

(132) Bijlsma, M. F.; Spek, C. A.; Zivkovic, D.; van de Water, S.; Rezaee, F.; Peppelenbosch, M. P. Repression of Smoothed by Patched-Dependent (Pro-)Vitamin D3 Secretion. *PLOS Biology* **2006**, *4* (8), e232. DOI: 10.1371/journal.pbio.0040232.

(133) Kinto, N.; Iwamoto, M.; Enomoto-Iwamoto, M.; Noji, S.; Ohuchi, H.; Yoshioka, H.; Kataoka, H.; Wada, Y.; Yuhao, G.; Takahashi, H. E.; et al. Fibroblasts expressing Sonic hedgehog induce osteoblast differentiation and ectopic bone formation. *FEBS Lett* **1997**, *404* (2-3), 319-323. DOI: 10.1016/s0014-5793(97)00014-8.

(134) Nakamura, T.; Aikawa, T.; Iwamoto-Enomoto, M.; Iwamoto, M.; Higuchi, Y.; Maurizio, P.; Kinto, N.; Yamaguchi, A.; Noji, S.; Kurisu, K.; et al. Induction of Osteogenic Differentiation by Hedgehog Proteins. *Biochemical and Biophysical Research Communications* **1997**, *237* (2), 465-469. DOI: <https://doi.org/10.1006/bbrc.1997.7156>.

(135) Spinella-Jaegle, S.; Rawadi, G.; Kawai, S.; Gallea, S.; Faucheu, C.; Mollat, P.; Courtois, B.; Bergaud, B.; Ramez, V.; Blanchet, A. M.; et al. Sonic hedgehog increases the commitment of pluripotent mesenchymal cells into the osteoblastic lineage and abolishes adipocytic differentiation. *J Cell Sci* **2001**, *114* (Pt 11), 2085-2094. DOI: 10.1242/jcs.114.11.2085.

(136) Ingram, W. J.; Wicking, C. A.; Grimmond, S. M.; Forrest, A. R.; Wainwright, B. J. Novel genes regulated by Sonic Hedgehog in pluripotent mesenchymal cells. *Oncogene* **2002**, *21* (53), 8196-8205. DOI: 10.1038/sj.onc.1205975.

(137) Oro, A. E.; Higgins, K. M.; Hu, Z.; Bonifas, J. M.; Epstein, E. H.; Scott, M. P. Basal Cell Carcinomas in Mice Overexpressing Sonic Hedgehog. *Science* **1997**, *276* (5313), 817-821. DOI: doi:10.1126/science.276.5313.817.

(138) Xie, J.; Murone, M.; Luoh, S.-M.; Ryan, A.; Gu, Q.; Zhang, C.; Bonifas, J. M.; Lam, C.-W.; Hynes, M.; Goddard, A.; et al. Activating Smoothed mutations in sporadic basal-cell carcinoma. *Nature* **1998**, *391* (6662), 90-92. DOI: 10.1038/34201.

(139) Aszterbaum, M.; Epstein, J.; Oro, A.; Douglas, V.; LeBoit, P. E.; Scott, M. P.; Epstein, E. H. Ultraviolet and ionizing radiation enhance the growth of BCCs and trichoblastomas in patched heterozygous knockout mice. *Nature Medicine* **1999**, *5* (11), 1285-1291. DOI: 10.1038/15242.

(140) Nitzki, F.; Becker, M.; Frommhold, A.; Schulz-Schaeffer, W.; Hahn, H. Patched knockout mouse models of Basal cell carcinoma. *Journal of skin cancer* **2012**, *2012*, 907543-907543. DOI: 10.1155/2012/907543.

(141) Goodrich Lisa, V.; Milenković, L.; Higgins Kay, M.; Scott Matthew, P. Altered Neural Cell Fates and Medulloblastoma in Mouse patched Mutants. *Science* **1997**, *277* (5329), 1109-1113. DOI: 10.1126/science.277.5329.1109.

(142) Hahn, H.; Wojnowski, L.; Zimmer, A. M.; Hall, J.; Miller, G.; Zimmer, A. Rhabdomyosarcomas and radiation hypersensitivity in a mouse model of Gorlin syndrome. *Nature Medicine* **1998**, *4* (5), 619-622. DOI: 10.1038/nm0598-619.

(143) Collins, A. T.; Lang, S. H. A systematic review of the validity of patient derived xenograft (PDX) models: the implications for translational research and personalised medicine. *PeerJ* **2018**, *6*, e5981-e5981. DOI: 10.7717/peerj.5981.

(144) Pawlowski, A.; Haberman, H. F. Heterotransplantation of human basal cell carcinomas in "nude" mice. *Journal of Investigative Dermatology* **1979**, *72* (6).

(145) Grimwood, R. E.; Johnson, C. A.; Ferris, C. F.; Mercill, D. B.; Mellette, J. R.; Huff, J. C. Transplantation of human basal cell carcinomas to athymic mice. *Cancer* **1985**, *56* (3), 519-523.

(146) Grimwood, R. E.; Tharp, M. D. Growth of Human Basal Cell Carcinomas Transplanted to C57/Balb/C bgJ/bgJ-nu/nu (Beige-Nude) Mice. *The Journal of dermatologic surgery and oncology* **1991**, *17* (8), 661-666.

- (147) Carlson, J. A.; Combates, N. J.; Stenn, K. S.; Prouty, S. M. Anaplastic neoplasms arising from basal cell carcinoma xenotransplants into SCID-beige mice. *Journal of cutaneous pathology* **2002**, *29* (5), 268-278.
- (148) Wang, G. Y.; So, P.-L.; Wang, L.; Libove, E.; Wang, J.; Epstein, E. H. Establishment of Murine Basal Cell Carcinoma Allografts: A Potential Model for Preclinical Drug Testing and for Molecular Analysis. *Journal of Investigative Dermatology* **2011**, *131* (11), 2298-2305. DOI: <https://doi.org/10.1038/jid.2011.204>.
- (149) Jiang, -. L.-P.; Shen, -. Q.-S.; Yang, -. C.-P.; Chen, -. Y.-B. - Establishment of basal cell carcinoma animal model in Chinese tree shrew (Tupaia belangeri chinensis). - *Zoological Research* **2017**, - 38 (- 4), - 180. DOI: - 10.24272/j.issn.2095-8137.2017.045.
- (150) Zhang, -. J.; Luo, -. R.-C.; Man, -. X.-Y.; Lv, -. L.-B.; Yao, -. Y.-G.; Zheng, -. M. - The anatomy of the skin of the Chinese tree shrew is very similar to that of human skin. - *Zoological Research* **2020**, - 41 (- 2), - 208. DOI: - 10.24272/j.issn.2095-8137.2020.028.

Chapter 2 References

- (1) Fujii, K.; Miyashita, T. Gorlin syndrome (nevroid basal cell carcinoma syndrome): Update and literature review. *Pediatrics International* **2014**, *56* (5), 667-674. DOI: 10.1111/ped.12461.
- (2) Sahebjam, S.; Siu, L. L.; Razak, A. A. The Utility of Hedgehog Signaling Pathway Inhibition for Cancer. *The Oncologist* **2012**, *17* (8), 1090-1099. DOI: 10.1634/theoncologist.2011-0450.
- (3) Dika, E.; Scarfi, F.; Ferracin, M.; Broseghini, E.; Marcelli, E.; Bortolani, B.; Campione, E.; Riefolo, M.; Ricci, C.; Lambertini, M. Basal Cell Carcinoma: A Comprehensive Review. *Int J Mol Sci* **2020**, *21* (15), 5572. DOI: 10.3390/ijms21155572.
- (4) Zhang, Y.; Bulkley, D. P.; Xin, Y.; Roberts, K. J.; Asarnow, D. E.; Sharma, A.; Myers, B. R.; Cho, W.; Cheng, Y.; Beachy, P. A. Structural Basis for Cholesterol Transport-like Activity of the Hedgehog Receptor Patched. *Cell* **2018**, *175* (5), 1352-1364.e1314. DOI: 10.1016/j.cell.2018.10.026.
- (5) Biehs, B.; Dijkgraaf, G. J. P.; Piskol, R.; Alicke, B.; Boumahdi, S.; Peale, F.; Gould, S. E.; de Sauvage, F. J. A cell identity switch allows residual BCC to survive Hedgehog pathway inhibition. *Nature* **2018**, *562* (7727), 429-433. DOI: 10.1038/s41586-018-0596-y.
- (6) Atwood, S. X.; Sarin, K. Y.; Whitson, R. J.; Li, J. R.; Kim, G.; Rezaee, M.; Ally, M. S.; Kim, J.; Yao, C.; Chang, A. L. S.; et al. Smoothened variants explain the majority of drug resistance in basal cell carcinoma. *Cancer cell* **2015**, *27* (3), 342-353. DOI: 10.1016/j.ccell.2015.02.002.
- (7) Atwood, S. X.; Chang, A. L. S.; Oro, A. E. Hedgehog pathway inhibition and the race against tumor evolution. *The Journal of Cell Biology* **2012**, *199* (2), 193-197. DOI: 10.1083/jcb.201207140.
- (8) Yao, C. D.; Haensel, D.; Gaddam, S.; Patel, T.; Atwood, S. X.; Sarin, K. Y.; Whitson, R. J.; McKellar, S.; Shankar, G.; Aasi, S.; et al. AP-1 and TGF β cooperativity drives non-canonical Hedgehog signaling in resistant basal cell carcinoma. *Nature Communications* **2020**, *11* (1), 5079. DOI: 10.1038/s41467-020-18762-5.
- (9) Takeuchi, T.; Böttcher, A.; Quezada, C. M.; Meade, T. J.; Gray, H. B. Inhibition of thermolysin and human α -thrombin by cobalt(III) Schiff base complexes. *Bioorganic & Medicinal Chemistry* **1999**, *7* (5), 815-819. DOI: [https://doi.org/10.1016/S0968-0896\(98\)00272-7](https://doi.org/10.1016/S0968-0896(98)00272-7).

- (10) Jumper, J.; Evans, R.; Pritzel, A.; Green, T.; Figurnov, M.; Ronneberger, O.; Tunyasuvunakool, K.; Bates, R.; Žídek, A.; Potapenko, A.; et al. Highly accurate protein structure prediction with AlphaFold. *Nature* **2021**, *596* (7873), 583-589. DOI: 10.1038/s41586-021-03819-2.
- (11) Varadi, M.; Anyango, S.; Deshpande, M.; Nair, S.; Natassia, C.; Yordanova, G.; Yuan, D.; Stroe, O.; Wood, G.; Laydon, A.; et al. AlphaFold Protein Structure Database: massively expanding the structural coverage of protein-sequence space with high-accuracy models. *Nucleic Acids Research* **2022**, *50* (D1), D439-D444. DOI: 10.1093/nar/gkab1061.
- (12) Pavletich Nikola, P.; Pabo Carl, O. Crystal Structure of a Five-Finger GLI-DNA Complex: New Perspectives on Zinc Fingers. *Science* **1993**, *261* (5129), 1701-1707. DOI: 10.1126/science.8378770.
- (13) Laity, J. H.; Lee, B. M.; Wright, P. E. Zinc finger proteins: new insights into structural and functional diversity. *Current Opinion in Structural Biology* **2001**, *11* (1), 39-46. DOI: [https://doi.org/10.1016/S0959-440X\(00\)00167-6](https://doi.org/10.1016/S0959-440X(00)00167-6).
- (14) Infante, P.; Mori, M.; Alfonsi, R.; Ghirga, F.; Aiello, F.; Toscano, S.; Ingallina, C.; Siler, M.; Cucchi, D.; Po, A.; et al. Gli1/DNA interaction is a druggable target for Hedgehog-dependent tumors. *The EMBO Journal* **2015**, *34* (2), 200-217. DOI: <https://doi.org/10.15252/embj.201489213>.
- (15) Agyeman, A.; Jha, B. K.; Mazumdar, T.; Houghton, J. A. Mode and specificity of binding of the small molecule GANT61 to GLI determines inhibition of GLI-DNA binding. *Oncotarget* **2014**, *5* (12), 4492-4503. DOI: 10.18632/oncotarget.2046.
- (16) Zhang, R.; Wu, J.; Ferrandon, S.; Glowacki, K. J.; Houghton, J. A. Targeting GLI by GANT61 involves mechanisms dependent on inhibition of both transcription and DNA licensing. *Oncotarget* **2016**, *7* (49), 80190-80207. DOI: 10.18632/oncotarget.13376.
- (17) Wang, J.; Gu, S.; Huang, J.; Chen, S.; Zhang, Z.; Xu, M. Inhibition of autophagy potentiates the efficacy of Gli inhibitor GANT-61 in MYCN-amplified neuroblastoma cells. *BMC Cancer* **2014**, *14*, 768-768. DOI: 10.1186/1471-2407-14-768.
- (18) Agyeman, A.; Jha, B. K.; Mazumdar, T.; Houghton, J. A. Mode and specificity of binding of the small molecule GANT61 to GLI determines inhibition of GLI-DNA binding. *Oncotarget* **2014**, *5* (12), 4492-4503. DOI: 10.18632/oncotarget.2046.

(19) Gottesfeld, J. M.; Neely, L.; Trauger, J. W.; Baird, E. E.; Dervan, P. B. Regulation of gene expression by small molecules. *Nature* **1997**, *387*, 202. DOI: 10.1038/387202a0.

(20) Lauth, M.; Bergström, Å.; Shimokawa, T.; Toftgård, R. Inhibition of GLI-mediated transcription and tumor cell growth by small-molecule antagonists. *Proceedings of the National Academy of Sciences of the United States of America* **2007**, *104* (20), 8455-8460. DOI: 10.1073/pnas.0609699104.

(21) Kim, J.; Lee, J. J.; Kim, J.; Gardner, D.; Beachy, P. A. Arsenic antagonizes the Hedgehog pathway by preventing ciliary accumulation and reducing stability of the Gli2 transcriptional effector. *Proceedings of the National Academy of Sciences* **2010**, *107* (30), 13432, 10.1073/pnas.1006822107.

(22) Beauchamp, E. M.; Üren, A. Chapter fifteen - A New Era for an Ancient Drug: Arsenic Trioxide and Hedgehog Signaling. In *Vitamins & Hormones*, Litwack, G. Ed.; Vol. 88; Academic Press, 2012; pp 333-354.

(23) Harney, A. S.; Lee, J.; Manus, L. M.; Wang, P.; Ballweg, D. M.; LaBonne, C.; Meade, T. J. Targeted inhibition of Snail family zinc finger transcription factors by oligonucleotide-Co(III) Schiff base conjugate. *Proceedings of the National Academy of Sciences* **2009**, *106* (33), 13667, 10.1073/pnas.0906423106.

(24) Harney, A. S.; Meade, T. J.; LaBonne, C. Targeted Inactivation of Snail Family EMT Regulatory Factors by a Co(III)-Ebox Conjugate. *Plos One* **2012**, *7* (2), e32318. DOI: 10.1371/JOURNAL.PONE.0032318.

(25) Hurtado, R. R.; Harney, A. S.; Heffern, M. C.; Holbrook, R. J.; Holmgren, R. A.; Meade, T. J. Specific Inhibition of the Transcription Factor Ci by a Cobalt(III) Schiff Base–DNA Conjugate. *Molecular Pharmaceutics* **2012**, *9* (2), 325-333. DOI: 10.1021/mp2005577.

(26) Harney, A. S.; Sole, L. B.; Meade, T. J. Kinetics and thermodynamics of irreversible inhibition of matrix metalloproteinase 2 by a Co(III) Schiff base complex. *Journal of biological inorganic chemistry : JBIC : a publication of the Society of Biological Inorganic Chemistry* **2012**, *17* (6), 853-860. DOI: 10.1007/s00775-012-0902-3.

(27) Heffern, M. C.; Kurutz, J. W.; Meade, T. J. Spectroscopic elucidation of the inhibitory mechanism of Cys2His2 zinc finger transcription factors by cobalt(III) Schiff base complexes. *Chemistry (Weinheim an der Bergstrasse, Germany)* **2013**, *19* (50), 17043-17053. DOI: 10.1002/chem.201301659.

- (28) Brue, C. R.; Dukes, M. W.; Masotti, M.; Holmgren, R.; Meade, T. J. Functional Disruption of Gli1-DNA Recognition via a Cobalt(III) Complex. *ChemMedChem* **2022**, *n/a* (n/a), e202200025, <https://doi.org/10.1002/cmdc.202200025>. DOI: <https://doi.org/10.1002/cmdc.202200025> (accessed 2022/04/16).
- (29) Slusarski, D. C.; Motzny, C. K.; Holmgren, R. Mutations that alter the timing and pattern of cubitus interruptus gene expression in *Drosophila melanogaster*. *Genetics* **1995**, *139* (1), 229-240. DOI: 10.1093/genetics/139.1.229.
- (30) Alexandre, C.; Lecourtois, M.; Vincent, J. Wingless and Hedgehog pattern *Drosophila* denticle belts by regulating the production of short-range signals. *Development* **1999**, *126* (24), 5689-5698. DOI: 10.1242/dev.126.24.5689.
- (31) Chong, Z. X.; Yeap, S. K.; Ho, W. Y. Transfection types, methods and strategies: a technical review. *PeerJ* **2021**, *9*, e11165-e11165. DOI: 10.7717/peerj.11165.
- (32) Kim, T. K.; Eberwine, J. H. Mammalian cell transfection: the present and the future. *Analytical and Bioanalytical Chemistry* **2010**, *397* (8), 3173-3178. DOI: 10.1007/s00216-010-3821-6.
- (33) Mali, S. Delivery systems for gene therapy. *Indian J Hum Genet* **2013**, *19* (1), 3-8. DOI: 10.4103/0971-6866.112870.
- (34) Al-Dosari, M. S.; Gao, X. Nonviral gene delivery: principle, limitations, and recent progress. *AAPS J* **2009**, *11* (4), 671-681. DOI: 10.1208/s12248-009-9143-y.
- (35) Geim, A. K.; Novoselov, K. S. The rise of graphene. *Nature Materials* **2007**, *6*, 183. DOI: 10.1038/nmat1849.
- (36) Castro Neto, A. H.; Guinea, F.; Peres, N. M. R.; Novoselov, K. S.; Geim, A. K. The electronic properties of graphene. *Reviews of Modern Physics* **2009**, *81* (1), 109-162. DOI: 10.1103/RevModPhys.81.109.
- (37) Priyadarsini, S.; Mohanty, S.; Mukherjee, S.; Basu, S.; Mishra, M. Graphene and graphene oxide as nanomaterials for medicine and biology application. *Journal of Nanostructure in Chemistry* **2018**, *8* (2), 123-137. DOI: 10.1007/s40097-018-0265-6.

(38) Hung, A. H.; Duch, M. C.; Parigi, G.; Rotz, M. W.; Manus, L. M.; Mastarone, D. J.; Dam, K. T.; Gits, C. C.; MacRenaris, K. W.; Luchinat, C.; et al. Mechanisms of Gadographene-Mediated Proton Spin Relaxation. *The Journal of Physical Chemistry C* **2013**, *117* (31), 16263-16273. DOI: 10.1021/jp406909b.

(39) Hung, A. H.; Holbrook, R. J.; Rotz, M. W.; Glasscock, C. J.; Mansukhani, N. D.; MacRenaris, K. W.; Manus, L. M.; Duch, M. C.; Dam, K. T.; Hersam, M. C.; et al. Graphene Oxide Enhances Cellular Delivery of Hydrophilic Small Molecules by Co-incubation. *ACS Nano* **2014**, *8* (10), 10168-10177. DOI: 10.1021/nn502986e.

(40) Sadeghi, Z.; Maleki, P.; Mohammadi Bondarkhilli, S. A.; Mohammadi, M.; Raheb, J. Dataset on cytotoxicity effect of polyethylenimine-functionalized graphene oxide nanoparticles on the human embryonic carcinoma stem cell, NTERA2 cell line. *Data Brief* **2019**, *26*, 104487-104487. DOI: 10.1016/j.dib.2019.104487.

(41) Chen, B.; Liu, M.; Zhang, L.; Huang, J.; Yao, J.; Zhang, Z. Polyethylenimine-functionalized graphene oxide as an efficient gene delivery vector. *Journal of Materials Chemistry* **2011**, *21* (21), 7736-7741, 10.1039/C1JM10341E. DOI: 10.1039/C1JM10341E.

(42) Zhang, L.; Xia, J.; Zhao, Q.; Liu, L.; Zhang, Z. Functional Graphene Oxide as a Nanocarrier for Controlled Loading and Targeted Delivery of Mixed Anticancer Drugs. *Small* **2010**, *6* (4), 537-544. DOI: 10.1002/sml.200901680.

(43) Liu, B.; Salgado, S.; Maheshwari, V.; Liu, J. DNA adsorbed on graphene and graphene oxide: Fundamental interactions, desorption and applications. *Current Opinion in Colloid & Interface Science* **2016**, *26*, 41-49. DOI: <https://doi.org/10.1016/j.cocis.2016.09.001>.

(44) Wu, X.; Xing, Y.; Zeng, K.; Huber, K.; Zhao, J. X. Study of Fluorescence Quenching Ability of Graphene Oxide with a Layer of Rigid and Tunable Silica Spacer. *Langmuir* **2018**, *34* (2), 603-611. DOI: 10.1021/acs.langmuir.7b03465.

(45) Wu, M.; Kempaiah, R.; Huang, P.-J. J.; Maheshwari, V.; Liu, J. Adsorption and Desorption of DNA on Graphene Oxide Studied by Fluorescently Labeled Oligonucleotides. *Langmuir* **2011**, *27* (6), 2731-2738. DOI: 10.1021/la1037926.

(46) Liu, H.; Zhou, Y.; Yang, Y.; Zou, K.; Wu, R.; Xia, K.; Xie, S. Synthesis of polyethylenimine/graphene oxide for the adsorption of U(VI) from aqueous solution. *Applied Surface Science* **2019**, *471*, 88-95. DOI: <https://doi.org/10.1016/j.apsusc.2018.11.231>.

(47) Qiao, Y.; Zheng, X. Investigation of the fluorescence quenching behavior of PEI-doped silica nanoparticles and its applications. *RSC Advances* **2016**, *6* (99), 97187-97193, 10.1039/C6RA21543B. DOI: 10.1039/C6RA21543B.

(48) Rathore, B.; Sunwoo, K.; Jangili, P.; Kim, J.; Kim, J. H.; Huang, M.; Xiong, J.; Sharma, A.; Yang, Z.; Qu, J.; et al. Nanomaterial designing strategies related to cell lysosome and their biomedical applications: A review. *Biomaterials* **2019**, *211*, 25-47. DOI: <https://doi.org/10.1016/j.biomaterials.2019.05.002>.

(49) Sigafos, A. N.; Paradise, B. D.; Fernandez-Zapico, M. E. Hedgehog/GLI Signaling Pathway: Transduction, Regulation, and Implications for Disease. *Cancers (Basel)* **2021**, *13* (14), 3410. DOI: 10.3390/cancers13143410.

(50) Didiasova, M.; Schaefer, L.; Wygrecka, M. Targeting GLI Transcription Factors in Cancer. *Molecules* **2018**, *23* (5), 1003. DOI: 10.3390/molecules23051003.

(51) Liang, C.-C.; Park, A. Y.; Guan, J.-L. In vitro scratch assay: a convenient and inexpensive method for analysis of cell migration in vitro. *Nature Protocols* **2007**, *2* (2), 329-333. DOI: 10.1038/nprot.2007.30.

Chapter 3 References

- (1) Bøgelund, F. S.; Philipsen, P. A.; Gniadecki, R. Factors affecting the recurrence rate of basal cell carcinoma. *Acta Derm Venereol* **2007**, *87* (4), 330-334. DOI: 10.2340/00015555-0236.
- (2) Bartos, V. Development of Multiple-Lesion Basal Cell Carcinoma of the Skin: A Comprehensive Review. *Sisli Etfal Hastan Tip Bul* **2019**, *53* (4), 323-328. DOI: 10.14744/semb.2019.08058.
- (3) Bartos, V.; Kullová, M. Basal Cell Carcinoma Multiplicity - a Retrospective Analysis of 899 Biopsy-proven Patients from a Single Institute. *Klin Onkol* **2017**, *30* (3), 197-201. DOI: 10.14735/amko2017197.
- (4) Adachi, K.; Yoshida, Y.; Noma, H.; Goto, H.; Yamamoto, O. Characteristics of multiple basal cell carcinomas: The first study on Japanese patients. *J Dermatol* **2018**, *45* (10), 1187-1190. DOI: 10.1111/1346-8138.14576.
- (5) Richmond-Sinclair, N. M.; Pandeya, N.; Ware, R. S.; Neale, R. E.; Williams, G. M.; van der Pols, J. C.; Green, A. C. Incidence of basal cell carcinoma multiplicity and detailed anatomic distribution: longitudinal study of an Australian population. *J Invest Dermatol* **2009**, *129* (2), 323-328. DOI: 10.1038/jid.2008.234.
- (6) Raasch, B. A.; Buettner, P. G. Multiple nonmelanoma skin cancer in an exposed Australian population. *Int J Dermatol* **2002**, *41* (10), 652-658. DOI: 10.1046/j.1365-4362.2002.01573.x .
- (7) Mantese, S. A. O.; Berbert, A. L. C. V.; Gomides, M. D. A.; Rocha, A. Basal cell Carcinoma-Analysis of 300 cases observed in Uberlândia-MG, Brazil. *Anais Brasileiros de Dermatologia* **2006**, *81* (2), 136-142.
- (8) Stang, A.; Ziegler, S.; Büchner, U.; Ziegler, B.; Jöckel, K. H.; Ziegler, V. Malignant melanoma and nonmelanoma skin cancers in Northrhine-Westphalia, Germany: a patient- vs. diagnosis-based incidence approach. *Int J Dermatol* **2007**, *46* (6), 564-570. DOI: 10.1111/j.1365-4632.2006.03056.x.
- (9) Flohil, S. C.; Koljenović, S.; de Haas, E. R.; Overbeek, L. I.; de Vries, E.; Nijsten, T. Cumulative risks and rates of subsequent basal cell carcinomas in the Netherlands. *Br J Dermatol* **2011**, *165* (4), 874-881. DOI: 10.1111/j.1365-2133.2011.10488.x.

- (10) Verkouteren, J. A. C.; Smedinga, H.; Steyerberg, E. W.; Hofman, A.; Nijsten, T. Predicting the Risk of a Second Basal Cell Carcinoma. *J Invest Dermatol* **2015**, *135* (11), 2649-2656. DOI: 10.1038/jid.2015.244.
- (11) Pellegrini, C.; Maturo, M. G.; Di Nardo, L.; Ciciarelli, V.; Gutiérrez García-Rodrigo, C.; Fargnoli, M. C. Understanding the Molecular Genetics of Basal Cell Carcinoma. *Int J Mol Sci* **2017**, *18* (11), 2485. DOI: 10.3390/ijms18112485.
- (12) Jacobsen, A. A.; Aldahan, A. S.; Hughes, O. B.; Shah, V. V.; Strasswimmer, J. Hedgehog Pathway Inhibitor Therapy for Locally Advanced and Metastatic Basal Cell Carcinoma: A Systematic Review and Pooled Analysis of Interventional Studies. *JAMA Dermatol* **2016**, *152* (7), 816-824. DOI: 10.1001/jamadermatol.2016.0780.
- (13) Mancuso, M.; Pazzaglia, S.; Tanori, M.; Hahn, H.; Merola, P.; Rebessi, S.; Atkinson, M. J.; Di Majo, V.; Covelli, V.; Saran, A. Basal Cell Carcinoma and Its Development: Insights from Radiation-Induced Tumors in Ptch1-Deficient Mice. *Cancer Research* **2004**, *64* (3), 934-941. DOI: 10.1158/0008-5472.CAN-03-2460.
- (14) Mercurio, L.; Albanesi, C.; Madonna, S. Recent Updates on the Involvement of PI3K/AKT/mTOR Molecular Cascade in the Pathogenesis of Hyperproliferative Skin Disorders. *Front Med (Lausanne)* **2021**, *8*, 665647-665647. DOI: 10.3389/fmed.2021.665647.
- (15) Bonilla, X.; Parmentier, L.; King, B.; Bezrukov, F.; Kaya, G.; Zoete, V.; Seplyarskiy, V. B.; Sharpe, H. J.; McKee, T.; Letourneau, A.; et al. Genomic analysis identifies new drivers and progression pathways in skin basal cell carcinoma. *Nat Genet* **2016**, *48* (4), 398-406. DOI: 10.1038/ng.3525.
- (16) Ingram, W. J.; Wicking, C. A.; Grimmond, S. M.; Forrest, A. R.; Wainwright, B. J. Novel genes regulated by Sonic Hedgehog in pluripotent mesenchymal cells. *Oncogene* **2002**, *21* (53), 8196-8205. DOI: 10.1038/sj.onc.1205975.
- (17) Chen, J. K.; Taipale, J.; Cooper, M. K.; Beachy, P. A. Inhibition of Hedgehog signaling by direct binding of cyclopamine to Smoothened. *Genes Dev* **2002**, *16* (21), 2743-2748. DOI: 10.1101/gad.1025302.
- (18) Maity, T.; Fuse, N.; Beachy Philip, A. Molecular mechanisms of Sonic hedgehog mutant effects in holoprosencephaly. *Proceedings of the National Academy of Sciences* **2005**, *102* (47), 17026-17031. DOI: 10.1073/pnas.0507848102.

(19) Ingram, W. J.; McCue, K. I.; Tran, T. H.; Hallahan, A. R.; Wainwright, B. J. Sonic Hedgehog regulates Hes1 through a novel mechanism that is independent of canonical Notch pathway signalling. *Oncogene* **2008**, *27* (10), 1489-1500. DOI: 10.1038/sj.onc.1210767.

(20) Nakamura, T.; Aikawa, T.; Iwamoto-Enomoto, M.; Iwamoto, M.; Higuchi, Y.; Pacifici, M.; Kinto, N.; Yamaguchi, A.; Noji, S.; Kurisu, K.; et al. Induction of osteogenic differentiation by hedgehog proteins. *Biochem Biophys Res Commun* **1997**, *237* (2), 465-469. DOI: 10.1006/bbrc.1997.7156.

(21) Ingram, W. J.; Wicking, C. A.; Grimmond, S. M.; Forrest, A. R.; Wainwright, B. J. Novel genes regulated by Sonic Hedgehog in pluripotent mesenchymal cells. *Oncogene* **2002**, *21* (53), 8196-8205. DOI: 10.1038/sj.onc.1205975.

(22) Buczkowicz, P.; Ma, J.; Hawkins, C. GLI2 Is a Potential Therapeutic Target in Pediatric Medulloblastoma. *Journal of Neuropathology & Experimental Neurology* **2011**, *70* (6), 430-437. DOI: 10.1097/NEN.0b013e31821b94db.

(23) Roussel, M. F.; Hatten, M. E. Cerebellum: Development and Medulloblastoma. *Current topics in developmental biology* **2011**, *94*, 235-282. DOI: 10.1016/B978-0-12-380916-2.00008-5.

(24) Kim, D. P.; Kus, K. J. B.; Ruiz, E. Basal Cell Carcinoma Review. *Hematol Oncol Clin North Am* **2019**, *33* (1), 13-24. DOI: 10.1016/j.hoc.2018.09.004.

(25) Feehan, R. P.; Shantz, L. M. Molecular signaling cascades involved in nonmelanoma skin carcinogenesis. *Biochemical Journal* **2016**, *473* (19), 2973-2994. DOI: 10.1042/BCJ20160471.

(26) Li, Z.-R.; Jiang, Y.; Hu, J.-Z.; Chen, Y.; Liu, Q.-Z. SOX2 knockdown inhibits the migration and invasion of basal cell carcinoma cells by targeting the SRPK1-mediated PI3K/AKT signaling pathway. *Oncol Lett* **2019**, *17* (2), 1617-1625. DOI: 10.3892/ol.2018.9810.

(27) Olesen, U. H.; Bojesen, S.; Gehl, J.; Haedersdal, M. Anticancer drugs and the regulation of Hedgehog genes GLI1 and PTCH1, a comparative study in nonmelanoma skin cancer cell lines. *Anticancer Drugs* **2017**, *28* (10), 1106-1117. DOI: 10.1097/cad.0000000000000551.

Chapter 4 References

- (1) Gailani, M. R.; Bale, S. J.; Leffell, D. J.; DiGiovanna, J. J.; Peck, G. L.; Poliak, S.; Drum, M. A.; Pastakia, B.; McBride, O. W.; Kase, R.; et al. Developmental defects in Gorlin syndrome related to a putative tumor suppressor gene on chromosome 9. *Cell* **1992**, *69* (1), 111-117. DOI: 10.1016/0092-8674(92)90122-s.
- (2) Hahn, H.; Wicking, C.; Zaphiropoulos, P. G.; Gailani, M. R.; Shanley, S.; Chidambaram, A.; Vorechovsky, I.; Holmberg, E.; Uden, A. B.; Gillies, S.; et al. Mutations of the human homolog of *Drosophila* patched in the nevoid basal cell carcinoma syndrome. *Cell* **1996**, *85* (6), 841-851. DOI: 10.1016/s0092-8674(00)81268-4.
- (3) Johnson, R. L.; Rothman, A. L.; Xie, J.; Goodrich, L. V.; Bare, J. W.; Bonifas, J. M.; Quinn, A. G.; Myers, R. M.; Cox, D. R.; Epstein, E. H., Jr.; et al. Human homolog of patched, a candidate gene for the basal cell nevus syndrome. *Science* **1996**, *272* (5268), 1668-1671. DOI: 10.1126/science.272.5268.1668.
- (4) Klein, R. D.; Dykas, D. J.; Bale, A. E. Clinical testing for the nevoid basal cell carcinoma syndrome in a DNA diagnostic laboratory. *Genet Med* **2005**, *7* (9), 611-619. DOI: 10.1097/01.gim.0000182879.57182.b4.
- (5) Epstein, E. H. Basal cell carcinomas: attack of the hedgehog. *Nat Rev Cancer* **2008**, *8* (10), 743-754. DOI: 10.1038/nrc2503.
- (6) Frampton, J. E.; Basset-Séguin, N. Vismodegib: A Review in Advanced Basal Cell Carcinoma. *Drugs* **2018**, *78* (11), 1145-1156. DOI: 10.1007/s40265-018-0948-9.
- (7) Jain, S.; Song, R.; Xie, J. Sonidegib: mechanism of action, pharmacology, and clinical utility for advanced basal cell carcinomas. *Onco Targets Ther* **2017**, *10*, 1645-1653. DOI: 10.2147/ott.S130910.
- (8) Justus, C. R.; Leffler, N.; Ruiz-Echevarria, M.; Yang, L. V. In vitro cell migration and invasion assays. *J Vis Exp* **2014**, (88), 51046. DOI: 10.3791/51046.
- (9) Kramer, N.; Walzl, A.; Unger, C.; Rosner, M.; Krupitza, G.; Hengstschläger, M.; Dolznig, H. In vitro cell migration and invasion assays. *Mutation Research/Reviews in Mutation Research* **2013**, *752* (1), 10-24.
- (10) Li, Z.-R.; Jiang, Y.; Hu, J.-Z.; Chen, Y.; Liu, Q.-Z. SOX2 knockdown inhibits the migration and invasion of basal cell carcinoma cells by targeting the SRPK1-mediated PI3K/AKT signaling pathway. *Oncol Lett* **2019**, *17* (2), 1617-1625. DOI: 10.3892/ol.2018.9810.
- (11) Hu, P.; Ma, L.; Wu, Z. Q.; Zheng, G. Y.; Li, J. T. Effect of endostatin on proliferation, invasion and epithelial-mesenchymal transition of basal cell carcinoma cell A431. *Eur Rev Med Pharmacol Sci* **2019**, *23* (2), 877-884. DOI: 10.26355/eurrev_201901_16902.

- (12) Quan, Z.; Zhang, B.-B.; Yin, F.; Du, J.; Zhi, Y.-T.; Xu, J.; Song, N. DDX5 Silencing Suppresses the Migration of Basal cell Carcinoma Cells by Downregulating JAK2/STAT3 Pathway. *Technol Cancer Res Treat* **2019**, *18*, 1533033819892258-1533033819892258. DOI: 10.1177/1533033819892258.
- (13) Yang, Y.; Liang, Y. H.; Zheng, Y.; Tang, L. J.; Zhou, S. T.; Zhu, J. N. SHARPIN regulates cell proliferation of cutaneous basal cell carcinoma via inactivation of the transcriptional factors GLI2 and c-JUN. *Mol Med Rep* **2020**, *21* (4), 1799-1808. DOI: 10.3892/mmr.2020.10981.
- (14) Dukes, M. W.; Bajema, E. A.; Whittemore, T. J.; Holmgren, R. A.; Meade, T. J. Delivery of Targeted Co(III)–DNA Inhibitors of Gli Proteins to Disrupt Hedgehog Signaling. *Bioconjugate Chemistry* **2022**. DOI: 10.1021/acs.bioconjchem.2c00063.
- (15) Gunti, S.; Hoke, A. T. K.; Vu, K. P.; London, N. R., Jr. Organoid and Spheroid Tumor Models: Techniques and Applications. *Cancers* **2021**, *13* (4), 874. DOI: 10.3390/cancers13040874.
- (16) Rheinwald, J.; Green, H. Serial cultivation of strains of human epidermal keratinocytes: the formation of keratinizing colonies from single cells. *Cell* **1975**, *6*, 331-343.
- (17) Rikken, G.; Niehues, H.; van den Bogaard, E. H. Organotypic 3D Skin Models: Human Epidermal Equivalent Cultures from Primary Keratinocytes and Immortalized Keratinocyte Cell Lines. *Methods Mol Biol* **2020**, *2154*, 45-61. DOI: 10.1007/978-1-0716-0648-3_5.
- (18) Regnier, M. Growth and differentiation of adult human epidermal cells on dermal substrates. *Front matrix biol* **1981**, *9*, 4-35.
- (19) Anacker, D.; Moody, C. Generation of organotypic raft cultures from primary human keratinocytes. *J Vis Exp* **2012**, (60), 3668. DOI: 10.3791/3668.
- (20) Brauchle, E.; Johannsen, H.; Nolan, S.; Thude, S.; Schenke-Layland, K. Design and analysis of a squamous cell carcinoma in vitro model system. *Biomaterials* **2013**, *34* (30), 7401-7407.
- (21) Temblador, A.; Topalis, D.; van den Oord, J.; Andrei, G.; Snoeck, R. Organotypic Epithelial Raft Cultures as a Three-Dimensional In Vitro Model of Merkel Cell Carcinoma. *Cancers* **2022**, *14* (4), 1091. DOI: 10.3390/cancers14041091.
- (22) Beck, B.; Lehen'kyi, V.; Roudbaraki, M.; Flourakis, M.; Charveron, M.; Bordat, P.; Polakowska, R.; Prevarskaya, N.; Skryma, R. TRPC channels determine human keratinocyte differentiation: new insight into basal cell carcinoma. *Cell Calcium* **2008**, *43* (5), 492-505. DOI: 10.1016/j.ceca.2007.08.005.
- (23) Frommherz, L.; Küsel, J.; Zimmer, A.; Fischer, J.; Has, C. Skin fragility caused by biallelic KRT10 mutations: an intriguing form of self-improving epidermolytic ichthyosis. *Br J Dermatol* **2020**, *182* (3), 780-785. DOI: 10.1111/bjd.18325.

- (24) Roth, W.; Kumar, V.; Beer, H.-D.; Richter, M.; Wohlenberg, C.; Reuter, U.; Thiering, S.; Staratschek-Jox, A.; Hofmann, A.; Kreusch, F.; et al. Keratin 1 maintains skin integrity and participates in an inflammatory network in skin through interleukin-18. *Journal of Cell Science* **2012**, *125* (22), 5269-5279. DOI: 10.1242/jcs.116574.
- (25) Depianto, D.; Kerns, M. L.; Dlugosz, A. A.; Coulombe, P. A. Keratin 17 promotes epithelial proliferation and tumor growth by polarizing the immune response in skin. *Nat Genet* **2010**, *42* (10), 910-914. DOI: 10.1038/ng.665.
- (26) Markey, A. C.; Lane, E. B.; Macdonald, D. M.; Leigh, I. M. Keratin expression in basal cell carcinomas. *Br J Dermatol* **1992**, *126* (2), 154-160. DOI: 10.1111/j.1365-2133.1992.tb07813.x.
- (27) Chen, J.-G.; Fan, H.-Y.; Wang, T.; Lin, L.-Y.; Cai, T.-G. Silencing KRT16 inhibits keratinocyte proliferation and VEGF secretion in psoriasis via inhibition of ERK signaling pathway. *The Kaohsiung Journal of Medical Sciences* **2019**, *35* (5), 284-296.
- (28) Knöbel, M.; O'Toole, E. A.; Smith, F. J. D. Keratins and skin disease. *Cell and Tissue Research* **2015**, *360* (3), 583-589. DOI: 10.1007/s00441-014-2105-4.
- (29) Lessard, J. C.; Piña-Paz, S.; Rotty, J. D.; Hickerson, R. P.; Kaspar, R. L.; Balmain, A.; Coulombe, P. A. Keratin 16 regulates innate immunity in response to epidermal barrier breach. *Proceedings of the National Academy of Sciences of the United States of America* **2013**, *110* (48), 19537-19542. DOI: 10.1073/pnas.1309576110.
- (30) Markey, A. C.; Lane, E. B.; Macdonald, D. M.; Leigh, I. M. Keratin expression in basal cell carcinomas. *British Journal of Dermatology* **1992**, *126* (2), 154-160.
- (31) Sankar, S.; Tanner, J. M.; Bell, R.; Chaturvedi, A.; Randall, R. L.; Beckerle, M. C.; Lessnick, S. L. A novel role for keratin 17 in coordinating oncogenic transformation and cellular adhesion in Ewing sarcoma. *Mol Cell Biol* **2013**, *33* (22), 4448-4460. DOI: 10.1128/mcb.00241-13.
- (32) Mikami, Y.; Fujii, S.; Nagata, K.; Wada, H.; Hasegawa, K.; Abe, M.; Yoshimoto, R. U.; Kawano, S.; Nakamura, S.; Kiyoshima, T. GLI-mediated Keratin 17 expression promotes tumor cell growth through the anti-apoptotic function in oral squamous cell carcinomas. *Journal of Cancer Research and Clinical Oncology* **2017**, *143* (8), 1381-1393. DOI: 10.1007/s00432-017-2398-2.
- (33) Bhawan, J.; Bansal, C.; Whren, K.; Schwertschlag, U.; The, I. L. P. S. G. K16 expression in uninvolved psoriatic skin: a possible marker of pre-clinical psoriasis. *Journal of Cutaneous Pathology* **2004**, *31* (7), 471-476.
- (34) Leigh, I. M.; Navsaria, H.; Purkis, P. E.; McKay, I. A.; Bowden, P. E.; Riddle, P. N. Keratins (K16 and K17) as markers of keratinocyte hyperproliferation in psoriasis in vivo and in vitro. *Br J Dermatol* **1995**, *133* (4), 501-511. DOI: 10.1111/j.1365-2133.1995.tb02696.x.

- (35) Politiek, K.; Loman, L.; Pas, H. H.; Diercks, G. F. H.; Lemmink, H. H.; Jan, S. Z.; van den Akker, P. C.; Bolling, M. C.; Schuttelaar, M. L. A. Hyperkeratotic hand eczema: Eczema or not? *Contact Dermatitis* **2020**, *83* (3), 196-205. DOI: 10.1111/cod.13572.
- (36) Hartsock, A.; Nelson, W. J. Adherens and tight junctions: structure, function and connections to the actin cytoskeleton. *Biochim Biophys Acta* **2008**, *1778* (3), 660-669. DOI: 10.1016/j.bbamem.2007.07.012.
- (37) Cheng, X.; Koch, P. J. In vivo function of desmosomes. *The Journal of dermatology* **2004**, *31* (3), 171-187.
- (38) McMillan, J. R.; Shimizu, H. Desmosomes: structure and function in normal and diseased epidermis. *J Dermatol* **2001**, *28* (6), 291-298. DOI: 10.1111/j.1346-8138.2001.tb00136.x.
- (39) Schmidt, A.; Koch, P. J. Desmosomes: just cell adhesion or is there more? *Cell Adh Migr* **2007**, *1* (1), 28-32. DOI: 10.4161/cam.1.1.4204.
- (40) Cheng, X.; Den, Z.; Koch, P. J. Desmosomal cell adhesion in mammalian development. *European journal of cell biology* **2005**, *84* (2-3), 215-223.
- (41) Garrod, D.; Chidgey, M. Desmosome structure, composition and function. *Biochimica et Biophysica Acta (BBA) - Biomembranes* **2008**, *1778* (3), 572-587.
- (42) Pizarro, A.; Benito, N.; Navarro, P.; Palacios, J.; Cano, A.; Quintanilla, M.; Contreras, F.; Gamallo, C. E-cadherin expression in basal cell carcinoma. *British Journal of Cancer* **1994**, *69* (1), 157-162. DOI: 10.1038/bjc.1994.26.
- (43) Pogorzelska-Dyrbus, J.; Szepietowski, J. C. Adhesion Molecules in Non-melanoma Skin Cancers: A Comprehensive Review. *In Vivo* **2021**, *35* (3), 1327. DOI: 10.21873/invivo.12385.
- (44) Vanjaka-Rogošić, L.; Puizina-Ivić, N.; Mirić, L.; Rogošić, V.; Kuzmić-Prusac, I.; Babić, M. S.; Vuković, D.; Mardešić, S. Matrix metalloproteinases and E-cadherin immunoreactivity in different basal cell carcinoma histological types. *Acta Histochem* **2014**, *116* (5), 688-693. DOI: 10.1016/j.acthis.2013.12.007.
- (45) Tada, H.; Hatoko, M.; Tanaka, A.; Kuwahara, M.; Muramatsu, T. Expression of desmoglein I and plakoglobin in skin carcinomas. *Journal of Cutaneous Pathology* **2000**, *27* (1), 24-29.
- (46) Hammers, C. M.; Stanley, J. R. Desmoglein-1, differentiation, and disease. *The Journal of Clinical Investigation* **2013**, *123* (4), 1419-1422. DOI: 10.1172/JCI69071.
- (47) Pogorzelska-Dyrbus, J.; Szepietowski, J. C. Adhesion Molecules in Non-melanoma Skin Cancers: A Comprehensive Review. *In Vivo* **2021**, *35* (3), 1327-1336. DOI: 10.21873/invivo.12385.
- (48) Markey, A. C.; Tidman, M. J.; Churchill, L. J.; Aplin, J. D.; Leigh, I. M.; Purkis, P.; MacDonald, D. M. The epidermal basement membrane in basal cell carcinoma: an

immunohistochemical study. *Br J Dermatol* **1991**, *125* (1), 21-26. DOI: 10.1111/j.1365-2133.1991.tb06033.x.

(49) Getsios, S.; Simpson, C. L.; Kojima, S.; Harmon, R.; Sheu, L. J.; Dusek, R. L.; Cornwell, M.; Green, K. J. Desmoglein 1-dependent suppression of EGFR signaling promotes epidermal differentiation and morphogenesis. *J Cell Biol* **2009**, *185* (7), 1243-1258. DOI: 10.1083/jcb.200809044.

(50) Elias, P. M. Skin barrier function. *Curr Allergy Asthma Rep* **2008**, *8* (4), 299-305. DOI: 10.1007/s11882-008-0048-0.

(51) Jensen, J. M.; Proksch, E. The skin's barrier. *G Ital Dermatol Venereol* **2009**, *144* (6), 689-700.

(52) van Smeden, J.; Janssens, M.; Gooris, G. S.; Bouwstra, J. A. The important role of stratum corneum lipids for the cutaneous barrier function. *Biochimica et Biophysica Acta (BBA) - Molecular and Cell Biology of Lipids* **2014**, *1841* (3), 295-313.

(53) Elias, P. M. Epidermal lipids, barrier function, and desquamation. *Journal of Investigative Dermatology* **1983**, *80*.

(54) Kim, Y.; Lim, K.-M. Skin barrier dysfunction and filaggrin. *Archives of Pharmacal Research* **2021**, *44* (1), 36-48. DOI: 10.1007/s12272-021-01305-x.

(55) Sandilands, A.; Sutherland, C.; Irvine, A. D.; McLean, W. H. I. Filaggrin in the frontline: role in skin barrier function and disease. *Journal of Cell Science* **2009**, *122* (9), 1285-1294. DOI: 10.1242/jcs.033969.

(56) Vanderbeck, K.; Orr, C. E.; Parvinnejad, N.; Wang, T.; Bradshaw, S.; Wang, A.; Asai, Y. Filaggrin expression via immunohistochemistry in basal cell carcinoma and squamous cell carcinoma. *Journal of Cutaneous Pathology* **2021**, *48* (7), 877-883.

(57) Nawrocka, P. M.; Galka-Marciniak, P.; Urbanek-Trzeciak, M. O.; I, M. T.; Szostak, N.; Philips, A.; Susok, L.; Sand, M.; Kozlowski, P. Profile of Basal Cell Carcinoma Mutations and Copy Number Alterations - Focus on Gene-Associated Noncoding Variants. *Front Oncol* **2021**, *11*, 752579. DOI: 10.3389/fonc.2021.752579.

Appendix 1

Non-invasive Detection of Stem Cell Therapies Facilitated by Metal Ion-Based Contrast Agents

This chapter was reformatted from:

Dukes, M.W., Modo, M., Meade, T.J. Non-invasive Detection of Stem Cell Therapies Facilitated by Metal Ion-Based Contrast Agents in *Molecular Biosensors and the Role of Metal Ions (MILS-23)*. Sigel, A., Freisinger, E., Sigel, R.K.O., Eds.; Thomas J Meade, GmbH: Berlin, Germany. In final print stages.

ABSTRACT

1. INTRODUCTION

2. MAGNETIC RESONANCE IMAGING

2.1 Molecular contrast agents

2.1.1 Gd(III) agents

2.1.2 Mn(II) agents

2.1.3 ParaCEST Agents

2.2 Nanoparticle Contrast Agents

2.2.1 Gd(III) Particle Core

2.2.2 Superparamagnetic Iron Oxide Nanoparticles

2.2.3 Cobalt Alloy Nanoparticles

3. NUCLEAR MEDICINE AND COMPUTED TOMOGRAPHY IMAGING

3.1 Molecular PET/SPECT Agents

3.2 Gold Nanoparticle Enhanced CT

4. OPTICAL IMAGING

4.1 Two-Photon Molecular Agents

4.2 Quantum Dots

5. MULTI-MODAL IMAGING STRATEGIES

5.1 Molecular MRI/Optical Agents

5.2 Molecular PET/MRI

5.3 Nanoparticle Strategies

6. CONCLUDING REMARKS

Abstract: Stem cell therapy is a unique approach to regenerative medicine as the fundamental pathways of cell lineage can be hijacked to renew damaged tissue in the body. Such therapies have clinical interest in numerous fields and disorders such as oncology, cardiovascular disease, neurological disorders, spinal cord/bone injury, and more. However, translation of these therapies toward clinical approval necessitates the ability to accurately investigate in preclinical and clinical trials *where* cells are located following transplantation and *how* they behave. Clinically available non-invasive imaging techniques such as magnetic resonance imaging, nuclear medicine imaging, and optical imaging are the most promising methods to monitor these advanced therapeutic products. This chapter will evaluate each imaging modality for its utility in stem cell tracking, and describe metal-ion containing contrast agents that promote specific detection of stem cell populations *in vivo*. We will focus on how each modality and the associated contrast agents are designed to not interfere with the activity and function of native stem cells. We will report on the current strategies for longitudinal imaging studies that provide

1. Introduction

Stem cell therapies have garnered attention in the past few decades as safe intervention strategies for several disease conditions characterized by a loss of cells.[1, 2] Essentially, pluripotent (or multipotent cells), also known as stem cells, can differentiate and restore damaged tissues when directed to the site of an injury, disease, or malfunction.[3] Embryonic stem cells (ESCs) are desirable for stem cell therapy for their ability to differentiate into all cell lineages, but a number of ethical concerns and the logistics of sourcing embryonic tissues have hindered clinical translation.[4] However, the advent of induced pluripotent stem cells (iPS)

have provided a readily available source of human cells for clinical translation without the need to use embryonic tissue.

Herein, we focus primarily on regenerative therapies in the central nervous system for which multipotent neuronal stem cells (NSCs) provide a tissue-specific cell. NSCs can be harvested from fetal brain tissue with the same challenges as ESCs or NSCs. Today, these cells can be derived from iPS. Several iPS-derived NSCs are commercially available. Human mesenchymal stem cells (MSCs), harvested most commonly from bone marrow, can also be used if the therapeutic target involves the secretion of growth factors rather than the replacement of brain cells.[5] While few MSCs have received clinical approval, preclinical investigations of ESCs, MSCS, and NSCs have shown great promise for stem cell therapies.[6, 7]

Cancer, cardiovascular diseases, inflammatory diseases, neurological disorders, and bone injuries are the most investigated conditions for stem cell therapy. In oncology, MSCs are used to target tumors to deliver anticancer drugs[8, 9], and treat leukemia and other blood cancers and disorders.[10-12] Cell therapies in cardiovascular disease can promote improved cardiac function and decreased infarct size following a myocardial infarction.[13-15] Stem cells have also successfully aided in reducing inflammation in simple wound healing processes as well as more involved nephritis associated with autoimmune disorders.[16, 17]

The primary focus of this chapter is on stem cell therapies for disorders and diseases of the central nervous system and bone regeneration. Preclinical investigations include stem cell therapy for multiple sclerosis, Alzheimer's Disease, Motor Neuron Disease, Parkinson's disease, stroke, and spinal cord injuries.[18-20] In clinical trials, MSCs have promoted functional recovery in patients following a stroke with no adverse side effects out to one year.[21] A similar clinical trial saw no adverse side effects when evaluating MSCs to treat a spinal cord injury;

however, the study could not draw any conclusions about treatment efficacy.[1] Preclinical investigations of bone regeneration have shown promise, and clinical trials are still ongoing.[22] In general, the safety of stem cells therapies has been established, but their potential for therapeutic efficacy remains unproven. A major challenge in establishing efficacy is our ability to ascertain in a clinical setting that cells were delivered to the target site, survived, and elicited their therapeutic effects.

Given such wide applicability for stem cell therapies, clinical translation will require the ability to accurately and reliably monitor stem cells non-invasively in deeply seated organ.[23, 24] Issues with therapeutic efficacy often arise from either incomplete cell differentiation or stem cells not homing to the injured or diseased part of the body. Inappropriate migration to undesired areas or even uncontrolled growth in the desired area can also lead to unwanted tumorigenesis.[25] As such, the ultimate clinical approval of stem cell therapy will require preclinical and clinical investigations of cellular tracking methodologies that can 1) accurately determine where stem cells are localizing and 2) report on their function. It is imperative for cell tracking methods to be nontoxic to stem cell viability and inert to its differentiation potential, to have reproducible and sufficient cellular internalization, to produce a strong signal *in vivo*, and to promote longitudinal studies that track cell location/function over time.

We will discuss current progress towards developing metal-ion based non-invasive imaging strategies for tracking cellular based therapies. We will evaluate the utility of contrast agents (CAs) developed for Magnetic Resonance Imaging (MRI) (Section 2), nuclear medicine and Computed Tomography (CT, Section 3), and optical imaging modalities (Section 4), as they are most widely used in clinical and preclinical settings. Lastly, we will examine multi-modal combinations of available CAs. We will scrutinize each modality for stem cell tracking, as well

as a few major advances in metal-ion based CAs in the context of the above-mentioned design principles. We will explore both molecular and nanoparticle CAs. Nanoparticle agents are defined as having a core made of metal ions, but molecular agents are chelated complexes even if the study utilizes nano-encapsulation delivery methods.

2. Magnetic Resonance Imaging

Since the early 1980s, MR imaging has become the top-choice diagnostic imaging technique for neurological, cardiovascular, and musculoskeletal diseases and disorders, and its use has expanded rapidly in utility in the past 20 years.[26] One reason for this is the safety profile of MRI which uses non-ionizing radiation for imaging.[27] During an MRI scan, a magnetic field B_0 is applied to the body and the nuclear spins of biological protons (mostly water) preferentially align with the magnetic field. This produces a net magnetization vector along the z-axis, M_0 . A radio frequency pulse is then applied to tip the net magnetization vector into the xy-plane. Signal is produced as detectors measure the radiofrequency relaxation of the nuclear spins back to M_0 . Longitudinal relaxation time, T_1 , is measured by the time it takes for the net magnetization to relax back to M_0 along the z-axis. The signal in T_1 -weighted MR imaging is proportional to the inverse of the time T_1 , also defined as the relaxation rate R_1 . This makes shorter T_1 times desirable for T_1 -weighted MR imaging. Transverse relaxation time, T_2 , describes the time it takes for the loss of net magnetization in the xy plane via dephasing.[28] The signal in T_2 -weighted MR imaging is similarly proportional to the inverse of the transverse relaxation rate, R_2 . Contrast agents can be used in MRI to modulate T_1 and T_2 times of analytes of interest and obtain more information from the experiment. The values of these relaxation times are then converted into a black and white signal scale to produce an image.

For most populations, MRI is a reliably safe non-invasive imaging modality. The use of non-ionizing radiofrequency pulses prevents risks associated with multiple scans that would be necessary for tracking stem cells in a longitudinal study. Additionally, an MRI scan can be taken immediately after the administration of a contrast agent, and has unlimited depth penetration and excellent spatial resolution.[29, 30] While inherent differences in tissue environment create excellent soft tissue contrast in MRI, paramagnetic CAs are used to produce even more significant differences in signals in an area of interest by influencing either T_1 or T_2 relaxation processes.[29] However, a major disadvantage of MRI is the lack of sensitivity of CAs in imaging experiments.[31]

A positive CA will predominantly shorten the T_1 relaxation time, producing a brighter signal compared to surrounding tissue. A negative CA will predominantly shorten T_2 , creating negative contrast observed by a loss in signal compared to surrounding tissue. For a T_1 contrast agent to be detectable, the tissue concentration needs to be in the high μM to mM range.[32] T_2 strategies tend to require a lower concentration of agent to create distinguishable negative contrast.[30] T_1 contrast agents are still preferred, as a bright signal is visually more compelling than a loss of signal.

2.1 Molecular Contrast Agents

Since the approval of the first CA in 1988, 10 molecular CAs have received full approval for clinical use in the United States. Among these, nine rely on paramagnetic Gd(III) to produce contrast and one is Mn(II)-based. In comparison, only two nanoparticle CAs have received full approval for clinical use by the US Food and Drug Administration (FDA).[33] As such, molecular CAs for MRI are among the most heavily explored as stem cell tracking agents.

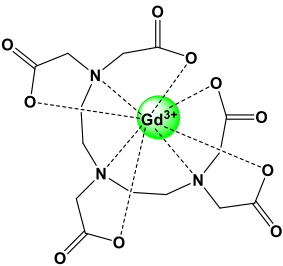
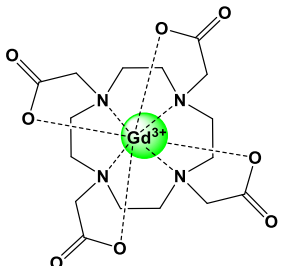
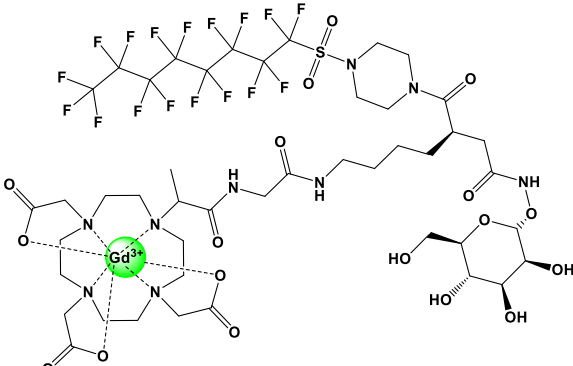
2.1.1 Gd(III) agents

Gadolinium-based contrast agents are used in approximately 40% of all MRI scans, with almost 50 tons of gadolinium administered annually.[29, 34] Gadolinium is a T_1 contrast agent that shortens the longitudinal relaxation time of hydrogen in water molecules directly bound to gadolinium itself, hydrogen bound to a chelating ligand, and hydrogen simply in the proximity of the strongly paramagnetic ion.[35] Signal enhancement comes predominately from inner-sphere water molecules that are exchanging with bulk water in proximity to the complex.[35] Gd(III) complexes discussed in this section are summarized in **Table 1**.

Gadolinium chelated by the linear molecule diethylenetriaminepentaacetic acid (forming Gd-DTPA, Magnevist®) was FDA approved for clinical use in 1988. However, Gd(III) complexes have poor cellular permeability, thus requiring creative strategies for delivery into stem cells before implantation back into the body to be detected by MRI. One study delivered Gd-DTPA into MSCs using non-liposomal transfection agents prior to direct stereotaxic injection into a murine model of stroke. Contrast was detectable out to seven days, but efficacy of the treatment or continued imaging capability over time was not evaluated.[36] In contrast, delivery of Gd-DTPA into MSCs by liposomal transfection agents promoted imaging out to two weeks.[37]

Another study evaluated the efficacy of commercially available jetPolyethyleneimine as a transfection agent for Gd-DTPA into MSCs, and also saw contrast out to two weeks in a model of spinal cord injury.[38] While each of these studies reported a final imaging timepoint, they do not discuss at what point signal could no longer be detected. This makes comparisons between methodologies difficult.

Table 1. Gd(III) complexes for T_1 -weighted MR imaging

Structure	Notes	Refs.
	<p>Gd-DTPA</p> <p>Magnevist®</p> <p>FDA approved in 1988</p> <p>Linear chelate that is sensitive to Gd(III) displacement in acidic conditions</p>	[36-38]
	<p>Gd-DOTA</p> <p>Dotarem®</p> <p>FDA Approved in 2013</p> <p>Macrocyclic chelate with better thermodynamic stability</p>	[46, 47]
	<p>Gadofluorine</p> <p>Gd-DOTA derivative</p> <p>Further potential for use in ^{19}F MRI</p>	[48]

While initial studies with Gd-DTPA were promising, linearly chelated Gd(III) complexes are less stable than macrocyclic alternatives and can result in unwanted gadolinium retention in a patient following administration. Dissociation of the metal ion from the ligand has been observed in the acidic environment of endosomes following internalization.[39] Because of this, the FDA has warned clinicians to exercise caution when administering linear Gd(III) chelates. This will be a common point of discussion throughout this chapter. Gadolinium retention is often benign, but free Gd(III)-ions can cause damage to tissues by blocking calcium channels and interfering with

protein functions.[40-42] An additional concern is for patients with kidney disease, as unstable gadolinium chelates may be causative of nephrogenic systemic fibrosis.[43] One study's solution to this was to bind Gd(III) ions directly to melanin nanoparticles to deliver into MSCs. As a proof of concept, Gd(III)-melanin labeled MSCs were injected directly into the thigh muscle of rats and were imaged out to four weeks post injection. Cai et. al. found these particles to be more stable than Gd-DTPA with greater signal contrast.[44]

Other studies have focused on developing macrocyclic chelating strategies for Gd(III) agents, as three macrocyclic agents are approved for clinical use and are known to bind Gd(III) more stably.[45] One example of this is FDA approved 1,4,7,10-tetraazacyclododecane macrocyclic chelate (Gd-DOTA, Dotarem®) to label MSCs. While Gd-DOTA has been explored in some stem cell tracking, cellular permeability remains a major issue.[46, 47] Giesel et. al. evaluated Gadophrin-2, a functionalized derivative of Gd-DOTA, both with and without transfection agents and found the transfection agents to still be necessary for producing sufficient MRI signal. Labeled MSCs were stereotaxically injected into the brain, but a longitudinal study was not performed to see how far out signal contrast could still be detected.[48] An untapped benefit of this complex is the ability to simultaneously perform ^{19}F MRI. As fluorine has a negligible background signal, areas of appreciable ^1H signal contrast seen in T_1 images could be correlated with colocalization of fluorine MRI signals.

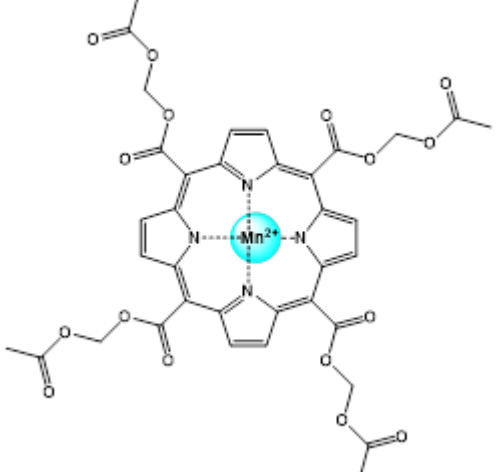
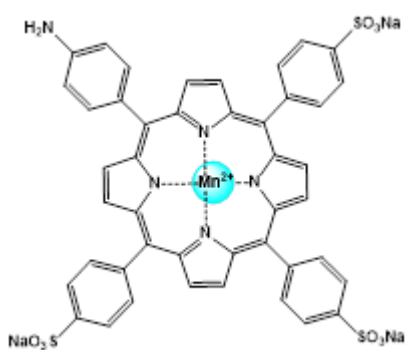
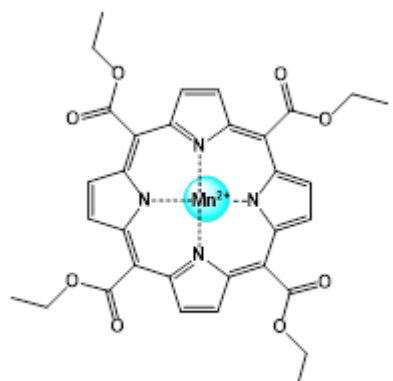
2.1.2 *Mn(II) agents*

The rapid rate of clearance of molecular gadolinium CAs is the primary attraction for utility in most MRI applications since metal retention can be associated with negative side effects. As such, we question their long-term utility as tracking agents for cellular based

therapies. One method to avoid this possible complication is the use of paramagnetic metal species that are found endogenously in healthy tissue, such as manganese. Mn(II) contrast agents present a unique substitute to Gd(III), as Mn(II) is an essential metal in biological function which increases its overall biocompatibility.[49] To date, the only clinically approved injectable Mn(II)-based contrast agent is Teslascan, which is a Mn(II) ion chelated by dipyridoxaldiphosphate (DPDP). Mn(II)-DPDP is used clinically for liver imaging and the overall safety profile is significantly higher than that of Gd(III)-DTPA.[49] Even so, an over-exposure to manganese can present serious health concerns; as with gadolinium, chelate stability is an important consideration for these complexes.[49-51] Herein, we discuss the progression of a family of Mn(II)-porphyrin complexes (**Table 2**) and their application for T_1 weighted MR imaging for STEM cell tracking.

The first generation of Mn(II) porphyrin complexes designed by the Chen group was Mn(II)-[(acetoxymethoxycarbonyl)porphyrin] (MnAMP), an enzyme-activatable contrast agent first explored *in vitro* in ESCs.[52, 53] As a major advantage compared to Gd(III) complexes, Mn(II)-porphyrin complexes do not require aid from cellular internalization agents. Initial investigations showed promise for these complexes as they did not impede ESC viability, proliferation, or differentiation potential.[52] However, synthetic challenges encouraged the group to make a second generation of Mn(II)-[5-(4-aminophenyl)-10,15,20-tris(4-sulfonatophenyl) porphyrin] (MnPNH₂) complexes. MnPNH₂ was synthetically more favorable than MnAMP and maintained the inert profile to cell function, but exhibited worse uptake in ESCs. Labeled cells were injected subcutaneously into rats and imaged, but a longitudinal study was not performed to assay signal strength over time.[54] A third generation of complexes, Mn(II)-[5,10,15,20-tetrakis(ethoxycarbonyl) porphyrin] (MnEtP), was found to satisfy both

Table 2. Mn(II)-porphyrin complexes for T_1 -weighted MR imaging

Structure	Notes	Refs.
	<p>Generation 1</p> <p>MnAMP</p> <p>Excellent cellular permeability and signal production</p> <p>Challenging synthetic scalability</p>	[52, 53]
	<p>Generation 2</p> <p>MnPNH₂</p> <p>Facile 2-step synthesis</p> <p>Diminished cellular internalization and signal production</p>	[54]
	<p>Generation 3</p> <p>MnEtP</p> <p>Facile 2-step synthesis</p> <p>Improved cellular internalization and signal production</p>	[55]

synthetic ease and cellular uptake profiles. The Cheng group indeed observed superior internalization with retained inertness to ESC cellular function. Subcutaneous injections of labeled ESCs revealed superior signal enhancement over unlabeled ESCs, but again a longitudinal study was not performed. [55] In order to assess the utility of this family of CAs

more thoroughly, a longitudinal study is imperative. However, initial findings for these complexes show promise for further optimization and preclinical investigation as Gd(III) substitutes.

2.1.3 ParaCEST Agents

Chemical Exchange Saturation Transfer (CEST) is an alternative method to T_1 and T_2 contrast that relies on the exchange properties of a proton on a CEST CA with bulk water. In a CEST experiment, saturation of a specific MR frequency corresponding to an exchangeable proton on the CA results in decreased bulk water signal due to exchange of the saturated nuclei with water protons.[56] Paramagnetic chemical exchange saturation transfer (ParaCEST) agents contain a paramagnetic ion that shifts the MR frequency of the exchangeable proton away from biological frequencies to promote selective saturation of just the one signal.[57, 58] As an added benefit, different paramagnetic ions shift proton signals to different frequencies, allowing simultaneous detection of multiple probes.[59]

Nicholls et. al. utilized this strategy to study the co-injection of endothelial cells with NSCs to improve regenerative properties following a stroke. Little is understood about how the interplay between the two cell types results in more complete regeneration than NSCs alone.[60] To explore this, Nicholls et. al. labeled endothelial cells with a europium ParaCEST CA (Eu-HPDO3A) and labeled the NSC population with an ytterbium ParaCEST CA (Yb-HPDO3A) via electroporation (**Figure 1**). Because the lanthanide identify creates unique proton saturation frequencies, the two cell populations were visualized simultaneously in the stroke cavity of a rat model.[61] A longitudinal study was not performed, but this study highlights a unique advantage for ParaCEST imaging in stem cell tracking.

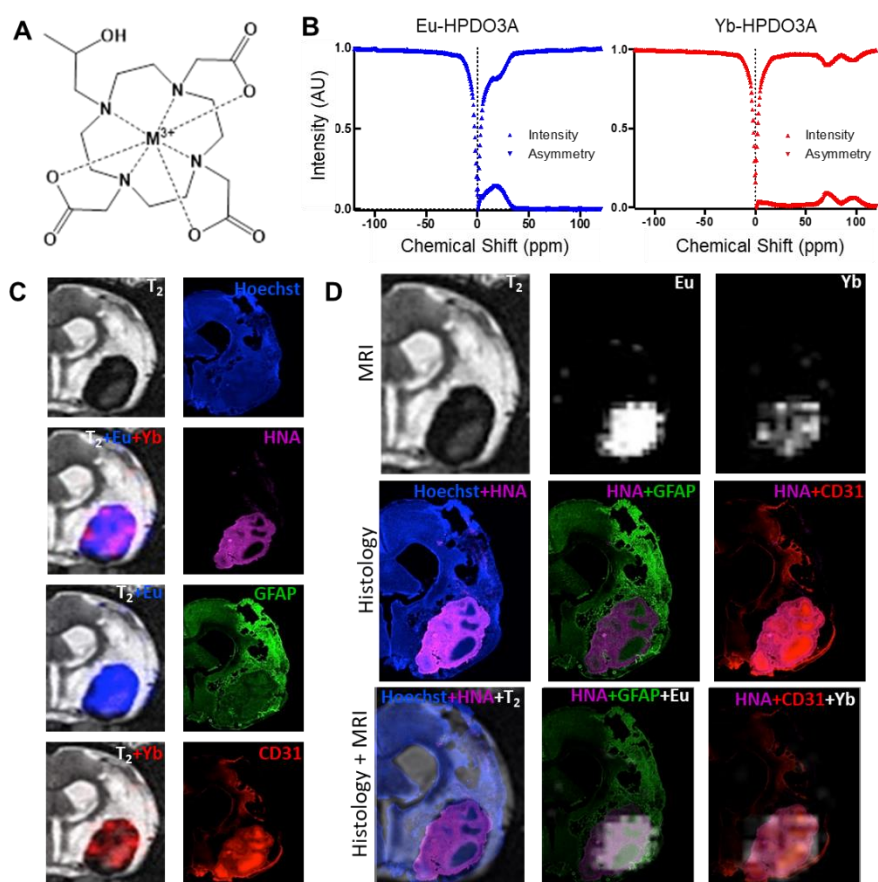


Figure 1: ParaCEST tracking endothelial cell and NSC populations in a rat model of stroke. (A) Chemical structure of M(III)-HPDO3A. Eu(III) chelates were used to label transplanted endothelial cells, and Yb(III) chelates were used to label NSCs. (B) z spectra of agent solutions showing signal intensity compared to the reference at -120ppm for both Eu-HPDO3A (Eu) and Yb-HPDO3A (Yb). Asymmetry highlights the regions of chemical shift that can be exploited to achieve specific imaging of each agent. Eu (18 ppm) and Yb (69 ppm) regions are non-overlapping, hence affording selective imaging. (C) There is a good correspondence between the distribution of transplanted cells as visualized by paraCEST and the histological marker for human cells (Human Nuclei Antigen, HNA). The Eu (18ppm) image indicated a fairly homogenous distribution of NSCs, which was paralleled by its histological validation using GFAP as a marker within the transplant area. Yb (97ppm) imaging also truthfully reflects the macroscopic distribution of transplanted ECs, as detected by CD31. (D) To further validate the accuracy of the MR images, partially transparent histological overlays of transplanted cells (HNA) with NSCs (GFAP) and ECs (CD31) specific markers were co-registered based on landmark identification to the relevant MRI images. This further highlights the regional specificity of the MR images as well as a correct mapping of relative cell distribution.[61]

An interesting future application for this dual-agent system is the ability to create activatable probes that will shift saturation frequency upon interaction with a molecular marker. A marker could be chosen to report back on stem cell differentiation or another process by which therapeutic effect could be imaged alongside cellular localization. ParaCEST agents would be superior to T_1 and T_2 agents for this application as it avoids the uncertainty of grey scale images. A change in signal is observed as a shift in the exchange frequency, not a slightly brighter or darker image that cannot be accurately quantified. However, this benefit must be cautiously weighted with some of the inherent disadvantages of ParaCEST. Like T_1 and T_2 CAs, ParaCEST suffers from low sensitivity.[62] Additionally, the specific absorption rate (SAR) of a ParaCEST agents presents a major challenge. The power required to detect ParaCEST signal over time can have a negative impact on surrounding tissue viability.[63]

2.2 *Nanoparticle Contrast Agents*

The lack of sensitivity for MRI as an imaging modality presents a challenge for molecular CAs. A concern will always be having enough agent in tissue to detect, especially as cells divide and the intracellular CA concentration is diluted. Nanoparticle strategies have emerged as an alternative because their core can be very densely packed with paramagnetic metal ions with bulk magnetic properties. Here, we discuss advances in nanoparticles that contain metal ions in their cores for MRI tracking of stem cells.

2.2.1 *Gd(III) Particle Core*

Even though several monomer gadolinium agents have received clinical approval, nanoparticle formulations with Gd(III) ions at the core are far less abundant. In one study, Gd(III) complexes chelated by three 2,4-hexanedione ligands were emulsified in wax and Brij78

surfactant to produce a densely packed Gd(III) core. Cellular internalization and signal contrast were superior to that of Gd-DTPA at identical concentrations *in vitro*, and cellular function of MSCs was not significantly hindered.[64] This study did not perform any *in vivo* tracking studies, and a follow-up study was not found. It is likely that the non-covalent nanoemulsion would not be stable in the intracellular milieu long-term, and the hexanedione ligands would not be thermodynamically stable for preventing free Gd(III) ion escape. This highlights the challenges of translating favorable T_1 molecular imaging properties of Gd(III) into nanoparticle formulations.

2.2.2 Superparamagnetic Iron Oxide Nanoparticles

Dense core structures of iron oxide are the most clinically used MRI nanoparticle structures and function as T_2 CAs. Two superparamagnetic iron oxide (SPIO) formulations, ferumoxides (Feridex® and Endorem®) and ferucarbotran (Resovist®), have received approval in the US and Europe.[65] Clinical investigations of SPIOs have been largely halted due to financial considerations, but many preclinical studies have proceeded for evaluating SPIOs for stem cell tracking.[66] SPIOs have been reviewed extensively for stem cell tracking elsewhere in terms of particle coating to promote cellular internalization.[24, 67-69] Herein, we highlight a few studies with the focus on the longitudinal aspect of stem cell tracking.

The first few studies performed imaging out to two to four weeks post cell transplantation in models of stroke and brain/spinal cord injury. On the low end of this time frame, Reddy et. al. coated SPIOs with chitosan and successfully imaged labeled MSCs up to 16 days.[70] Another study labeled SPIOs with poly-L-lysine prior to incubation with MSCs. Cells were transplanted into a model of traumatic brain injury and imaged out to three weeks.[71] Jiang et. al. incubated

NSCs with uncoated SPIOs and imaged transplanted cells out to four weeks in a rat ischemic model.[72] In a more comprehensive study, ESCs, MSCs, and CD34+ cells were labeled with Endorem® for tracking in models of spinal cord lesions, stroke, and spinal cord injury, respectively. Signal was observed out to 30 days.[73] One study went further, tracking NSCs labeled with ferumoxides coated with protamine sulfate in a rat model of ischemia for as long as nine weeks.[74] Obenaus et. al. went even further out to 58 weeks, successfully imaging SPIO labeled NSCs in a rat model of ischemic injury with no adverse side effects observed.[75]

As the stem cell tracking field transitions from asking the first question of “Can we image the specific cell population?” into the second question of “Can we report on functional activity?”, imaging strategies need to be compatible with long-term imaging studies. While these examples show that cells labeled with SPIOs can be imaged on longer time scales, it becomes apparent that inconsistencies in the literature make drawing comparisons between different labeling strategies difficult. These papers discuss how long they chose to image for, but they do not provide any commentary on the time point at which signal enhancement can no longer be detected.

It has become apparent that Gd(III) and SPIOs are the leading choice CAs for MRI. To compare Gd(III) and SPIOs directly, one study focused on the functional aspect of being able to detect viable from non-viable MSCs with either Gd(III) or SPIOs.[76] Guenoun et. al. found that non-viable cells labeled with Gd(III) exhibit significantly less contrast enhancement than viable, proliferative cells. In contrast, non-viable and viable MSCs labeled with SPIOs could not be easily distinguished, as non-viable cells produce the same signal void as viable ones. The paper concludes that this is a valuable method for monitoring if a transplant is going to be rejected. Furthermore, the group noticed that the transplanted cells exhibited rapid tumor-like proliferation

at the transplant site through 15 days. This was not expected and not wanted. This poignantly illustrates the general necessity for tracking stem cell therapies, as well as within the context of each individual tracking strategy to report on cellular behavior. It is possible that the presence of the tracking agents caused the over-proliferation.

2.2.3 Cobalt Alloy Nanoparticles

Nanoparticles with cobalt cores were found to have superior influences on water molecules as T_2 CAs at smaller core sizes compared to iron oxide.[77] This sensitivity increase is due to higher saturation magnetization of cobalt over iron.[78] Meng et. al. labeled NSCs with CoPt alloy nanoparticles coated in a variety of shells to protect cells from any harmful toxicity. CoPt particles did not hinder NSC viability, proliferation, or neuronal differentiation. They did not test the particles in a traditional *in vivo* study, but labeled cells were transplanted into a spinal cord slice culture and imaged.[79] Although a follow-up study was not found, initial testing of these particles shows promise for further preclinical investigations. However, another study found that CoZn ferrite ($\text{Co}_{0.5}\text{Zn}_{0.5}\text{Fe}_2\text{O}_4$) particles were not suitable for MR imaging compared to their purely iron oxide ferrite counterparts due to decreased proliferation in labeled cells, as well as inferior relaxation rates.[80] Further optimization of cobalt alloy nanoparticles will be instrumental for determining any future utility in stem cell tracking.

3. Nuclear Medicine and Computed Tomography Imaging

Positron emission tomography (PET), single photon emission computed tomography (SPECT), and computed tomography (CT) are three other main clinical imaging modalities. Unlike MRI, all three techniques require some form of ionizing radiation to produce a signal. For PET, a radiotracer CA undergoes beta decay via positron emission from the nucleus. The

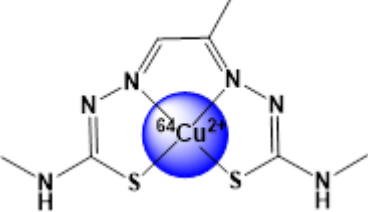
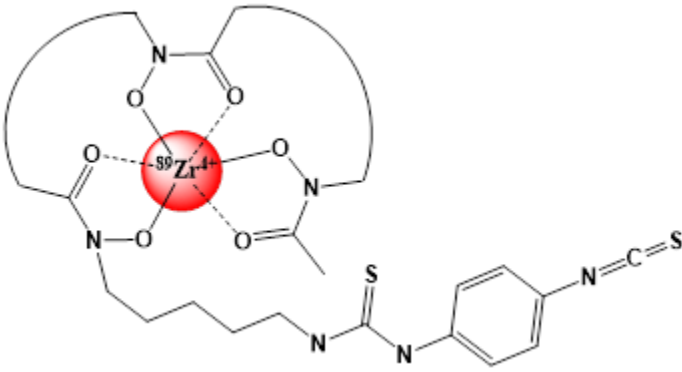
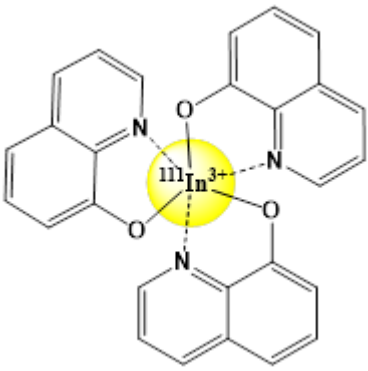
positron collides with an electron in the surrounding tissue, causing a detectable annihilation event that releases two photons. Common organic radiotracers contain ^{11}C , ^{13}N , ^{15}O or ^{18}F . [81] Although SPECT similarly relies on radioactive decay of a radiotracer, the difference is that the wavelength emitted falls in the gamma region of the electromagnetic spectrum. [82] CT, on the other hand, functions as a 3-dimensional X-ray. X-rays are emitted from the instrument itself and are detected opposite of where they are emitted, producing an image that shows where the beams were blocked by objects like bone. [83] For both PET and SPECT, a CA is the radiotracer itself, whereas CT CAs are anything that block X-ray beams better than the surrounding tissue. While the use of ionizing radiation is not ideal, these techniques are far superior to MRI in terms of sensitivity, significantly decreasing the amount of CA required for detection. [32] Since the risk of radiation exposure is considered low in many clinical settings when compared to the ability to reliably diagnose cancer and other diseases, these techniques should not be excluded outright as potential choices for stem cell tracking. However, as discussed throughout this section, careful consideration must be given to the limitations of these techniques in long-term studies.

3.1 Molecular PET/SPECT Agents

^{18}F is the most commonly used radioisotope for PET with a half-life around two hours. Radioisotopes of metal ions have also gained interest in the clinic due to ideal decay lifetimes for typical imaging needs. [84, 85] One example of this is ^{68}Ga with a half-life around one hour. A patient injected with a ^{68}Ga radiotracer could reasonably undergo an imaging scan within a 30 minute to one hour time frame, and within a few hours the majority of harmful ionization coming from decay will be complete. [86] However, a short lifetime is not ideal for a stem cell tracking study as it would be impossible to collect a longitudinal experiment once the number of

molecules emitting has fallen below the limit of detection. A summary of the radiotracers discussed in this section can be found in **Table 3**.

Table 3. Molecular radiotracers for nuclear medicine imaging

Structure	Notes	Refs.
	<p>⁶⁴Cu-PTSM</p> <p>PET imaging agent</p> <p>$T_{1/2} = 13$ hours</p>	[87-89]
	<p>⁸⁹Zr-DBN (simplified structure)</p> <p>PET imaging agent</p> <p>$T_{1/2} = 3.5$ days</p> <p>NCS functionality allows covalent linkage to cellular membrane</p>	[90]
	<p>¹¹¹In-oxyquinoline</p> <p>SPECT imaging agent</p> <p>$T_{1/2} = 2.5$ days</p> <p>Rapid efflux prevents utility in stem cell tracking</p>	[93]

Early studies evaluated the efficacy of ⁶⁴Cu-pyruvaldehyde bis(*N*⁴-methylthiosemi carbazone) (⁶⁴Cu-PTSM) complexes with a slightly longer half-life around 13 hours.[87] These studies revealed that stem cells were only detectable for less than one day due to rapid clearance of the agent coupled with the still relatively short half-life.[88, 89] As a solution to this, Bansal et. al. evaluated the tracing capability of ⁸⁹Zr-DBN labeled MSCs where labeling was achieved

via direct conjugation to the cellular membrane surface.[90] ^{89}Zr has a half-life around 3.5 days, an improvement from the scale of hours, but still not sufficient for weeks to months-long studies.[91] However, signal was observed out to seven days post-injection and likely would have been observed a few days longer if the study had continued.[90]

Radiotracers that emit gamma radiation often have longer half-lives than positron emitters, making SPECT a potentially better methodology for stem cell tracking.[85] However, the cost/benefit of more harmful gamma radiation must also be considered in both the short and long terms. ^{111}In , for example, has a half-life around 2.5 days. This half-life is on a similar time scale to ^{89}Zr and has been used rather extensively in clinical imaging of cardiovascular diseases (see review [92].) ^{111}In is often chelated by oxyquinoline for stem cell tracking, but these complexes are rapidly effluxed and require lipophilic delivery vehicles. As a recent solution, Krekorian et. al. chelated ^{111}In ions to poly(lactic-co-glycolic acid) (PLGA) nanoparticles and found superior *in vivo* signal generation compared to traditional oxyquinoline formulations for tracking transplanted dendritic cells.[93] While this strategy was evaluated in a model of lung infection, it could also be applied successfully to other stem cell therapies.

5.3.2 Gold Nanoparticle Enhanced CT

While useful in shorter-term imaging studies due to excellent sensitivity, both PET and SPECT imaging techniques ultimately fall short in terms of longitudinal imaging due to the inevitability of radio decay past a limit of detection. Additionally, the ability to monitor specific stem cell populations from nearby tissue is significantly limited by the poor spatial resolution associated with PET and SPECT (1-2 mm vs 25-100 μm in MRI).[32] CT is a widely used imaging technique due to its cost effectiveness, high spatial resolution (50-200 μm), and ease of use, with an estimated 70 million scans performed annually in the US alone. [32, 94] It is broadly

clinically available and a promising candidate for future translation of stem cell tracking techniques. CAs in CT function by attenuating X-ray beams. Therefore, metal ions with high molecular mass densely packed into nanoparticle cores are the best choices for labeling stem cells for *in vivo* tracking by CT.

Gold nanoparticles (AuNPs) are ideal CT contrast agents. The retention of AuNPs intracellularly provides an additional benefit of improvement in longitudinal imaging potential over PET and SPECT.[94] As an example, Betzer et. al. coated AuNPs in glucose to track MSCs in a rat model of depression. Cells were transplanted into rat brains via direct stereotaxic injection and were detectable via CT imaging as early as 24 hours and as late as one month post-injection. Results from a functional study revealed that behavioral signs of depression were decreased in animals that received the AuNP labeled stem cells.[95] Ongoing work from this group focuses on optimization of MSC labeling protocols.[6] This comprehensive study highlights the importance of both longitudinal imaging studies and functional assays to evaluate stem cell therapeutic efficacy. Overall, AuNP enhanced CT is valuable for stem cell tracking, and as will be discussed in Section 5, is an ideal platform for more advanced multi-modal strategies.

4. Optical Imaging

In contrast to PET, SPECT, and CT, optical imaging does not rely on ionizing radiation to produce a signal.[96] It relies solely on light. Laser light is shone on tissue that contains a light absorbing CA. The energy is absorbed into the CA, causing wavelength-dependent electronic excitation. Fluorescent molecules relax back to their ground state via a process that releases a photon in the ultraviolet-visible (UV-vis) spectra. The photon is thebookn detected by the instrument by its unique wavelength.[97] Similar to PET and SPECT, the body does not contain

many endogenous fluorophores, making background signal low and positive signal easily detected in an optical scan. Fluorescence is also very sensitive, capable of detecting small amounts of CA.[32] However, depth penetration through biological tissue is a majorly limiting factor, complicating the clinical utility of optical imaging. To date, the only clinically approved fluorescence technologies are for image-guided surgery.[98, 99] As such, fluorescent CAs are not ideal candidates for stem cell tracking clinically, but do have utility in preclinical models where tissues are thinner. Most fluorescence applications for stem cell therapy have been reserved for multi-modal strategies, which we will discuss in Section 5.

4.1 Two-Photon Molecular Agents

As discussed above, the most limiting factor for optical imaging in biological systems is highly limited depth penetration. Of all the wavelengths in the visible spectrum, lower energy red light penetrates deepest. However, molecules that absorb red and near-IR light are less common than absorbers of higher energy wavelengths. Two-photon absorption, or non-linear absorption, occurs when two photons of a longer wavelength (low energy) are absorbed simultaneously to induce electronic excitation that should only occur with a shorter wavelength (higher energy).[100] Another advantage of two-photon CAs is reduced signal interference from the excitation beam. The excitation wavelength is significantly shifted from the emission wavelength and is easily filtered out in image acquisition. This technique promotes a depth penetration greater than 500 μM , as opposed to less than 100 μM for traditional one-photon absorption.[101] To put this into perspective, this is still only as deep as the skin on our eyelids is thick.

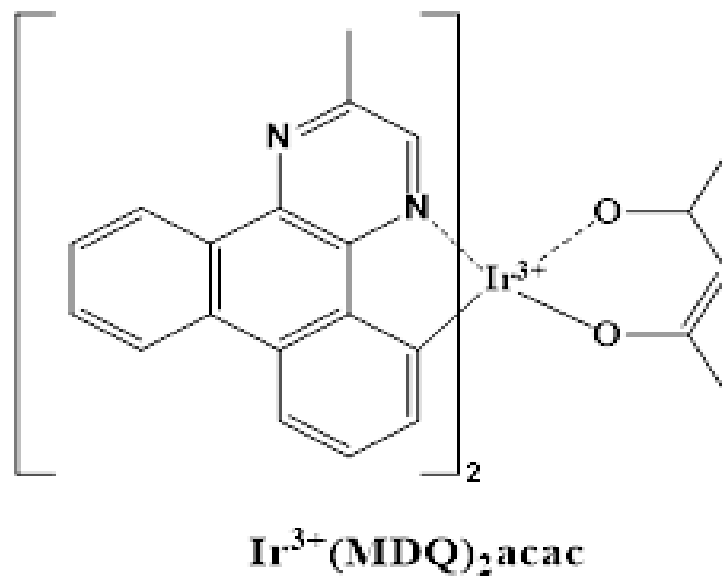


Figure 2: Structure of Ir(III)-(MDQ)₂acac, a molecular two-photon absorber used in stem cell tracking. [104] Nanoparticle delivery assistance promotes imaging out to 21 days following subcutaneous injection.

Cyclometallated Ir(III) complexes readily undergo two-photon absorption.[102, 103] However, their utility in stem cell tracking has previously been further compromised by toxicity both *in vitro* and *in vivo*. [104] To overcome this, Li et. al. formulated Ir(III)-[Bis(9,2-dimethyl-dibenzo[f,h]quinoxaline)(acetylacetonate)] (Ir(MDQ)₂acac, **Figure 2**) molecular two-photon absorption CAs into a nanoparticle that would better protect the biological tissues from any Ir(III) induced toxicity. NSCs were labeled with these agents prior to subcutaneous implantation into the back of an athymic mouse model. While this study did not observe migration of transplanted cells past the injection point, they successfully imaged out to 21 days with strong signal still observed.[104] While a molecular fluorophore alone is unlikely to translate to a clinical cell tracking study, it paves the way for promising utility of these complexes in multi-modal agents or studies that do not require great depth penetration, like skin tissue regeneration.

4.2 *Quantum Dots*

Quantum dots (QDs) are fluorescent semi-conducting nanocrystals that have modular structure and tunable band gaps. As such, QDs can be synthesized to absorb/emit anywhere on the UV-visible spectrum.[105] The most commonly studied QDs for cell tracking applications contain a CdSe/ZnS core-shell structure. [106-109] While some of these studies imaged successfully out to 8 weeks, structures containing Cd are known to be quite toxic, inhibiting their utility in stem cell tracking beyond depth penetration considerations.[110]

As an attempt to retain the longitudinal properties of CdSe quantum dots but mitigate unwanted toxicity, Chen et. al. synthesized Ag₂S QDs and fully characterized their biocompatibility with MSCs by assessing cytotoxicity, apoptosis induction, DNA damage, and differentiation potential. Labeled MSCs were then transplanted into a mouse model of liver failure via tail vein injection, where signal was observed in the liver for 30 days post-injection.[111] This study highlights perfectly the need for tracking studies, as signal was also observed strongly in the lungs. This is an undesired location for transplanted MSCs to locate and would require either further optimization of transplantation protocol to avoid off-target localization, or longer-term imaging studies to confirm that localization in the lungs is not problematic.

5. Multi-Modal Imaging Strategies

The appeal of multi-modal imaging lies in the ability to combine the best aspects of different imaging modalities to overcome the inherent disadvantages of each on its own. As imaging techniques and strategies advance, this also promotes the ability to simultaneously

monitor stem cell localization with one modality and function with another. It also presents the opportunity to compound the benefits of both molecular and nanoparticle approaches.

5.1 Molecular MRI/Optical Agents

The most common multi-modal strategies for preclinical stem cell tracking combine the *in vivo* safety profile and depth penetration of MRI with *in vivo* and *ex vivo* validation via fluorescence. As mentioned previously, fluorescence strategies are not well-translated into the clinic, but are nonetheless valuable tools in preclinical investigations. Preliminary studies evaluated the combination of non-covalently tethered Gd-DTPA and fluorescent organic molecules. [112, 113] The main drawback of this strategy is the uncertainty that the MRI contrast agent and fluorescent probe will remain together in the same tissue if they are not covalently linked. One response to this was to chemically couple both Gd-DTPA and a fluorescent dye to a silica nanoparticle, improving both cellular internalization and colocalization confidence. [113]

A similar strategy that has gained much attention for stem cell tracking is the gadolinium-rhodamine dextran (GRID) conjugate. Gd-DTPA and rhodamine are chemically coupled to a dextran backbone, promoting cellular internalization and colocalization of MRI agent and fluorophore. One of the first studies in 2002 with this conjugate labeled NSCs with GRID prior to injection into a rat model of global ischemia. Transplanted cells were detectable out to 14 days *ex vivo*. [114] In a follow-up in 2004, GRID labeled NSCs were injected directly into the brains of rats three months following induced stroke. The cells were transplanted into the right side of the brain, and migration to the lesion on the left side was tracked for 14 days. **(Figure 3)** [115]

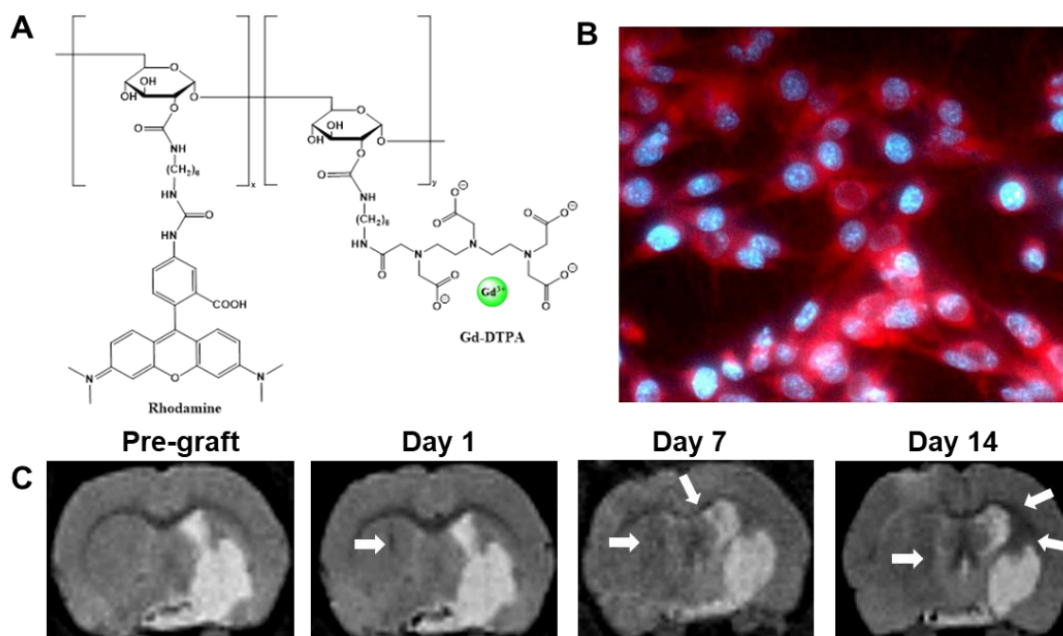


Figure 3: Gadolinium rhodamine dextran (GRID) utilized to track NSCs in a rat model of stroke by Modo et. al. (A) Structure of GRID. (B) Validation of NSC labeling *in vitro*. (C) *In vivo* tracking of NSC migration from the site of injection to the lesion site over 14 days. NSCs indeed hone to the site of injury as visualized by MRI.[115]

While GRID showed initial promise for stem cell tracking, a chronic behavioral study in 2009 revealed that early successful tracking does not necessarily correlate to successful therapeutic efficacy. Animals were monitored for one year post-implantation to evaluate changes in brain lesion size over time following a stroke. The researchers found that stem cells labeled with PKH26 red fluorescent dye reduced lesion size by approximately 35%, but lesion sizes of GRID labeled therapies showed no significant improvement from non-treated controls. [116] They postulate this is due to Gd(III) toxicity associated with thermodynamic instability of Gd-DTPA, which would be heightened by the retention of the imaging agent due to dextran conjugation. These results further confirm the necessity of functional analysis of the actual therapeutic component in the presence of any given imaging agent.

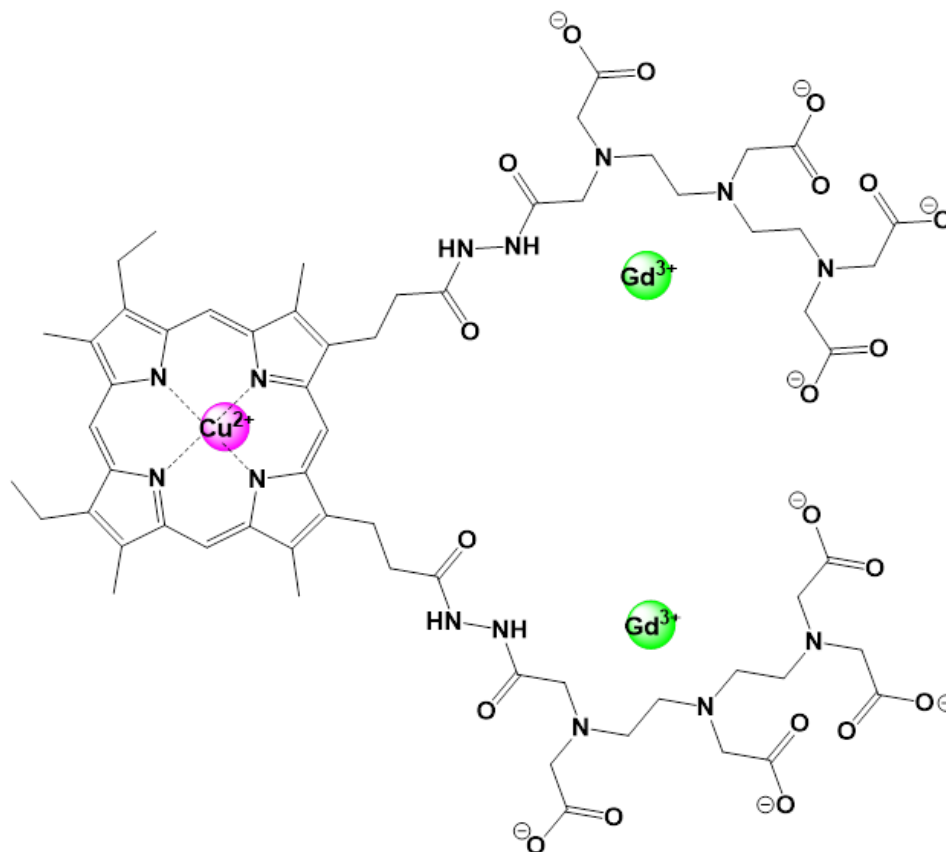


Figure 4: Structure of Gadophrin-2. Two units of Gd-DTPA are conjugated to a Cu(II) porphyrin for dual-modal molecular MRI/optical imaging. Analysis reveals that this conjugate has utility for short-term optimization of cellular transplantation methods. [117]

Another molecular combination of MRI and fluorescence for stem cell tracking is Gadophrin-2, a complex that contains two linearly chelated Gd(III) ions and a Cu(II) porphyrin fluorophore (**Figure 4**). While not tested in a disease model, peripheral blood cells were successfully labeled with Gadophrin-2 and imaged *in vivo* 24 hours post-injection. The conclusions of this study emphasize the utility of this conjugate to evaluate cellular localization based on transplantation technique and desired localization target. [117] This analysis can be applied to any of the aforementioned Gd-DTPA/fluorescent strategies, as both components present complications for clinical utility. Discussion in this study raise an excellent point that

even complications for clinical translation do not completely annihilate preclinical value. Proper care and rigorous evaluation must be taken though, for any agents seeking to reach clinical use.

5.2 *Molecular PET/MRI Agents*

While seemingly an unlikely combination, a unique study performed by Lewis et. al. in 2015 sought to take advantage of divalent metal transporters (DMTs) for the uptake of $^{52}\text{Mn}/\text{Mn}$ for dual-modal PET/MRI imaging. Specifically, NSCs were engineered to overexpress DMT-1 and directly injected into the brains of rats. [118] The premise is that the over-expression of these ion channels would improve uptake of systemically delivered $^{52}\text{Mn}/\text{Mn}$ for PET/MRI imaging that does not require labeling of stem cells prior to injection. In this regard, the Mn agents can be delivered multiple times throughout a longitudinal imaging study and then cleared by the body to avoid issues associated with prolonged retention. Increased signal was observed in engineered cells *in vivo*, though not reliably to the extent that was hypothesized. Additionally, the study does not report any consideration on the impact of engineering NSCs on proliferation and differentiation potential. [118] Follow-ups will be necessary to optimize this technique for potential clinical translation. Initial promise of the overall idea and results do suggest this optimization is worth pursuing.

5.3 *Nanoparticle Strategies*

As opposed to purely molecular strategies, the possibilities for nanoparticle-based multi-modal CAs are almost endless. SPIOs, AuNPs, and even QDs that we have discussed previously are modular platforms with functionalizable surfaces where any number of molecular MRI, PET/SPECT, or optical CAs could be added to build a dual or multi-modal agent. Herein, we will focus on a few examples of SPIO and AuNP platforms.

SPIOs have been combined with organic fluorescent dyes to label MSCs for proof-of-concept *in vivo* detection, as well as in stem cell therapies following stroke and myocardial infarction.[119-121] Similarly to the purely molecular combinations of MRI and optical imaging, the depth penetration and excellent resolution of MRI pairs well with the sensitivity of fluorescence. That said, negative T_2 contrast will always be inferior to positive T_1 contrast. As we have discussed previously, nanoparticle T_1 agents are more challenging to generate. However, one example of successfully generating a nanoparticle-based T_1 MRI/optical agent came as a response to the long-term therapeutic failure of GRID-labeled stem cells. The Modo group loaded AuNPs with Gd(III)-DOTA macrocyclic chelates chemically coupled to DNA strands. **(Figure 5)** The DNA imparts stability to the AuNPs to promote cellular internalization and retention, with Gd(III)-DOTA providing T_1 MRI contrast. The DNA strands were also capped with a Cy3 dye for dual-modal MRI/fluorescence imaging. Excellent *in vivo* contrast was observed between labeled and unlabeled cells, and there was no initial evidence for hinderance of cell functionality.[122] While the CT contrast enhancement of the AuNP was not evaluated and a longitudinal study was not preformed, this study amplifies the benefits that multi-modal nanoparticle strategies may exhibit over purely molecular strategies. Mainly for MRI, higher concentrations of Gd(III) agents are internalized, improving the overall signal enhancement and bypassing sensitivity challenges.

CT contrast by AuNPs has shown promise as a single modality of stem cell tracking, encouraging its utility in dual-modal formulations. Combinations of CT and optical imaging have been explored via functionalization of AuNPs with fluorescent molecules.[123] In one study, the near IR dye indocyanine green was loaded onto AuNPs to label MSCs for transplantation into a model of lung injury, and cells were successfully detected out to three

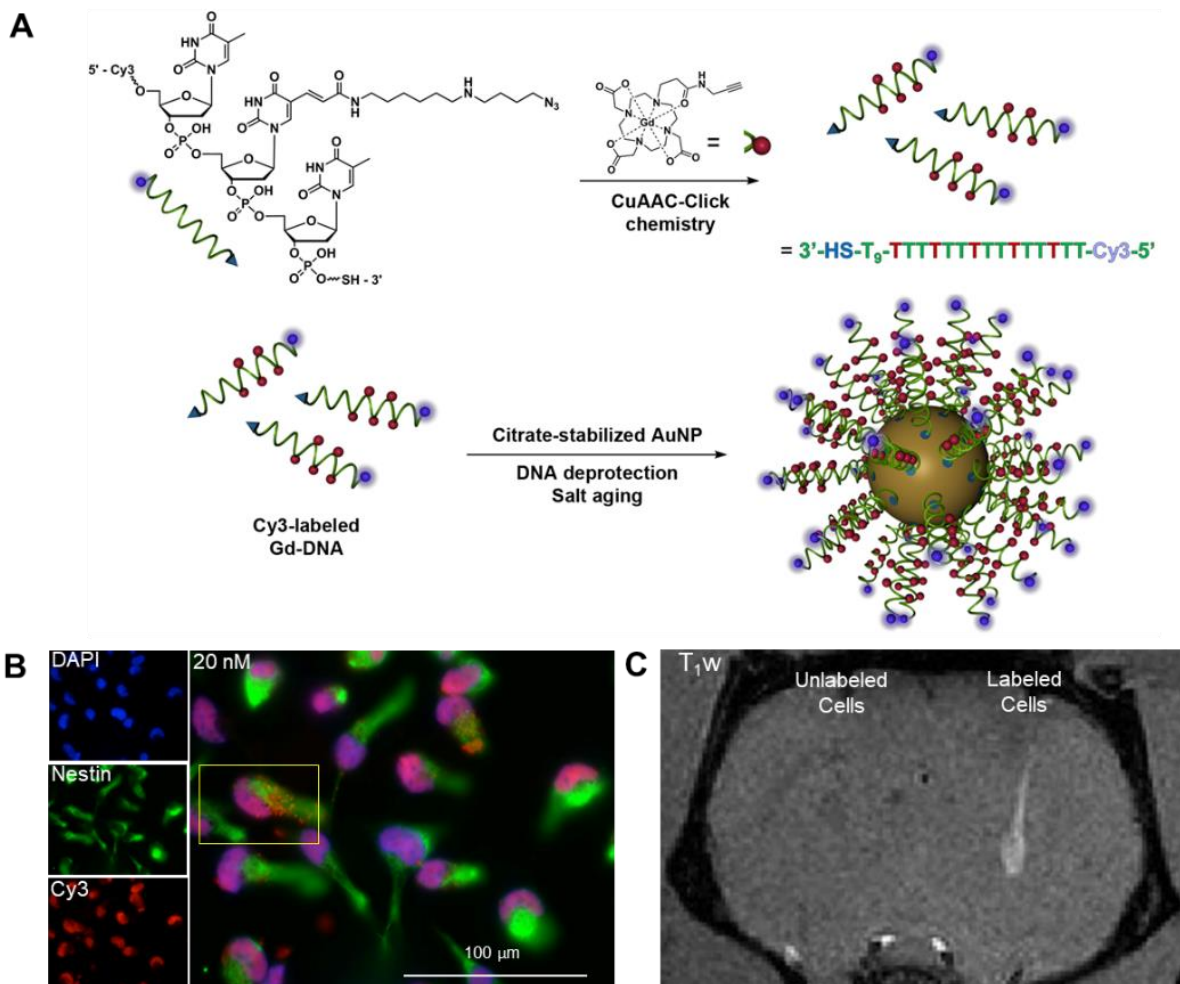


Figure 5: A dual-modal MRI/optical nanoparticle strategy for stem cell tracking. (A) Schematic for the formulation of DNA-capped AuNPs for dual-modal MRI/optical imaging. MRI enhancement is gained from Gd(III)-DOTA CAs chemically coupled to the DNA backbone. (B) Validation of internalization *in vitro* via confocal microscopy. Red signal represents endosomal located Cy3/AuNPs. (C) Contrast enhancement is observed in labeled cells over non-labels cells at the injection site or a rat brain.[122]

weeks.[124] By histological staining, both labeled and unlabeled MSCs effectively reduced the inflammatory response associated with the injury compared to non-treated animals. [125] This study presents a successful example of cell labeling not compromising therapeutic efficacy, and showcases the importance of performing these functional assays.

6. Concluding Remarks

Stem cell therapy has emerged as a promising therapeutic strategy for regenerative medicine where traditional drug-based therapies have been elusive. However, the future clinical translation of stem cell therapies requires non-invasive tracking methods to evaluate the longer-term localization and function of the implanted cells employed during preclinical and clinical investigations. This chapter has specifically discussed tracking methods involving metal ion-based contrast agents for MRI (Section 2), PET, SPECT, CT (Section 3), optical imaging (section 4), and combinations of these modalities (Section 5). It is imperative when evaluating each modality/CA pair to consider the potential influence of the agent on stem cell behavior, the ability to perform longitudinal imaging studies, as well as the actual efficacy of the therapy.

After evaluation of the studies presented in this chapter, we conclude that for optimal clinical translation of long-term tracking agents, MRI and CT are superior to PET, SPECT, and optical techniques. This is primarily because PET and SPECT radiotracers are undetectable once sufficient decay has occurred, and fluorescence imaging has very limited clinical utility due to poor tissue penetration. However, we find that optical components of multi-modal imaging strategies have high utility in initial preclinical investigations as they may impart sensitivity specifically to an MRI contrast agent for localization validation. Human cells transplanted inside the human body cannot be tracked post-transplantation with human-specific markers. Pre-labeling the cells can distinguish transplanted cells from existing tissue.

When considering molecular vs. nanoparticle platforms, we find nanoparticle strategies to carry many advantages. The first is the ability to incorporate multiple imaging modalities more modularly. Molecular agents are limited by synthetic coupling needed to ensure proper co-localization at all times. In contrast, the large surface area of nanoparticles can adsorb high

amounts of molecular contrast agents with imaging modality that differs from the nanoparticle itself. This allows for the conjugation of two or more imaging modalities into one system very easily, creating an avenue for more readily incorporating activatable agents to report on therapeutic efficacy. Nanoparticles may be further functionalized with ligands for improved cellular internalization and retention for longitudinal imaging studies.

While it seems that the “perfect” CA for stem cell tracking is yet to be tested, there are discrepancies across studies in the literature that make comparing previously evaluated strategies difficult. For example, many studies do not record at what time points signal is no longer detected *in vivo*. Even fewer studies performed analysis of actual stem cell therapeutic function in the presence of metallo-contrast agents. As the field progresses and tracking strategies are chosen for translation into clinical investigations, these analyses will be imperative.

REFERENCES

- [1] R. Pal, N.K. Venkataramana, A. Bansal, S. Balaraju, M. Jan, R. Chandra, A. Dixit, A. Rauthan, U. Murgod, S. Totey, *Cytotherapy*, 11 (2009) 897-911.
- [2] J.C. Ra, I.S. Shin, S.H. Kim, S.K. Kang, B.C. Kang, H.Y. Lee, Y.J. Kim, J.Y. Jo, E.J. Yoon, H.J. Choi, E. Kwon, *Stem Cells and Development*, 20 (2011) 1297-1308.
- [3] T. O'Brien, F.P. Barry, *Mayo Clin Proc*, 84 (2009) 859-861.
- [4] A. Abbott, *Nature*, 471 (2011) 280-280.
- [5] A. Andrzejewska, S. Dabrowska, B. Lukomska, M. Janowski, *Adv Sci (Weinh)*, 8 (2021) 2002944-2002944.
- [6] O. Betzer, R. Meir, T. Dreifuss, K. Shamalov, M. Motiei, A. Shwartz, K. Baranes, C.J. Cohen, N. Shraga-Heled, R. Ofir, G. Yadid, R. Popovtzer, *Scientific Reports*, 5 (2015) 15400.
- [7] T. Negoro, H. Okura, M. Maehata, S. Hayashi, S. Yoshida, N. Takada, A. Matsuyama, *npj Regenerative Medicine*, 4 (2019) 20.
- [8] Z. Gao, L. Zhang, J. Hu, Y. Sun, *Nanomedicine: Nanotechnology, Biology and Medicine*, 9 (2013) 174-184.
- [9] D. Dapkute, M. Pleckaitis, D. Bulotiene, D. Daunoravicius, R. Rotomskis, V. Karabanovas, *ACS Applied Materials & Interfaces*, 13 (2021) 43937-43951.

- [10] S.E. Freedman, *Seminars in Oncology Nursing*, 4 (1988) 3-8.
- [11] C. Nabhan, J. Mehta, M.S. Tallman, *Bone Marrow Transplant*, 28 (2001) 219-226.
- [12] M. Demagalhaes-Silverman, A.D. Donnenberg, S.M. Pincus, E.D. Ball, *Cell Transplantation*, 2 (1993) 75-98.
- [13] G.J. Bittle, D. Morales, K.B. Deatrick, N. Parchment, P. Saha, R. Mishra, S. Sharma, N. Pietris, A. Vasilenko, C. Bor, C. Ambastha, M. Gunasekaran, D. Li, S. Kaushal, *Circ Res*, 123 (2018) 288-300.
- [14] M.B. Britten, N.D. Abolmaali, B. Assmus, R. Lehmann, J. Honold, J. Schmitt, T.J. Vogl, H. Martin, V. Schächinger, S. Dimmeler, A.M. Zeiher, *Circulation*, 108 (2003) 2212-2218.
- [15] R. Rikhtegar, M. Pezeshkian, S. Dolati, N. Safaie, A. Afrasiabi Rad, M. Mahdipour, M. Nouri, A.R. Jodati, M. Yousefi, *Biomed Pharmacother*, 109 (2019) 304-313.
- [16] J.-W. Chang, S.-P. Hung, H.-H. Wu, W.-M. Wu, A.-H. Yang, H.-L. Tsai, L.-Y. Yang, O.K. Lee, *Cell Transplantation*, 20 (2011) 245-258.
- [17] W.J. Ennis, A. Sui, A. Bartholomew, *Adv Wound Care (New Rochelle)*, 2 (2013) 369-378.
- [18] I. Garitaonandia, R. Gonzalez, G. Sherman, A. Semechkin, A. Evans, R. Kern, *Stem Cells Dev*, 27 (2018) 951-957.
- [19] A. Uccelli, A. Laroni, M.S. Freedman, *The Lancet Neurology*, 10 (2011) 649-656.
- [20] M. Li, K. Guo, S. Ikehara, *Int J Mol Sci*, 15 (2014) 19226-19238.
- [21] O.Y. Bang, J.S. Lee, P.H. Lee, G. Lee, *Annals of Neurology*, 57 (2005) 874-882.
- [22] M. Barba, G. Di Taranto, W. Lattanzi, *Expert Opin Biol Ther*, 17 (2017) 677-689.
- [23] J.V. Frangioni, R.J. Hajjar, *Circulation*, 110 (2004) 3378-3383.
- [24] J.W.M. Bulte, H.E. Daldrup-Link, *Radiology*, 289 (2018) 604-615.
- [25] X. Zhang, T. Lei, H. Du, *Stem Cell Research & Therapy*, 12 (2021) 457.
- [26] D.A. Rosman, R. Duszak, W. Wang, D.R. Hughes, A.B. Rosenkrantz, *American Journal of Roentgenology*, 210 (2017) 364-368.
- [27] A. Berger, *BMJ*, 324 (2002) 35-35.
- [28] F. Bloch, *Physical Review*, 70 (1946) 460-474.
- [29] J. Wahsner, E.M. Gale, A. Rodríguez-Rodríguez, P. Caravan, *Chem Rev*, 119 (2019) 957-1057.

- [30] A. Hengerer, J. Grimm, *Biomed Imaging Interv J*, 2 (2006) e8-e8.
- [31] M.E. Ladd, P. Bachert, M. Meyerspeer, E. Moser, A.M. Nagel, D.G. Norris, S. Schmitter, O. Speck, S. Straub, M. Zaiss, *Progress in Nuclear Magnetic Resonance Spectroscopy*, 109 (2018) 1-50.
- [32] F.-M. Lu, Z. Yuan, *Quantitative imaging in medicine and surgery*, 5 (2015) 433-447.
- [33] V.C. Pierre, M.J. Allen, P. Caravan, *J Biol Inorg Chem*, 19 (2014) 127-131.
- [34] V.M. Runge, *Investigative Radiology*, 52 (2017).
- [35] V. Jacques, S. Dumas, W.C. Sun, J.S. Troughton, M.T. Greenfield, P. Caravan, *Invest Radiol*, 45 (2010) 613-624.
- [36] K. Geng, Z.X. Yang, D. Huang, M. Yi, Y. Jia, G. Yan, X. Cheng, R. Wu, *Mol Med Rep*, 11 (2015) 954-960.
- [37] J. Guenoun, G.A. Koning, G. Doeswijk, L. Bosman, P.A. Wielopolski, G.P. Krestin, M.R. Bernsen, *Cell Transplant*, 21 (2012) 191-205.
- [38] Y. Liu, Z.-J. He, B. Xu, Q.-Z. Wu, G. Liu, H. Zhu, Q. Zhong, D.Y. Deng, H. Ai, Q. Yue, Y. Wei, S. Jun, G. Zhou, Q.-Y. Gong, *Brain Research*, 1391 (2011) 24-35.
- [39] E. Di Gregorio, E. Gianolio, R. Stefania, G. Barutello, G. Digilio, S. Aime, *Analytical Chemistry*, 85 (2013) 5627-5631.
- [40] Z. Zhou, Z.-R. Lu, *Wiley Interdiscip Rev Nanomed Nanobiotechnol*, 5 (2013) 1-18.
- [41] J.B. Lansman, *J Gen Physiol*, 95 (1990) 679-696.
- [42] B.A. Biagi, J.J. Enyeart, *Am J Physiol*, 259 (1990) C515-520.
- [43] H.S. Thomsen, *European radiology*, 16 (2006) 2619-2621.
- [44] W.-W. Cai, L.-J. Wang, S.-J. Li, X.-P. Zhang, T.-T. Li, Y.-H. Wang, X. Yang, J. Xie, J.-D. Li, S.-J. Liu, W. Xu, S. He, Z. Cheng, Q.-L. Fan, R.-P. Zhang, *Journal of Biomedical Materials Research Part A*, 105 (2017) 131-137.
- [45] Y.-D. Xiao, R. Paudel, J. Liu, C. Ma, Z.-S. Zhang, S.-K. Zhou, *Int J Mol Med*, 38 (2016) 1319-1326.
- [46] M. Zhang, X. Liu, J. Huang, L. Wang, H. Shen, Y. Luo, Z. Li, H. Zhang, Z. Deng, Z. Zhang, *Nanomedicine*, 14 (2018) 2475-2483.
- [47] P. Zhang, Y. Zhang, B. Li, H. Zhang, H. Lin, Z. Deng, B. Tan, *J Pept Sci*, 24 (2018) e3077.

- [48] F.L. Giesel, M. Stroick, M. Griebe, H. Tröster, C.W. von der Lieth, M. Requardt, M. Rius, M. Essig, H.-U. Kauczor, M.G. Hennerici, M. Fatar, *Investigative Radiology*, 41 (2006) 868-873.
- [49] D. Pan, A.H. Schmieder, S.A. Wickline, G.M. Lanza, *Tetrahedron*, 67 (2011) 8431-8444.
- [50] A. Bertin, A.I. Michou-Gallani, J.L. Gallani, D. Felder-Flesch, *Toxicol In Vitro*, 24 (2010) 1386-1394.
- [51] M. Thuen, M. Berry, T.B. Pedersen, P.E. Goa, M. Summerfield, O. Haraldseth, A. Sandvig, C. Brekken, *J Magn Reson Imaging*, 28 (2008) 855-865.
- [52] S. Loai, I. Haedicke, Z. Mirzaei, C.A. Simmons, X.-a. Zhang, H.L. Cheng, *Journal of Magnetic Resonance Imaging*, 44 (2016) 1456-1463.
- [53] I.E. Haedicke, T. Li, Y.L.K. Zhu, F. Martinez, A.M. Hamilton, D.H. Murrell, J.T. Nofiele, H.-L.M. Cheng, T.J. Scholl, P.J. Foster, X.-a. Zhang, *Chemical Science*, 7 (2016) 4308-4317.
- [54] A. Venter, D.A. Szulc, S. Loai, T. Ganesh, I.E. Haedicke, H.-L.M. Cheng, *Scientific Reports*, 8 (2018) 12129.
- [55] I.E. Haedicke, S. Loai, H.-L.M. Cheng, *Contrast Media & Molecular Imaging*, 2019 (2019) 3475786.
- [56] G. Liu, M.M. Ali, B. Yoo, M.A. Griswold, J.A. Tkach, M.D. Pagel, *Magnetic Resonance in Medicine*, 61 (2009) 399-408.
- [57] S. Aime, A. Barge, D. Delli Castelli, F. Fedeli, A. Mortillaro, F.U. Nielsen, E. Terreno, *Magn Reson Med*, 47 (2002) 639-648.
- [58] M.T. McMahon, A.A. Gilad, J. Zhou, P.Z. Sun, J.W. Bulte, P.C. van Zijl, *Magn Reson Med*, 55 (2006) 836-847.
- [59] I. Hancu, W.T. Dixon, M. Woods, E. Vinogradov, A.D. Sherry, R.E. Lenkinski, *Acta Radiol*, 51 (2010) 910-923.
- [60] N. Nakagomi, T. Nakagomi, S. Kubo, A. Nakano-Doi, O. Saino, M. Takata, H. Yoshikawa, D.M. Stern, T. Matsuyama, A. Taguchi, *Stem Cells*, 27 (2009) 2185-2195.
- [61] F.J. Nicholls, W. Ling, G. Ferrauto, S. Aime, M. Modo, *Scientific reports*, 5 (2015) 14597-14597.
- [62] M. Modo, J. Kolosnjaj-Tabi, F. Nicholls, W. Ling, C. Wilhelm, O. Debarge, F. Gazeau, O. Clement, *Contrast Media & Molecular Imaging*, 8 (2013) 439-455.
- [63] E. Vinogradov, A.D. Sherry, R.E. Lenkinski, *J Magn Reson*, 229 (2013) 155-172.

- [64] C.-L. Tseng, I.L. Shih, L. Stobinski, F.-H. Lin, *Biomaterials*, 31 (2010) 5427-5435.
- [65] F. Azzabi, M. Rottmar, V. Jovaisaite, M. Rudin, T. Sulser, A. Boss, D. Eberli, *Tissue Eng Part C Methods*, 21 (2015) 182-191.
- [66] Y.X. Wang, *Quant Imaging Med Surg*, 1 (2011) 35-40.
- [67] M. Mahmoudi, H. Hosseinkhani, M. Hosseinkhani, S. Boutry, A. Simchi, W.S. Journeay, K. Subramani, S. Laurent, *Chemical Reviews*, 111 (2011) 253-280.
- [68] M.P. Nucci, I.S. Filgueiras, J.M. Ferreira, F.A. de Oliveira, L.P. Nucci, J.B. Mamani, G.N.A. Rego, L.F. Gamarra, *World J Stem Cells*, 12 (2020) 381-405.
- [69] M.R. Bernsen, J. Guenoun, S.T. van Tiel, G.P. Krestin, *The British Journal of Radiology*, 88 (2015) 20150375.
- [70] A.M. Reddy, B.K. Kwak, H.J. Shim, C. Ahn, H.S. Lee, Y.J. Suh, E.S. Park, *J Korean Med Sci*, 25 (2010) 211-219.
- [71] S.K. Mishra, S. Khushu, A.K. Singh, G. Gangenahalli, *Stem Cell Reviews and Reports*, 14 (2018) 888-900.
- [72] L. Jiang, R. Li, H. Tang, J. Zhong, H. Sun, W. Tang, H. Wang, J. Zhu, *Cell Transplantation*, 28 (2018) 747-755.
- [73] E. Sykova, P. Jendelova, *In vivo tracking of stem cells in brain and spinal cord injury*, in: J.T. Weber, A.I.R. Maas (Eds.) *Progress in Brain Research*, Elsevier, 2007, pp. 367-383.
- [74] C. Da-Jeong, lt, sup, gt, lt, sup, gt, M. Hyeyoung, lt, sup, gt, lt, sup, gt, L. Yong Hyun, lt, sup, gt, lt, sup, gt, L. Nayeon, lt, sup, gt, lt, sup, gt, J.L. Hong, lt, sup, gt, lt, sup, gt, J. Iksoo, lt, sup, gt, lt, sup, gt, L. Hyunseung, lt, sup, gt, lt, sup, gt, H. Tae-Sun, lt, sup, gt, lt, sup, gt, O. Seung-Hun, lt, sup, gt, lt, sup, gt, S. Dong Ah, lt, sup, gt, lt, sup, gt, U.K. Seung, lt, sup, gt, lt, sup, gt, H. Kwan Soo, lt, sup, gt, lt, sup, gt, S. Jihwan, lt, sup, gt, lt, sup, gt, *IJSC*, 5 (2012) 79-83.
- [75] A. Obenaus, N. Dilmac, B. Tone, H.R. Tian, R. Hartman, M. Digicaylioglu, E.Y. Snyder, S. Ashwal, *Annals of neurology*, 69 (2011) 282-291.
- [76] J. Guenoun, A. Ruggiero, G. Doeswijk, R.C. Janssens, G.A. Koning, G. Kotek, G.P. Krestin, M.R. Bernsen, *Contrast Media & Molecular Imaging*, 8 (2013) 165-174.
- [77] L.M. Parkes, R. Hodgson, T. Lu le, D. Tung le, I. Robinson, D.G. Fernig, N.T. Thanh, *Contrast Media Mol Imaging*, 3 (2008) 150-156.
- [78] M. Edmundson, N.T.K. Thanh, B. Song, *Theranostics*, 3 (2013) 573-582.

- [79] X. Meng, H.C. Seton, L.T. Lu, I.A. Prior, N.T.K. Thanh, B. Song, *Nanoscale*, 3 (2011) 977-984.
- [80] K. Jiráková, M. Šeneklová, D. Jirák, K. Turnovcová, M. Vosmanská, M. Babič, D. Horák, P. Veverka, P. Jendelová, *Int J Nanomedicine*, 11 (2016) 6267-6281.
- [81] A. Berger, *BMJ*, 326 (2003) 1449-1449.
- [82] F.J. Beekman, C. Kamphuis, M.A. King, P.P. van Rijk, M.A. Viergever, *Computerized Medical Imaging and Graphics*, 25 (2001) 135-146.
- [83] H. Jiang, F. Thomas, *Journal of Medical Imaging*, 8 (2021) 1-24.
- [84] M.A. Said, M. Musarudin, N.F. Zulkaffli, *Ann Nucl Med*, 34 (2020) 884-891.
- [85] S. Adak, R. Bhalla, K.K.V. Raj, S. Mandal, R. Pickett, S.K. Luthra, 100 (2012) 95-107.
- [86] V.S. Suzanne, J. Marian, H. Vanessa, (2011).
- [87] C.J. Anderson, R. Ferdani, *Cancer Biother Radiopharm*, 24 (2009) 379-393.
- [88] N. Adonai, K.N. Nguyen, J. Walsh, M. Iyer, T. Toyokuni, M.E. Phelps, T. McCarthy, D.W. McCarthy, S.S. Gambhir, *Proceedings of the National Academy of Sciences*, 99 (2002) 3030.
- [89] K. Chen, Z. Miao, Z. Cheng, *Journal of Nuclear Medicine*, 52 (2011) 521.
- [90] A. Bansal, M.K. Pandey, Y.E. Demirhan, J.J. Nesbitt, R.J. Crespo-Diaz, A. Terzic, A. Behfar, T.R. DeGrado, *EJNMMI Research*, 5 (2015) 19.
- [91] G.W. Severin, J.W. Engle, T.E. Barnhart, R.J. Nickles, *Med Chem*, 7 (2011) 389-394.
- [92] C. Kawai, A. Matsumori, T. Nishimura, K. Endo, *Kaku Igaku*, 27 (1990) 1419-1432.
- [93] M. Krekorian, G.G.W. Sandker, K.R.G. Cortenbach, O. Tagit, N.K. van Riessen, R. Raavé, M. Srinivas, C.G. Figdor, S. Heskamp, E.H.J.G. Aarntzen, *Bioconjugate Chemistry*, 32 (2021) 1802-1811.
- [94] R. Meir, R. Popovtzer, *WIREs Nanomedicine and Nanobiotechnology*, 10 (2018) e1480.
- [95] O. Betzer, A. Shwartz, M. Motiei, G. Kazimirsky, I. Gispan, E. Damti, C. Brodie, G. Yadid, R. Popovtzer, *ACS Nano*, 8 (2014) 9274-9285.
- [96] K. Nguyen Phan, D. Trinh, T. Thanh, H. Chuduc, *International Journal of Science and Research (IJSR)*, Volume 4 (2015).
- [97] J.W. Lichtman, J.-A. Conchello, *Nature Methods*, 2 (2005) 910-919.

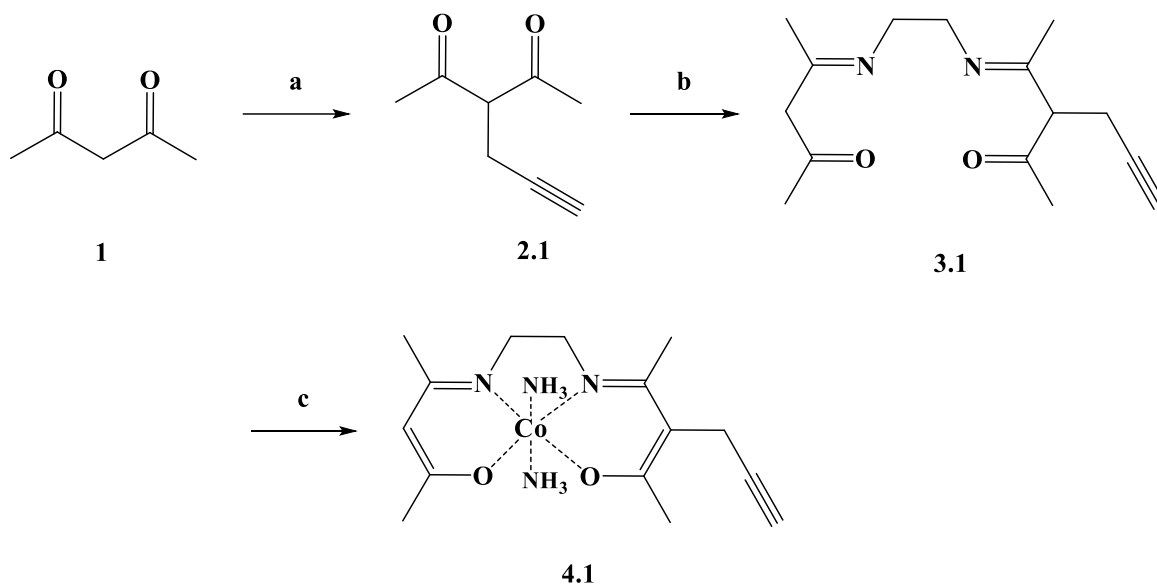
- [98] S. van Keulen, N. Nishio, S. Fakurnejad, A. Birkeland, B.A. Martin, G. Lu, Q. Zhou, S.U. Chirita, T. Forouzanfar, A.D. Colevas, N.S. van den Berg, E.L. Rosenthal, *J Nucl Med*, 60 (2019) 758-763.
- [99] T. Nagaya, Y.A. Nakamura, P.L. Choyke, H. Kobayashi, *Front Oncol*, 7 (2017) 314-314.
- [100] P.T.C. So, C.Y. Dong, B.R. Masters, K.M. Berland, *Annual Review of Biomedical Engineering*, 2 (2000) 399-429.
- [101] H.M. Kim, C. Jung, B.R. Kim, S.-Y. Jung, J.H. Hong, Y.-G. Ko, K.J. Lee, B.R. Cho, *Angewandte Chemie International Edition*, 46 (2007) 3460-3463.
- [102] J. Massue, J. Olesiak-Banska, E. Jeanneau, C. Aronica, K. Matczyszyn, M. Samoc, C. Monnereau, C. Andraud, *Inorganic Chemistry*, 52 (2013) 10705-10707.
- [103] Y. You, S. Cho, W. Nam, *Inorganic Chemistry*, 53 (2014) 1804-1815.
- [104] D. Li, X. Yan, Y. Hu, Y. Liu, R. Guo, M. Liao, B. Shao, Q. Tang, X. Guo, R. Chai, Q. Zhang, M. Tang, *ACS Biomaterials Science & Engineering*, 5 (2019) 1561-1568.
- [105] S. Pleskova, E. Mikheeva, E. Gornostaeva, *Using of Quantum Dots in Biology and Medicine*, in: Q. Saquib, M. Faisal, A.A. Al-Khedhairi, A.A. Alatar (Eds.) *Cellular and Molecular Toxicology of Nanoparticles*, Springer International Publishing, Cham, 2018, pp. 323-334.
- [106] A.B. Rosen, D.J. Kelly, A.J. Schuldt, J. Lu, I.A. Potapova, S.V. Doronin, K.J. Robichaud, R.B. Robinson, M.R. Rosen, P.R. Brink, G.R. Gaudette, I.S. Cohen, *Stem Cells*, 25 (2007) 2128-2138.
- [107] H. Yukawa, M. Watanabe, N. Kaji, Y. Okamoto, M. Tokeshi, Y. Miyamoto, H. Noguchi, Y. Baba, S. Hayashi, *Biomaterials*, 33 (2012) 2177-2186.
- [108] H. Yukawa, Y. Baba, *Analytical Chemistry*, 89 (2017) 2671-2681.
- [109] J.-S. Ni, Y. Li, W. Yue, B. Liu, K. Li, *Theranostics*, 10 (2020) 1923-1947.
- [110] K.C. Nguyen, P. Rippstein, A.F. Tayabali, W.G. Willmore, *Toxicological Sciences*, 146 (2015) 31-42.
- [111] G. Chen, F. Tian, Y. Zhang, Y. Zhang, C. Li, Q. Wang, *Advanced Functional Materials*, 24 (2014) 2481-2488.
- [112] J. Shen, L.-N. Cheng, X.-M. Zhong, X.-H. Duan, R.-M. Guo, G.-b. Hong, *European Journal of Radiology*, 75 (2010) 397-405.
- [113] J.-K. Hsiao, C.-P. Tsai, T.-H. Chung, Y. Hung, M. Yao, H.-M. Liu, C.-Y. Mou, C.-S. Yang, Y.-C. Chen, D.-M. Huang, *Small*, 4 (2008) 1445-1452.

- [114] M. Modo, D. Cash, K. Mellodew, S.C.R. Williams, S.E. Fraser, T.J. Meade, J. Price, H. Hodges, *NeuroImage*, 17 (2002) 803-811.
- [115] M. Modo, K. Mellodew, D. Cash, S.E. Fraser, T.J. Meade, J. Price, S.C.R. Williams, *NeuroImage*, 21 (2004) 311-317.
- [116] M. Modo, J.S. Beech, T.J. Meade, S.C.R. Williams, J. Price, *NeuroImage*, 47 Suppl 2 (2009) T133-T142.
- [117] H.E. Daldrup-Link, M. Rudelius, S. Metz, G. Piontek, B. Pichler, M. Settles, U. Heinzmann, J. Schlegel, R.A.J. Oostendorp, E.J. Rummeny, *European Journal of Nuclear Medicine and Molecular Imaging*, 31 (2004) 1312-1321.
- [118] C.M. Lewis, S.A. Graves, R. Hernandez, H.F. Valdovinos, T.E. Barnhart, W. Cai, M.E. Meyerand, R.J. Nickles, M. Suzuki, *Theranostics*, 5 (2015) 227-239.
- [119] C.K. Sung, K.A. Hong, S. Lin, Y. Lee, J. Cha, J.-K. Lee, C.P. Hong, B.S. Han, S.I. Jung, S.H. Kim, K.S. Yoon, *Korean J Radiol*, 10 (2009) 613-622.
- [120] S. Lim, H.Y. Yoon, H.J. Jang, S. Song, W. Kim, J. Park, K.E. Lee, S. Jeon, S. Lee, D.K. Lim, B.S. Kim, D.E. Kim, K. Kim, *ACS Nano*, 13 (2019) 10991-11007.
- [121] Y. Li, Y. Yao, Z. Sheng, Y. Yang, G. Ma, *Int J Nanomedicine*, 6 (2011) 815-823.
- [122] F.J. Nicholls, M.W. Rotz, H. Ghuman, K.W. MacRenaris, T.J. Meade, M. Modo, *Biomaterials*, 77 (2016) 291-306.
- [123] H. Bao, Y. Xia, C. Yu, X. Ning, X. Liu, H. Fu, Z. Chen, J. Huang, Z. Zhang, *Small*, 15 (2019) e1904314.
- [124] X. Ning, H. Bao, X. Liu, H. Fu, W. Wang, J. Huang, Z. Zhang, *Nanoscale*, 11 (2019) 20932-20941.
- [125] J. Huang, J. Huang, X. Ning, W. Luo, M. Chen, Z. Wang, W. Zhang, Z. Zhang, J. Chao, *Journal of Materials Chemistry B*, 8 (2020) 1713-1727.

Appendix 2

Synthetic Efforts Towards Alkyne and Azide Modified Co(III)-
SB Complexes

A2.1 An alkyne modified Co(III)-SB

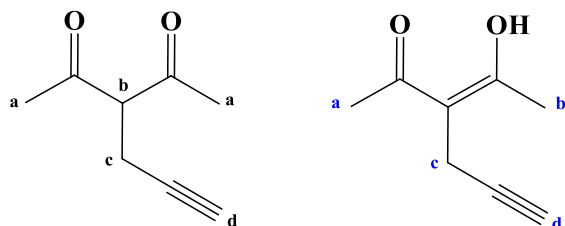


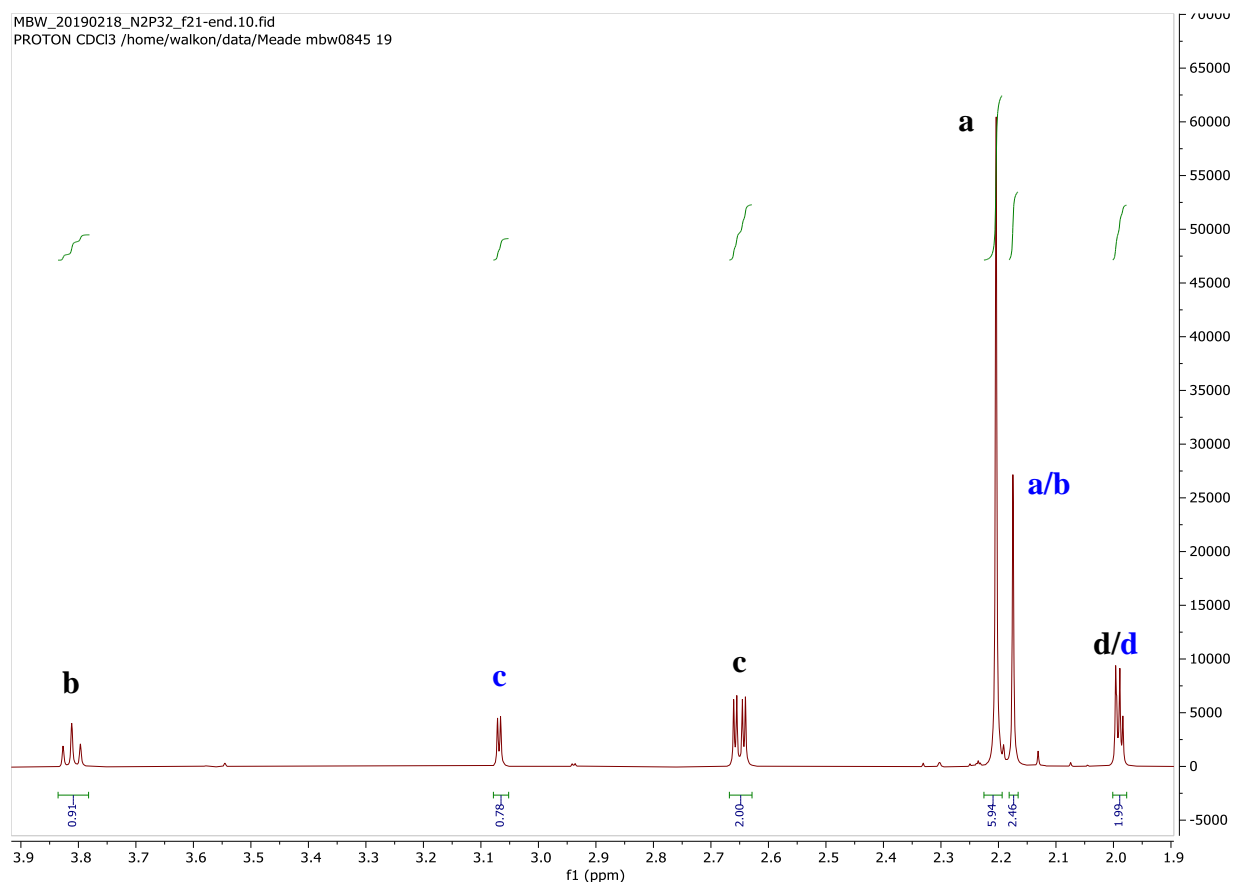
Scheme A2.1: Synthesis of an alkyne modified Co(III)-SB complex. A) Propargyl bromide, acetone, K_2CO_3 , 55°C O/N, wintertime yield $63 \pm 14\%$, summertime yield $31 \pm 13\%$. B) **1** (1eq), ethylenediamine (1eq), CHCl_3 , RT for 48 hrs, 13%. C) 1. $\text{CoCl}_2 \cdot 6\text{H}_2\text{O}$, MeOH. 2. $\text{NH}_3(\text{l})$, 55°C for 2hr, RT O/N, 72%. Conditions listed were ultimately found to be optimal for both yield and purity.

3-(propargyl)penta-2,4-dione (Compound **2.1**): Acetylacetone (4.4 mL, 45 mmol) and potassium bicarbonate (1.5g, 11 mmol) were dissolved in 100 mL of dry acetone and heated to 55°C under constant N_2 gas. Propargyl bromide (1 mL of 80% in toluene, 9 mmol) was added via syringe. The reaction was stirred under N_2 at 55°C for 24 hours. The mixture was allowed to slowly come to RT while stirring by turning off the oil bath. Once cooled, the reaction mixture was filtered to remove undissolved potassium bicarbonate via Buchner funnel and the potassium

carbonate was rinsed with acetone to collect any residual organics. The solvent was removed from the filtrate via low vacuum pressure rotary evaporation. The product was purified via column chromatography with silica gel in a 7:3 hexane/dichloromethane running buffer with 5 mL of ethyl acetate added to every 1 L of solvent prepared. The product, a yellow oil, comes off in the final fraction of the column (MW=138.16 g/mol). Notably, this product exists both in the diketone and mono ketone/mono enol form in solution. The following NMR data represents peaks from the diketone and the mono enol (in blue) from this representative NMR. The majority of NMRs collected on this product reflect a 1:0.4 ratio of diketone to the mono enol.

^1H NMR (500 MHz, CDCl_3) 3.81 (t, 1H (b) , $J=7.5$ Hz), 3.07 (d, 2H (c), $J=2.7$ Hz), 2.65 (dd, 2H (c), $J^1=7.5$ Hz, $J^2=2.7$ Hz), 2.20 (s, 6H (a)), 2.17 (s, 6H (a/b)), 1.99 (t, 2H, (d/d) $J=2.5$ Hz).

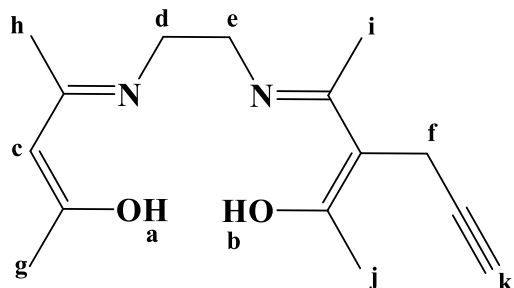




Interestingly, this reaction produces significantly different results in yield depending upon the season in which the reaction is performed. This is likely attributed to differences in humidity, which suggests that water significantly reduces the reaction process.

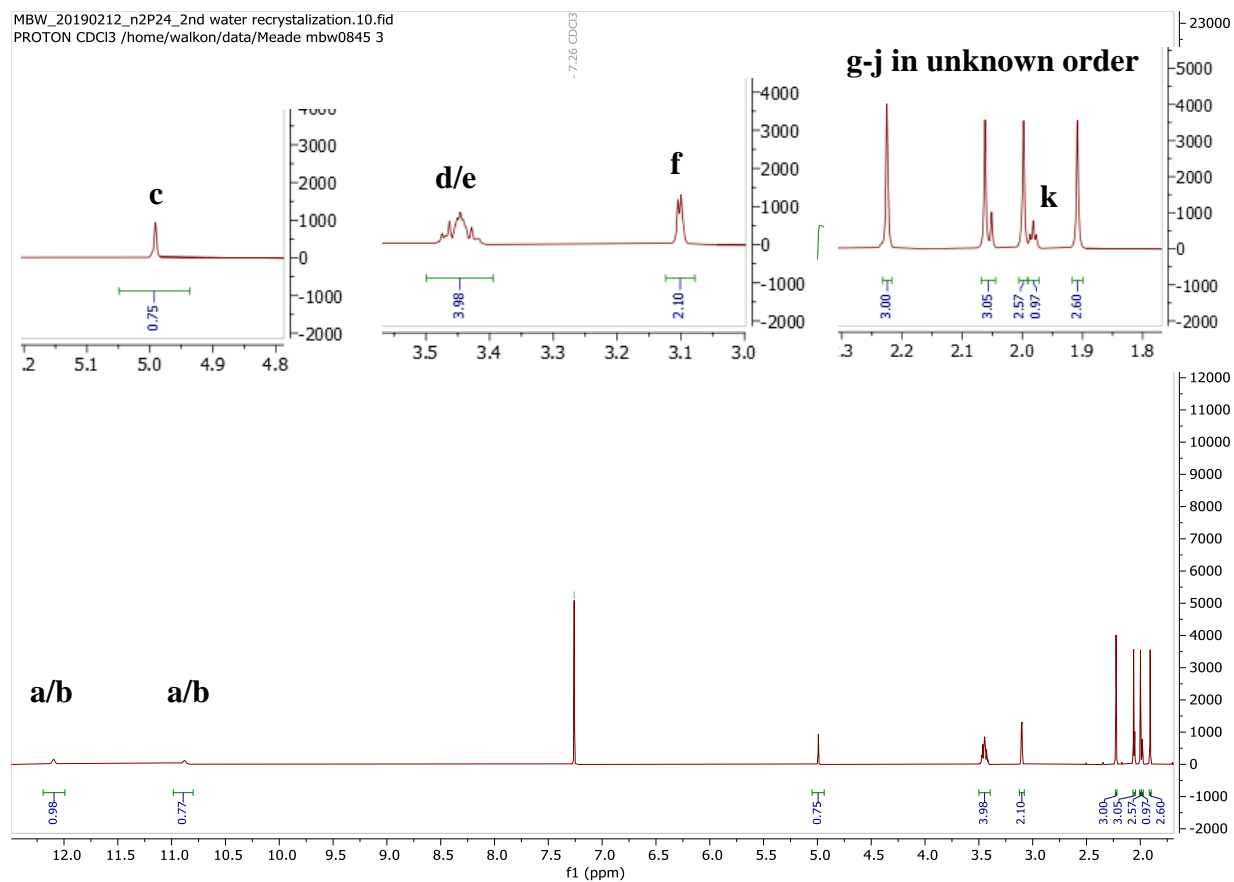
3-(E-1-((2-((E-4-oxopentan-2-ylidene)amino)ethyl)imino)ethyl)hex-5-yn-2-one (3-propargyl-acacen, Compound **3.1**): Ethylenediamine (0.40 mL, 6 mmol) was dissolved in 25 mL of chloroform (not dried) in a 250 mL round bottom flask with a stir bar. Acetylacetone (0.565 mL, 5.5 mmol) was dissolved in 25 mL of chloroform in a dropper funnel. Acetylacetone was dropped slowly into ethylenediamine and then stirred for 4 hours. Compound **2.1** was dissolved in 5 mL of chloroform in the same dropper funnel and added dropwise to the reaction mixture. The resulting mixture was left to stir for 48 hours. Chloroform was removed via low pressure

rotary evaporation and the product was purified via column chromatography in 1% MeOH/DCM. (MW= 262.33 g/mol).

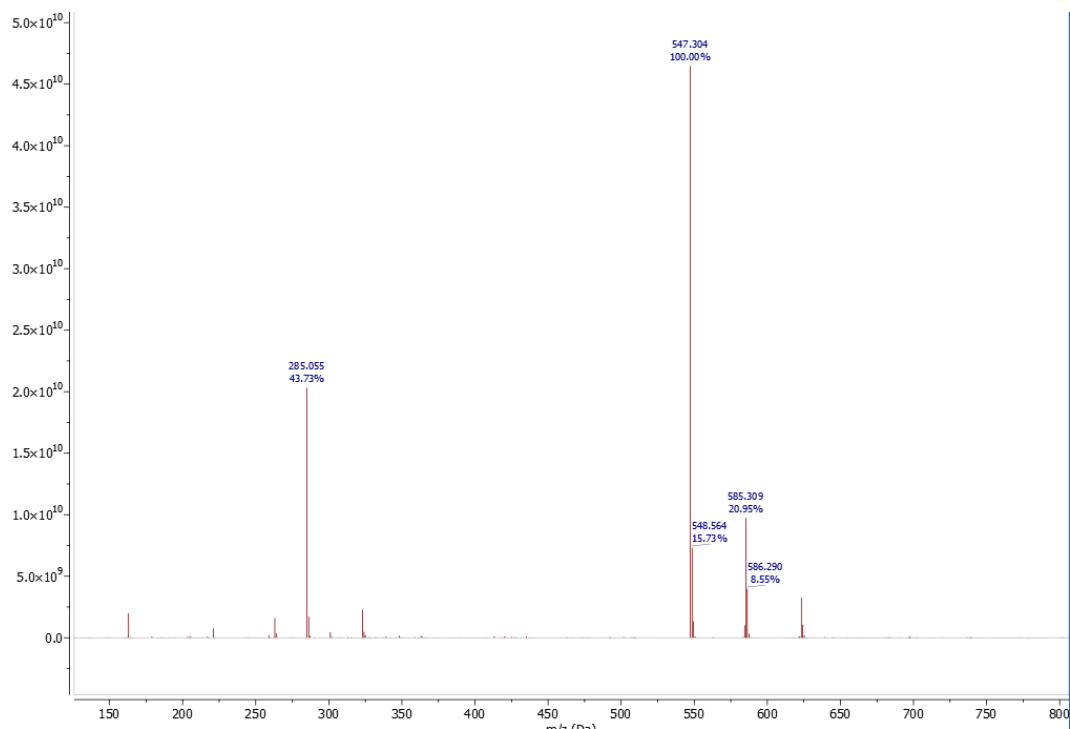


$^1\text{H NMR}$ (500 MHz CDCl_3) 12.10 (s, 1H) 10.88 (s, 1H) 4.99 (s, 1H) 3.45 (m, 4H) 3.10 (d, 2H, $J=2.2$ Hz) 2.23 (s, 3H) 2.06 (s, 3H) 2.0 (s, 3H) 1.98 (t, 1H, $J=2.6$ Hz) 1.91 (s, 3H)

Letters represent most likely assignments



ESI-MS m/z $C_{15}H_{22}N_2O_2$ $[M+Na]^+$: 285.16 found 285.055 $[2M+Na]^+$: 547.33 found 547.304



While column chromatography in 1%MeOH/DCM proved effective for purification, recrystallizations were also attempted. After rotary evaporation, minimal boiling water was used to dissolve the product. Upon rapid cooling in an ice bat, the disubstituted propargyl acacen product crashed out of solution. When the filtrate was left at 4°C overnight, a minimal amount of monosubstituted product **3.1** was recovered. These recrystallization could be further explored for purification.

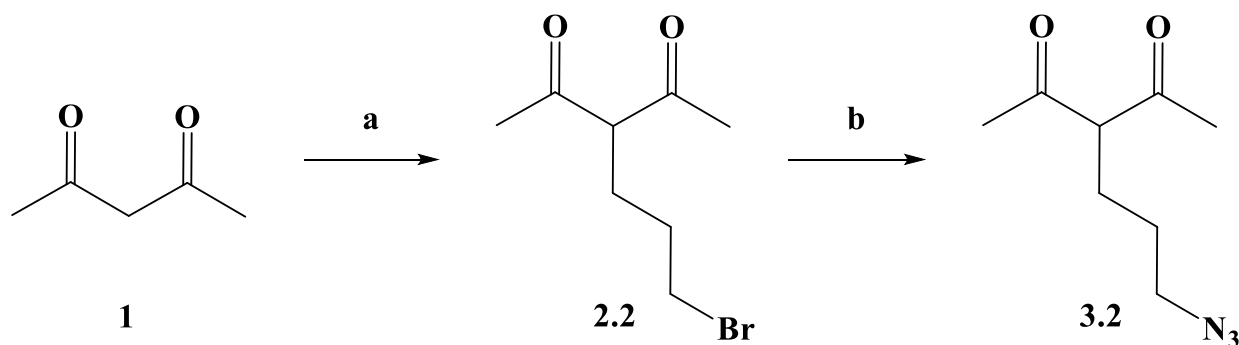
For future improvement of this reaction, it would be recommended to explore bone dry chloroform as a solvent. As water is produced throughout the reaction, it is likely that excess water present in the reaction mixture may prevent complete conversion to the desired product.

[Co(III)(3-Propargyl-acacen)(NH₃)₂]⁺Cl⁻ (Complex **4.1):** Compound **3.1** (33 mg, 0.126 mmol) was dissolved in 1 mL of methanol in a 5 mL round bottom flask with a stir bar under N₂ gas.

Cobalt(II) chloride hexahydrate (16.3 mg, 0.126 mmol) was dissolved in 1 mL of methanol and added to the vessel via syringe. The resulting mixture was stirred at room temperature for 15 minutes with continuous N₂ atmosphere. The mixture was exposed to air, heated to 55° C, and liquid ammonia (75 μL of 7N, 0.504 mmol) was added. The mixture stirred exposed to air for 2 hours before heat was removed and allowed to cool and react overnight. After at least 12 hours, the mixture was transferred to a 50 mL conical tube and diluted to 50 mL with diethyl ether slowly. The tube was centrifuged for 10 minutes to pellet the product before decanting over a Buchner funnel, washed with diethyl ether, and dried. (MW=388.78)

ESI-MS m/z C₁₅H₂₀CoN₂O₂ [M-Cl-2NH₃]⁺: 319.09. Found 319.06.

A2.2 Efforts towards an azide modified acetylacetone for click chemistry

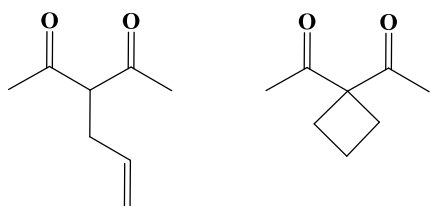


Scheme A2.2: Synthesis of an azide modified acetylacetone. A) 1,3-dibromopropane, K₂CO₃, DMF, 50° C 24 hours, 24% yield. B) NaN₃, DMSO, 24 hours. Was not purified for yield calculations.

3-(2-bromopropyl)penta-2,4-dione (Compound **2.2**): Dry potassium bicarbonate (1.5g, 11 mmol) was suspended in 150 mL of dry dimethyl formalin and heated to 50°C with a stir bar under N₂ atmosphere. Acetylacetone (1.14 mL, 10.86 mmol) was added via syringe. Once

heated, 1,3-dibromopropane (1.21 mL, 11.95 mmol) was added via syringe. The reaction proceeded under N₂ for 24 hours. To extract, 100mL of brine was added before extracting 5x 50 mL in diethyl ether. The resulting extract was washed with brine and dried over MgSO₄ for 30 minutes, filtered and ether was removed under low vacuum rotary evaporation. The resulting crude yellow oil was purified via column chromatography in 20% ethylacetate/80% hexanes. The desired product is the first to elute. (MW=221.09 g/mol). ESI data represents co-eluted products of the desired product and one of the potential side products.

Potential biproduct A Potential Biproduct B



MW of both=140.08

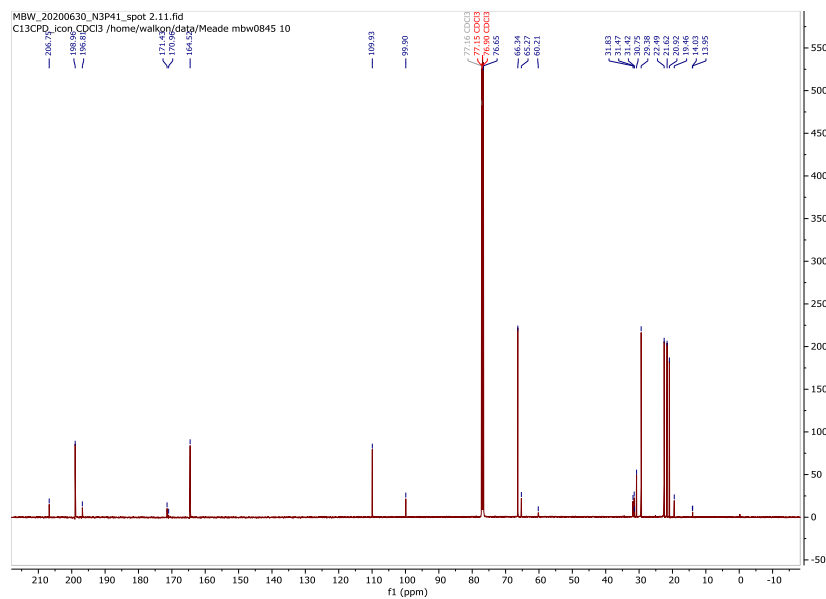
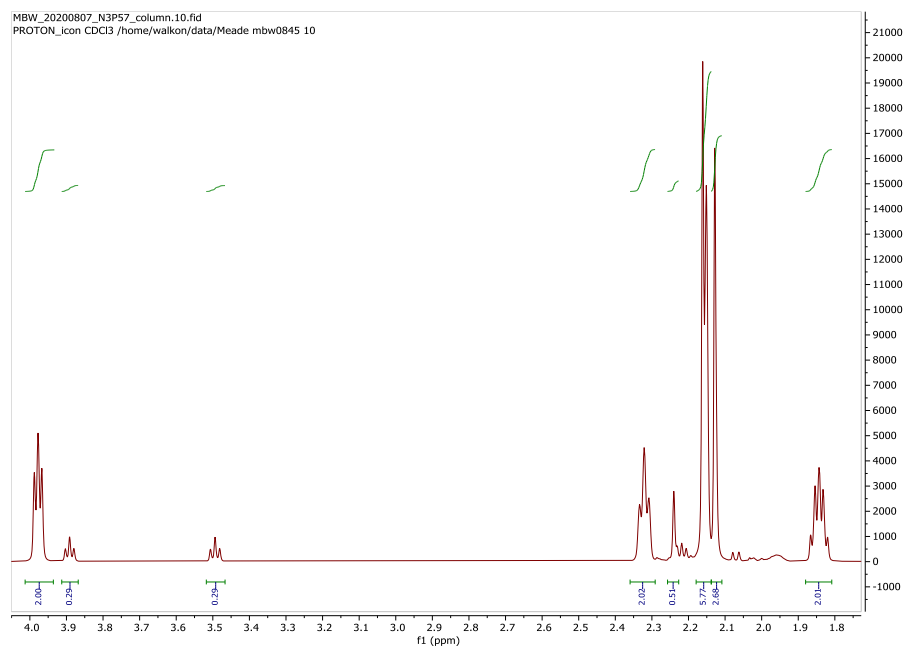
¹HNMR (500 MHz, CDCl₃) 3.98 (t, 2H, *J*=5.2 Hz) 2.32 (t, 2H, *J*=6.6 Hz) 2.16 (d, 6H, *J*=5 Hz)
1.84 (m, 2H, *J*=6 Hz)

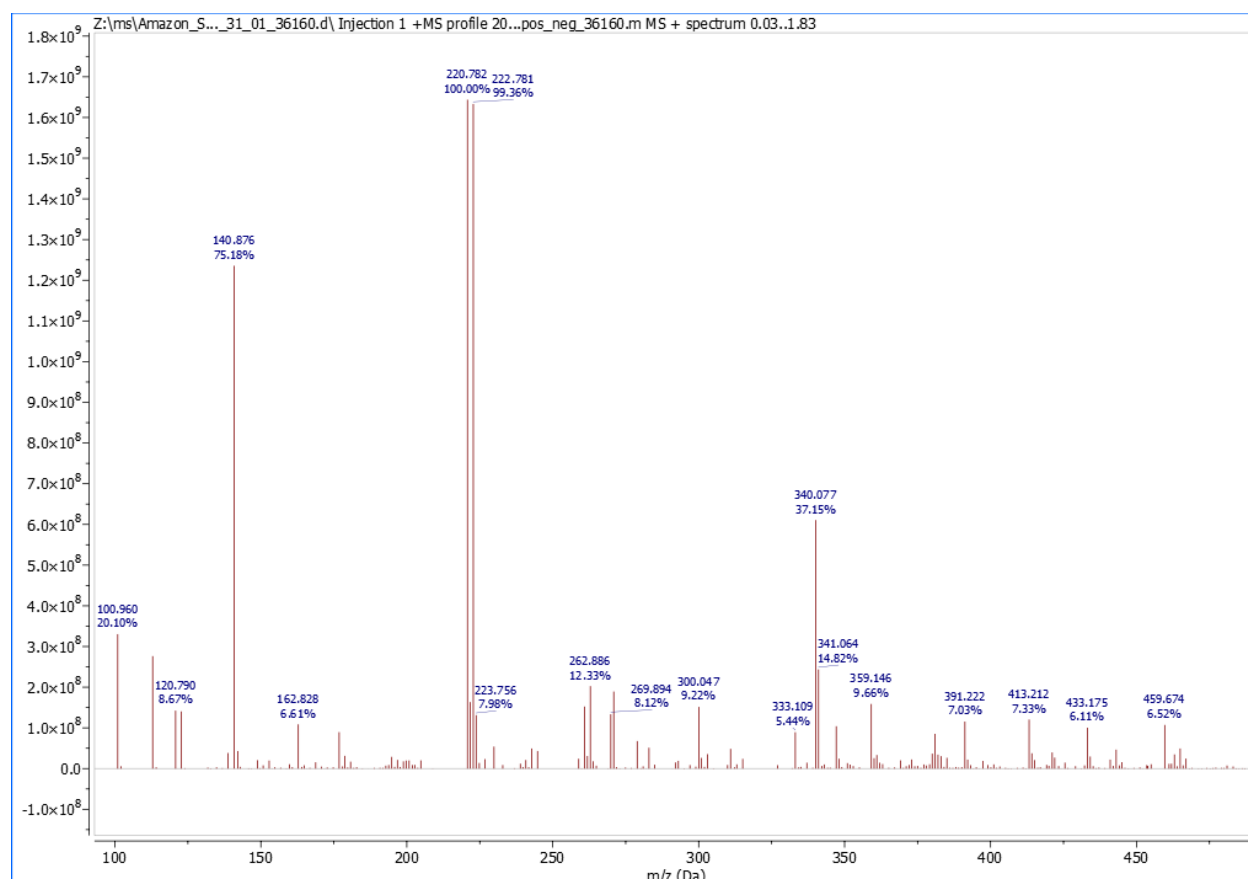
Impurities are observed at 3.89 (t, *J*=5.8 Hz) 3.49 (t, *J*=6.34 Hz) 2.24 (s) 2.13

¹³CNMR (500 MHz, CDCl₃) 198.96, 164.52, 100.93, 66.34, 29.38, 22.49, 21.62, 90.92

The presence of 8 main peaks in ¹³CNMR suggests that the product is primarily in the mono enol form. This is corroborated by the presence of only 4 main peaks in the ¹HNMR, as a peak for the 1H in the alpha position is not found.

ESI-MS m/z C₈H₁₃⁷⁹BrO₂ [M+H]: 221.01 found 220.794 C₈H₁₃⁸¹BrO₂ [M+H]: 223.0 found 222.796

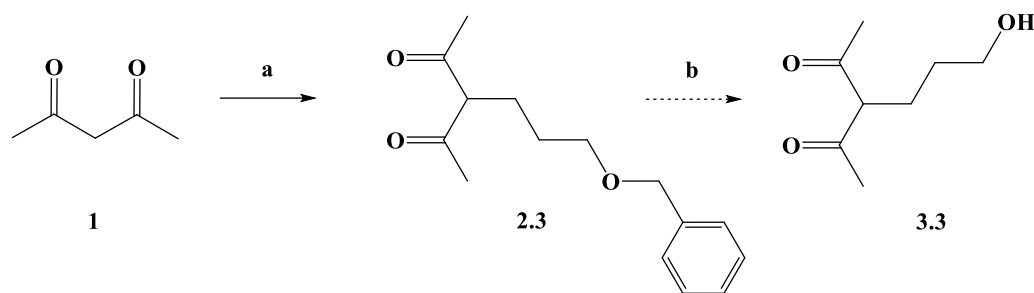




3-(2-azidopropyl)penta-2,4-dione (Compound **3.2**): Compound **2.2** (230 mg, 1 mmol) and sodium azide (230 mg, 3 mmol) were dissolved in 15 mL of dimethylsulfoxide at room temperature and stirred for 24 hours. 20 mL of water was added, and the product was extracted in diethylether. Column conditions could not be found to separate the desired product from side products, and MS data represent the crude mixture. (MW=183.10)

Extra Notes: Compound **2.2** was also used to attempt condensation reactions with ethylene diamine. Regardless of solvent and time, condensation with an intact bromine was never observed. For this strategy to ultimately be successful, the bromine will have to be substituted prior to condensation.

A.3 Efforts towards an alcohol-modification for functionalization



Scheme A.3: Route 1 for an alcohol appended acac molecule. A) Benzyl-3-bromopropylether, K_2CO_3 , DMF, $50^\circ C$ 90% yield. B) Attempted hydrogenolysis with Pd/C with both N_2 gas and triethylsilane as H_2 sources. No deprotection was observed.

3-(3-(benzyloxy)propyl)penta-2,4-dione (Compound **2.3**): In a small round bottom flask, potassium bicarbonate (60 mg) was dissolved in 5 mL of DMF. The solution was heated to $50^\circ C$ under N_2 atmosphere. Acetylacetone (45 μL , 0.436 mmol) was added via syringe. After 20 minutes, benzyl-3-bromopropylether (77 μL , 0.436 mmol) was added to the yellow solution via syringe and the resulting brown reaction mixture was stirred under N_2 atmosphere for 24 hours. Heat was removed and the reaction cooled slowly to room temperature. 50 mL of brine was added to dilute the DMF and the product was readily extracted x2 with 50 mL of diethylether. The organic layers were collected, washed with brine, and dried over $MgSO_4$. Ether was removed via low vacuum rotary evaporation. (MW=248.14 g/mol)

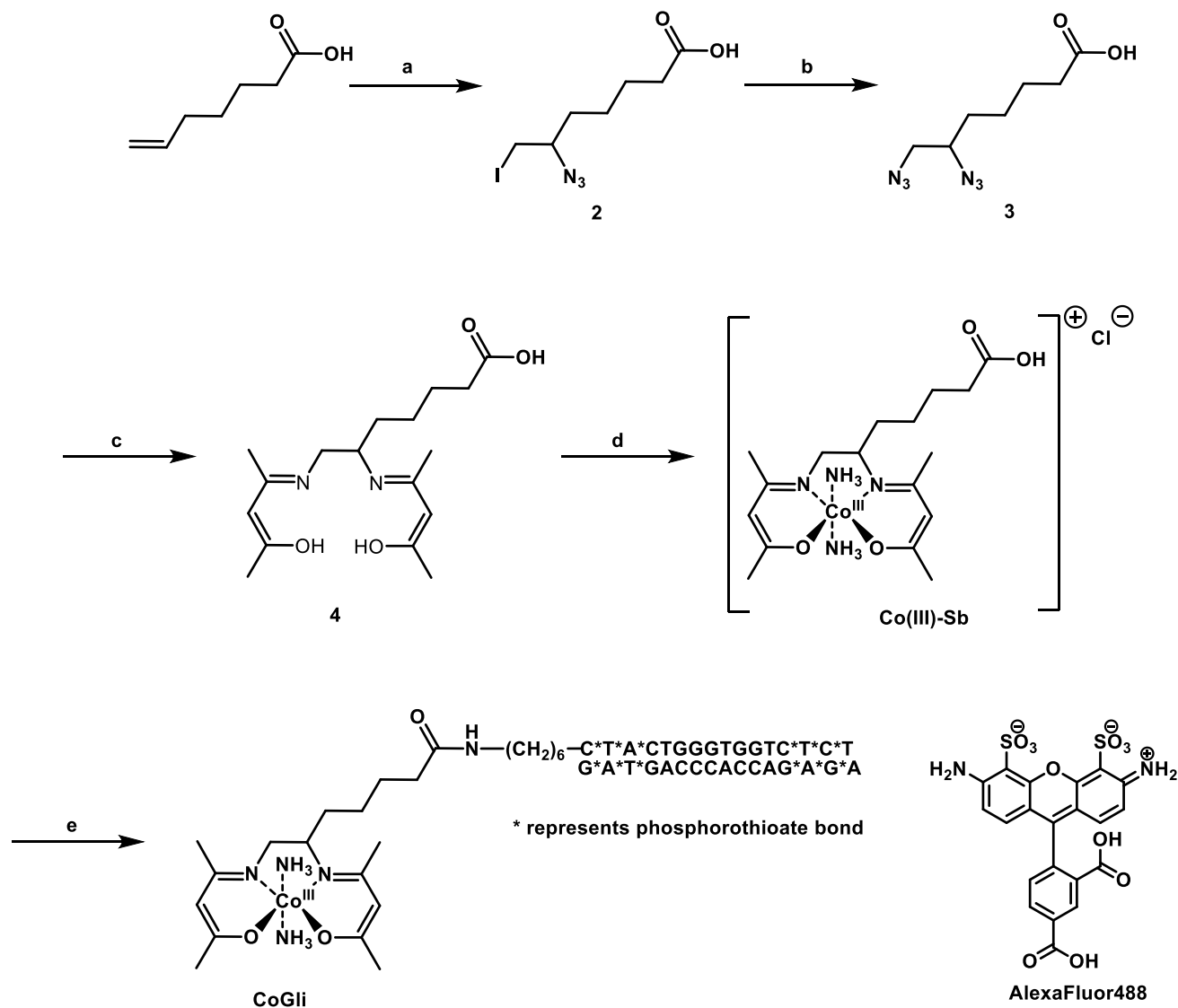
3-(3-hydroxypropyl)penta-2,4-dione (Compound **3.3**): The crude product **2.3** was dissolved in 10 mL of methanol and one small scoop of Pd/C was added. The reaction mixture was purged with N_2 gas for 5 minutes, purged with H_2 gas for 5 minutes, and held under H_2 pressure for 24 hours. After 24 hours, conversion was not observed and the mixture was purged again with H_2 and held under constant H_2 pressure for 4 days. Conversion was still not observed.

As a final attempt, the mixture was purged with N₂ for 20 minutes before triethylsilane (700μL) was added as an in-situ hydrogen source. After 24 hours, conversion was still not observed.

While this strategy was worthy to explore, substitution of azide from a halide will result in fewer synthetic steps and more synthetic feasibility. That is the recommended strategy for future exploration of an azide modified Co(III)-SB complex.

Appendix 3

Synthesis of Co(III)-DNA Complexes



Scheme 3.1: Synthesis of CoGli. a) ICL, NaN_3 , CH_3CN , 83%. b) NaN_3 , DMF, 55°C , 76%. c) 1. H_2 , Pd/C, MeOH, 67%. 2. 4-pentadione, MeOH/EtOH (2:3), 0°C , 9.8%. d) 1. $\text{CoCl}_2 \cdot 6\text{H}_2\text{O}$, MeOH. 2. NH_3 (l) 99%. e) 1. NHS, DCC, DMF. 2. 5'-amino-modified Gli ssDNA (5'-amino- $(\text{CH}_2)_6\text{-C}^*\text{T}^*\text{A}^*\text{CTGGGTGGTC}^*\text{T}^*\text{C}^*\text{T}^*-\text{3}'$), 100 mM MES, pH 6.0. 3. Complementary Gli ssDNA (3'- $\text{G}^*\text{A}^*\text{T}^*\text{GACCCACCAG}^*\text{A}^*\text{G}^*\text{A}^*-\text{5}'$). For CoGliF, complementary Gli ssDNA is modified at the 5' end with AlexaFluor488.

6-azido-7-iodoheptanoic acid (Compound 2): Iodinemonochloride (0.74 mL, 14.8 mmol) was diluted in 15 mL of acetonitrile and added dropwise via addition funnel to a suspension of sodium azide (1.9 g, 29.5 mmol) in 10 mL of acetonitrile with stirring at 0°C . The resulting

solution is a dark orange. Once addition is complete, the reaction is warmed slowly to room temperature by allowing the ice bath to slowly melt. Dissolved in 5 mL of acetonitrile, 6-heptenoic acid (1.0 mL, 7.38 mL) is added dropwise via addition funnel. Reaction completion was determined via TLC analysis. Water was added to dilute the reaction mixture, and the aqueous layer was extracted with diethyl ether. The combined organic layers were washed with 5% (w/v) sodium thiosulfate until the color disappears from the organic and aqueous layer. The organic layer was decanted, dried over magnesium sulfate, and concentrated under reduced pressure. The product was purified via flash chromatography in 2:3 ethylacetate:hexanes to give a pale yellow oil (MW=296.09 g/mol). ^1H NMR (600 MHz, CDCl_3) δ 3.41 (dd, $J = 10.6, 16.5$, 1H), 3.26 (d, $J = 5.7$, 2H), 2.40 (t, 2H), 1.83–1.37 (m, 6H). ^{13}C NMR (151 MHz, CDCl_3) δ 179.62, 62.45, 34.12, 33.73, 25.26, 24.17, 8.21. Analysis calculated (Anal. Calcd.) for compound 2: C, 28.30; H, 4.07; N, 14.14. Found: C, 28.43; H, 4.12; N, 14.80.(1)

6,7-diazidoheptanoic acid (Compound 3): Sodium azide (1.95 g, 30 mmol) and compound 2 (1.776 g, 6.0 mmol) were stirred in 15 mL of N,N'-dimethylformamide at 55 °C overnight. The organic layer was diluted with water and extracted with diethylether. The organic layers were washed with brine, dried over magnesium sulfate, and concentrated under reduced pressure. The crude product was not purified further, and gave a light yellow oil (MW=211.20 g/mol). ^1H NMR (500 MHz, CDCl_3) δ 3.61–3.23 (m, 3H), 2.40 (t, $J = 7.0$, 2H), 1.77–1.36 (m, 6H). ^{13}C NMR (126 MHz, CDCl_3) δ 179.36, 61.79, 54.80, 33.64, 31.45, 25.33, 24.24. Electrospray ionization mass spectrometry (ESI-MS) (m/z) $\text{C}_7\text{H}_{12}\text{N}_2\text{O}_2$ $[\text{M}-\text{H}]^-$: Calc. 211.0960, found 211.09504.(1)

6,7-Bis(2-Imino-4-Oxopentyl)Heptanoic Acid (Compound 4): Compound 3 (0.993 g, 4.7 mmol) was dissolved in 50 mL of methanol and purged with nitrogen gas before adding

palladium on carbon (10% by weight). A full balloon filled with hydrogen gas was purged through the reaction mixture before leaving the mixture under hydrogen pressure overnight. Reaction progress was monitored via TLC in 5% methanol in dichloromethane and stained by ninhydrin. The mixture was filtered over celite to remove palladium on carbon and concentrated under reduced pressure. (MW= 160.21 g/mol). Without further purification, the diamine (0.6148 g, 4.01 mmol) was dissolved in 10 mL 2:3 methanol to ethanol and added dropwise to a solution of 2,4-pentadione (0.824 mL, 8.02 mmol) in 10 mL 2:3 methanol to ethanol at 0 °C. The corn yellow reaction mixture was then warmed slowly to room temperature by allowing the ice bath to melt. The product is concentrated under reduced pressure to give a yellow solid. The crude material is recrystallized in hot toluene to give a white solid (MW= 324.2 g/mol). ¹H NMR (600 MHz, CDCl₃) δ 11.00 (s, 1H), 10.89 (d, *J* = 10.1, 1H), 4.97 (s, 1H), 4.95 (s, 1H), 3.61 (bs, 1H), 3.36–3.26 (m, 2H), 2.34 (dd, *J* = 7.0, 13.9, 2H), 2.00 (s, 6H), 1.87 (d, *J* = 15.1, 6H), 1.70–1.37 (m, 6H). ¹³C NMR (151 MHz, CDCl₃) δ 195.36, 195.26, 176.16, 163.77, 163.48, 96.11, 96.02, 54.29, 48.70, 33.72, 33.02, 28.71, 28.64, 25.29, 24.49, 19.05, 18.75. ESI-MS (*m/z*) C₁₇H₂₇N₂O₄ [M-H]⁻: Calc. 323.1976, found 323.19764. Anal. Calcd. for compound 4: C, 62.94; H, 8.70; N, 8.64. Found: C, 63.12; H, 8.67; N, 8.53.(1)

[Co(III)(Heptanoic Acido)(Acacen)(NH₃)₂]⁺Cl⁻ [Co(III)-sb]: Compound 4 (0.128 g, 0.4 mmol) was combined with cobalt(II) chloride hexahydrate (0.13 g, 0.47 mmol) in 10 mL of methanol and purged with nitrogen gas for 15 minutes. The reaction mixture was raised to 55 °C and stirred for 30 minutes. A solution of 7N NH₃ (1 mL, 1 mmol), was added and the mixture was stirred for another 2 hours. The mixture was opened to air and stirred overnight at RT. The resulting mixture was concentrated under reduced pressure to give a brown solid. (MW=381.12 g/mol). ESI-MS (*m/z*) C₁₇H₂₅CoN₂O₄ [M-2NH₃]⁺: 381.12. found 381.16.

CoGli: In a DNA low-bind Eppendorf tube, Co(III)-Sb (25 mg,), N-hydroxysuccinimide (69.4 mg,), and N, N'-dicyclohexylcarbodiimide (40.8 mg,) were dissolved in 1 mL of dry DMF and vortexed until all solids dissolved. The Eppendorf was turned end-over-end for two hours before 500 μ L were split into another low-bind tube. To each tube, 675 μ L of MES buffer were added along with 5'-amino modified Gli ssDNA (125 nmol) before turning end-over/end overnight. The tubes were then centrifuged to remove urea-biproduct solids. The supernatant was removed and recombined into a 15 mL centrifuge tube. The urea biproduct solids in the eppendorfs were resuspended with 200 μ L of UltraPure water and washed by centrifugation. The supernatant from the wash was also added to the 15 mL centrifuge tube before centrifugation to remove any remaining solids. The final supernatant was transferred to a 50 mL centrifuge tube and concentrated under reduced pressure on a Schelk line. Once dry, the product was dissolved in 7.5 mL of sterilized UltraPure water and combined with complementary Gli ssDNA (250 nmol). The mixture was heated at 95 °C for 3.5 minutes before transferring to an enclosed, insulated Styrofoam block for slow cooling overnight. The solution was freeze-dried and resuspended in 2 mL of MES buffer for purification via NAP25 size exclusion chromatography. After running through two columns, fractions were analyzed for DNA concentration by UV-Visible Spectroscopy and for Cobalt concentration by ICP-MS.

Appendix 4

Cell Culture Protocols

ASZ Cells

Making Media

Ingredients

- 1 full M154CF (calcium free) base
- 10 mL chelexed FBS
- 5mL pen/step
- 125 μ L CaCl₂

Add to top of filtration system, pull through w/vacuum. Label with name, media type, cell type, ingredients, and date.

*For serum free media, follow same recipe *without* FBS

Thawing

- Pre-warm media in water bath
- Remove cells from cane and mark it on the spreadsheet. Thaw by rubbing with 2 hands
- In the hood, add 4 mL of media to a sterile T25 flask (25 cm²)
- Add 1 mL of cells to the flask and rock to disperse. Label flask with passage number
- Incubate, swap media the next morning

Splitting from T25

- Pre-warm media in water bath
- Aspirate off media. Wash x1 with DPBS and aspirate it off. Wash once more with DPBS, and incubate for 10 minutes at 37°C. Aspirate.
- Add 1 mL of Trypsin and rock to cover surface. Let incubate *at least 10 minutes*, more if necessary. Make sure cells are completely detached.

- Add 4 mL of media and pipette up and down, making sure cell chunks are suspended well. Transfer to 15 mL conical tube.
- Centrifuge at 200 rcf for 10 minutes. Aspirate carefully.
- Add 5mL of media to new sterile T75 flask.
- Resuspend cells in 5 mL of media. Pipette up and down to fully resuspend
- Add cell suspension to T75. Incubate.

Splitting from T75

- Same procedure as above, but :
 - Use 2 mL of trypsin
 - when adding to new T75, use appropriate volumes of media and cell suspension for the desired split ratio. (Remember: a 1:10 split means taking 1/10 of the previous cell number and passaging them forward.) Total media volume should be between 10-12 mL.
 - Typically best split is a 1:5 for 2-3 days until the next split

C3H/10T_{1/2} Cells

Making Media

Ingredients

- 1 full BME base
- 50 mL of FBS
- 5mL L-Glu (2mM conc.)

Add ingredients to filtration system and pull through with vacuum in the hood. Label with name, media type, cell type, ingredients, and date.

*For serum free media, follow same recipe *without* FBS

Thawing

- Remove cells from can (mark on spreadsheet) and thaw in hand.
- In the hood, add 9 mL of media to a sterile T75 flask.
- Add 1 mL of cells to T75 and rock to distribute. Label dish with passage number
- Incubate, swap media next morning.

Splitting Cells must be split prior to reaching 70% confluency to maintain stemness

- Aspirate off media.
- Wash x1 with DPBS
- Add 1 mL Trypsin and incubate for about 5 minutes at 37°C. Check to make sure cells have detached.
- Add 5 mL of media. Use to wash bottom of plate, and pipette cells up and down to suspend homogeneously.
- Add appropriate amount of media and cell suspension to a new sterile T75 flask for desired split. 1:10 is typically ideal

J2 Fibroblast cells

Making Media

Ingredients

- 1 full D5671 base
- 50 mL of normal calf serum (NCS)
- 10 mL L-Glu
- 100 μ L gentamicin and 500 μ L amphotericin B antibiotics

:Label with name, media type, cell type, ingredients, and date.

Thawing

- Remove cells from cryofreezer and thaw in hand.
- In the hood, add 9 mL of media to a sterile 100 cm² cell culture dish.
- Add 1-2 mL of cells to dish and rock to distribute. Label dish with passage number.
- Incubate, swap media next morning.

Splitting Cells must be split prior to reaching 70% confluency to maintain identity

- Aspirate off media. Wash x1 with DPBS
- Add 1 mL Trypsin and incubate for 4-5 minutes at room temp. Check to make sure cells have detached.
- Add 5 mL of media. Use to wash bottom of plate, and pipette cells up and down to suspend homogeneously.
- Centrifuge at 200 rcf for 10 minutes. Aspirate carefully.
- Add 10mL of media to new sterile culture dish.
- Resuspend cells in 5 mL of media. Pipette up and down to fully resuspend
- Split to desired ratio

Normal human primary keratinocytes (NHEKs)

Making Media

Ingredients

- 1 full M154CF (calcium free) base
- 1 human keratinocyte growth serum kit (5 mL)
- 100 μ L gentamicin and 500 μ L amphotericin B antibiotics
- 175 μ L CaCl_2

Label with name, mark as “complete” and label date

Thawing

- Remove cells from cryofreezer and thaw in hand.
- In the hood, add 9 mL of media to a sterile 100 cm^2 cell culture dish.
- Add 1-2 mL of cells to dish and rock to distribute. Label dish with passage number and days since isolation
- Incubate, swap media next morning.

Splitting **Cells cannot be used passed passage 4 day 21 since isolation**

- Pre-warm media in water bath
- Aspirate off media. Wash x1 with DPBS and aspirate it off.
- Add 2 mL of Trypsin. Let 7 minutes. Make sure cells are completely detached.
- Add 4 mL of media and pipette up and down, making sure cell chunks are suspended well. Transfer to 15 mL conical tube.
- Centrifuge at 200 rcf for 10 minutes. Aspirate carefully.
- Add 10 mL of media to new sterile culture dish
- Resuspend cells in 5 mL of media. Split to desired ratio

Appendix 5

Antibody Information and qPCR Primer Sequences

Table A5.1: Primary Antibody Information

Name	Clone	Dilution Factor	Company
K10	EP1607IHCY	1:500	Abcam
K16	LL025	1:200	Neomarkers (Santa Cruz Biotechnology)
K17	D12E5	1:200	Cell Signaling
pan-ECAD	24E10	1:100	Cell Signaling
HECD-1		1:100	
DSG1	4B2 (lot) WL3448367A	1:50	Invitrogen
DSC1		1:100	
Ki67	8D5	1:2000	Cell Signaling
FLG	Poly19058	1:100	Biolegend
pan-Laminin	NB 300-144	1:100	Novus Biologicals

Table A5.2: qPCR primer sequences from 5' → 3'

Transcript	Fwd/Rev	Sequence
RPLPO	F R	CAGATTGGCTACCCAACCTGTT GGGAAGGTGTAATCCGTCTCC
mRpl19	F R	GAAGGTCAAAGGGAATGTGTTCAA TTTCGTGCTTCCTTGGTCTTAGA
KRT10	F R	TTCAGCGGCGGCTCTTTTAG GTCTCCTCCGAATCCACCA
KRT16	F R	TCCTGAATGAGATGCGTGACCAGT GCTGTTGGAGGCCACTTCTTTGTT
KRT17	F R	GTGGGTGGTGAGATCAATGT CGTTCCTTCTCTGCCATCTT
KRT75	F R	ACCGAGAGGGGCAGGCTTGAAG GAGTGGATGAAGTTGATCTCCTCGGG
DSG1	F R	TCCATAGTTGATCGAGAGGTCAC CTGCGTCAGTAGCATTGAGTATC
DSC1	F R	GTCAGAGACGGGAACAACAAG CCCAACGAGTTCTCCATCAATG
CDH1	F R	GTCATTGAGCCTGGCAATTTAG GTTGAGACTCCTCCATTCCTTC
FLG	F R	AATACGGTCAGGACACCATTC CCTGAGTGTCCAGAGCTATCTA
GLI1	F R	AGCTAGAGTCCAGAGGTTCAA TAGACAGAGGTTGGGAGGTAAG

HHIP	F R	GTCATGGAGGTGTCTGTGTAG GTCACTCTGCGGATGTTTCT
msGli1	F R	ACCACCCTACCTCTGTCTATTTC TTCAGACCATTGCCCATCAC
msHhip	F R	CCTGCTACTGTCTCACCTAAAC GGAGAAGGAGTTGGAAGAAGAG

All sequences were purchased from Integrated DNA Technologies and dissolved at 100 μ M for long term storage. Primer mixes (Fwd + Rev) were made at concentrations of 10 μ M of each primer (10 μ L of fwd + 10 μ L of rev + 80 μ L of water).

Meghan W. Dukes

1644 W Morse Ave Apt 2W | Chicago, IL 60626 | (865)-209-4110
 Meghanward2022@u.northwestern.edu

Education

Northwestern University; Evanston, Illinois	September 2017-July 2022
Ph.D. Candidate in Chemistry	GPA: 3.790
Advisor: Thomas J. Meade	
Ruth L. Kirschstein National Research Service Award Pre-Doctoral Fellow	
Edmund W. Gelewitz Award for Excellence in Research and Service Finalist	
Auburn University; Auburn, Alabama	August 2013-May 2017
BS Chemistry, Suma Cum Laude	GPA: 3.980
Presidential Scholar, C. Harry Knowles Scholar, University Honors Scholar	

Research Experience

Northwestern University

Under Professor Thomas J. Meade
September 2017-July 2022

Inorganic Coordination Chemistry for Inhibition of Transcription Factors

Exploring the efficacy of transition metal complexes as inhibitors of transcription factors associated with cancer cell proliferation. Will further develop skills of molecular characterization, as well as *in vitro* experimentation.

Ruth L. Kirchestein National Research Service Award Pre-Doctoral Fellow

National Science Foundation Graduate Research Fellowships Program Honorable Mention

In collaboration with Professor Bethany Perez-White
April 2021-July 2022

Primary Epidermal Keratinocytes as Basal Cell Carcinoma Models

Studying exogenous activation of oncogenic pathways to elucidate molecular mechanisms associated with cancer onset. Further studying the communication between healthy keratinocytes and cancerous basal cells during differentiation processes as models of cancer progression. Developing biochemical analysis skills and stem cell isolation and culture.

Auburn University

Under Professor Christian R. Goldsmith
2015-July 2017

May

Synthetic Inorganic Chemistry: Biosensors as Anti-Oxidant Pharmaceuticals

Worked with transition metal complexes as mimetics of biological Superoxide Dismutase. Learned molecular characterization techniques and biological activity assays.

Auburn University Cellular and Molecular Biology Summer Research Scholar 2015

Publications

Dukes, M.W., Bajema, L. Whittemore, T. J., Holmgren, R., Meade, T.J. Delivery of Targeted Cobalt(III)-DNA Inhibitors of Gli Transcription Factors for Disruption of Hedgehog Signaling. *Bioconjug. Chem.* **2022**, *33*, 643-653.

Dukes, M.W., Modo, M., Meade, T.J. Non-invasive Detection of Stem Cell Therapies Facilitated by Metal Ion-Based Contrast Agents in *Molecular Biosensors and the Role of Metal Ions (MILS-23)*. Sigel, A., Freisinger, E., Sigel, R.K.O., Eds.; Thomas J Meade, GmbH: Berlin, Germany. In final print stages.

Brue, C.R., **Dukes, M.W.**, Masotti, M., Holmgren, R., Meade, T.J. Disruption of Gli1-DNA Recognition Via a Cobalt(III) Complex. *ChemMedChem*. **2022**, *17*.

Ward, M.; Yu, M.; Scheitler, A.; Zillmann, A.; Gorden, J.; Schwartz, D.; Ivanović-Burmazović, I.; Goldsmith, C. Superoxide Dismutase Mimicry by a Zinc(II) Complex with a Redox-Active Ligand. *Nature Chem*. **2018**, *10*, 1207-1212.

Yu, M.; **Ward, M.B.**; Ambrose, S.L.; Whaley, Z.L.; Bradford, T.M.; Gorden, J.D.; Beyers, R.; Cattley, C.R.; Schwartz, D.D.; Goldsmith, C.R., (2016) Adding a Second Quinol to a Redox-Responsive MRI Contrast Agent Improves its Relaxivity Response to H₂O₂. *Inorg. Chem*. **2017**, *56*, 2812-2826.

Presentations

- Modeling basal cell carcinoma in 3D organotypic raft cultures
Society of Investigative Dermatology Annual Meeting, Portland, Oregon; May 19 2022; poster
- Co(III)-DNA nanoconstructs against mammalian hedgehog signaling
Symposia of the American Chemical Society,; San Diego, California; March 23, 2022; virtual oral presentation
- Modeling Basal Cell Carcinoma in 3D Organotypic Raft Cultures
Northwestern Cancer Club Oral Presentation, December 1, 2021
- Modulating Transcription in Cancer: Cobalt-DNA Conjugates for the Inhibition of Transcription Factors
Lurie Cancer Center's Cancer and Physical Sciences Seminar Series, Virtual Oral presentation, April 22, 2020
- Cobalt-Based Gli Inhibitor Constructs for the Treatment of Basal Cell Carcinoma
- Cobalt-Based Gli Inhibitor Constructs for the Treatment of Basal Cell Carcinoma
Northwestern University Skin Disease Research Center Annual Symposium, July 2018
- Exploring Zinc (II) Compounds as Potential Anti-Oxidant Pharmaceuticals
Auburn Honors College Colloquium, November 1, 2016
- Exploring Zinc (II) Compounds as Potential Anti-Oxidant Pharmaceuticals
Auburn University Spring Research Symposium, April 2016
- Exploring Zinc (II) Compounds as Potential Anti-Oxidant Pharmaceuticals
AU-Cellular and Molecular Biology Summer Research Scholarship Symposium, Auburn University, July 23, 2016

Abstracts

Dukes, M.W., Meade, T.J., Perez-White, B.E. Modeling basal cell carcinoma in 3D organotypic raft cultures. Society of Investigative Dermatology Annual Meeting. Portland, Oregon; 18-20 May 2022.

Dukes, M.W., Whittemore, T.J., Meade, T.J. Co(III)-DNA nanoconstructs against mammalian hedgehog signaling. Symposia of the American Chemical Society,; San Diego, California; 20-24 March 2022.

Ward, M.; Yu, M.; Scheitler, A.; Ivanovic-Burmazovic, I.; Goldsmith, C. Catalysis of superoxide degradation by a Zn(II) complex with a quinol-containing ligand. Conference of The American Chemical Society. New Orleans, LA 18-22 March 2018.

Ronald J Beyers, Dean Schwartz, Tessa Hutchinson, **Meghan Ward**, Nouha Salibi, Christian Goldsmith, and Thomas Denney. Simultaneous Cardiac and Renal oblique-slice T1-Mapping Differentiates Contrast Agent Activity in Normal and Doxorubicin-treated Rats. ISMRM 25th Annual Meeting & Exhibition. Honolulu, Hawaii 22-27 April 2017.

Goldsmith, C.; Yu, M.; **Ward, M.**; Schwartz, D.; Beyers, R.; Cattle, R. Water speciation chemistry and ex vivo cardiac imaging with a redox-responsive MRI contrast agent. Conference of The American Chemical Society. Philadelphia, PA 21-25 August 2016.

Honors and Awards

- Edmund W. Gelewitz Award for Excellence in Research and Service Finalist, 2022
- Ruth L. Kirschstein National Research Service Award Pre-Doctoral Fellow, 2019-present
- National Science Foundation Graduate Research Fellowships Program Honorable Mention, 2019
- Philanthropic Education Organization (P.E.O.) Scholarship Nominee 2019
- Graduated University Honors Scholar from Auburn University, May 2017
- C. Harry Knowles Scholar via Auburn University College of Science and Mathematics, August 2013-May 2017
- Auburn University Presidential Scholar, August 2013-May 2017
- Auburn University Cellular and Molecular Biology Summer Research Scholar 2015

Leadership and Service

Women in Science and Engineering Research (WISER)

May 2018-May 2021

- Spearheaded WISER Resource Navigators initiative to provide a safe and confidential resource board for graduate students who witness or experience violations of discrimination, harassment, or sexual misconduct policy. October 2018-May 2021.
- Serve as outreach co-chair to provide assistance to outreach events in the Chicago area. May 2019-May 2021
- Serve as General Assistance board member May 2018-May 2019

HerStory

April 2018-2022

- Serve as Co-Director for HerStory June 2018-present. Oversaw the expansion to include the University of Chicago as an organization partner for HerStory 2019 and work to maintain that partnership for all future events.
- Volunteered as a presenter for HerStory 2018.

Expanding Your Horizons (EYH) Chicago-Winter

July 2019-January 2020

- Assistant Co-Chair. Assisted in building framework for first EYH Chicago-Winter and assist organizing committee members
- Chair of the Registration subcommittee. Organize the application process for interested students.
- Fundraising subcommittee member. Interface with donors for the event.

Teaching

Graduate Teaching Assistant

September 2017-March 2019

- Graduate level Chemistry of Life Processes Course at NU (CHEM 405): Instructed by Professor Thomas V. O'Halloran, Winter Quarter 2019
- Undergraduate Organic Chemistry 2 and 3 Lab (CHEM 232-1, CHEM 232-2): Instructed by Professor Derek Nelson, Winter and Spring of 2018
- Undergraduate General Chemistry Lecture (CHEM 131): Instructed by Professor Fred Northrup, Fall of 2017
- Undergraduate General Chemistry Lab (CHEM 141): Instructed by Professor Stephanie Knezz, Fall of 2017

Tutor for Northwestern Athletic Department**September 2020-present**

- Lead CLT weekly group classes for athletes. Have lead classes for Organic Chemistry 1, 2, & 3; General Chemistry 1, and Calculus 1. Prepare a lesson plan that covers what students should have learned throughout the week.
- Individual tutor for students participating in my CLTs

Mentorship

Undergraduate Research Mentor

- Graduate student mentor for Olivia Pura, a biology undergraduate student at NU. Trained her in experimental techniques such as nanoparticle synthesis and cell culture, literature research, independent thinking, and ethical practice. December 2018-January 2020.
- Graduate student mentor for Kalea Bartolotto, a biology undergraduate student at NU. Am training her in more advanced cell differentiation assays, biochemical analysis techniques, literature research, scientific writing, and ethical practice. May 2021-present

Northwestern Medical Scientist Training Program Rotation and PhD Student Mentor**July 2019-present**

- Oversaw the summer rotation of Hendryck Gellineau, an MD/PhD student at NU. July 2019
- Graduate student mentor for Hendryck Gellineau, an MD/PhD student at NU. Train him in chemical synthesis and characterization techniques and assisting in the development of his F31 NIH application. July 2021-present

Skills

Chemical

- Synthetic techniques: Organic and inorganic reactions, recrystallization, column chromatography, Thin Layer chromatography, fractional distillation
- Characterization techniques: Nuclear Magnetic Resonance, Mass Spectroscopy, Inductively-Coupled Plasmon Mass Spectroscopy, Infrared Radiation, UV-Visible Spectrometry
- Nanoparticle characterization techniques: Thermogravimetric Analysis, Atomic Force Microscopy, Dynamic Light Scattering, Zeta Potential

Biological

- Cell culture: Sterile technique, culturing of multiple cell types (skin cancer, brain cancer, HeLa, pluripotent fibroblast), *in vitro* assays (flow cytometry, uptake of transition metal therapeutics via Inductively Coupled Plasmon- Mass Spectroscopy, differentiation assays, migration assays, 3D cell differentiation
- Biochemical: Western Blot, quantitative-Polymerase Chain Reaction, Immunohistochemistry
- Protein expression: Growing bacterial cultures, electroporation, SDS-PAGE, Fast Performance Liquid Chromatography, protein quantification
- Other: Confocal microscopy

Software

- Microsoft: Word, Excel, PowerPoint
- Other: Chemdraw, Image J, R-studio

Professional Memberships

- The American Chemical Society
- Phi Lambda Upsilon

References

Professor Thomas J. Meade

Title: Eileen M. Foell Professor of Chemistry, Molecular Biosciences, Neurobiology, Radiology, and Biomedical Engineering; Director of the Center for Advanced Molecular Imaging at NU

tmeade@northwestern.edu

847-491-2481

Northwestern University, Evanston, IL

Professor Bethany Perez-White

Title: Assistant Professor of Dermatology, Co-Director of Skin Tissue Engineering & Morphology Core at NU

bethany.perez-white@northwestern.edu

312-213-4646

Northwestern University, Chicago, IL

Professor Robert A. Holmgren

Title: Professor of Molecular Biosciences; Director of Program in Biological Sciences at NU

r-holmgren@northwestern.edu

847-491-5460

Northwestern University, Evanston, IL

Professor Thomas V. O'Halloran

Title: Charles E. and Emma H. Morrison Professor of Chemistry, Molecular Biosciences, and Medicine; Founding Director of the Chemistry of Life Processes Institute and the Quantitative Biological Imaging Center at NU

t-ohalloran@northwestern.edu

847-491-5060

Northwestern University, Evanston, IL

Dr. Shuji Otsuka

Title: Learning Strategist/Study Skills Coordinator

shuji.otsuka@northwestern.edu

847-644-9393

Northwestern University, Evanston, IL

Professor Christian R. Goldsmith

Title: Professor of Chemistry and Biochemistry

crg0005@auburn.edu

334-844-6463

Auburn University, Auburn, AL